

**University of Alberta**

A study of interactions between an air bubble and a solid surface in a liquid

by

Louxiang Wang

A thesis submitted to the Faculty of Graduate Studies and Research  
in partial fulfillment of the requirements for the degree of

Doctor of Philosophy

in

Chemical Engineering

Department of Chemical and Materials Engineering

©Louxiang Wang

Spring 2013

Edmonton, Alberta

Permission is hereby granted to the University of Alberta Libraries to reproduce single copies of this thesis and to lend or sell such copies for private, scholarly or scientific research purposes only. Where the thesis is converted to, or otherwise made available in digital form, the University of Alberta will advise potential users of the thesis of these terms.

The author reserves all other publication and other rights in association with the copyright in the thesis and, except as herein before provided, neither the thesis nor any substantial portion thereof may be printed or otherwise reproduced in any material form whatsoever without the author's prior written permission.

## **Abstract**

As one of the most critical steps to recover valuable particles from a slurry using flotation, knowledge of the drainage of the thin liquid film between an air bubble and a solid surface is required. The main focus of this thesis is to develop and use an integrated thin film drainage apparatus (ITFDA) to investigate the physicochemical properties of the aqueous liquid film between an air bubble and a solid surface under dynamic conditions.

The ITFDA was designed to measure drainage dynamics of thin liquid films confined between a solid particle, a gas bubble or/and an immiscible liquid droplet. Equipped with a bimorph force sensor, a computer-interfaced video capture device and a data acquisition system, this custom-made ITFDA allowed us to measure directly and simultaneously hydrodynamic forces, true liquid film drainage time under a well controlled external force, receding and advancing contact angles, capillary force, and detachment force between an air bubble or oil droplet and a solid, a liquid or an air bubble in an immiscible liquid. Using a diaphragm of a high frequency speaker as the drive mechanism for the air bubble or oil droplet attached to a capillary tube, this new device is capable of accurately and independently measuring forces over a wide range of hydrodynamic conditions, including bubble approach and retract velocity up to 50 mm/s and displacement range up to 1 mm.

Using this device, interactions between an air bubble and a hydrophilic or hydrophobized glass sphere were measured. The results showed that the ITFDA

was capable to accurately measure hydrodynamic resistance between air bubbles and solid particles in aqueous solutions, providing direct evidence of the critical roles of hydrodynamic forces and particle hydrophobicity in air bubble and particle interactions. The results from this study also showed a close relationship between bubble drive velocity, solid hydrophobicity and force barrier before three phase contact of air bubbles on hydrophobized solids in aqueous solutions. Solution pH, salt concentration and surfactant all have effects on the solid hydrophobicity, and hence change the bubble-hydrophobic solid interactions.

### **Key Words**

Force apparatus, Bubble-particle attachment, thin film drainage, film drainage time, induction time, hydrodynamic force, hydrophobicity, force barrier, oil sands, bitumen extraction.

## Acknowledgements

I would like to thank my supervisors, Dr. Zhenghe Xu and Dr. Jacob H. Masliyah for their guidance and support in conducting this research and throughout each and every stage of my graduate studies. I am grateful for the wonderful opportunities they provided me and the enthusiasm they have devoted towards my work.

I would like to thank Dr. Derek Chan for the collaboration in modeling of the bubble-particle interaction force. I appreciate Mr. Les Dean, Robert Smith and Walter Boddez for their useful discussions and suggestions on the design of the new induction timer. My gratitude also goes to Dr. Trong Dang-Vu for his suggestions on fine particle wettability measurement and Dr. Shengqun Wang for providing the AFM images of glass sphere surfaces. I acknowledge Mr. Jim Skwarok, Ms. Lisa Carreiro, Ms. Shaiu-yin Wu, Ms. Leanne Swekla and Ms. Jie Ru for being accommodating and resourceful on every occasion. I would also like to thank Dr. Alexandre Englert for the cooperation with the review paper, Ms. Meghan Curran and Ms. Meijiao Deng for their contributions on the sea water crude oil project. I thank Ms. Chendi Wu, Mr. Henry Tseng, Mr. Tenny Thomas, Mr. Ren Zhu, Ms. Lujie Yan and all other fellow group members of the Oil Sands Research Group and summer students who worked with me, you made my research experience most enjoyable.

I am thankful for financial support from NSERC Industrial Research Chair in Oil Sands Engineering that covered both tuition fee and living allowance.

Finally, my deepest gratitude goes to my parents and friends. I am forever grateful for the everlasting love and support of my parents and my girl friend. Their trust and confidence in me is my greatest impetus in everything I do.

## Statement of Contributions to Jointly Authored Papers Contained in this Thesis

- (1) Wang, L.; Englert, A.H.; Masliyah, J.H. and Xu, Z. Oil sands processing: Role of colloidal chemistry, *Encyclopedia of Surface and Colloid Science*, Second Edition, Taylor & Francis, **2011**, pp1-7. Wang was responsible for reviewing the bitumen extraction and tailings treatment sections of the paper, and overall organization of the paper; Englert was responsible for the introduction and froth treatment sections of the paper; Masliyah and Xu were responsible for the critics and proof reading.
- (2) Wang, L.; Dang-Vu, T.; Xu, Z. and Masliyah, J.H. Use of short-chain amine in processing of weathered/oxidized oil sands ores, *Energy & Fuels*, **2010**, 24(6), 3581-3588. Wang performed all the experiments and data analysis, and wrote the entire paper; all other authors contributed to the discussions on experimental design and interpretation of the results, and commented on the manuscript.
- (3) Wang, L.; Sharp, D.; Xu, Z. and Masliyah, J.H. Measurement of interactions between solid particles, liquid droplets and/or gas bubbles in a liquid using an integrated thin film drainage apparatus, submitted to *Langmuir*. Wang performed all the experiments and data analysis, and wrote the entire paper; all other authors contributed to the discussion on experimental design and interpretation of results, and commented on the manuscript.
- (4) Wang, L.; Xu, Z. and Masliyah, J.H. Dissipation of film drainage resistance by hydrophobic surfaces in aqueous solutions, submitted to *Proceedings of the National Academy of Sciences*. Wang performed all experiments and data analysis, and wrote the entire paper; all other authors

contributed to the discussion on experimental design and interpretation of the results, and commented on the manuscript.

- (5) Wang, L.; Sharp, D.; Xu, Z. and Masliyah, J.H. A novel induction timer to study interactions between an air bubble and bitumen surface, in *Separation Technologies for Minerals, Coal and Earth Resources*, SME, **2012**, ed. Courtney A. Young and Gerald H. Luttrell, Englewood, CO, pp. 47-55. Wang performed all experiments and data analysis, and wrote the entire paper; all other authors contributed to the discussion on experimental design and interpretation of the results, and commented on the manuscript.
- (6) Wang, L.; Curran, M.; Deng, M.; Liu, Q.; Xu, Z. and Masliyah, J.H. Physicochemical properties of heavy oil/water interfaces in the context of oil removal from sea water by froth flotation, John Wiley & Sons, **2011**, accepted. Wang was responsible for 20% of the experiments and data analysis, and wrote the majority of the paper; Curran was responsible for 60% of the experiments and wrote the introduction part of the paper; Deng was responsible for 20% of the experiments; all other authors contributed to the discussions on experimental design and interpretation of the results, and commented on the manuscript.
- (7) Shahalami, M.; Wang, L.; Wu, C.; Chan, D.; Xu, Z.; Masliyah, J.H. Measurements of hydrodynamic forces and deformations in bubble-solid interactions with the integrated thin film drainage apparatus (ITFDA), *manuscript in preparation*. Wang performed all experiments and data analysis, and wrote 70% of the paper; Shahalami was responsible for the modeling section of the paper and wrote 30% of the paper; Wu and Chan provided supports on the modeling and valuable suggestions; all other authors contributed to the discussion on experimental design and interpretation of the results, and commented on the manuscript.
- (8) Wang, L.; Xu, Z. and Masliyah, J.H. A study of interactions between an air bubble and a hydrophobic glass surface under dynamic conditions,

*manuscript in preparation.* Wang performed all the experiments and data analysis, and wrote the entire paper; all other authors contributed to the discussion on experimental design and interpretation of the results, and commented on the manuscript.

## Table of Contents

Abstract .....	ii
Key Words .....	iii
Acknowledgements .....	iv
Statement of Contributions to Jointly Authored Papers Contained in this Thesis.....	v
Table of Contents .....	viii
List of Tables .....	xiii
List of Figures .....	xiv
Nomenclature .....	xxv
Symbols.....	xxv
Abbreviations .....	xxvii
CHAPTER 1 INTRODUCTION .....	1
1.1 Main Hypothesis and Sub-hypotheses .....	2
1.2 Approach.....	3
1.3 Major Contributions.....	4
1.4 Scope of the Thesis .....	4
1.5 Structure of the Thesis .....	5
CHAPTER 2 OIL SANDS PROCESSING: ROLE OF COLLOID CHEMISTRY .....	8
2.1 Introduction.....	9
2.2 Bitumen Extraction from Oil Sands.....	10
2.2.1 Bitumen-sand interaction (liberation).....	11
2.2.2 Bitumen-bubble interaction (aeration).....	15
2.2.3 Factors influencing bitumen extraction .....	16
2.2.3.1 Effect of slurry pH .....	16
2.2.3.2 Effect of divalent metal cations .....	18
2.2.3.3 Effect of bicarbonate ions .....	21
2.2.3.4 Effect of temperature .....	22

2.2.3.5 Effect of fine clays .....	22
2.2.3.6 Effect of solids hydrophobicity .....	25
2.3 Bitumen Froth Treatment.....	26
2.3.1 Role of bitumen components in stabilizing water-in-diluted-bitumen emulsions .....	27
2.3.2 Reagents for destabilizing water-in-diluted-bitumen emulsions .....	31
2.4 Tailings Treatment .....	32
2.4.1 Characteristics of fine tailings .....	32
2.4.2 Coagulation.....	34
2.4.3 Flocculation .....	36
2.5 Conclusions.....	38
2.6 References.....	39

## CHAPTER 3 USE OF SHORT CHAIN AMINE IN PROCESSING OF

WEATHERED/OXIDIZED OIL SANDS ORES .....	46
3.1 Introduction.....	47
3.2 Materials and Methods.....	50
3.2.1 Materials .....	50
3.2.2 Induction time measurement .....	51
3.2.2.1 Preparation of the bitumen surfaces.....	51
3.2.2.2 Induction time determination .....	51
3.2.3 Bitumen displacement .....	53
3.2.4 Bitumen recovery determination .....	54
3.2.5 Surface characterization of bitumen and solids.....	54
3.3 Results.....	55
3.3.1 Air bubble-bitumen attachment.....	55
3.3.1.1 Induction time measurement in process water.....	55
3.3.1.2 Effect of amine addition on induction time .....	57
3.3.2 Effect of n-butylamine addition on bitumen liberation .....	59
3.3.3 Effect of n-butylamine on bitumen recovery.....	61
3.3.4 Effect of n-butylamine on solid wettability .....	63

3.4 Discussion.....	65
3.5 Conclusions.....	67
3.6 References.....	67

## CHAPTER 4 INTRODUCTION OF THE INTEGRATED THIN LIQUID

FILM DRAINAGE APPARATUS.....	71
4.1 Introduction.....	72
4.2 Instrumentation.....	74
4.2.1 Instrument design.....	74
4.2.2 Operation.....	77
4.3 Materials and Methods.....	82
4.4 Results and Discussion.....	84
4.4.1 Force profiles.....	84
4.4.1.1 Solid-air bubble.....	84
4.4.1.2 Two deformable surfaces.....	93
4.4.2 Image analysis.....	96
4.4.3 Bitumen-air bubble interactions.....	100
4.4.3.1 Induction time.....	100
4.4.3.2 Contact angle.....	100
4.4.3.3 Detachment force.....	102
4.5 Conclusions.....	103
4.6 References.....	104

## CHAPTER 5 PHYSICOCHEMICAL PROPERTIES OF HEAVY

### OIL/WATER INTERFACE IN THE CONTEXT OF OIL REMOVAL

### FROM SEA WATER BY FROTH FLOTATION..... 109

5.1 Introduction.....	110
5.2 Materials and Methods.....	112
5.2.1 Materials and sample preparations.....	112
5.2.2 Measurement of oil/water interfacial properties.....	113
5.2.3 Measurement of coalescence and induction times.....	114
5.2.4 Micro-flotation test.....	116

5.3 Results and Discussion .....	116
5.3.1 Interfacial tension and zeta potentials .....	116
5.3.2 Interactions between oil droplets .....	118
5.3.2.1 Effect of solution pH.....	118
5.3.2.2 Effect of oil droplet size and droplet approach velocity .....	121
5.3.3 Air bubble – oil droplet interactions.....	122
5.3.4 Micro-flotation of crude oil .....	125
5.4 Conclusions.....	126
5.5 References.....	126
CHAPTER 6 STUDYING DYNAMIC FORCES BETWEEN AN AIR	
BUBBLE AND A HYDROPHILIC GLASS SURFACE WITH AN	
INTEGRATED THIN FILM DRAINAGE APPARATUS (ITFDA) .....	
	130
6.1 Introduction.....	131
6.2 Experimental Methods .....	133
6.3 Formulation of the Problem (model) .....	138
6.4 Results.....	141
6.4.1 Bubble-glass interactions in KCl solutions .....	142
6.4.2 Effect of surface tension .....	147
6.4.3 Effect of viscosity.....	151
6.4.4 Effect of bubble drive velocity .....	154
6.5 Discussion.....	156
6.6 Conclusions.....	158
6.7 References.....	159
CHAPTER 7 STUDY OF AIR BUBBLE - HYDROPHOBIC SOLID	
INTERACTIONS USING AN INTEGRATED THIN FILM	
DRAINAGE APPARATUS .....	
	163
7.1 Introduction.....	164
7.2 Materials and Methods.....	167
7.2.1 Materials and sample preparation.....	167
7.2.2 Treatment of glass sphere.....	168

7.2.3 Experimental.....	170
7.3 Results and Discussion .....	174
7.3.1 Effect of bubble drive velocity, V .....	174
7.3.2 Effect of electrolyte concentration and pH.....	177
7.3.3 Effect of solids hydrophobicity .....	179
7.3.4 Effect of surface tension .....	183
7.3.5 Effect of surfactant .....	185
7.4 Reduction of Film Drainage Resistance .....	186
7.5 Conclusions.....	189
7.6 References.....	189
 CHAPTER 8 CONCLUSIONS AND RECOMMENDATIONS FOR FUTURE RESEARCH .....	
8.1 Conclusions.....	196
8.2 Recommendations for future research .....	198
 CHAPTER 9 APPENDIX.....	
9.1 Fabrication of bimorph force sensor .....	201
9.2 Bimorph sensor calibration .....	203
9.3 Data Processing.....	206
9.4 Sensitivity study.....	210
9.5 Contact angle measurement .....	211

## List of Tables

Table 3-1 Composition (wt %) of two weathered oil sands ores .....	50
Table 3-2 Concentration of major ions in the plant recycle process water of pH 7.7.....	51
Table 3-3 Zeta potential (mV) of bitumen and solids in extraction tailings water at pH 8.6 with and without 10 mM <i>n</i> -butylamine addition.....	57
Table 3-4 WDPT (s) for fine solids isolated from different tailings water.....	63
Table 3-5 Solids surface composition (atomic weight percentage) from different ores by XPS.....	64
Table 5-1 Properties and composition of crude oil and water used in this study	113
Table 6-1 Value of key parameters used in this study, either measured or taken from literature. <sup>18, 19</sup> .....	138
Table 6-2 Zeta potential (mV) of air bubble and glass sphere in KCl solutions. <sup>20</sup> .....	138

## List of Figures

<b>Fig. 2-1</b> Bitumen production from oil sands by open-pit mining technology. Reproduced from Gray et al. <sup>2</sup> .....	10
<b>Fig. 2-2</b> Schematic diagram showing the fundamental steps of bitumen liberation and aeration in a hot water extraction process. <sup>4</sup> .....	11
<b>Fig. 2-3</b> Interaction force (F/R) measured by AFM between a silica sphere (of radius R) and a flat bitumen surface as a function of separation distance in 1 mM KCl at different solution pHs. <sup>7</sup> .....	17
<b>Fig. 2-4</b> Induction time of air bubble–bitumen attachment as a function of temperature: (a) in clear process water and (b) in process water containing 0.5% fine solids. <sup>19</sup> .....	19
<b>Fig. 2-5</b> Schematics showing the influence of calcium on silica-bitumen interactions. Negatively charged (a) bitumen and (b) silica surfaces in alkaline solution. (c) Calcium acts as a binder between the silica and bitumen surfaces. <sup>26</sup> .....	20
<b>Fig. 2-6</b> Effect of temperature on the normalized long-range interaction forces (F/R) between bitumen and silica. The inset shows the adhesion forces between bitumen and silica as a function of temperature. <sup>27</sup> .....	23
<b>Fig. 2-7</b> Schematic zeta potential distributions for a binary particulate component system that can be interpreted for particle interactions. (a) Zeta potential distribution of the two components measured separately; (b) binary mixture without attraction; (c) strong attraction (bitumen droplets fully covered and excessive clay particles present); (d) strong attraction (bitumen droplets partially covered with insufficient amount of clay particles). <sup>30</sup> .....	24

<b>Fig. 2-8</b> Water drop (a) formed at the tip of a micropipette and (b) during withdrawal. Surrounding oil phase is composed of bitumen (0.1%) diluted in a heptane/toluene mixture. <sup>50</sup> .....	29
<b>Fig. 2-9</b> The interaction energy profiles between different clay surfaces in 1 mM KCl solution at pH 8.5 in the absence of calcium and magnesium. The basal planes and edge planes have Stern potential (zeta-potential) of -35 mV and -5 mV, respectively. ....	34
<b>Fig. 2-10</b> Effect of slurry pH and calcium addition on zeta-potential of kaolinite in 1 mM KCl solutions. Reproduced from Liu et al. <sup>61</sup> .....	35
<b>Fig. 2-11</b> Measured force (F/R) between two silica surfaces in 20 mM KCl solutions as a function of separation distance: (a) approach, (b) retract. The inset plot in figure (a) shows the force profile at close separation distance. <sup>62</sup> .....	36
<b>Fig. 2-12</b> Measured force (F/R) between clay - silica surfaces as a function of separation distance. <sup>64</sup> The inset shows the clay-silica adhesion forces as a function of Al-PAM dosage. ....	37
<b>Fig. 3-1</b> Schematics of natural surfactant and short-chain amine adsorption at interfaces in an oil sands processing system: (a) bitumen, (b) solids. ....	49
<b>Fig. 3-2</b> Attachment percentage of 20 contacts between air bubble and bitumen as a function of contact time. ....	53
<b>Fig. 3-3</b> (a) Effect of pH and amine addition on the induction time of air bubble-bitumen attachment. The concentration of amine solution is 1 mM; (b) Surface tension of de-ionized water with and without contact with bitumen as a function of pH. ....	56
<b>Fig. 3-4</b> Induction time of air bubble-bitumen attachment as a function of <i>n</i> -butylamine concentration in recycle process water. ....	59

**Fig. 3-5** Photographs of bitumen displacement from a glass surface in a process water at different stages: (a) initial stage of immersing the sample in the process water; (b) and (c) bitumen recession from glass surface in the process water, and (d) equilibrium shape of bitumen in the process water..... 60

**Fig. 3-7** Effect of n-butylamine addition on bitumen recovery from weathered oil sands ores at 35 °C and pH=8.5: (a) ore I; (b) ore II..... 62

**Fig. 3-8** Effect of amine addition on bitumen froth quality: (a) ore I; (b) ore II .. 62

**Fig. 4-1** A schematic view of the integrated thin film drainage apparatus (ITFDA): (a) chamber configuration; (b) description of a piezoelectric bimorph and a high input impedance charge amplifier used to measure the charge generated on the bimorph cantilever under an external force. .... 75

**Fig. 4-2** Calibration of bimorph force sensor with proportional gain of 25 and 125..... 78

**Fig. 4-3A** schematic view of the integrated thin liquid film drainage apparatus (ITFDA). .... 78

**Fig. 4-4** Raw data recorded by the ITFDA between an air bubble and a hydrophilic glass sphere in a 1 mM KCl solution at  $20 \pm 0.5^\circ\text{C}$ : (a) triangular wave generated by the computer and applied to the speaker diaphragm (two successive cycles: 0-4 and 4-8 seconds are shown); (b) corresponding displacement signal of the speaker diaphragm (glass capillary tube); and (c) bimorph response and displacement indicating interactions between air bubble and hydrophilic glass surfaces. .... 79

**Fig. 4-5** A typical force profile as interpreted by bimorph deflection collected during a measurement cycle between an air bubble and a partially hydrophobized glass surface ( $\theta_a = 52^\circ$ ) in 1 mM KCl solutions at pH 7.7 with approach and retract velocity ( $V_a$  and  $V_r$ ) of  $120 \mu\text{m/s}$  at  $20 \pm 0.5^\circ\text{C}$ .

The still images at various key locations of signal profile are shown to help interpret the profile.....	85
<b>Fig. 4-6</b> Glass tube displacement (a) and bimorph response (b) as a function of measurement time between an air bubble and a hydrophobized glass sphere ( $\theta_a = 52^\circ$ ) in a 1mM KCl solution at pH 7.7 with $V_a$ and $V_r$ of 120 $\mu\text{m/s}$ and $T = 20 \pm 0.5^\circ\text{C}$ . The inset in (b) shows the bimorph response during the intervening liquid film drainage and rupture processes.....	86
<b>Fig. 4-7</b> Bimorph response as a function of measurement time between an air bubble and a hydrophobized glass sphere of $\theta_a = 103^\circ$ in 1mM KCl solutions of pH 7.7 with $V_a$ and $V_r$ of 240 $\mu\text{m/s}$ and $T = 20 \pm 0.5^\circ\text{C}$ . The still images at various key locations of force profile are shown to help interpret the force profile. ....	90
<b>Fig. 4-8</b> Bimorph response as a function of measurement time showing the film drainage period with $V_a$ and $V_r$ of 240 $\mu\text{m/s}$ and $T = 20 \pm 0.5^\circ\text{C}$ : (a) between an air bubble and an orphan air bubble on a hydrophobized glass sphere of $\theta_a=103^\circ$ in 1mM KCl solutions at pH 7.7, (b) between an air bubble and a hydrophobized glass sphere of $\theta_a = 103^\circ$ in degassed 1mM KCl solutions. The still images at various key locations of force profile are shown to help interpret the force profile. ....	92
<b>Fig. 4-9</b> Bimorph response as a function of measurement time of an air bubble approaching a crude oil surface in sea water of pH 7.6 at $V_a$ and $V_r$ of 240 $\mu\text{m/s}$ and $T = 20 \pm 0.5^\circ\text{C}$ . The still images at various key locations of force profile are shown to help interpret the force profile. ....	94
<b>Fig. 4-10</b> Bimorph signal profile (raw data) for coalescence time determination of two deformable surfaces using ITFDA with $V_a$ and $V_r$ of 240 $\mu\text{m/s}$ and $T = 20 \pm 0.5^\circ\text{C}$ : (a) two air bubbles in 1 mM KCl solution	

at pH 5.6, with maximum glass tube displacement of 360 $\mu\text{m}$ ; (b) two oil droplets in sea water at pH 7.6.....	96
<b>Fig. 4-11</b> A schematic diagram of imaging analysis to determine dynamic (advancing and receding) contact angles and capillary forces using a vision analysis program built on LabVIEW 8.0: (a) approaching (dynamic receding contact angle) and (b) retracting (dynamic advancing contact angle) in 1mM KCl solution of pH 7.7 at $T = 20 \pm 0.5^\circ\text{C}$ .....	97
<b>Fig. 4-12</b> Validation of the toroidal approximation and the contact angle measurement. (a) Two successive cycles of the triangular movement of glass capillary tube after the TPC between air bubble and hydrophobized glass surfaces; (b) Comparison of the measured and calculated capillary force during this process in 1 mM KCl solution of pH 7.7 at $V_a = V_r = 24 \mu\text{m/s}$ .....	99
<b>Fig. 4-13</b> Effect of pH on induction time of air bubble-bitumen attachment in 1mM KCl solution with approach and retract velocity ( $V_a$ and $V_r$ ) of 240 $\mu\text{m/s}$ at $20 \pm 0.5^\circ\text{C}$ , the diameter of the air bubble and bitumen surface is $1.5 \pm 0.03$ and $4.6 \pm 0.03$ mm, respectively.....	101
<b>Fig. 4-14</b> Effect of pH on receding and advancing contact angle of bitumen surface in 1mM KCl solution at $20 \pm 0.5^\circ\text{C}$ .....	102
<b>Fig. 4-15</b> Effect of pH on bubble-bitumen detachment force and work of adhesion, $\Delta G$ in 1mM KCl solutions at $20 \pm 0.5^\circ\text{C}$ .....	103
<b>Fig. 5-1</b> Bimorph signal profile for coalescence time determination of two oil drops using ITFDA. The inset figure shows the two oil droplets of diameters 1.49 mm (A) and 8.52 mm (B). The measurement was conducted in sea water at pH 7.6 and an approach and retract velocity of 240 $\mu\text{m/s}$ .....	115

<b>Fig. 5-2</b> Interfacial tension of heavy oil/sea water and naphtha/sea water interface as a function of solution pH. ....	117
<b>Fig. 5-3</b> Zeta potential of oil droplets in tap water and sea water as a function of pH. ....	118
<b>Fig. 5-4</b> Coalescence time of heavy oil droplets in tap water and sea water as a function of solution pH at a droplet approach velocity of 240 $\mu\text{m/s}$ . ....	119
<b>Fig. 5-5</b> Effect of upper heavy oil droplet size on coalescence time in sea water at pH 7.6 with oil droplet approach velocity of 240 $\mu\text{m/s}$ . ....	121
<b>Fig. 5-6</b> Coalescence time of heavy oil droplets in sea water at pH 6.0 as a function of drive velocity of the upper oil droplet. ....	123
<b>Fig. 5-7</b> Aging of air bubble on induction time of air bubble-oil droplet attachment in sea water at natural pH of 7.6 and bubble approach velocity of 240 $\mu\text{m/s}$ . Inset shows the effect of pH on induction time. ....	124
<b>Fig. 5-8</b> Photographs of samples: (a) heavy oil in sea water emulsion; (b) tailings of emulsion after 20 min of flotation and (c) sea water. ....	126
<b>Fig. 6-1</b> Schematic diagram of dynamic force measurement between an air bubble and a glass sphere, showing the key geometric configuration of the ITFDA. ....	134
<b>Fig. 6-2</b> Contact mode AFM (Agilent Technologies, Inc., Chandler, AZ) images of clean glass surfaces in air. ....	135
<b>Fig. 6-3</b> Time dependence of the glass tube displacement (a) and the actual glass tube velocity (b) in a measurement cycle with the setting $V_a = -V_r = 33 \mu\text{m/s}$ . ....	136
<b>Fig. 6-4</b> Comparison between the experimentally measured (dash lines) and theoretically calculated (solid lines) interaction forces as a function of $\Delta X$	

in one measurement cycle, between an air bubble and a hydrophilic glass sphere in (a) 1 mM KCl solution of pH 5.6; (b) 1 mM KCl solution of pH 10; (c) 1 mM KCl solution of pH 2 and (d) 100 mM KCl solution of pH 5.6..... 144

**Fig. 6-5** Variations of film thickness  $h(r,t)$ , hydrodynamic pressure  $p^*(r,t)$ , disjoining pressure  $\Pi^*(r,t)$  and film pressure  $p_{\text{film}}^*(r,t)$  in one measurement cycle between an air bubble and a hydrophilic glass sphere in 1 mM KCl solutions of pH 5.6: (a) approach and (b) retract braches. ... 146

**Fig. 6-6** Comparison of the measured and predicted force between an air bubble and a hydrophilic glass sphere as a function of measurement time over a force measurement cycle in 1 mM KCl solutions (a) and ethanol (b) with the bubble drive velocity of 33  $\mu\text{m/s}$ ..... 148

**Fig. 6-7** Film pressure  $p_{\text{film}}^*(0,t)$  of an air bubble approaching a hydrophilic glass sphere as a function of film thickness in liquid of 1 mM KCl and ethanol with bubble drive velocity of 33  $\mu\text{m/s}$ . The film pressure is normalized by the scaling parameters,  $p_c$ , given in **Eqn. 6-8**. .... 149

**Fig. 6-8** Comparison of the film thickness profile  $h(r,t)$  during the approaching of an air bubble towards the glass sphere in liquid of ethanol (a) and 1 mM KCl solutions (b) with bubble drive velocity of 33  $\mu\text{m/s}$ ..... 150

**Fig. 6-9** Comparison of the measured and predicted force between an air bubble and a hydrophilic glass sphere as a function of measurement time over a force measurement cycle in ethanol (a) and silicon oil (b) with the bubble drive velocity of 33  $\mu\text{m/s}$ . .... 152

**Fig. 6-10** Film pressure  $p_{\text{film}}^*(0,t)$  of an air bubble approaching a hydrophilic glass sphere as a function of film thickness in liquid of ethanol and silicon oil with bubble drive velocity of 33  $\mu\text{m/s}$ . .... 153

- Fig. 6-11** Comparison of the film thickness profile  $h(r,t)$  during the approaching of an air bubble towards a glass sphere in liquid of silicon oil (a) and ethanol (b) with bubble drive velocity of  $33 \mu\text{m/s}$ . ..... 153
- Fig. 6-12** Comparison of measured and modeled interaction force between an air bubble and a hydrophilic glass sphere in 1 mM KCl solutions at pH 5.6 as a function of measurement time in a force measurement cycle with bubble drive velocity of (a)  $33 \mu\text{m/s}$  and (b)  $134 \mu\text{m/s}$ . ..... 154
- Fig. 6-13** Film pressure  $p^*_{\text{film}}(0,t)$  of an air bubble approaching a hydrophilic glass sphere as a function of film thickness in 1 mM KCl solutions at pH 5.6 with bubble drive velocity of 33 and  $134 \mu\text{m/s}$ . ..... 155
- Fig. 6-14** Comparison of the film thickness profile  $h(r,t)$  during the approaching of an air bubble towards a glass sphere in 1 mM KCl solutions with bubble drive velocity of (a)  $134 \mu\text{m/s}$  and (b)  $33 \mu\text{m/s}$ . ..... 155
- Fig. 6-15** Effect of bubble drive velocity,  $V$ , surface tension,  $\gamma$ , and viscosity,  $\mu$ , on film pressure  $p^*_{\text{film}}(0,t)$  of an air bubble approaching a hydrophilic glass sphere as a function of dimensionless film thickness,  $h^*(0,t)$ . ..... 157
- Fig. 6-16** Comparison of experimentally measured and theoretically predicted dimple size at different stages of interactions in various sets of experiment conditions. .... 157
- Fig. 7-1** Contact mode AFM (Agilent Technologies, Inc., Chandler, AZ) images of glass surfaces in air: (a) clean glass surface; and (b) treated with 1mM OTS in toluene solution for 10 min. The lower figures show the corresponding cross-section topographic traces of the glass surface. .... 168
- Fig. 7-2** Receding ( $\theta_r$ ) and advancing ( $\theta_a$ ) contact angles of glass surfaces reacted with OTS for different period of time in 1 mM KCl – ethanol solutions as a function of ethanol volume content, at  $T = 20 \pm 0.5 \text{ }^\circ\text{C}$ . The

inset shows the effect of ethanol content on surface tension of 1 mM KCl - ethanol solutions. ....	170
<b>Fig. 7-3</b> A representative glass tube displacement (top) and bimorph signal (bottom) as a function of measurement time between an air bubble and a hydrophobic glass sphere ( $\theta_a = 38^\circ$ ) in 1 mM KCl solutions of pH 5.6. The bubble drive velocity was set at 240 $\mu\text{m/s}$ . Inset graph shows a schematic configuration of the integrated thin film drainage apparatus (ITFDA). ....	172
<b>Fig. 7-4</b> Effect of bubble drive velocity, $V$ , on interaction forces, $F(t)$ , of an air bubble approaching to and retracting from a glass sphere in 1 mM KCl solutions. The receding ( $\theta_r$ ) and advancing ( $\theta_a$ ) contact angle of glass surface were measured to be $21.1 \pm 0.1^\circ$ and $37.4 \pm 0.9^\circ$ , respectively. ....	174
<b>Fig. 7-5</b> Effects of electrolyte concentration and solution pH on air bubble-hydrophobized glass sphere interactions in KCl solutions with $V = 33 \mu\text{m/s}$ . ....	178
<b>Fig. 7-6</b> Effect of glass sphere hydrophobicity on force barrier ( $F_{bar}$ ) between an approaching air bubble and a hydrophobized glass sphere prior to TPC formation in 1 mM KCl solutions at pH 5.6 and $20 \pm 0.5^\circ\text{C}$ as a function of bubble drive velocity, $V$ . ....	180
<b>Fig. 7-7</b> (a) A schematic configuration of the experimental set up; (b) Effect of glass tube velocity (48 - 4800 $\mu\text{m/s}$ ) on the force measurement of the bimorph. ....	181
<b>Fig. 7-8</b> Effect of air bubble drive velocity ( $V$ ) and glass sphere hydrophobicity ( $\theta_a$ ) on induction time of bubble-glass sphere attachment in 1 mM KCl solutions at pH 5.6 and $20 \pm 0.5^\circ\text{C}$ . ....	183

**Fig. 7-9** Effect of surface tension on induction time of air bubble-glass sphere attachment in ethanol - 1 mM KCl solutions as a function of air bubble drive velocity,  $V$ . Numbers in the figure show the hydrophobicity of the glass sphere ( $\theta_a$ ) in corresponding solution. .... 184

**Fig. 7-10** Effect of DF 250 and pH on force barrier ( $F_{bar}$ ) between air bubble and hydrophobized glass sphere attachment before TPC with a function of bubble drive velocity ( $V$ ). The inset photos illustrate the determination of  $\theta_a$  using the image analysis program: (a)  $\theta_a = 51.4^\circ$  in 1 mM KCl solutions at pH 5.6; (b)  $\theta_a = 43.6^\circ$  in 0.03 mM DF 250 + 1 mM KCl solutions at pH 5.6 and (c)  $\theta_a = 22.2^\circ$  in 0.03 mM DF 250 + 1 mM KCl solutions at pH 10. .... 185

**Fig. 7-11** Effect of glass hydrophobicity ( $\theta_a$ ) on film drainage resistance ( $p$ ) between an approaching air bubble and a hydrophobized glass sphere prior to three phase contact formation in a 1 mM KCl solution at pH 5.6 and  $20 \pm 0.5^\circ\text{C}$ . Solid lines show a linear fitting of the pressure as a function of bubble drive velocity. The inset illustrates the effect of glass hydrophobicity on the slope,  $k$ , as given by **Eqn. 7-1**. .... 187

**Fig. 9-1** Photographs of the bimorph force sensor: (a) original ceramic actuator; (b) ceramic actuator with wires removed. The inset in (b) shows the wire connection diagram of the bimorph. .... 201

**Fig. 9-2** Photographs showing the procedures of fabricating the bimorph force sensor. .... 202

**Fig. 9-3** Schematic view of the soldering procedures to solder a wire on to a ceramic actuator surface..... 203

**Fig. 9-4** Photograph of bimorph force sensor used in the experiments. .... 203

**Fig. 9-5** Example of a stable bimorph signal with electrical noise..... 204

<b>Fig. 9-6</b> Example of screen shot showing the change of bimorph signal when placing a small piece of platinum at the end of the bimorph cantilever. ....	205
<b>Fig. 9-7</b> Calibration of bimorph force sensor with proportional gain of 25 and 125.....	205
<b>Fig. 9-8</b> Bimorph signal obtained from a single measurement between an air bubble and a hydrophilic glass sphere in 1 mM KCl solution with bubble drive velocity of 33 $\mu\text{m/s}$ . Black solid line represents the raw signal and the red dash line shows the filtered data. ....	207
<b>Fig. 9-9</b> Processed bimorph signal (solid line) and the interaction force (circle symbol) as a function of measurement time between an air bubble and a hydrophilic glass sphere. The bimorph constant is 15.2 V/mN.....	207
<b>Fig. 9-10</b> Glass tube displacement data, $X(t)$ , obtained from a single measurement. Black solid line represents the raw signal and the red dash line shows the filtered data.....	208
<b>Fig. 9-11</b> Processed glass tube displacement, $X(t)$ , as a function of measurement time in unit of V (solid line) and $\mu\text{m}$ (circle symbol).....	209
<b>Fig. 9-12</b> Interaction force between an air bubble and a hydrophilic glass sphere as a function of glass tube displacement, $X(t)$ . ....	209
<b>Fig. 9-13</b> Four consecutive force curves measured by the ITFDA between an air bubble and a hydrophobized glass sphere of $\theta_a = 37.4^\circ$ in 1 mM KCl solution at pH 5.6. Insets show the signal profiles where the film rupture happened. ....	210
<b>Fig. 9-14</b> A schematic view showing the determination of the contact angle $\theta$ at intersection C between two circles.....	212

## Nomenclature

### Symbols

$V_T$	Total interaction energy, $\text{J}\cdot\text{m}^{-2}$
$V_A$	van der Waals interaction energy, $\text{J}\cdot\text{m}^{-2}$
$V_E$	Electrostatic double layer interaction energy, $\text{J}\cdot\text{m}^{-2}$
$D$	Separation distance between two surfaces, m
$A_{132}$	Hamaker constant of phase 1 and phase 2 through a medium 3, J
$a_1, a_2$	Radii of spherical particles, m
$F_{vdw}$	van der Waals force, N
$F_e$	Electrostatic double layer force, N
$F_h$	Hydrophobic force, N
$F_H$	Hydrodynamic force, N
$F_{ad}$	Adhesive force, N
$R$	Radius, m
$\psi$	Stern potential, mV
$e$	Charge of electron, C
$\varepsilon$	Relative permittivity
$\varepsilon_0$	Permittivity of vacuum, $8.854 \times 10^{-12} \text{ CV}^{-1}\text{m}^{-1}$
$z_i$	Valence of ion $i$ in solution
$n_{i\infty}$	Number density of ion $i$ with valance $z_i$ in the bulk solution
$k_B$	Boltzmann constant, $1.38 \times 10^{-23} \text{ J/K}$
$T$	Absolute temperature, K
$\kappa^{-1}$	Debye length, m
$\mu$	Viscosity of solution, Pa s
$\theta$	Contact angle, degrees
$\theta_r, \theta_a$	Receding and advancing contact angle, degrees
$\theta_e$	Equilibrium contact angle, degrees

$k$	Displacement rate constant, $s^{-1}$
$V$	Glass tube drive velocity, m/s
$F$	Interaction force, N
$Q$	Charge accumulated at the bimorph surface, C
$L, l$	Length, m
$t$	Thickness, m
$d_{31}$	Piezo material charge constant
$y$	Deformation along the central axis, m
$K$	Effective spring constant, N/m
$V_a$	Approach velocity, m/s
$V_r$	Retract velocity, m/s
$\alpha$	Half filling angle of the sphere-capillary bridge, degree
$\gamma_{lv}, \sigma$	Liquid/vapour interfacial tension, mN/m
$F_{bar}$	Force barrier, N
$\Delta P$	Laplace pressure drop across interface, $N/m^2$
$F_C$	Capillary force, N
$\Delta G$	Work of adhesion, J
$h(r,t)$	Film profile or local film thickness, m
$S(t)$	Deflection of bimorph end, m
$X(t)$	Displacement of glass capillary, m
$r_c$	Inner radius of the glass tube, m
$R_b$	Bubble radius of curvature, m
$R_g$	Radius of glass sphere, m
$p(r,t)$	Hydrodynamic pressure in the film relative to the bulk pressure, $N/m^2$
$R_0$	Unperturbed radii of curvature, m
$h_0$	Initial separation distance, m
$\Pi$	Disjoining pressure, $N/m^2$
$r_{max}$	Outer boundary condition, m
$\Delta X_{max}$	Maximum glass tube displacement, m
$T_c$	Critical film thickness, m

## Abbreviations

AFM	Atomic force microscopy
CCD	Charge-coupled device
DF250	Dowfroth 250
DLVO	Derjaguin-Landau-Verwey-Overbeek
DSA	Drop shape analysis
EO	Ethylene oxide
FEP	Fluorinated ethylene propylene
ITFDA	Integrated thin film drainage apparatus
KCl	Potassium chloride
OTS	Octadecyltrichlorosilane
ORS	Organic rich sands
PO	Propylene oxide
SRYL	Stokes-Reynolds-Young-Laplace
TIOM	Toluene insoluble organic matter
TPC	Three phase contact
TPCL	Three phase contact line
XPS	X-ray photoelectron spectroscopy
WDPT	Water drop penetration time
SDS	Sodium dodecylsulfate

# **Chapter 1**

## **Introduction**

Flotation is a very important separation process to recover valuable minerals. This complex process includes many physicochemical and hydrodynamic subprocesses in a dynamic system which consists of solid particles, air bubbles and aqueous solutions with different chemical compositions. The attachment between air bubbles and naturally or artificially prepared hydrophobic particles is one of the most critical sub-processes for the successful flotation. The attachment depends largely on drainage kinetics of intervening liquid film between solid particles and air bubbles in a dynamic system. Although much attention has been focused on understanding and controlling the interactions between colliding air bubbles and particles, a more complete comprehension of the process, especially under dynamic conditions, remains to be established.

### **1.1 Main Hypothesis and Sub-hypotheses**

The main hypothesis addressed in this thesis is *“In a flotation system, the control of the solid surface hydrophobicity and hydrodynamic force is vital for a successful air bubble-particle attachment.”*

The sub-hypotheses in this research are:

- Adsorption of short-chain amine at bitumen/water interface could increase the bitumen hydrophobicity and meanwhile change the hydrophobicity of solids to a minimum extent, thus one would expect an increase of bitumen recovery without a detrimental effect on froth quality.
- As a piezo ceramic actuator, the bimorph was employed for successful force measurements, thus the integration of bimorph force sensor with the conventional induction timer would make a powerful device to study the most important parameters involved in the bubble-solid interactions.
- The dynamic film drainage between deformable surfaces has been successfully modelled using the Stokes-Reynolds-Young-Laplace

equations, thus this model could be employed to model the interaction forces measured by the new device.

- Increase of solid hydrophobicity and decrease of bubble drive velocity could reduce induction time, thus there is a link between the solid hydrophobicity, bubble drive velocity and the film drainage resistance prior to the establishment of a three phase contact.
- Considering the large separation distance between an air bubble and a solid surface, lowering the force barrier or the film drainage resistance before three phase contact on a hydrophobized solid is believed due to the change of solid boundary condition from non-slip to a slip boundary.

## **1.2 Approach**

- Measure the induction time of air bubble-bitumen attachment with three different short-chain amines for different amine concentration and solution pH. Conduct the flotation tests of weathered/oxidized oil sands ores under the condition where the minimum induction time was reached.
- Design and develop a novel induction timer (or integrated thin film drainage apparatus) which is capable of providing direct and simultaneous measurements of hydrodynamic forces, bubble/solid geometrical properties, true film drainage time, receding and advancing contact angles, capillary force, and detachment force between an air bubble or oil droplet and a solid, a liquid or an air bubble in an immiscible liquid.
- Measure the interaction force between an air bubble and a solid surface as a function of bubble drive velocity and solid hydrophobicity in bulk solutions of different chemical and physical properties, meanwhile obtaining all geometrical parameters of the interactions.

- Collaborate with others to model the measured interaction forces using the Stokes-Reynolds-Young-Laplace equations based on the obtained parameters to better understand the interaction.

### **1.3 Major Contributions**

Improving our understanding of thin liquid film stability is of profound importance as it plays a critical role in a broad range of industrial and biological processes. Over the past two decades a various experimental techniques have been developed to quantify the interaction between two surfaces across the liquid film. The main challenge is to develop accurate and reliable methods of controlling the relative motion and at the same time measure variations of the interaction force, surface deformation between the two surfaces and separation distance. Available experimental methods are able to focus on one of aspect of this problem: either the interfacial deformations are measured and the forces are inferred from a model or the forces are measured and a theory is used to deduce the deformations. Moreover, the current available techniques only cover low Reynolds number and high Reynolds number regions. The integrated thin film drainage apparatus (ITFDA) developed through this thesis filled in the small to intermediate Reynolds number regime that is common in mineral and oil recovery applications ( $0.01 < Re < 100$ ). Furthermore, it has the capacity to measure simultaneously time-dependent forces and interfacial deformations without relying on model assumptions and interpretations. There is therefore significant potential in using the design principles of the ITFDA for fundamental and developmental research on the liquid film between bubble-solid, bubble-bubble, bubble-droplet and droplet-droplet surfaces.

### **1.4 Scope of the Thesis**

In the first part of the thesis, the importance of the colloidal chemistry and interfacial science in the oil sands processing was discussed. It was illustrated that by manipulating the interfacial properties, one would be able to improve the bubble-bitumen attachment efficiency and hence bitumen recovery from oil sands.

Although the induction time provides critical information for a flotation system, the inability of measuring the interaction force greatly limits its use in a theoretical study. Hence, an alternative approach needs to be employed. In the second part of the thesis, the integrated thin film drainage apparatus was developed to systematically study the bubble-particle interactions. To illustrate the versatility of the new device, other systems such as air bubble-oil droplet, oil droplet-oil droplet and air bubble-air bubble were also studied. Comparison of measured and predicted interactions between an air bubble and a hydrophilic glass surface was attempted in the third part of the thesis. The model reveals the spatial-temporal evolution of liquid film during the interaction. It also illustrates the accuracy of the force measurement of the bimorph sensor. In the last part of the thesis, the interactions between an air bubble and a hydrophobic glass surface were measured, mainly focus on the effect of solid hydrophobicity and bubble drive velocity on the film drainage resistance.

### **1.5 Structure of the Thesis**

The thesis has been structured in the form of papers. **Chapters 2-7** are published or submitted papers in scientific journal or books. **Chapter 2** is a review paper, while **Chapters 3 to 7** are research papers.

**Chapter 1** presents the overall introduction of the thesis which includes the main hypothesis, sub-hypotheses, approach and the scope of the thesis.

**Chapter 2** provides a comprehensive literature review of the role of colloidal chemistry in processing of oil sands ores using water based extraction technology. (Wang, L.; Englert, A.H.; Masliyah, J.H. and Xu, Z. Oil sands processing: Role of colloidal chemistry, *Encyclopedia of Surface and Colloid Science*, Second Edition, Taylor & Francis, **2011**, pp. 1-7.)

**Chapter 3** illustrates the use of short-chain amine to improve the air bubble-bitumen attachment in the context of processing low recovery oil sands ores. (Wang, L.; Dang-Vu, T.; Xu, Z. and Masliyah, J.H. Use of short-chain amine in

processing of weathered/oxidized oil sands ores, *Energy & Fuels*, **2010**, 24(6), 3581-3588.)

**Chapter 4** introduces the integrated thin film drainage apparatus (ITFDA) developed by the author. This chapter consists of three research papers:

- 1) Wang, L.; Xu, Z. and Masliyah, J.H. Dissipation of film drainage resistance by hydrophobic surfaces in aqueous solutions, submitted to *Proceedings of the National Academy of Sciences*.
- 2) Wang, L.; Sharp, D.; Xu, Z. and Masliyah, J.H. Measurement of interactions between solid particles, liquid droplets and/or gas bubbles in a liquid using an integrated thin film drainage apparatus, submitted to *Langmuir*.
- 3) Wang, L.; Sharp, D.; Xu, Z. and Masliyah, J.H. A novel induction timer to study interactions between an air bubble and bitumen surface, in *Separation Technologies for Minerals, Coal and Earth Resources*, SME, **2012**, ed. Courtney A. Young and Gerald H. Luttrell, Englewood, CO, pp. 47-55.

**Chapter 5** describes the use of the ITFDA to investigate the interfacial properties of heavy oil/sea water interface. (Wang, L.; Curran, M.; Deng M.; Liu, Q.; Xu, Z. and Masliyah, J.H. Physicochemical properties of heavy oil/water interfaces in the context of oil removal from sea water by froth flotation, John Wiley & Sons, **2011**, accepted.)

**Chapter 6** shows the modelling of the interaction forces measured by the ITFDA. (Shahalami, M.; Wang, L.; Wu, C.; Chan, D.; Xu, Z.; Masliyah, J.H. Measurements of hydrodynamic forces and deformations in bubble-solid interactions with the integrated thin film drainage apparatus (ITFDA), *manuscript in preparation*.)

**Chapter 7** discusses the effect of solid hydrophobicity and bubble drive velocity on the bubble-hydrophobized glass interactions. This chapter consists of two research papers:

- 1) Wang, L.; Xu, Z. and Masliyah, J.H. Dissipation of film drainage resistance by hydrophobic surfaces in aqueous solutions, submitted to *Proceedings of the National Academy of Sciences*.
- 2) Wang, L.; Xu, Z. and Masliyah, J.H. A study of interactions between an air bubble and a hydrophobic glass surface under dynamic conditions, *manuscript in preparation*.

**Chapter 8** presents the conclusions of this thesis and recommendations for future research.

The Appendix at the end of the thesis provides more detailed information on the experiments and data analysis of the ITFDA.

# **Chapter 2**

## **Oil Sands Processing: Role of Colloid Chemistry**

## 2.1 Introduction\*

Oil sands are a complex mixture of bitumen (a form of heavy oil), mineral sand, fine clay minerals, water and contained electrolytes. Surface mining method followed by aqueous bitumen recovery represents one of the two principal commercial methods to extract bitumen from this vast natural energy resource. Surface mining method currently constitutes about 60% of total crude bitumen production, which accounts for 30% of the total Canadian oil production (2011). As shown in **Fig. 2-1**, large oil sands lumps are carried to crushers by trucks, where the ores is crushed and mixed with hot water and chemicals to prepare a slurry at 40-50°C.<sup>1, 2</sup> The slurry is then pumped through a 3-5 km hydrotransport pipeline to a Primary Separation Cell (PSC) where the aerated bitumen is collected as bitumen froth at the top of the cell, while the coarse sand falls rapidly to the bottom to form the tailings. The middling stream (mixture of sand, clay and residual bitumen) is sent back to flotation to maximize bitumen recovery. Extracting bitumen from mineable oil sands by water-based extraction method involves colloidal interactions between bitumen and solids in liberation, between bitumen and bubble, solid and bubble, and solid and bitumen (slime coating) in flotation, between water-in-oil droplet and water-in-oil droplet in froth cleaning, and between solid and solid in tailings management. Understanding these colloidal interactions is therefore of great importance for effective bitumen recovery at reduced costs and environmental impact.

The purpose of this chapter is to present an overview on the importance of colloidal chemistry involved in bitumen recovery from oil sands by water-based processes, summarizing the main finding from colloid/interface research related to bitumen extraction (bitumen liberation/aeration) and bitumen froth treatment, as well as treatment of oil sands tailings generated as a waste product of oil sands processing.

---

\*A version of this chapter has been published. Wang, L.; Englert, A.H.; Masliyah, J.H. and Xu, Z. Oil sands processing: Role of colloidal chemistry, *Encyclopedia of Surface and Colloid Science*, Second Edition, Taylor & Francis, **2011**, pp1-7.

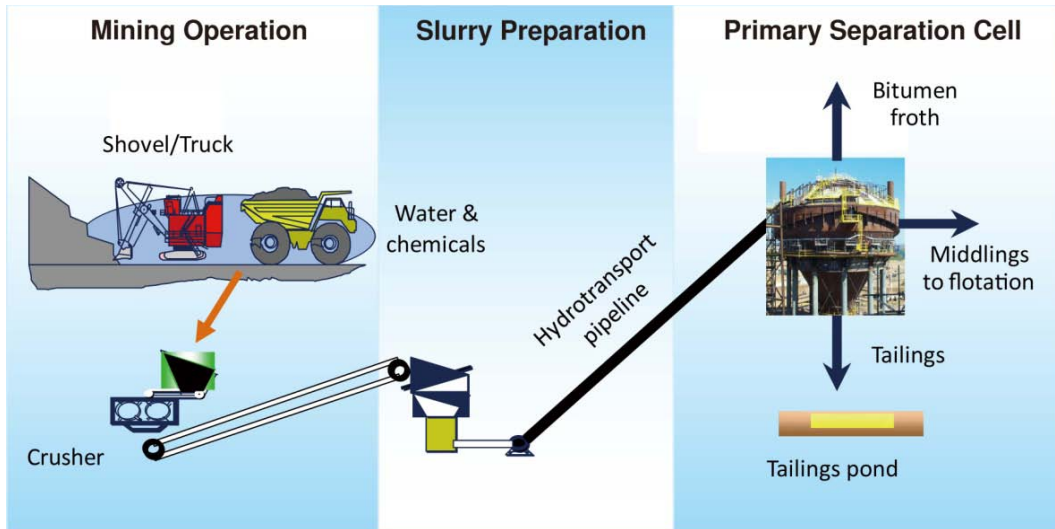


**Fig. 2-1** Bitumen production from oil sands by open-pit mining technology.

Reproduced from Gray et al.<sup>2</sup>

## 2.2 Bitumen Extraction from Oil Sands

In a typical water-based bitumen extraction process, oil sands lumps are mixed with water and process aids (such as sodium hydroxide) to form a slurry.<sup>3,4</sup> During the conditioning of the slurry, bitumen is separated (or “liberated”) from the sand grains. The liberated bitumen attaches to entrained or introduced air bubbles (a step usually called “aeration”) and the bubble-bitumen aggregates float to the top of the slurry, forming a bitumen froth in a process somewhat similar to conventional mineral flotation.<sup>3-5</sup> A schematic diagram summarizing the bitumen liberation and aeration steps is shown in **Fig. 2-2**.

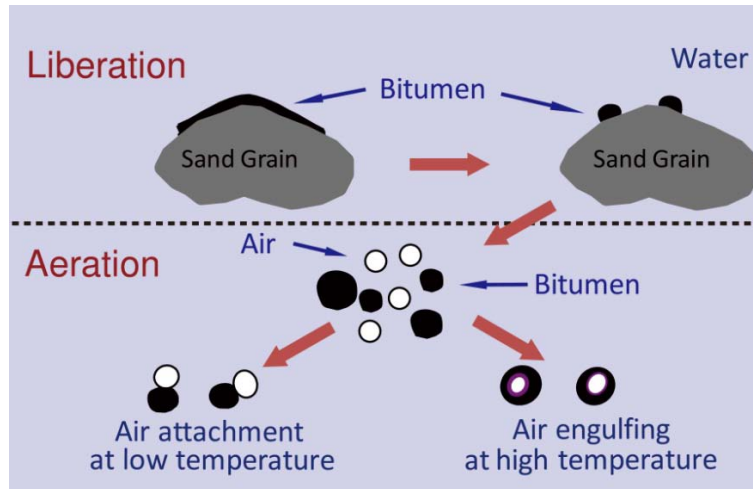


**Fig. 2-2** Schematic diagram showing the fundamental steps of bitumen liberation and aeration in a hot water extraction process.<sup>4</sup>

### **2.2.1 Bitumen-sand interaction (liberation)**

The first fundamental step regarding the separation of bitumen from sand grains is usually called “liberation”.<sup>5-8</sup> For the bitumen to liberate (i.e. disengage) from an individual sand grain, a three-phase contact (TPC) must be first to form. Once a TPC is established, the bitumen recedes to form a globule on the sand grain. Upon formation of a bitumen globule, it can disengage from the sand grain with the aid of mechanical or hydrodynamic forces present in the processing unit. This process of bitumen recession and disengagement from a sand grain is controlled by many factors that include:

- 1) Formation of a TPC line: The formation of a TPC depends on the generation of surface-active agents (i.e. surfactants) from bitumen in the slurry (oil sand + hot water). The generation of these (natural) surfactants is controlled by the pH and multivalent metal ion content of the aqueous phase.
- 2) Bitumen recession along a sand grain surface: The rate of bitumen recession along the sand grain surface is controlled by the viscosity of the bitumen and interfacial tension of the bitumen-aqueous solution, bitumen-sand and sand-aqueous solution interfaces, which dictate the contact angle at the TPC of bitumen, aqueous solution and sand. In turn, the interfacial

properties are influenced by the surfactants and electrolytes present in the system, pH of solution and temperature.

- 3) Bitumen disengagement: Once the bitumen has receded to a globule residing on the sand surface, it needs to be detached from sand surfaces. For a given hydrodynamic condition, the ease of the detachment from sand grains is controlled by the contact angle of the bitumen globule on the sand grain. The contact angle is controlled by the interfacial properties of the system, which are, in turn, controlled by the surfactants present in the system and pH. Clearly, for easy detachment, it is preferable to have a hydrophilic sand surface.

Bitumen liberation from sand grains is controlled by the interaction between bitumen and sand surfaces.<sup>6</sup> The adhesion between bitumen and sand determines the easiness of bitumen detachment from sand grains, while the heterocoagulation between liberated bitumen droplets and solid particles (sand or clay) is controlled by the surface forces acting before contact and also by the adhesion between the surfaces after establishing the contact.<sup>7</sup>

The surface forces between bitumen and solid surfaces can be described by the classical DLVO theory (Derjaguin-Landau-Verwey-Overbeek), where the total interaction energy is given by the summation of van der Waals forces and electrical double layer force:<sup>9,10</sup>

$$V_T = V_A + V_E \quad \text{Eqn. 2-1}$$

The contributions of van der Waals forces to the interaction energy ( $V_A$ ) of two spherical particles of radii  $a_1$  and  $a_2$  interacting in a liquid or gas (medium 3) as a function of separation distance  $D$  can be calculated using the following equation:<sup>10, 11</sup>

$$V_A = -\frac{A_{132}}{6D} \frac{a_1 a_2}{(a_1 + a_2)} \quad \text{Eqn. 2-2}$$

where  $A_{132}$  is the Hamaker constant for the given system and the subscripts represent the particle 1 and 2 in a medium 3. In bitumen liberation, the van der Waal forces of bitumen-silica interaction across water are attractive. This

attractive force is less sensitive to the change of environment, such as temperature and solution chemistry.

The electrostatic potential around a charged surface in an electrolyte solution can be described by Poisson-Boltzmann equation:<sup>10, 11</sup>

$$\nabla^2\psi = -\frac{e}{\varepsilon\varepsilon_0} \sum_i z_i n_{i\infty} e^{-\frac{ez_i\psi}{k_B T}} \quad \text{Eqn. 2-3}$$

where  $\psi$  is the stern potential which is often substituted by the zeta-potential as an approximation;  $e$  is the charge of electron;  $\varepsilon$  and  $\varepsilon_0$  are the relative permittivity of the medium and the permittivity of vacuum respectively;  $n_{i\infty}$  is the number density of ion  $i$  with valance  $z_i$  in the bulk solution;  $k_B$  is the Boltzmann constant and  $T$  is the absolute temperature.

There will be an attractive or repulsive osmotic pressure when two charged surfaces approach each other due to the overlap of the electric double layers. The interaction force  $F_e(D)$  and energy  $V_E$  between two parallel plates at separation distance  $h$  can be expressed by **Eqn. 2-4** and **Eqn. 2-5**, respectively:<sup>10, 11</sup>

$$F_e(D) = n_{i\infty} k_B T \left( \frac{z_i e \psi}{k_B T} \right)^2 - \frac{\varepsilon \varepsilon_0}{2} \left( \frac{d\psi}{dD} \right)^2 \text{ per unit area} \quad \text{Eqn. 2-4}$$

$$V_e = - \int_{\infty}^D F_e(D) dD \text{ per unit area} \quad \text{Eqn. 2-5}$$

Both bitumen and silica surfaces are highly negatively charged at bitumen flotation conditions. A strong electrostatic repulsive force is therefore anticipated. This repulsive force increases with pH due to an increase in negative charges on surfaces, and decreases with increasing electrolyte concentration and presence of divalent cations. Relatively high electrostatic repulsive force compared with small attractive van der Waals forces results in a net repulsive force between bitumen and silica surfaces, which facilitates bitumen liberation from sand grains.

Liu et al.<sup>7</sup> pioneered measurement of interaction forces between a flat bitumen surface (i.e. very thin bitumen layer spin-coated on a silica wafer) and a silica sphere in aqueous solutions using an atomic force microscope (AFM). They reported a stronger repulsive force (before contact between the two surfaces) and weaker adhesion force,  $F_{ad}$  (i.e. pull-off force measured for separating the particle

from the bitumen surface) at higher pH, lower salinity and divalent cation ( $\text{Ca}^{2+}$ ) concentrations, and higher temperatures. Such conditions are favourable for bitumen detachment from the silica surface and for the subsequent stabilization against bitumen-silica heterocoagulation. These authors found that the classical DLVO theory of colloid stability described well the long-range repulsive force measured experimentally, suggesting that the electrostatic double-layer force plays a dominant role in bitumen-silica interactions in aqueous systems.

The adhesion force between bitumen and silica determines the strength of bitumen attachment to silica surfaces, while the long-range interaction force (i.e. non-contact) is crucial for dispersion or heterocoagulation of silica-bitumen colloidal systems.<sup>7, 8</sup> Zhou et al.<sup>8</sup> studied experimentally the effect of natural surfactants present in bitumen on bitumen-silica heterocoagulation by developing a model system composed of dissolved surfactants (dodecylamine or/and palmitic acid) in a hydrocarbon oil (hexadecane). Their results showed that at low pH values, the silica surface was rendered hydrophobic by attracting the positively charged amine head groups of dodecylamine surfactant, thus inducing heterocoagulation of silica with hexadecane drops. At such low pHs, the addition of  $\text{Ca}^{2+}$  ions decreased the extent of heterocoagulation by their adsorption on silica surfaces, setting up a barrier for the cationic amine group to interact with silica.<sup>8</sup> Over the alkaline pH range, the authors found that palmitic acid did not induce oil-silica heterocoagulation that was observed when calcium ions were present. They suggested that, at high pH ( $> 10$ ), specifically adsorbed  $\text{CaOH}^+$  ions on the silica surface interact with anionic carboxylate groups of surfactant (palmitic acid) on the oil surface, bringing together the oil droplets and silica particles. A good agreement in heterocoagulation between bitumen and silica and between oil (with dissolved surfactants) and silica was obtained only when both surfactants (cationic and anionic) were present in the oil, suggesting a synergistic effect of various surfactant constituents.<sup>8</sup>

### ***2.2.2 Bitumen-bubble interaction (aeration)***

As illustrated in **Fig. 2-2**, the liberated bitumen droplets remain suspended in the slurry due to its similar density to water. Air bubble, used as carrier, is generated and attached to bitumen surfaces to create a bitumen-bubble aggregate, known as aerated bitumen. This aerated bitumen has much lower density than the slurry, and thus get floated to the top of the slurry where it is collected as bitumen-rich froth. In low temperature processes, the bitumen droplets simply attach to air bubbles, while at high temperatures the bitumen engulfs air bubbles due to a decrease of the bitumen viscosity.

The bitumen-bubble attachment includes collision of the air bubble with bitumen droplets, thinning of the intervening liquid film between these two surfaces and stability of the aggregates. The air bubble-bitumen collision is determined by the hydrodynamic properties of the flotation machine, which is normally unchanged. The bitumen spreads on the bubble surface to form a bitumen-engulfed air bubble upon bitumen-bubble attachment in hot water extraction process, where detachment of bitumen-bubble is unlikely to happen. Hence, the attachment of air bubbles to bitumen droplets is the limiting step to extraction of bitumen from oil sands.

When an air bubble approaches a bitumen droplet, the affinity of water to air bubble and bitumen surfaces will create a barrier to resist the thinning of the intervening liquid film. This barrier is mainly the result of the surface forces and hydrodynamic force between the two surfaces.<sup>10, 12</sup> It is well documented that both bitumen droplets and air bubbles are highly negatively charged at bitumen flotation conditions.<sup>13-15</sup> As a result, the electrical double layer force between a bubble and a bitumen surface is strongly repulsive. Furthermore, the van der Waal forces of bitumen-bubble interaction across water are also repulsive, although smaller than that for typical mineral-air interactions. Based on the classical DLVO theory, an infinitely high repulsive barrier is anticipated, which is obviously inappropriate as it would not predict the observed air-bitumen attachment. The extended DLVO theory should therefore be used,<sup>10,12,16</sup> which, in addition to the

van der Waals force and electrical double layer force components, considers attractive hydrophobic force, repulsive hydration force, repulsive steric force,<sup>17</sup> and attractive bridging force.<sup>18</sup> The attractive force that originates from the surface hydrophobicity is the main driving force for bitumen-bubble attachment.

The attachment of air bubbles to bitumen droplets can be divided into the sub-processes of thinning and rupture of the intervening liquid film, followed by spreading of the TPC line to a stable state. The time needed for the attachment to occur is known as the induction time. Apparently, there will be no attachment unless the contact time between bubble and bitumen droplet upon collision is longer than the induction time. It is well established that the induction time between air bubble and bitumen is determined by the interfacial properties of bitumen/water and air/water interfaces.<sup>14, 19, 20</sup> Decreasing the repulsive force and/or increasing the attractive force will lower the energy barrier and result in a smaller induction time. Factors such as slurry pH, aqueous ionic strength, high-valence electrolyte and temperature, which affect the interfacial properties of bitumen/water and air/water interfaces, on bitumen-bubble attachment will be discussed from a colloid chemistry perspective.

### ***2.2.3 Factors influencing bitumen extraction***

#### ***2.2.3.1 Effect of slurry pH***

Solution pH is a critical operating parameter in bitumen recovery and, in most cases, the controlling parameter for surface charges.<sup>4, 7</sup> The effect of pH on the interaction force between bitumen and silica immersed in a 1 mM KCl solution, measured directly with an AFM, is shown in **Fig. 2-3**.<sup>7</sup> As shown in **Fig. 2-3**, the long-range force profiles for pH values higher than 3.5 were monotonically repulsive and the repulsion increased with increasing pH. For a pH of 3.5, a weak long-range repulsive force was observed. At separations greater than 2-5 nm (approximately), the measured force profiles were reasonably well fitted by the classical DLVO theory, suggesting that the force measured was dominated by electrostatic double-layer interactions. However, at short separation distances

(lower than 2-5 nm), an additional repulsive force was observed and attributed by the authors to a polymer-like steric force.

To fully understand interactions of colloidal particles in a dynamic system, the adhesion forces have to be considered.<sup>7</sup> The adhesion (pull-off) force between bitumen and silica is shown in the inset of **Fig. 2-3**, where a decrease of adhesion force with increasing pH is observed. The close correspondence between the long-range interactions and adhesion forces shows the important role of interfacial chemistry in controlling colloidal interactions between bitumen and silica particles.<sup>7</sup>

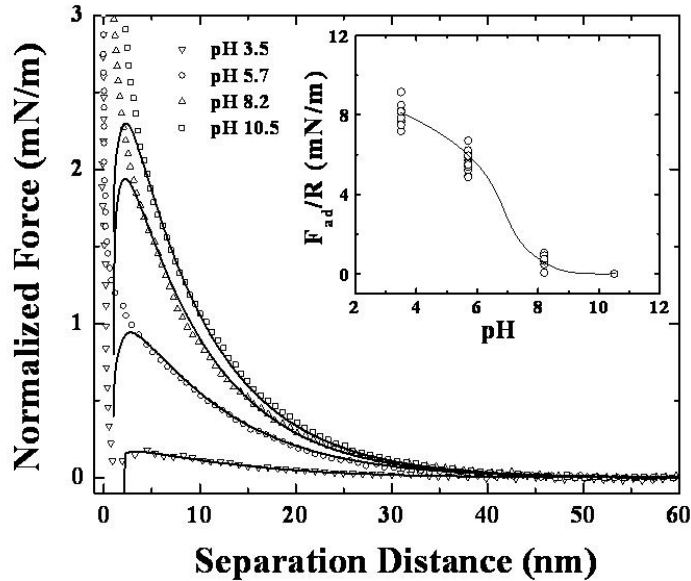


**Fig. 2-3** Interaction force ( $F/R$ ) measured by AFM between a silica sphere (of radius  $R$ ) and a flat bitumen surface as a function of separation distance in 1 mM KCl at different solution pHs. Solid lines represent DLVO model fittings and the inset shows the adhesive force ( $F_{ad}/R$ ) as a function of pH.<sup>7</sup>

The induction time of air bubble-bitumen attachment was measured in process water (water that is recycled from an oil sands tailings pond) to study the effect of pH on bitumen aeration. The induction time is determined as the minimum contact time needed for an air bubble attaches to the bitumen surface. It has been found that the induction time changed marginally between pH 8 and 9, and increased dramatically with a further increase of pH above 9.<sup>14</sup> In the study by Liu et al.,

contact angle was also found to remain unchanged at pH below 8 and decrease significantly at pHs higher than 8.<sup>6</sup> Such changes at high pH are related to the increased adsorption and enhanced dissociation of natural surfactants at bitumen/water and air/water interfaces. More surfactants are released from bitumen to aqueous solutions with increasing pH higher than 9, which reduces bitumen/water and air/water interfacial tensions.<sup>14</sup> The dissociation of natural surfactants at bitumen/water interface makes the bitumen and air bubble more negatively charged and less hydrophobic. Thus, an increase in repulsive double layer force and a reduction in hydrophobic forces between air bubble and bitumen surfaces make their attachment more difficult at high pH.

High repulsion and low adhesion force between bitumen and silica surfaces indicate that a high pH is favourable for bitumen liberation. However, at this condition, the reduction of interfacial tension and bitumen hydrophobicity increases the induction time of bitumen-bubble attachment and reduces the tendency of bitumen coagulation/coalescence<sup>21</sup>, which are not favourable for bitumen aeration. Currently, bitumen extraction from oil sands is commercially operated at pH around 8.5 to compromise between bitumen liberation and aeration. The recent laboratory study showed optimization of bitumen recovery by decoupling liberation and aeration and by using short chain amines.<sup>14</sup>

#### 2.2.3.2 Effect of divalent metal cations

Calcium ion ( $\text{Ca}^{2+}$ ) is one of the divalent ions normally present in an aqueous-based bitumen extraction system.<sup>4, 7</sup> A significant amount of  $\text{Ca}^{2+}$  is introduced into the bitumen extraction system by recycling the water from tailings treatment, in which gypsum ( $\text{CaSO}_4 \cdot 2\text{H}_2\text{O}$ ) is added as a process aid.<sup>4, 7</sup> Liu et al.<sup>7</sup> reported that the measured long-range repulsive force between a silica sphere and a bitumen surface in aqueous electrolyte solutions was much more significantly reduced with increasing calcium ion concentration than with increasing monovalent electrolyte (KCl) concentration.<sup>7</sup> Such change of interaction force behaviour can be simply attributed to a diminished electrical double-layer repulsive force due to the specific adsorption of calcium ions on the silica and

bitumen surfaces, reducing the magnitude (and even reversing the sign, depending on the  $\text{Ca}^{2+}$  concentration) of the negative surface charges.<sup>7</sup> According to Liu et al.<sup>7</sup> calcium ions have specific affinity for a bitumen surface mainly through the binding with carboxylic groups of natural surfactants contained in bitumen.

Several authors reported from experimental findings that calcium and magnesium ions in the process water have a detrimental effect on bitumen recovery when using a hot water extraction process.<sup>22, 23</sup> Fong et al.<sup>22</sup> found that on a weight basis,  $\text{Mg}^{2+}$  had a more pronounced (negative) effect on bitumen recovery than  $\text{Ca}^{2+}$  ions. However, a marginal effect of  $\text{Ca}^{2+}$  and/or  $\text{Mg}^{2+}$  content alone on bitumen recovery was also reported.<sup>24, 25</sup> Based on AFM studies, both Liu et al.<sup>7</sup> and Zhao et al.<sup>26</sup> found that calcium and magnesium have a negative effect on bitumen liberation by increasing bitumen-silica adhesion and depressing the long-range repulsion between the two surfaces in aqueous solutions.<sup>7, 26</sup>

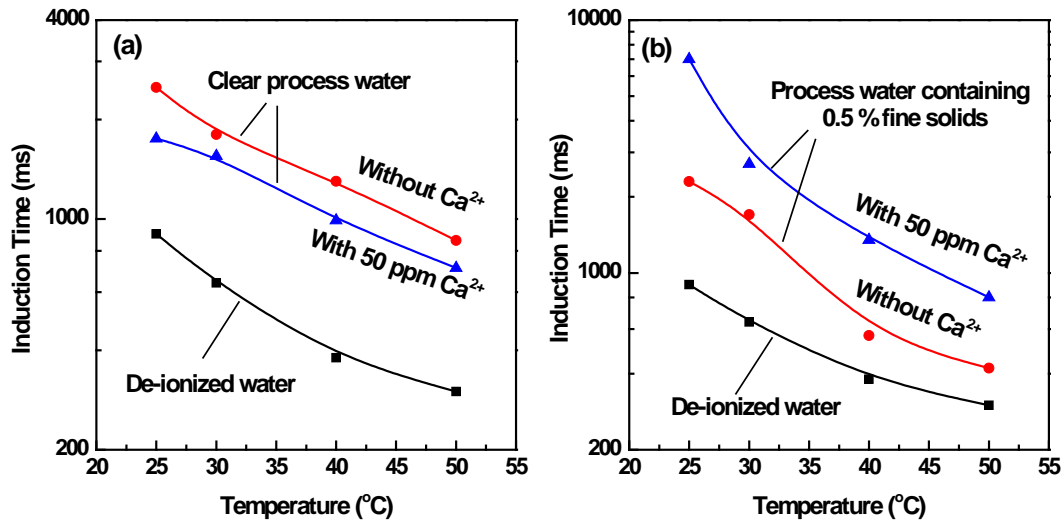


**Fig. 2-4** Induction time of air bubble-bitumen attachment as a function of temperature: (a) in clear process water and (b) in process water containing 0.5% fine solids. De-ionized water is used as a reference. Reproduced from Gu et al.<sup>19</sup>

Air bubble surface is also negatively charged. In the absence of fine solids, the introduction of divalent cations into the solution depresses the energy barrier between air bubble and bitumen surfaces, contributing to an easier attachment between the air bubble and bitumen. As shown in **Fig. 2-4(a)**, the presence of 50

ppm calcium ions led to a lower induction time of air bubble-bitumen attachment. In the presence of fine solids, the introduction of calcium ions led to a higher induction time. This increase in induction time is most probably due to the fact that the solids coated bitumen surfaces and possibly air bubbles, forming a slime coating, thereby causing the difficulties in bitumen-air bubble attachment and hence increasing the induction time.

Silica and bitumen surfaces are both negatively charged at alkaline pH as shown by the schematics of **Fig. 2-5(a)** and **b** (bitumen and silica surfaces).<sup>26</sup> When divalent cations are present in the aqueous solution, they act as binders to connect the negatively charged silica and bitumen surfaces together (**Fig. 2-5(c)**), leading to a strong adhesion force and hence poor liberation. For bitumen and bubble surfaces in the presence of fine solids, the presence of divalent cations results in a longer induction time and poor aeration. It is clear that the presence of calcium in industrial operations is detrimental to bitumen recovery.

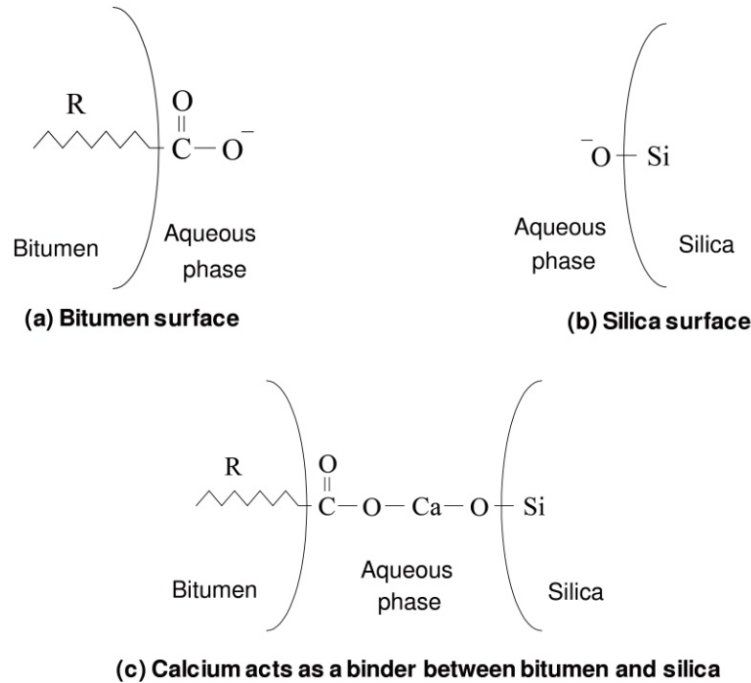
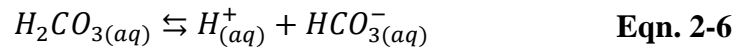


**Fig. 2-5** Schematics showing the influence of calcium on silica-bitumen interactions. Negatively charged (a) bitumen and (b) silica surfaces in alkaline solution. (c) Calcium acts as a binder between the silica and bitumen surfaces.<sup>26</sup>

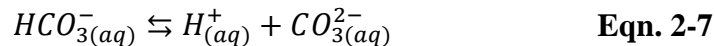
### 2.2.3.3 Effect of bicarbonate ions

Bicarbonate ( $\text{HCO}_3^-$ ) ions are a dominant anionic species in recycle process water used in industrial bitumen extraction.<sup>4</sup> Its concentration can reach up to 600-650 mg L<sup>-1</sup> in some industrial plant operations.<sup>4</sup> Zhao and co-workers conducted experimental studies on the influence of bicarbonate ions on bitumen extraction and concluded that they are good process aids in buffering the extraction slurry, precipitating  $\text{Ca}^{2+}$  from the extraction process water, dispersing fine solids, and decreasing solid-bitumen adhesion.<sup>4</sup>

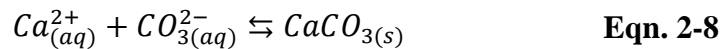
The presence of bicarbonate ions can affect the slurry pH and soluble calcium ion concentration (and/or magnesium).<sup>4</sup> Bicarbonate is an essential component of a pH buffering system at alkaline pH values, providing resistance to pH changes. For example, if a small amount of (strong) acid is added into the water having bicarbonate ions, the equilibrium of the following chemical reaction (**Eqn. 2-6**) will be driven to the left to counterbalance the increase in the hydrogen ion concentration:<sup>4</sup>



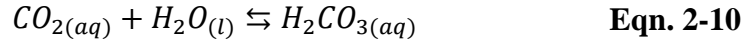
Also, the following chemical equilibrium **Eqn. 2-7** is applicable in an aqueous solution containing bicarbonate:



Therefore, the divalent cations (e.g.  $\text{Ca}^{2+}$ ) in the solution can react with the carbonate ( $\text{CO}_3^{2-}$ ) ions to form a precipitate of calcium carbonate (calcite):



Since  $\text{Ca}^{2+}$  ions act as bridging ions to connect the negatively charged silica and bitumen surfaces (see “Effect of divalent metal cations” subsection and **Fig. 2-5**), leading to a strong adhesion force between silica and bitumen, one can see that the precipitation of calcium carbonate (**Eqn. 2-8**) due to the presence of bicarbonate ions in the aqueous solution is beneficial to bitumen liberation from sand grains. Another important source of carbonate ions for such precipitation to occur comes from dissolution of atmospheric  $\text{CO}_2$ ,<sup>4</sup> where the following additional chemical equilibria are applicable (open system):



#### 2.2.3.4 Effect of temperature

Temperature is another critical operating parameter in bitumen extraction using the hot water process. The interaction forces between bitumen and silica at different temperatures were measured using AFM.<sup>27</sup> As shown in **Fig. 2-6**, the long-range repulsive forces between bitumen and silica surfaces increased with temperature and the adhesion between the two disappeared when the temperature was higher than 31°C. It is conceivable that such change is due to an increase in surface charge density at the bitumen/water and solid/water interfaces with increasing temperatures, caused by an enhancement in migration of natural surfactant molecules through the bitumen phase to the bitumen/water interface and an increase of solid hydrolysis. **Fig. 2-4** shows a decrease in induction time of bubble-bitumen attachment with temperature for all the different aqueous solutions. The induction time reduced from 7000 ms to 1000 ms in industrial process water containing 0.5 % fine solids when the temperature was increased from 25°C to 50°C. Correspondingly, the bitumen recovery increased dramatically from 10 % to 90 %, showing a vital impact of process temperature on bitumen recovery.<sup>28</sup>

#### 2.2.3.5 Effect of fine clays

The content of fine solids in an oil sand ore is well-documented to affect its processability.<sup>4</sup> The strong attachment of fine particles (“fines”) on bitumen is responsible for low bitumen flotation recovery.<sup>6</sup> Kasongo et al. found that when  $Ca^{2+}$  ion was present in concentrations above 30 mg L<sup>-1</sup> together with the addition of 1 wt% of montmorillonite clay, a sharp reduction in bitumen recovery was observed.<sup>24</sup> Ding et al. observed a similar effect when adding illite clay in the presence of divalent cations.<sup>25</sup> Basu et al. found experimentally a negative synergistic effect of clays and divalent cations in decreasing bitumen liberation from a glass surface.<sup>29</sup>

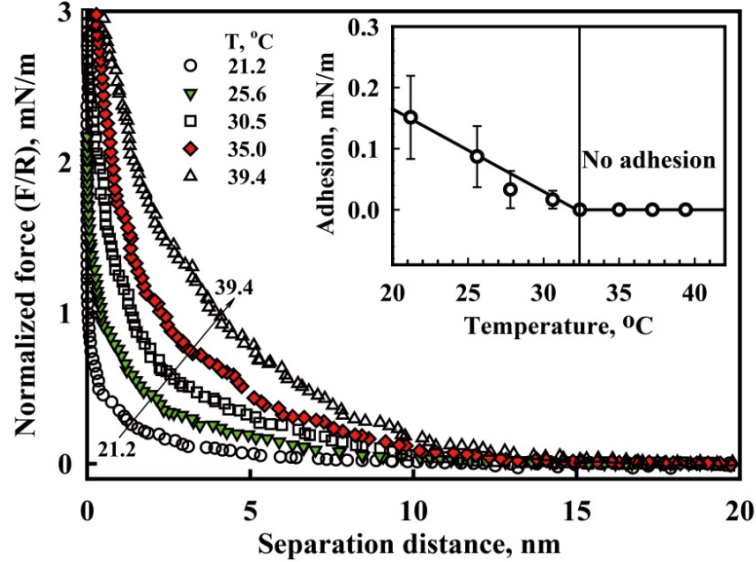


**Fig. 2-6** Effect of temperature on the normalized long-range interaction forces (F/R) between bitumen and silica. Here F and R are the force and the radius of the probe particle, respectively. The forces were directly measured in an industrial process water using an atomic force microscope (AFM). The inset shows the adhesion forces between bitumen and silica as a function of temperature.<sup>27</sup>

From zeta potential distribution measurements, Liu et al.<sup>30</sup> investigated the interactions between bitumen and clays in an aqueous solution. For a single component aqueous suspension (i.e. bitumen drops or montmorillonite clay particles), a single modal zeta potential distribution was obtained under a given solution condition (see **Fig. 2-7(a)**). In the absence of added calcium ( $\text{Ca}^{2+}$ ) ions, a mixture of bitumen emulsion and montmorillonite clay suspension exhibited two distinct zeta potential distribution peaks, corresponding to the peaks measured individually for the bitumen and montmorillonite clays, respectively (**Fig. 2-7(b)**). However, when calcium ions (1mM) were added to the dispersion mixture, only one zeta potential distribution peak was observed (**Fig. 2-7(c)** and (d)). In such case, a higher clay/bitumen ratio caused the peak to shift towards the value for montmorillonite clay suspensions (**Fig. 2-7(c)**).

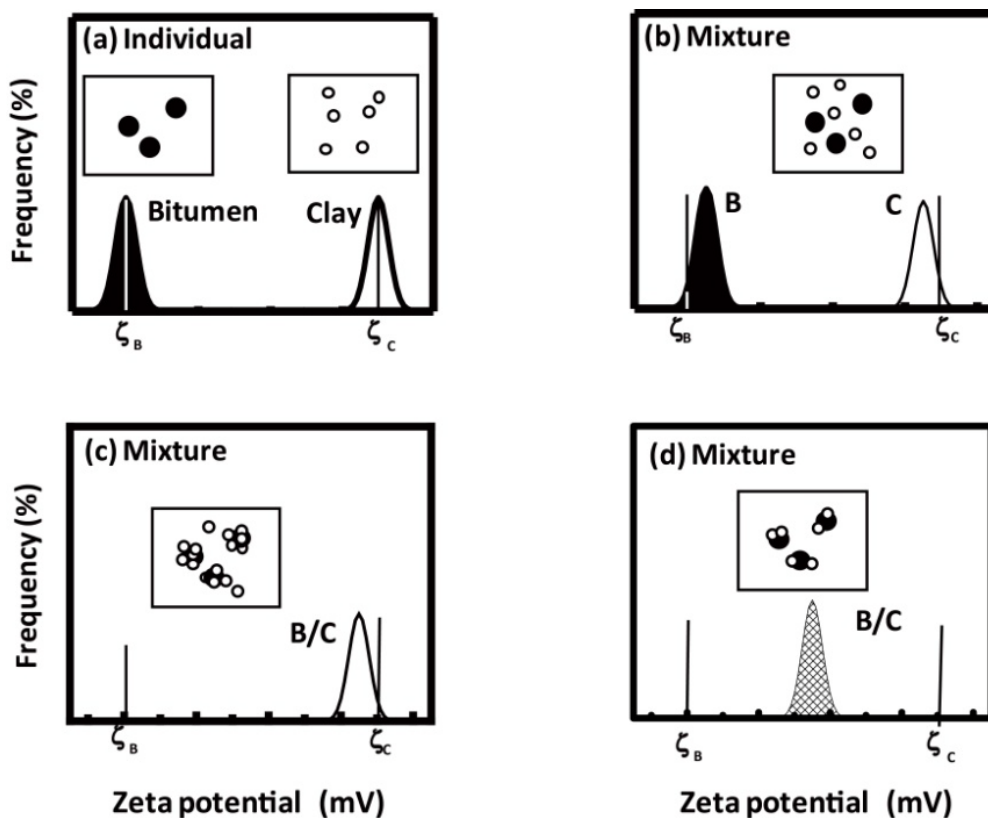


**Fig. 2-7** Schematic zeta potential distributions for a binary particulate component system that can be interpreted for particle interactions. In this figure, the black and white circles represent bitumen droplets and clay particles, respectively. (a) Zeta potential distribution of the two components measured separately; (b) binary mixture without attraction; (c) strong attraction (bitumen droplets fully covered and excessive clay particles present); (d) strong attraction (bitumen droplets partially covered with insufficient amount of clay particles).<sup>30</sup>

For kaolinite clay, the authors reported that the addition of 1 mM calcium ions did not cause a substantial change in the bimodal zeta potential distribution of the mixture, suggesting qualitatively a stronger interaction of bitumen with montmorillonite clay than with kaolinite. They concluded that the commonly observed depression of bitumen flotation by montmorillonite (but not by kaolinite clay) addition in the presence of  $\text{Ca}^{2+}$  correlated well with the differences in the measured zeta potential distributions, which showed itself to be a powerful tool to study slime coating phenomena in complex colloidal systems.<sup>30</sup> Slime coating, a

terminology used to describe the coverage of valuable mineral with fines in mineral processing language, is detrimental to bitumen aeration as the coverage of hydrophilic fines on bitumen surfaces changes the hydrophobic bitumen surface to a hydrophilic nature.

As shown in **Fig. 2-4(a)** in the absence of fine solids in process water, the addition of calcium ions slightly reduced the induction time of bubble-bitumen attachment. In contrast, the presence of fine solids increased the induction time considerably when calcium ions were introduced. The reason is clear: calcium ions triggered the slime coating of hydrophilic fines on bitumen surfaces and increased the induction time of bubble-bitumen attachment, leading to the observed depression of bitumen recovery.

#### 2.2.3.6 Effect of solids hydrophobicity

The important role of solid wettability in bitumen recovery has been well documented.<sup>22,31,32</sup> The wettability (hydrophobicity) of mineral solids isolated from different Athabasca oil sands ores were determined by water drop penetration time measurement and partitioning test. It was found that the presence of hydrophobic solids in oil sands ores depresses bitumen recovery.<sup>33</sup> By directly measuring the colloidal interaction forces between bitumen and solid particles isolated from oil sands ores, Ren et al.<sup>34</sup> observed that the weathering of oil sand ores increases hydrophobicity of solids contained in the ore. Such increase in solids hydrophobicity reversed the long-range interaction forces between bitumen and solids from repulsive to attractive, with a corresponding increase in the adhesion force. Similar results were observed when measuring the interaction forces between bitumen and solids isolated from poor processing oil sands ores. The attractive long-range force and increased adhesion force make the separation of bitumen from solids more difficult and the attachment of fine solids on liberated bitumen easier, thereby leading to poorer bitumen liberation and lower aeration efficiency, respectively. The heterocoagulation of fines and bitumen leading to slime coating of fines on bitumen was proved by zeta-potential distribution measurement.<sup>6</sup>

## 2.3 Bitumen Froth Treatment

The purpose of bitumen froth treatment, or in other words bitumen froth cleaning, is to remove water and solids present in the bitumen froth, collected as product from PSC, flotation cells, and hydrocyclones in water-based extraction processes. Most of the free water and solids in the bitumen froth can be easily removed. However, even after use of centrifuges and several stages of settling, there remains some emulsified water within the diluted bitumen. Such water-in-diluted bitumen emulsions have been a major concern in the oil sands industry because the chloride ions in the emulsified water droplets can adversely affect downstream bitumen upgrading to sweet crude oil.<sup>35, 37, 38</sup> The presence of entrained fine solids in the bitumen fed to an upgrader can cause problems such as equipment fouling and reactor plugging.

Bitumen froth contains typically 60% bitumen, 30% water and 10% solids by weight.<sup>1,35,36</sup> To facilitate the separation of water and solids from the froth, naphtha or paraffinic solvents are used in the bitumen froth treatment (i.e. bitumen froth cleaning). In the paraffinic froth treatment, water droplets and fine solids aggregate with the precipitated asphaltenes, which act as a binder between the emulsified water drops and fine solid particles. The aggregates settle quickly, producing nearly dry and clean supernatant (diluted) bitumen. However, in the naphtha-based froth treatment process, typically 2-5% emulsified water and 0.3-1% solids (by weight) remain in the diluted bitumen product.<sup>35</sup>

It is widely reported that the stability of water-in-oil emulsions is steric in nature. The stabilization of the water drops has been attributed to accumulation of various surface active species at oil/water interfaces present in bitumen, such as asphaltenes, resins, saturates and aromatics along with suspended fine solids in the ores. It has been shown by many researchers that asphaltenes and/or fine solids form a steric interfacial film covering the water drops, thereby providing stabilization against water drop coalescence.<sup>39, 40</sup> Such components adsorbed at the water/oil interface create a protective shield around the water drops.

In order to eliminate the emulsified water, it is necessary to bring the water droplets in contact either by coagulation or flocculation. The subsequent coalescence of water droplets would greatly enhance water removal from emulsions. To achieve both flocculation and coalescence, chemical aids (demulsifiers) are added, aiming at weakening the steric barrier between the water drops and inducing their coalescence.

### ***2.3.1 Role of bitumen components in stabilizing water-in-diluted-bitumen emulsions***

Several studies have been carried out to understand the role of bitumen components (e.g. asphaltenes, resins and other naturally occurring surfactants) and suspended fine solids in stabilizing water-in-diluted-bitumen emulsions.<sup>37, 40-45</sup> The stability of water-in-oil emulsions is believed to originate from a steric asphaltene-rich interface at the emulsified water droplet surface.<sup>35, 41</sup>

Asphaltenes, the highest molecular weight fractions of bitumen, are soluble in light aromatic hydrocarbons (i.e. toluene and benzene) but insoluble in paraffinic solvents (i.e. hexane, heptane and pentane).<sup>38, 41</sup> Asphaltenes are adsorbed slowly and irreversibly at the (organic solvent) diluted-bitumen/water interface and to form rigid films that resist the deformation of the interface.<sup>46</sup>

“Washing” experiments, where water is mixed with (hexane/toluene) diluted-bitumen, followed by proper liquid/liquid separation in subsequent steps, were conducted by Yan et al.<sup>44</sup> and Xu et al.<sup>39</sup> The main conclusions drawn from such experiments were that the surface active materials present in the diluted bitumen were “washed” away in the first several mixing/separation steps, and that no further surface active material was present in the washed diluted bitumen when water was subsequently added, as shown by unsuccessful emulsification of added water. It is evident that during the washing stage, the water/diluted bitumen interface of the emulsified water droplets acts as a milieu for the collection of surface-active material, including fine solids, present in the bulk diluted bitumen.<sup>44</sup> Similar experiments were conducted by Gu et al.<sup>47</sup> In their study, element analyses were conducted together with emulsion stability tests. The

authors found that the asphaltene fractions of lower H/C ratio (i.e. more aromatic) and higher O/C ratio (i.e. more polar characteristics) contributed to the stability of water-in-toluene-diluted-bitumen emulsions.

A micropipette technique was utilized by several researchers to qualitatively study the water/diluted-bitumen interface and measure its interfacial properties (e.g., interfacial tension).<sup>37,41,48-51</sup> In this technique, a water-filled micropipette is first immersed in solvent-diluted bitumen. A water drop is then formed by expelling a small amount of water from its tip (**Fig. 2-8(a)**).<sup>50</sup> When the water drop is deflated by withdrawing the water into the pipette at low bitumen concentrations (less than ~ 1%), the surface crumples abruptly (**Fig. 2-8(b)**), revealing a rigid cortical structure.<sup>50</sup> However, when the water drop is exposed to a mixture of higher bitumen content, the interface loses its rigidity (i.e. it has transformed into a two-dimensional fluid) and the drop remains spherical throughout the deflation. In this case, small surface protrusions begin to appear on the shrinking water drop, leading to detachment of micrometer-sized droplets from the surface (budding process).

When bringing two water droplets attached to micropipettes to approach each other in a diluted bitumen environment (0.1%), Yeung et al.<sup>49, 50</sup> found that the droplets remained as separate entities (i.e. no coalescence) despite a forced contact up to 5 min. Yeung et al. performed similar drop-stretching experiments, where a water drop held by two suction pipettes in diluted bitumen is stretched, followed by release of the water droplet from one of the pipettes to allow the droplet to recover at constant volume conditions.<sup>50</sup> They observed that, when the bitumen concentration was below 1% (i.e. in the regime where crumpling was observed), the time for the droplet to recover to its spherical shape after release of the stretch (tension) was in the order of 1 second. However, when the bitumen content was higher (i.e. in the regime where budding was observed without crumpling), the recovery time was found to be in the order of 0.01 second. From these results, one can conclude that the film shear viscosity controlling the shape recovery is affected by changes in bitumen concentration.

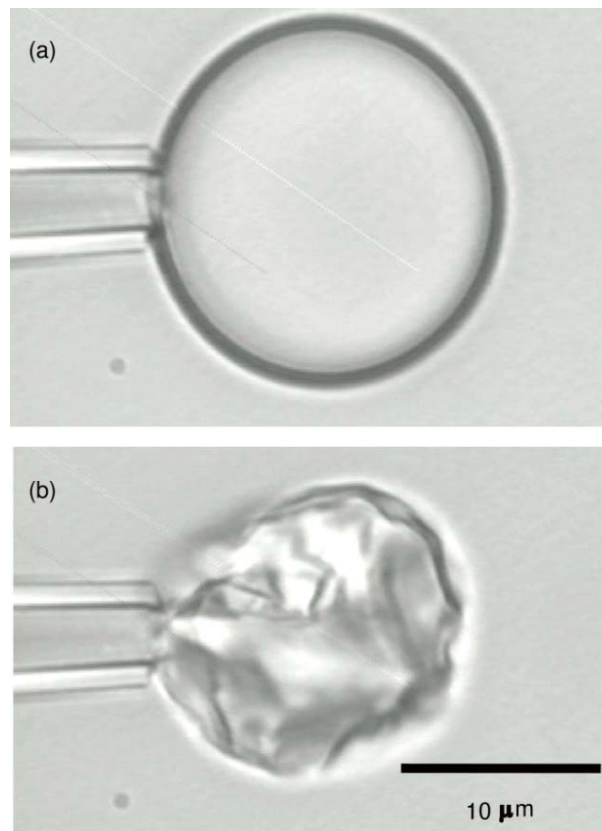


**Fig. 2-8** Water drop (a) formed at the tip of a micropipette and (b) during withdrawal. Surrounding oil phase is composed of bitumen (0.1%) diluted in a heptane/toluene mixture. A “protective layer”, which results from the adsorption of bitumen’s natural surfactants onto the oil/water interface, is revealed in (b) as the drop area is reduced.<sup>50</sup>

Adsorption of surface-active components from bitumen at an oil/water interface was studied by Solovyev using a Langmuir interfacial trough.<sup>38</sup> Langmuir films of bitumen, maltenes (i.e. deasphalted bitumen) and asphaltenes were prepared at a toluene/water interface. The films were subjected to multiple washings with toluene. Asphaltenes were found to be irreversibly adsorbed at the toluene/water interface, as shown by a negligible change in the interfacial pressure-area ( $\pi$ -A) isotherms when the corresponding films were repeatedly washed with toluene. In other words, the asphaltene monolayer was persistent at the interface and could not be washed away by fresh toluene. The results from

these tests indicate that, although asphaltenes are soluble in toluene they become insoluble in this organic solvent once they are contacted with water.

In conventional water-based bitumen extraction, sodium hydroxide is normally used as a process aid to release natural surfactants from the bitumen to the aqueous phase.<sup>41</sup> Studies have shown that the surfactants released from the bitumen were mainly carboxylic salts of naphthenic acids along with a smaller amount of sulfonic acids.<sup>41</sup> Naphthenic acids are a class of cyclic carboxylic acids that may contain aliphatic side chains, with a molecular weight ranging from about 166 to 450 g.mol<sup>-1</sup>.<sup>41</sup> Under the alkaline conditions of bitumen extraction, the naphthenic acids are easily converted to sodium naphthenates, which have been known to “soften” the interface of the emulsified water droplets.<sup>41</sup>

The colloidal forces between asphaltene surfaces in organic solvent of varying aromaticities were measured using AFM by Wang et al.<sup>52</sup> They concluded that the composition of organic solvent has a significant impact on asphaltene interactions: increasing the toluene content in heptol (a mixture of toluene and heptane) changed the interaction forces from attractive to repulsive. When the toluene content is higher than 0.2, the repulsion originates from the steric forces, which can be well described by the scaling theory of polymer brushes. When the toluene content is less than 0.2, van der Waals attraction dominates and becomes the driving force for asphaltene aggregation in paraffinic solvents. The aggregation of asphaltenes was also modeled by molecular dynamics simulations.  
53, 54

Furthermore, concentrated surfactant solutions can form liquid crystal phases, and the multilayered structure of a liquid crystal phase at the oil/water interface can directly influence the stability of water in hydrocarbon emulsions.<sup>41, 55</sup> As the formation of liquid crystals is strongly dependent on composition, the type of diluents and diluents/bitumen ratio used in froth treatment would play a major role in altering the stability of the water droplets.<sup>55</sup>

### ***2.3.2 Reagents for destabilizing water-in-diluted-bitumen emulsions***

Chemical demulsification has been widely employed in the petroleum industry to break up (i.e. destabilize) water-in-oil emulsions, being both economical and convenient.<sup>35</sup> Demulsifiers are amphiphilic compounds that can destabilize emulsions by changing the interfacial film properties, such as interfacial tension, mechanical strength, elasticity and thickness, promoting aggregation/coalescence of water droplets. For water-in-oil emulsions, the demulsifiers are exclusively oil-soluble to allow them to access the oil/water interface through the continuous oil phase.<sup>35, 36, 56</sup>

The commercial demulsifiers used for breaking up water-in-diluted-bitumen emulsions are mostly polymeric surfactants. Low-molecular-weight polymeric surfactants possess high interfacial activity and adsorb irreversibly at the oil/water interface, causing film rupture and coalescence of the water droplets.<sup>57</sup> High molecular weight polymeric surfactants are capable of flocculating water droplets and destabilize the emulsions.<sup>58</sup> In practice, ethylene oxide/propylene oxide (EO/PO) co-polymer-based demulsifiers are used for assisting the removal of water from naphtha-diluted bitumen.<sup>35</sup>

Chemical demulsification of water-in-diluted bitumen emulsions has been studied quite extensively.<sup>35</sup> Wu et al.<sup>56</sup> studied the performance of many low molecular weight surfactants and high molecular weight polymeric surfactants (all non-ionic) as demulsifiers in removing water from diluted bitumen. They found that both molecular weight and relative solubility number – RSN (within a given surfactant family) play an important role in demulsification. Xu et al.<sup>59</sup> investigated demulsification by polyoxyalkylated DETA (diethylenetriamine) of various PO and EO contents. They concluded that some of the tested polyoxyalkylated DETA could perform as well (or better) as demulsifiers currently used in commercial plants.

A nontoxic and biodegradable polymer, ethylcellulose, was investigated by Feng et al.<sup>35, 48</sup> as demulsifier of water in naphtha-diluted bitumen. The results indicated that the polymer was efficient in separating water from such emulsions,

as well as from bitumen froths (with less than 30 wt% solids content). Further, ethylcellulose was also found to assist removal of fine solids. Using micropipette method and AFM in combination with Langmuir film technique, the biodegradable polymer was found to displace the original interfacial protective materials, breaking up the water-in-bitumen emulsions by flocculation and coalescence mechanisms.

## **2.4 Tailings Treatment**

In order to produce one barrel of bitumen, approximately 3.3 m<sup>3</sup> of tailings slurry is discharged into tailings ponds. 80 to 85% by weight of the water in the tailings slurry originates from recycle tailings process water. In tailings ponds, coarse solids settle quickly to form beaches along the tailings pond while the fines (typically less than 44 microns in size) take much longer time to settle. Even after years of settling in the tailings ponds, the fine solids remain suspended in tailings water in the form of sludge (normally referred to as mature fine tailings) containing only 30 wt% solids, with no further noticeable consolidation. The objective of tailings treatment is to increase the solid particles settling velocity and the rate of consolidation by optimizing the physicochemical conditions of the tailings slurry. It is therefore important to study the colloidal properties of fine solids in tailings water.

### ***2.4.1 Characteristics of fine tailings***

The stability of a clay dispersion is controlled by the colloidal interaction forces between individual clay particles in the medium in which they are suspended. There are two main sources of the interactions: van der Waals forces and electrostatic double layer forces. van der Waals forces exist between two surfaces in any medium and are always attractive between similar particles.

Based on the clay charge mechanism, the basal plane of clays has a permanent negative charge resulting from isomorphous substitutions of lattice cations within the clay structure by cations of lower valences, while the charge on the edge surface arises from hydrolysis reactions of broken Al-O and Si-O bonds, which is

pH dependant. The basal plane can be considered to maintain a constant surface charge density and the edges to maintain a constant surface potential as the two surfaces approach each other. The electrical double layer interaction energy ( $V_E$ ) for the condition of constant potential ( $\psi$ - $\psi$ , edge-edge), constant surface charge ( $\sigma$ - $\sigma$ , basal-basal) and constant potential – constant charge ( $\psi$ - $\sigma$ , edge-basal) can be estimated using the following equations:<sup>60</sup>

$$V_E^{\psi-\psi} = \frac{\varepsilon\varepsilon_0 R_1 R_2}{(R_1 + R_2)} \left\{ 2\psi_1 \psi_2 \left[ \ln \frac{1 + \exp(-\kappa D)}{1 - \exp(-\kappa D)} \right] + (\psi_1^2 + \psi_2^2) \ln [1 - \exp(-2\kappa D)] \right\}$$

**Eqn. 2-11**

$$V_E^{\sigma-\sigma} = \frac{\varepsilon\varepsilon_0 R_1 R_2}{(R_1 + R_2)} \left\{ 2\psi_1 \psi_2 \left[ \ln \frac{1 + \exp(-\kappa D)}{1 - \exp(-\kappa D)} \right] - (\psi_1^2 + \psi_2^2) \ln [1 - \exp(-2\kappa D)] \right\}$$

**Eqn. 2-12**

$$V_E^{\psi-\sigma} = \frac{\varepsilon\varepsilon_0 R_1 R_2}{(R_1 + R_2)} \left\{ 2\psi_1 \psi_2 \left( \frac{\pi}{2} - \tan^{-1} \sinh \kappa D \right) - (\psi_2^2 - \psi_1^2) \ln [1 + \exp(-2\kappa D)] \right\}$$

**Eqn. 2-13**

where the term  $\kappa$  is the inverse Debye length of the electric double layer. According to the classical DLVO theory, the total interaction energy between two particles is the summation of  $V_A$  and  $V_E$  given by **Eqn. 2-1**.

To simplify the calculation, the interaction between clay particles with a -35 mV zeta-potential on the basal plane and -5 mV on the edge plane in a simple electrolyte solution of 1 mM KCl at pH 8.5 is considered. The results in **Fig. 2-9** show that there is a strong repulsive force between basal surfaces, a small energy barrier between edge-basal planes and a weak attraction between edge surfaces. Such interactions lead to a stable clay structure of edge-edge attachment orientation. The strong repulsion between basal planes leads to a substantial gap between the lamellae stacks, which is likely the main reason for trapping a large amount of water in fine tailings. In order to increase the tailings settling rate, one approach is to increase the size of fine particle by aggregation using coagulation and flocculation.

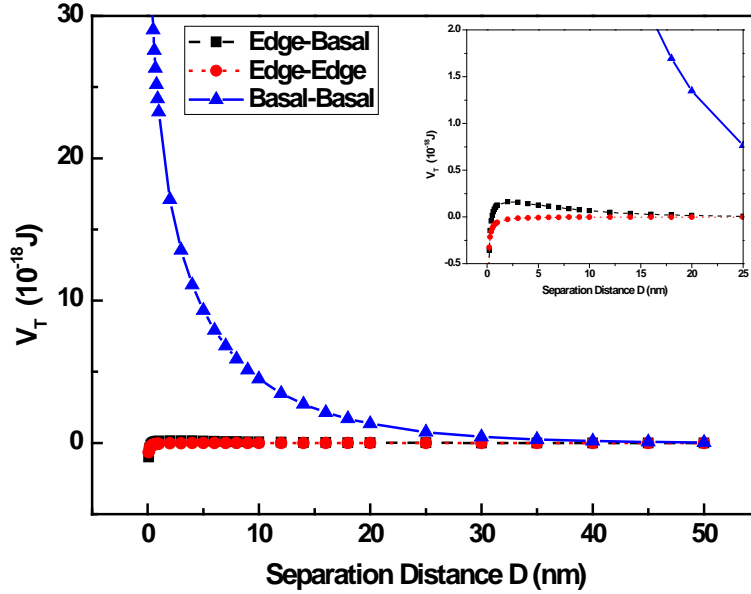


**Fig. 2-9** The interaction energy profiles between different clay surfaces in 1 mM KCl solution at pH 8.5 in the absence of calcium and magnesium. The basal planes and edge planes have Stern potential (zeta-potential) of -35 mV and -5 mV, respectively. The basal and edge planes are considered to be with constant surface charge and constant surface potential, and their corresponding particles having diameters of 0.1  $\mu\text{m}$  and 2  $\mu\text{m}$ , respectively. The Hamaker constant of clay-water-clay is set to be  $8 \times 10^{-21}$  J.

#### 2.4.2 Coagulation

The objective of coagulation is to depress the repulsive force between clays by adding coagulant which normally is an inorganic multivalent salt, to such an extent that the attractive van der Waals forces become dominant and bring the clay particles together. Gypsum, in which calcium ions act as coagulant, is used in the composite or consolidated tailings process to treat oil sands tailings. To study the effect of calcium ion and pH on the surface electrical properties of clay particles, the zeta-potential of kaolinite was measured by a Zetaphoremeter III (SEPHY/CAD).<sup>61</sup> **Fig. 2-10** shows the zeta-potential of kaolinite as a function of slurry pH and calcium ion concentration. Zeta-potential of kaolinite in 1mM KCl solutions decreases and becomes progressively more negative with increasing pH with an iso-electric point (iep) at pH 3.6. The addition of calcium substantially

increases surface charge of kaolinite and a noticeable shift of iep from pH 3.6 to 5.7 is observed when 1 mM  $\text{Ca}^{2+}$  is added, which indicates specific adsorption of calcium ions on kaolinite surfaces. The reduction in the magnitude of surface electrical potential and compression of electrical double layers by coagulant addition reduce repulsive forces between the particles, allowing them to stack more closely to each other and hence improving consolidation of the sediments.

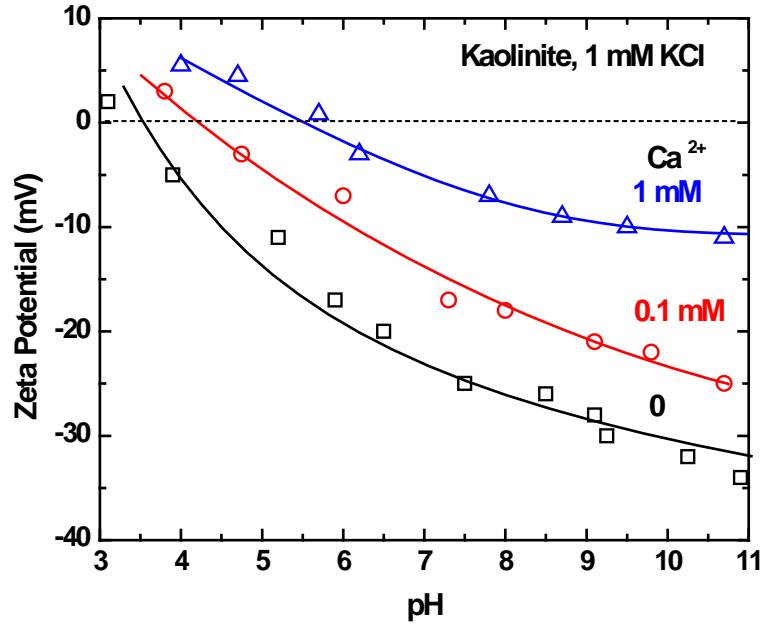


**Fig. 2-10** Effect of slurry pH and calcium addition on zeta-potential of kaolinite in 1 mM KCl solutions. Reproduced from Liu et al. <sup>61</sup>

Direct force measurements between silica and silica with calcium added in the prepared KCl solutions were conducted.<sup>62</sup> The results in **Fig. 2-11** show that the long-range force is purely repulsive and the addition of 2 mM  $\text{Ca}^{2+}$  reduces this repulsive force. During retraction, an adhesion force is observed when 2 mM  $\text{Ca}^{2+}$  is added. Moreover, the force curves can be well fitted by the classical DLVO theory at separation distances greater than 3 nm, which indicates that the electrostatic double layer force dominates the long-range force profile. The repulsive double layer force between particles is reduced due to less negatively charged surfaces. At the same time, the increase in solution salinity compresses the electrical double layer. Therefore, the energy barrier that prevents two

particles to approach each other is lowered, leading to a more effective clay particle aggregation. It should be noted that an overdose of calcium can also be detrimental since the charge of the particle can be reversed due to an excess specific adsorption of calcium ions onto clay surface.

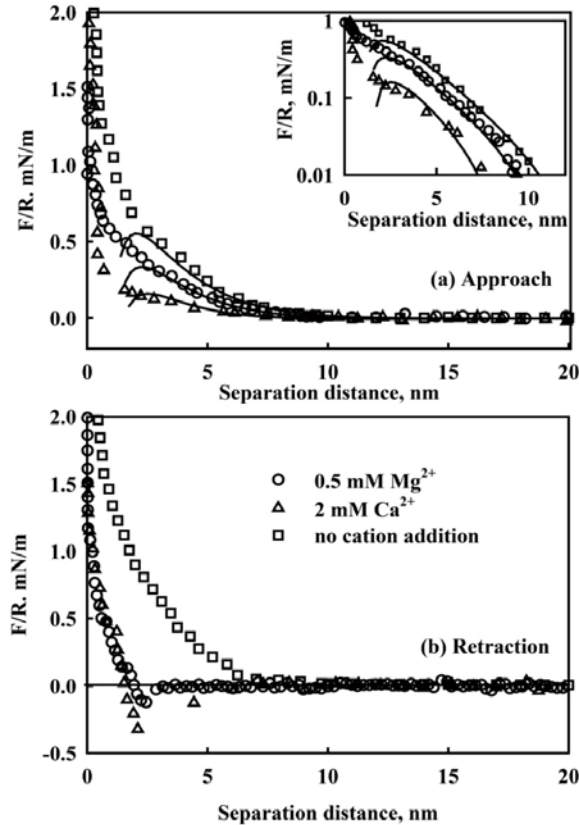


**Fig. 2-11** Measured force ( $F/R$ ) between two silica surfaces in 20 mM KCl solutions as a function of separation distance: (a) approach, (b) retract. The inset plot in figure (a) shows the force profile at close separation distance. The solid line is the force profile calculated by the classical DLVO theory, fitted with Hamaker constant  $A = 8 \times 10^{-12}$  J and zeta potential  $\zeta = -28$  mV for no cation addition and  $-20$  mV for calcium addition.<sup>62</sup>

### 2.4.3 Flocculation

Flocculation, on the other hand, involves the addition of polymer to bridge the particles into large flocs. The polymer adsorbs on solids mainly through hydrogen bonding. The binding strength of polymer with solids is determined by its

molecular weight and configuration. In flocculation, it is not necessary to reduce the repulsion between aggregating particles as the polymer chain can extend beyond the range of electrical double layer forces.

The effect of flocculant addition on tailings settling was studied extensively. The results showed that settling of oil sands fine tailings is marginal without flocculant addition. The addition of flocculants increased the tailings settling rate substantially.<sup>63,64</sup> It has been found that without flocculant addition, there is no adhesion force between clay and silica, and the repulsive long-range force makes the solid particles to remain in a well-dispersed state, resulting in an extremely low settling rate. The results in **Fig. 2-12** show that the addition of Al-PAM, a cationic organic-inorganic hybrid polymer, reduced the long range repulsive force and substantially increased adhesion force from 0 mN/m to 2 mN/m. Such a strong adhesion force is believed to be the formation of polymer bridges between solid particles. Consequently, a fast fines settling in tailings slurry is achieved when Al-PAM dosage is greater than 5 ppm.<sup>62</sup>

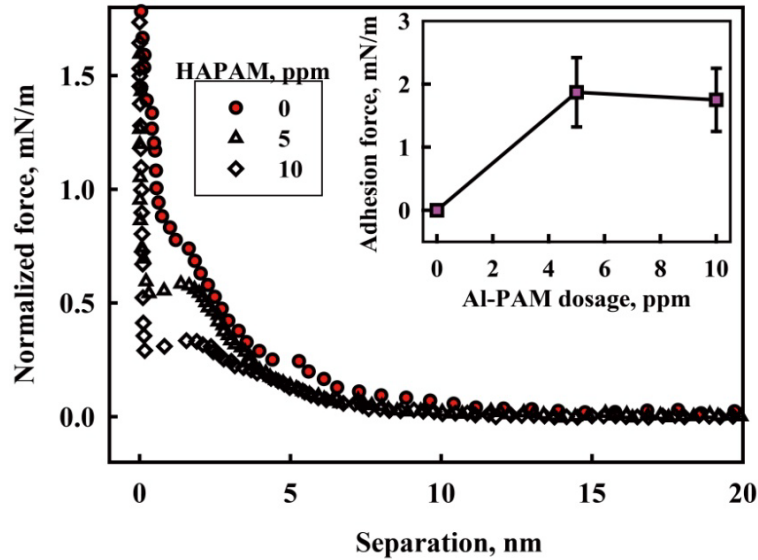


**Fig. 2-12** Measured force (F/R) between clay - silica surfaces as a function of separation distance.<sup>64</sup> The inset shows the clay-silica adhesion forces as a function of Al-PAM dosage.

In addition to this long-range attractive bridging force, there is a strong shorter range repulsion that results from compressing polymer strings. It is therefore very important to control the amount and conformation of adsorbed polymer molecules on particles. When the particle surfaces are fully covered by loops and tails, they are likely to be stabilized by steric stabilization. A recent study revealed that at large flocculant concentrations, the repulsive force becomes stronger and extends to a larger separation distance, at the same time the bridging adhesion force becomes and disappeared, leading to less effective settling of fine solids.<sup>62</sup>

The addition of coagulant and/or flocculant is capable of increasing fine solids settling rate; however, compacting of sediments to a desired level of self-supportive after discharge cannot be achieved by the natural gravity force. Hence, external forces are required to release the trapped water from sediments by additional physical forces as in filtration and centrifugation.

## **2.5 Conclusions**

Understanding the colloidal interactions taking place among oil sands components is of paramount importance for increasing bitumen recovery efficiency, reducing operating costs and minimizing environmental impact. The role of colloid chemistry in water-based oil sands processing was briefly reviewed in this chapter. The main research techniques and outcomes published in the scientific literature were summarized. Slurry pH, divalent metal and bicarbonate ion concentrations, temperature, presence of fine clays and solids hydrophobicity show a strong impact on bitumen extraction (bitumen liberation/aeration) efficiency. Indigenous bitumen components (i.e. asphaltenes, resins, and other naturally occurring surfactants) and fine solids play a significant role in stabilizing water-in-diluted-bitumen emulsions, which is central to bitumen froth treatment (i.e. froth cleaning). The main reagents (demulsifiers) utilized/researched for destabilizing such emulsions were briefly described. The strategies for tailings treatment (i.e. increase of fine particles settling velocity and the rate of solid/liquid separation) were summarized with a focus on optimizing the

physicochemical conditions of the tailings slurry, including main parameters and reagents of coagulation and/or flocculation.

## 2.6 References

- (1) Masliyah, J.; Zhou, Z.; Xu, Z.; Czarnecki, J.; Hamza, H. Understanding Water-Based Bitumen Extraction from Athabasca Oil Sands. *Can. J. Chem. Eng.* **2004**, *82*, 628-654.
- (2) Gray, M.; Xu, Z.; Masliyah, J. Physics in the Oil Sands of Alberta. *Phys Today* **2009**, *62*, 31-5.
- (3) Long, J.; Zhang, L.; Xu, Z.; Masliyah, J. H. Colloidal Interactions between Langmuir-Blodgett Bitumen Films and Fine Solid Particles. *Langmuir* **2006**, *22*, 8831-8839.
- (4) Zhao, H.; Dang-Vu, T.; Long, J.; Xu, Z.; Masliyah, J. H. Role of Bicarbonate Ions in Oil Sands Extraction Systems with a Poor Processing Ore. *J. Dispersion Sci. Technol.* **2009**, *30*, 809-822.
- (5) Czarnecki, J.; Radoev, B.; Schramm, L. L.; Slavchev, R. On the Nature of Athabasca Oil Sands. *Adv. Colloid Interface Sci.* **2005**, *114-115*, 53-60.
- (6) Liu, J.; Xu, Z.; Masliyah, J. Interaction Forces in Bitumen Extraction from Oil Sands. *J. Colloid Interface Sci.* **2005**, *287*, 507-520.
- (7) Liu, J.; Xu, Z.; Masliyah, J. Studies on Bitumen-Silica Interaction in Aqueous Solutions by Atomic Force Microscopy. *Langmuir* **2003**, *19*, 3911-3920.
- (8) Zhou, Z. A.; Xu, Z.; Masliyah, J. H.; Czarnecki, J. Coagulation of Bitumen with Fine Silica in Model Systems. *Colloids Surf., A; Colloids and Surfaces A* **1999**, *148*, 199-211.
- (9) Derjaguin, B. V.; Landau, L. Theory of the Stability of Strongly Charged Lyophobic Sols and of the Adhesion of Strongly Charged Particles in Solutions of Electrolytes. *Acta Physicochim. URSS* **1941**, *14*, 633-662.

- (10) Israelachvili, J. N. In *Intermolecular and surface forces*; Section Title: General Physical Chemistry; Academic Press: 1991, pp 449.
- (11) Jacob H. Masliyah, Subir Bhattacharjee, Ed.; In *Electrokinetic and colloid transport phenomena*; 2006, pp 736.
- (12) Nguyen, A.; Schulze, H. J., Eds.; In *Colloidal science of flotation*; surfactant science series; New York, 2004; Vol. 118, pp 850.
- (13) Zhao, H.; Long, J.; Masliyah, J. H.; Xu, Z. Effect of Divalent Cations and Surfactants on Silica-Bitumen Interactions. *Ind Eng Chem Res* **2006**, *45*, 7482-7490.
- (14) Wang, L.; Dang-Vu, T.; Xu, Z.; Masliyah, J. H. Use of Short-Chain Amine in Processing of weathered/oxidized Oil Sands Ores. *Energy Fuels* **2010**, *24*, 3581-3588.
- (15) Najafi, A. S.; Drelich, J.; Yeung, A.; Xu, Z.; Masliyah, J. A Novel Method of Measuring Electrophoretic Mobility of Gas Bubbles. *J. Colloid Interface Sci.* **2007**, *308*, 344-350.
- (16) Mao, L.; Yoon, R. Predicting Flotation Rates using a Rate Equation Derived from First Principles. *Int. J. Miner. Process.* **1997**, *51*, 171-181.
- (17) Sato, T.; Ruch, R. Stabilization of Colloidal Dispersions by Polymer Adsorption. **1980**, 155.
- (18) Hampton, M. A.; Nguyen, A. V. Nanobubbles and the Nanobubble Bridging Capillary Force. *Adv. Colloid Interface Sci.* **2010**, *154*, 30-55.
- (19) Gu, G.; Xu, Z.; Nandakumar, K.; Masliyah, J. Effects of Physical Environment on Induction Time of Air-Bitumen Attachment. *Int. J. Miner. Process.* **2003**, *69*, 235-250.
- (20) Su, L.; Xu, Z.; Masliyah, J. Role of Oily Bubbles in Enhancing Bitumen Flotation. *Minerals Eng* **2006**, *19*, 641-650.

- (21) Liu, J.; Xu, Z.; Masliyah, J. Colloidal Forces between Bitumen Surfaces in Aqueous Solutions Measured with Atomic Force Microscope. *Colloids Surf. Physicochem. Eng. Aspects* **2005**, *260*, 217-228.
- (22) Fong, N.; Ng, S.; Chung, K. H.; Tu, Y.; Li, Z.; Sparks, B. D.; Kotlyar, L. S. Bitumen Recovery from Model Systems using a Warm Slurry Extraction Process: Effects of Oilsands Components and Process Water Chemistry. *Fuel* **2004**, *83*, 1865-1880.
- (23) Speight, J. G.; Moschopedis, S. E. Factors Affecting Bitumen Recovery by the Hot Water Process. *Fuel Process Technol* **1978**, *1*, 261-268.
- (24) Kasongo, T.; Zhou, Z.; Xu, Z.; Masliyah, J. Effect of Clays and Calcium Ions on Bitumen Extraction from Athabasca Oil Sands using Flotation. *Can. J. Chem. Eng.* **2000**, *78*, 674-681.
- (25) Ding, X.; Repka, C.; Xu, Z.; Masliyah, J. Effect of Illite Clay and Divalent Cations on Bitumen Recovery. *Can. J. Chem. Eng.* **2006**, *84*, 643-650.
- (26) Zhao, H.; Long, J.; Masliyah, J. H.; Xu, Z. Effect of Divalent Cations and Surfactants on Silica-Bitumen Interactions. *Industrial and Engineering Chemistry Research* **2006**, *45*, 7482-7490.
- (27) Long, J.; Xu, Z.; Masliyah, J. H. On the Role of Temperature in Oil Sands Processing. *Energy Fuels* **2005**, *19*, 1440-1446.
- (28) Long, J.; Drelich, J.; Xu, Z.; Masliyah, J. H. Effect of Operating Temperature on Water-Based Oil Sands Processing. *Can. J. Chem. Eng.* **2007**, *85*, 726-738.
- (29) Basu, S.; Nandakumar, K.; Lawrence, S.; Masliyah, J. Effect of Calcium Ion and Montmorillonite Clay on Bitumen Displacement by Water on a Glass Surface. *Fuel* **2004**, *83*, 17-22.
- (30) Liu, J.; Zhou, Z.; Xu, Z.; Masliyah, J. Bitumen-Clay Interactions in Aqueous Media Studied by Zeta Potential Distribution Measurement. *J. Colloid Interface Sci.* **2002**, *252*, 409-418.

- (31) Dai, Q.; Chung, K. H. Hot Water Extraction Process Mechanism using Model Oil Sands. *Fuel* **1996**, *75*, 220-226.
- (32) Muster, T. H.; Prestidge, C. A.; Hayes, R. A. Water Adsorption Kinetics and Contact Angles of Silica Particles. *Colloids Surf. Physicochem. Eng. Aspects* **2001**, *176*, 253-266.
- (33) Dang-Vu, T.; Jha, R.; Wu, S.; Tannant, D. D.; Masliyah, J.; Xu, Z. Effect of Solid Wettability on Processability of Oil Sands Ores. *Energy Fuels* **2009**, *23*, 2628-2636.
- (34) Ren, S.; Zhao, H.; Long, J.; Xu, Z.; Masliyah, J. Understanding Weathering of Oil Sands Ores by Atomic Force Microscopy. *AIChE J.* **2009**, *55*, 3277-3285.
- (35) Feng, X.; Xu, Z.; Masliyah, J. Biodegradable Polymer for Demulsification of Water-in-Bitumen Emulsions. *Energy Fuels* **2009**, *23*, 451-456.
- (36) Czarnecki, J. In *Water-in-oil emulsions in recovery of hydrocarbons from oil sands*; Sjoblom, J., Ed.; Encyclopedic Handbook of Emulsion Technology; CRC Press: 2001.
- (37) Gao, S.; Moran, K.; Xu, Z.; Masliyah, J. Role of Bitumen Components in Stabilizing Water-in-Diluted Oil Emulsions. *Energy Fuels* **2009**, *23*, 2606-2612.
- (38) Solovyev, A.; Zhang, L. Y.; Xu, Z.; Masliyah, J. H. Langmuir Films of Bitumen at Oil/Water Interfaces. *Energy Fuels* **2006**, *20*, 1572-1578.
- (39) Xu, Y.; Dabros, T.; Hamza, H.; Shefantook, W. Destabilization of Water in Bitumen Emulsion by Washing with Water. *Pet. Sci. Technol.* **1999**, *17*, 1051-1070.
- (40) Gafonova, O. V.; Yarranton, H. W. The Stabilization of Water-in-Hydrocarbon Emulsions by Asphaltenes and Resins. *J. Colloid Interface Sci.* **2001**, *241*, 469-478.

- (41) Gao, S.; Moran, K.; Xu, Z.; Masliyah, J. Role of Naphthenic Acids in Stabilizing Water-in-Diluted Model Oil Emulsions. *The Journal of Physical Chemistry B* **2010**, *114*, 7710-7718.
- (42) Gu, G.; Zhou, Z.; Xu, Z.; Masliyah, J. H. Role of Fine Kaolinite Clay in Toluene-Diluted bitumen/water Emulsion. *Colloids Surf., A; Colloids and Surfaces, A: Physicochemical and Engineering Aspects* **2003**, *215*, 141-153.
- (43) Jiang, T.; Hirasaki, G.; Miller, C.; Moran, K.; Fleury, M. Diluted Bitumen Water-in-Oil Emulsion Stability and Characterization by Nuclear Magnetic Resonance (NMR) Measurements. *Energy Fuels* **2007**, *21*, 1325-1336.
- (44) Yan, Z.; Elliott, J. A. W.; Masliyah, J. H. Roles of various Bitumen Components in the Stability of Water-in-Diluted-Bitumen Emulsions. *J. Colloid Interface Sci.* **1999**, *220*, 329-337.
- (45) Menon, V. B.; Wasan, D. T. Particle—fluid Interactions with Application to Solid-Stabilized Emulsions Part I. the Effect of Asphaltene Adsorption. *Colloids and Surfaces* **1986**, *19*, 89-105.
- (46) Czarnecki, J.; Moran, K. On the Stabilization Mechanism of Water-in-Oil Emulsions in Petroleum Systems. *Energy and Fuels* **2005**, *19*, 2074-2079.
- (47) Gu, G.; Xu, Z.; Nandakumar, K.; Masliyah, J. H. Influence of Water-Soluble and Water-Insoluble Natural Surface Active Components on the Stability of Water-in-Toluene-Diluted Bitumen Emulsion. *Fuel* **2002**, *81*, 1859-1869.
- (48) Feng, X.; Mussone, P.; Gao, S.; Wang, S.; Wu, S.; Masliyah, J. H.; Xu, Z. Mechanistic Study on Demulsification of Water-in-Diluted Bitumen Emulsions by Ethylcellulose. *Langmuir* **2010**, *26*, 3050-3057.
- (49) Yeung, A.; Dabros, T.; Masliyah, J.; Czarnecki, J. Micropipette: A New Technique in Emulsion Research. *Colloids Surf. Physicochem. Eng. Aspects* **2000**, *174*, 169-181.

- (50) Yeung, A.; Dabros, T.; Czarnecki, J.; Masliyah, J. On the Interfacial Properties of micrometre-sized Water Droplets in Crude Oil. *Proceedings of the Royal Society of London. Series A: Mathematical, Physical and Engineering Sciences* **1999**, *455*, 3709-3723.
- (51) Vander Kloet, J.; Schramm, L. L.; Shelfantook, B. The Influence of Bituminous Froth Components on Water-in-Oil Emulsion Stability as Determined by the Micropipette Technique. *Colloids Surf. Physicochem. Eng. Aspects* **2001**, *192*, 15-24.
- (52) Wang, S.; Liu, J.; Zhang, L.; Masliyah, J.; Xu, Z. Interaction Forces between Asphaltene Surfaces in Organic Solvents. *Langmuir* **2010**, *26*, 183-190.
- (53) Headen, T. F.; Boek, E. S.; Skipper, N. T. In *Evidence for asphaltene nanoaggregation in toluene and heptane from molecular dynamics simulations*; American Chemical Society: 2540 Olentangy River Road, P.O. Box 3337, Columbus, OH 43210-3337, United States, 2009; Vol. 23, pp 1220-1229.
- (54) Kuznicki, T.; Masliyah, J. H.; Bhattacharjee, S. Aggregation and Partitioning of Model Asphaltenes at Toluene-Water Interfaces: Molecular Dynamics Simulations. *Energy Fuels* **2009**, *23*, 5027-5035.
- (55) Horváth-Szabó, G.; Masliyah, J. H.; Czarnecki, J. Emulsion Stability Based on Phase Behavior in Sodium Naphthenates Containing Systems: Gels with a High Organic Solvent Content. *J. Colloid Interface Sci.* **2003**, *257*, 299-309.
- (56) Wu, J.; Xu, Y.; Dabros, T.; Hamza, H. Effect of Demulsifier Properties on Destabilization of Water-in-Oil Emulsion. *Energy Fuels* **2003**, *17*, 1554-1559.
- (57) Sjoblom, J.; Johnsen, E. E.; Westvik, A.; Ese, M. H.; Djuve, J.; Auflem, I. H.; Kallevik, H. In *Demulsifiers in the oil industry*; Sjoblom, J., Ed.; Encyclopedic Handbook of Emulsion Technology; CRC Press: 2001; .

- (58) Pena, A. A.; Hirasaki, G. J.; Miller, C. A. Chemically Induced Destabilization of Water-in-Crude Oil Emulsions. *Ind Eng Chem Res* **2005**, *44*, 1139-1149.
- (59) Xu, Y.; Wu, J.; Dabros, T.; Hamza, H.; Wang, S.; Bidal, M.; Venter, J.; Tran, T. Breaking Water-in-Bitumen Emulsions using Polyoxyalkylated DETA Demulsifier. *Can. J. Chem. Eng.* **2004**, *82*, 829-835.
- (60) Kar, G.; Chander, S.; Mika, T. S. The Potential Energy of Interaction between Dissimilar Electrical Double Layers. *J. Colloid Interface Sci.* **1973**, *44*, 347-355.
- (61) Liu, J.; Xu, Z.; Masliyah, J. Role of Fine Clays in Bitumen Extraction from Oil Sands. *AIChE J.* **2004**, *50*, 1917-1927.
- (62) Long, J.; Li, H.; Xu, Z.; Masliyah, J. H. Role of Colloidal Interactions in Oil Sand Tailings Treatment. *AIChE J.* **2006**, *52*, 371-383.
- (63) Wang, X.; Feng, X.; Xu, Z.; Masliyah, J. H. Polymer Aids for Settling and Filtration of Oil Sands Tailings. *Can. J. Chem. Eng.* **2010**, *88*, 403-410.
- (64) Li, H.; Long, J.; Xu, Z.; Masliyah, J. H. Novel Polymer Aids for Low-Grade Oil Sand Ore Processing. *Can. J. Chem. Eng.* **2008**, *86*, 168-176.

## **Chapter 3**

### **Use of Short Chain Amine in Processing of Weathered/Oxidized Oil Sands Ores**

### 3.1 Introduction<sup>†</sup>

Water-based flotation technology is used to commercially extract bitumen from Athabasca oil sands. Among the various elementary processes, efficient attachment between bitumen and air bubble is critical for success of bitumen flotation. The fundamental requirement for the flotation of bitumen is that the bitumen should be non-water wettable (hydrophobic). In flotation, the induction time and contact angle are used to determine the floatability and flotation rate. In general, the contact angle reflects the thermodynamic equilibrium status of a system, while the induction time represents the dynamic property of a flotation system. A positive correlation between the measured contact angle and bitumen recovery was reported.<sup>1</sup> In some cases, however, the contact angle measurement was found not to provide a sensitive response or even failed to describe the behavior of flotation.<sup>2-5</sup>

In contrast, the induction time, a function of chemistry and hydrodynamics of the system, can provide kinetic information. It is therefore considered to be a better marker than the contact angle in reflecting the characteristics of a flotation system. The importance of the induction time on flotation was recognized in the early 1930s.<sup>6</sup> Since then, systematic studies have been conducted to determine the induction time. Generally, the induction time is measured by moving a captive bubble toward and then away from a particle bed or a flat mineral surface.<sup>4,5,7</sup> A strong correlation between the induction time and mineral recovery was established. For a given condition, a shorter induction time can always lead to higher mineral recovery in either quartz flotation,<sup>4</sup> coal flotation,<sup>5</sup> or bitumen flotation.<sup>2</sup> In this regard, the induction time is considered to be a better criterion to assess the factors affecting bitumen-air attachment.

One of the major challenges in the oil sands industry is to improve the processability of weathered/oxidized oil sands ores. The weathered/oxidized ores

---

<sup>†</sup> A version of this chapter has been published. Wang, L.; Dang-Vu, T.; Xu, Z. and Masliyah, J.H. Use of short-chain amine in processing of weathered/oxidized oil sands ores, *Energy & Fuels*, **2010**, 24(6), 3581-3588.

are usually obtained when the oil sands are in the formation with shallow/thin overburden. The characteristics of these ores are similar to that of good processing ore, which features about 14% bitumen grade and 10 wt % fines of total solids in the ore. The fines are defined in the oil sands industry as mineral solids of diameter smaller than 44  $\mu\text{m}$ . However, processing the weathered/ oxidized ores at conventional bitumen flotation conditions (pH = 8.5 at 35 °C) leads to very low bitumen recovery and low bitumen froth quality. The bitumen recovery and froth quality, measured by the bitumen/solids ratio, of the good processing ores can reach up to 95% and 7 wt/wt, respectively, while for weathered/oxidized ores, it can be as low as 60% bitumen recovery at a froth quality less than 2 wt/wt.<sup>8</sup> The recovery from weathered/oxidized ores is even lower than that from high fines (poor processing) ore, which features low bitumen grade (about 6 wt %) and high fine solids content (about 40 wt %). This type of ores is currently not processed and considered as a waste.

The low bitumen recovery and poor froth quality from weathered/oxidized ores are often attributed to the change of solids wettability because of the diminishment of water films between bitumen and sand grain. Previous studies show that some solids in oil sands ores are covered with toluene insoluble organic matter (TIOM), and those solids are termed as “organic rich sands” (ORS).<sup>9, 10</sup> The physically and/or chemically adsorbed organic substances on solids surfaces make the solids surface hydrophobic. The increase in hydrophobicity of solids in oil sands is a major reason for the low bitumen recovery of weathered/oxidized oil sands ores. An increasing percentage of hydrophobic solids in model oil sands drastically reduced bitumen recovery because of poor liberation.<sup>11, 12</sup> Recently, flotation tests with a wide range of oil sands ores confirmed that the amount of ORS in oil sands ore is a better indicator than bitumen and fines content to assess ore processability.<sup>13</sup> Furthermore, solids from weathered/oxidized ores are the most hydrophobic as compared to solids from good processing and high fines (poor processing) ores,<sup>8</sup> while the variation of bitumen surface wettability is negligible.<sup>10</sup> Therefore, another approach for improving bitumen recovery from weathered/oxidized ores is to decrease hydrophobicity of the solids by caustic addition to facilitate bitumen liberation from sand grains.

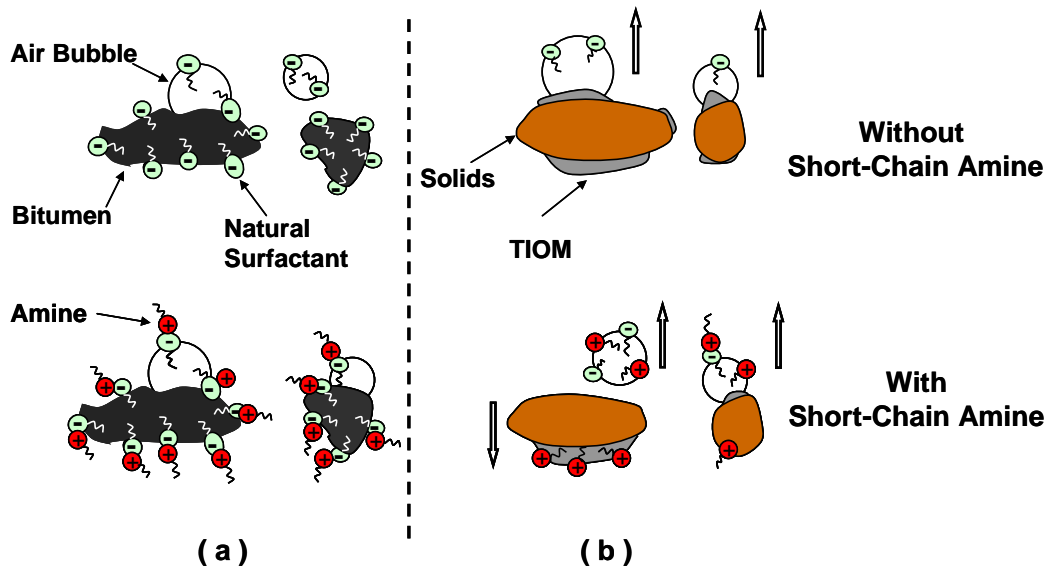


**Fig. 3-1** Schematics of natural surfactant and short-chain amine adsorption at interfaces in an oil sands processing system: (a) bitumen, (b) solids.

To achieve a desired level of bitumen liberation from weathered ores, excess caustic addition is required. The addition of caustic to oil sands slurry is known to ionize and extract more natural surfactants from bitumen to the bitumen/water interface and eventually migrate into the aqueous phase. As a result, the hydrophobicity of bitumen may be reduced by adsorption of ionized natural surfactants at the bitumen/water interface,<sup>14-16</sup> particularly in high alkaline solutions, reducing bitumen-bubble attachment efficiency, as shown in the top of **Fig. 3-1(a)**. Because the bitumen surface is negatively charged,<sup>17-19</sup> positively charged amine can adsorb on the bitumen surface with the amine group attaching to bitumen surface, increasing its hydrophobicity for more effective air-bitumen attachment, as showing in the bottom of **Fig. 3-1(a)**. Therefore, amine addition is anticipated to increase bitumen recovery from oil sands. However, solids in the slurry are also negatively charged. Amine adsorption on solid surfaces becomes inevitable. To maintain wettability or rather not to hydrophobize solids, short-chain amine is considered.

The objective of this study is to test this hypothesis, i.e. to improve bitumen recovery from weathered/oxidized ores using short-chain amines by increasing

bitumen hydrophobicity, focusing on scientific understanding of improved air bubble-bitumen attachment.

### 3.2 Materials and Methods

#### 3.2.1 Materials

Two different weathered/oxidized ores were used in this study. The composition (bitumen, solids, and water contents) of these two ores is given in Table 3-1. The composition of the oil sands ores was determined by the Soxhlet Dean-Stark apparatus.<sup>20</sup> To obtain fine solids content, the solids from the Dean-Stark apparatus were wet-screened by a 44  $\mu\text{m}$  sieve and both above- and under-sieve products were then dried in an oven. After accurate weighing of the solids in these two products, the fines content is calculated by dividing the mass of the under-sieve solids by the mass of total solids. The results in Table 3-1 are the average of two subsamples from each ore. The ores used in this study feature a high bitumen content and low fine solids content.

**Table 3-1 Composition (wt %) of two weathered oil sands ores**

Weathered ore	Bitumen	Water	Solids	Fines/Solids
I	12.3	2.3	85.4	9.8
II	11.5	3.2	85.3	12.4

Three short-chain amine, *n*-propylamine, *n*-butylamine and *n*-pentylamine (ACROS Organics), were used in this study. Plant recycle process water of pH 7.7 was provided by Syncrude Canada Ltd. (Fort McMurray, Canada). The major ion concentration of process water was analyzed by ion chromatography (DIONEX ICS-3000), with the results shown in Table 3-2. Amine in process water solutions were prepared by adding a given amount of amine to plant recycle process water to 1 or 10 mM amine concentration. Vacuum-distillation-feed bitumen obtained from Syncrude Canada Ltd. was used to prepare bitumen surfaces for induction time measurement, bitumen displacement test, and zeta potential measurements of bitumen emulsions. A smooth and flat bitumen surface was obtained by spin-coating of toluene-diluted bitumen on a single-crystal silicon wafer (Mitsubishi

Polysilicon America Corporation). Reagent-grade hydrochloric acid (Fisher Scientific) and sodium hydroxide solution (Aldrich) were used as pH modifiers. Reagent-grade toluene (Fisher Scientific) was used as a solvent in Soxhlet Dean-Stark extraction and bitumen dilution.

**Table 3-2 Concentration of major ions in the plant recycle process water of pH 7.7**

Major ions	Ca <sup>2+</sup>	Mg <sup>2+</sup>	K <sup>+</sup>	Na <sup>+</sup>	Cl <sup>-</sup>	NO <sub>3</sub> <sup>-</sup>	SO <sub>4</sub> <sup>2-</sup>	HCO <sub>3</sub> <sup>-</sup>
Concentration (ppm)	29.7	15.4	23.6	572.8	391.4	5.9	117.8	621.0

### 3.2.2 Induction time measurement

To investigate the effect of amine on the attachment of the air bubble to the bitumen surface, the induction time technique, measuring the minimum time required for an air bubble in contact with the bitumen surface to attach to the bitumen, was employed. The faster the attachment is, the shorter the induction time.

#### 3.2.2.1 Preparation of the bitumen surfaces

The bitumen surface was prepared with a P6700 spin-coater (Specialty Coating Systems, Inc.) following procedures reported elsewhere.<sup>17</sup> Briefly, 20 drops of 10 wt% bitumen-in-toluene solution were added in 30 s onto the silicon wafer surface spinning at 4000 rpm. The substrate was then spun for one additional minute to ensure a uniform spreading of bitumen and further evaporation of toluene. The obtained bitumen coating was kept in a dust-free horizontal laminar hood environment. Prior to induction time measurement, bitumen-coated samples were immersed in testing aqueous solutions prepared in plant recycle process water with or without amine addition for 2 h to reach dynamic equilibrium.<sup>2, 16</sup>

#### 3.2.2.2 Induction time determination

The induction time was measured using an in-house built induction timer.<sup>7</sup> A rectangular glass cell containing 10 mL of test aqueous solutions with a specific pH and a bitumen sample sitting on the bottom was placed on a three-axial

translation stage. The experiment was conducted by bringing an air bubble in contact with and then retracting away from the bitumen surface. An air bubble with a diameter of 1.5 mm was generated at the end of a glass capillary tube immersed in the glass cell using a microsyringe. After an equilibrium period of 15 min, the bubble was brought down in contact with the bitumen surface with an approaching speed of 40 mm/s. The air-bitumen contact was maintained for a given period, and then the air bubble was moved upward away from the bitumen surface at the same speed. With the aid of a charge coupled device (CCD) camera, one can easily judge whether the bubble attached to the bitumen surface or not. All experiments were conducted under ambient temperature, with the initial distance between the air bubble and the bitumen surface and the bubble displacement being kept constant at 0.25 and 0.4 mm, respectively.

The successful attachment of the air bubble to bitumen consists of three stages: film drains from an initial thickness to a critical thickness, where film rupture takes place spontaneously, followed by film rupture to form a three-phase contact line (TPCL), and TPCL expanding to a certain radius at which a stable attachment can be established.<sup>7, 21, 22</sup> Hence, it is clear that air bubble-bitumen attachment can only occur when the contact time is equal or larger than the sum of time required to accomplish these three stages. If there is no attachment, it means that the contact time is not sufficient to make a stable three phase contact. To obtain a percentage of attachment (number of attachments divided by the total trials), 20 measurements were repeated for a given contact time. The procedure was then repeated at different contact time values to generate a distribution percentage of attachment with contact time. The contact time at which 50% of attachment was observed is considered as the induction time.<sup>4, 5</sup> In general, as shown in **Fig. 3-2**, no attachment occurs when the contact time is short. The percentage of attachment increases with the contact time, and finally, it reaches 100% at a longer contact time. **Fig. 3-2** also shows a good reproducibility of the induction time measurement between the air bubble and bitumen in 1 mM *n*-butylamine process water solutions. From **Fig. 3-2**, we can determine the induction time for

air bubble-bitumen attachment to be 700 ms in recycle process water and 312 ms in 1 mM *n*-butylamine process water solution at pH 9.

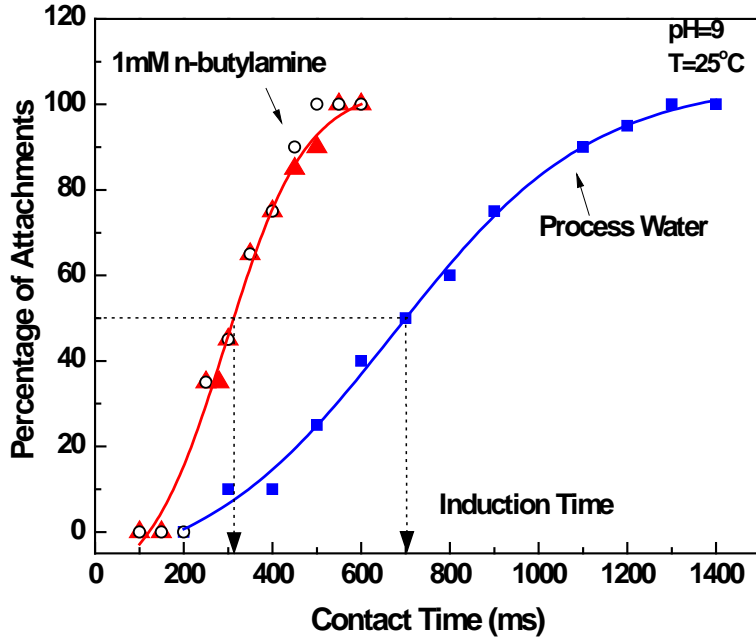


**Fig. 3-2** Attachment percentage of 20 contacts between air bubble and bitumen as a function of contact time. Open circle shows the reproducibility of induction time measurement in 1 mM *n*-butylamine process water solution. The bubble approach/retract velocity remained the same during the whole set of experiments.

### 3.2.3 Bitumen displacement

To study the effect of amine on bitumen liberation from sand grains, a simulated bitumen recession from a glass surface was analyzed using a drop shape analysis instrument (DSA 10, Krüss).<sup>14, 23</sup> A microscope glass plate with a smooth, hydrophilic surface was used as a substrate for the bitumen displacement test. The glass slide was cleaned by chromic acid and then hot water, followed by repetitive rinsing with deionized water. A thin sheet of bitumen in a disk shape (diameter of 8 mm; thickness of 0.8 mm) was placed on this clean and dry glass surface. The glass plate was placed at the bottom of a square glass cell, which was then gently filled with an aqueous solution of pH 8.5 at 70 °C. The bitumen recessed inward in the radial direction spontaneously and finally formed a bitumen droplet attached to the glass slide. The entire recession process was

recorded by a video camera for further analysis. The bitumen displacement from the glass surface was evaluated by the changing of the bitumen contact angle on the glass surface in aqueous solutions measured through the aqueous phase.

### ***3.2.4 Bitumen recovery determination***

The bitumen extraction test was conducted in a Denver flotation cell at 35 °C using plant recycle process water with or without *n*-butylamine addition. The pH of the slurry for flotation was adjusted to 8.5 before flotation. For each test, 300 g of oil sands ore and 950 mL of tested water were mixed in the Denver cell and conditioned for 5 min at 1500 rpm. The air flow of 150 mL/min was then introduced, and bitumen froth was collected at time intervals of 0-3, 3-5, 5-10, and 10-20 min. The composition (bitumen, solids, and water) of the obtained bitumen froth was determined using the Dean-Stark apparatus, with toluene as the reflux solvent.<sup>20</sup> The mass ratio of bitumen and solids of collected bitumen froth was used to evaluate the bitumen froth quality: a higher ratio represents a better bitumen froth quality. To collect the water in the tailings slurry (remaining slurry in the Denver cell) with minimum bitumen content for further testing, bitumen flotation was continued for another 40 min to remove the remaining bitumen in the tailings slurry. After flotation, the tailings slurry was allowed to settle for 30 min in a graduated cylinder and the upper portion without coarse solids was collected. The pH of the obtained tailings slurry was measured to be about 8.6, and it was fairly independent of the type of ores used.

### ***3.2.5 Surface characterization of bitumen and solids***

After settling for 24 h, the upper portion of the tailings slurry from the Denver cell flotation test was used for solids zeta potential measurements. Fine solids from the upper portion of the tailings slurry was recovered by centrifuging at 20000 g force for 30 min. The collected fine solids were washed several times by deionized water and then dried in an oven overnight. The fine solids collected as such were used for water drop penetration time (WDPT) measurement and X-ray photoelectron spectroscopy (XPS) analysis. For WDPT measurement, a fine solids disk with a 24.5 mm diameter was made using a manual hydraulic press

(Enerpac JH-5) with 26.7 kN of applied force. A deionized water droplet of 10  $\mu$ L volume was then placed onto the disk, and the penetration process of this drop on the solids disk was recorded by a video system in the DSA instrument.<sup>8, 10, 24</sup> The video was later used to obtain the WDPT, which is defined as the time needed for a water drop to penetrate completely into the disk. XPS analysis was performed on an AXIS 165 spectrometer (Kratos Analytical).<sup>10</sup>

Zeta potential of bitumen and fine solids in different solutions was determined using a Zeta PALS (Brookhaven Instruments Corp., New York). Clear tailings water at pH 8.6, obtained after removal of any fine solids and fugitive bitumen by filtration using 0.1  $\mu$ m filters was used for additional experiments. Bitumen emulsion was prepared by dispersing 1 g of bitumen in 100 mL of clear tailings water using a sonic dismembrator.<sup>18,19</sup> After creaming for 30 min, several drops of the bitumen emulsion were added into corresponding clear tailings water. All samples were conditioned in an ultrasonic bath for 10 min prior to zeta potential measurements. Two ores and two concentrations of *n*-butylamine process water solutions were used in flotation tests, giving four sets of experimental data. A total of 10 zeta potential measurements and 3 WDPT tests were performed for each sample, and the average value with the standard deviation are reported.

### **3.3 Results**

To recover bitumen, it must be first liberated from sand grains and then attach to air bubbles to float onto the surface of flotation slurry. In this section, the effect of amine addition on attachment of air bubble to bitumen surface and on liberation of bitumen from sand grains is discussed.

#### ***3.3.1 Air bubble-bitumen attachment***

##### **3.3.1.1 Induction time measurement in process water**

As a baseline, the induction time between the air bubble and bitumen surface was measured in recycle process water without amine addition. The results in **Fig. 3-3(a)** show a strong induction time dependence upon pH. The induction time remains at about 700 ms for pH 8 and 9 and increases drastically with a further

increase in pH above 9. The change of the chemical property of bitumen and air bubble surfaces with pH is responsible for such a pH dependence. As shown in **Fig. 3-3(b)**, surface tension of water in contact with bitumen drops significantly at pH above 10, in contrast to a pH independent surface tension of water which is not in contact with bitumen. Such a reduction in surface tension of water in contact with bitumen at pH greater than 10 indicates the release of natural surfactants at pH greater than 10, contributing to the observed increase in induction time at pH 10.

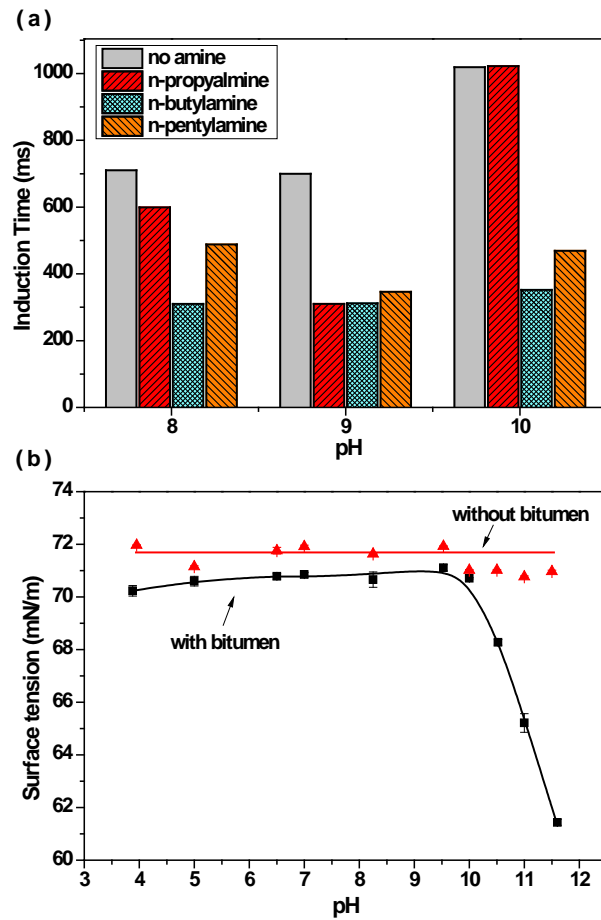


**Fig. 3-3** (a) Effect of pH and amine addition on the induction time of air bubble-bitumen attachment. The concentration of amine solution is 1 mM; (b) Surface tension of de-ionized water with and without contact with bitumen as a function of pH. In contact with bitumen, 4 g bitumen was placed at the bottom of a beaker in contact with 80 mL de-ionized water of desired pH. After 30 min soaking, the

clear aqueous solution was extracted and the surface tension was measured by a Processor tensiometer K12 (Krüss, Hamburg, Germany) using Du Noüy ring method. All measurements were performed at  $20.0 \pm 0.5$  °C.

### 3.3.1.2 Effect of amine addition on induction time

The results in **Fig. 3-3(a)** also show a significant reduction of the induction time over almost the entire pH range in 1 mM amine process water solutions. At pH 9, for example, the induction time decreased by almost 55%, from 700 ms to about 300 ms in 1 mM amine process water solutions. Among the three amines tested, *n*-butylamine appeared to be the most effective in reducing the induction time.

At solution pH higher than 6, the dissociation of natural surfactants at the bitumen/water interface will make the bitumen surface more negatively charged and less hydrophobic. When amines are added in process water, they will adsorb at bitumen/water interfaces, thus making bitumen less negatively charged and hydrophobic again, leading to an easier attachment between the air bubble and bitumen, as shown by a shorter induction time. The adsorption of amine is confirmed by zeta potential measurement in tailings water. The results in Table 3-3 show that the zeta potential of bitumen becomes less negative (from -48 to -40 mV) upon the addition of 10 mM *n*-butylamine to tailings water of ore I at pH 8.6. For ore II, again the zeta potential of bitumen became less negative (from -42 to -34 mV) with the addition of 10 mM *n*-butylamine. It is also possible that amine adsorbs at the air/water interface. The positive or less negatively charged air bubbles are attracted to the negative bitumen surface, contributing to an easier attachment.

**Table 3-3 Zeta potential (mV) of bitumen and solids in extraction tailings water at pH 8.6 with and without 10 mM *n*-butylamine addition**

Particle	Source of tailings water			
	ore I		ore II	
	without amine	with amine	without amine	with amine
bitumen	$-48 \pm 2$	$-40 \pm 2$	$-42 \pm 2$	$-34 \pm 1$
fine solids	$-38 \pm 2$	$-34 \pm 1$	$-31 \pm 1$	$-26 \pm 1$

At pH above 9, the reduction of the induction time with *n*-butylamine and *n*-pentylamine addition remained significant but almost negligible for *n*-propylamine at pH higher than 9 (i.e., pH 10). This could be attributed to the limited protonation of amine at this pH. Among the three amines, *n*-propylamine has the lowest pKa value of 10.61, as compared to 10.67 and 10.72 for *n*-butylamine and *n*-pentylamine, respectively.<sup>25</sup> Admittedly, the difference in pKa values among these three amines is marginal. Because the pH is very close to these pKa values, it is very likely that a small difference in pKa could be very likely to make a significant impact on the distribution between protonated and unprotonated amines and, hence, on the induction time at pH values close to their pKa. The neutral unprotonated amine predominant at pH near its pKa is ineffective to adsorb at the negatively charged bitumen/water interface, leading to a negligible improvement in the induction time.

Because *n*-butylamine was found to be the most effective in reducing the induction time of the air bubble-bitumen attachment, we will now focus on *n*-butylamine. The effect of the *n*-butylamine concentration on the induction time is presented in **Fig. 3-4**. With an increasing amine concentration in the process water at pH 9, the induction time decreased from 700 to 312 ms in 1 mM *n*-butylamine process water solution and to 190 ms in 10 mM *n*-butylamine process water solution. The observed improvement is attributed to an increased amount of *n*-butylamine adsorbed on the bitumen surface and at air-aqueous solution interfaces with an increasing amine concentration.

To determine the optimal pH for the induction time, further measurements were conducted in 10 mM *n*-butylamine process water solutions at 8.5 and 9.5. The results in **Fig. 3-4** show a shorter induction time at pH 8.5 (182 ms) and pH 9 (190 ms) than at pH 9.5 (355 ms), indicating that the best air-bitumen attachment or the shortest induction time of the air bubble-bitumen attachment can be achieved in 10 mM *n*-butylamine process water solution at pH between 8.5 and 9. This finding suggests bitumen flotation in 10mM *n*-butylamine process water solution at pH 8.5-9, preferably at pH 9.0 to maximize bitumen liberation.

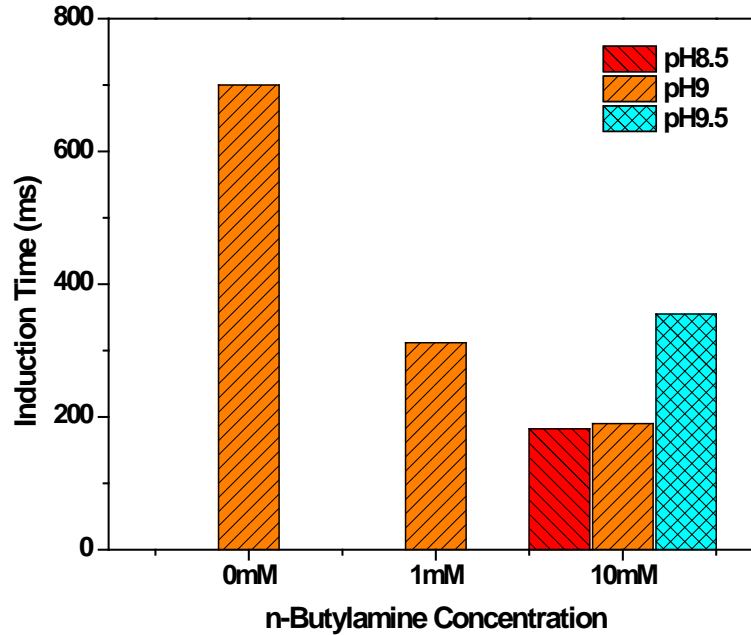


**Fig. 3-4** Induction time of air bubble-bitumen attachment as a function of *n*-butylamine concentration in recycle process water.

**3.3.2 Effect of *n*-butylamine addition on bitumen liberation**

**Fig. 3-5** shows photographs of bitumen displacement from a glass surface. After a bitumen sample (about 40 mg) was immersed in aqueous solutions, the imbalanced interfacial tension made the bitumen move inward, resulting in a smaller contact area between bitumen and glass. This also leads to a smaller contact angle of bitumen on the glass surface. **Fig. 3-5(a)** shows the initial shape of the bitumen drop, while panels b and c of **Fig. 3-5** are taken at different time of the displacement process, showing a decrease in the contact angle of bitumen on glass surface in water with time. **Fig. 3-5(d)** is the shape of the bitumen drop when the displacement reaches an equilibrium state. At this stage, the contact angle remains constant. Contact angles of bitumen on a glass surface measured in the process water with and without *n*-butylamine are shown in **Fig. 3-6**. The displacement rate constant  $k$  ( $s^{-1}$ ) and the equilibrium contact angle  $\theta_e$  (degree) were obtained by fitting the experimental data to the following exponential decay

equation. Constant A is the difference between the initial and equilibrium contact angle of bitumen on the glass surface.

$$\theta = \theta_e + Ae^{-kt} \quad \text{Eqn. 3-1}$$

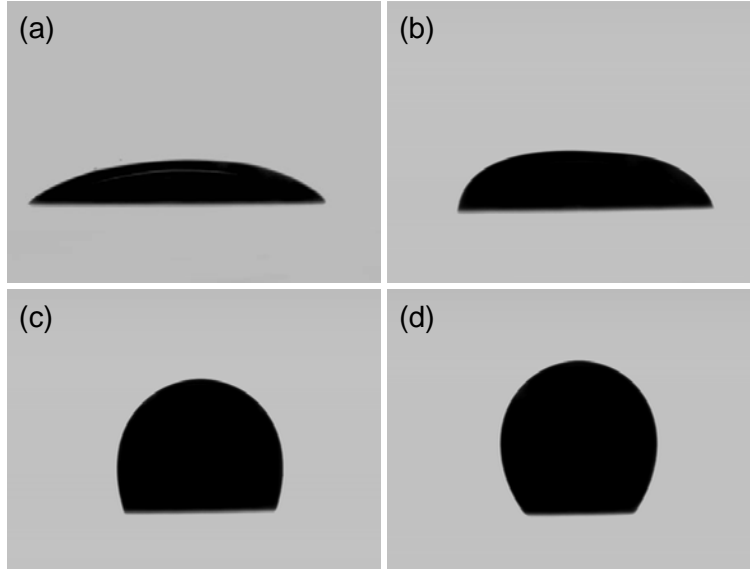


**Fig. 3-5** Photographs of bitumen displacement from a glass surface in a process water at different stages: (a) initial stage of immersing the sample in the process water; (b) and (c) bitumen recession from glass surface in the process water, and (d) equilibrium shape of bitumen in the process water.

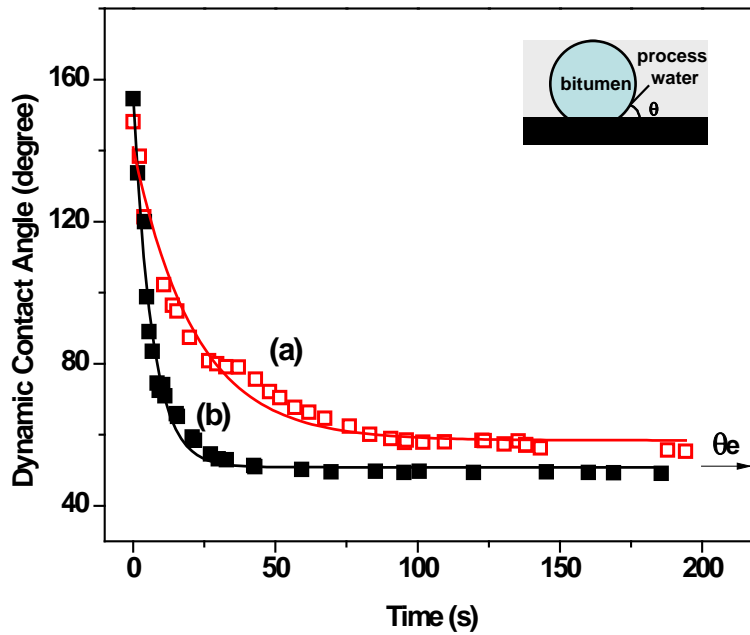


**Fig. 3-6** Dynamic contact angle of bitumen recession on glass surface in different aqueous solutions. Solid lines represent fitting of experimental data to **Eqn. 3-1**, leading to following parameters for process water: (a) plant process water without *n*-butylamine, ( $k = 0.04 \text{ s}^{-1}$ ,  $\theta_e = 58^\circ$ ) and (b) 10 mM *n*-butylamine process water solution ( $k = 0.15 \text{ s}^{-1}$  and  $\theta_e = 50^\circ$ ). All experiments were conducted at pH 8.5 and 70 °C.

The amine addition leads to a significant increase in the displacement rate constant from  $0.04 \text{ s}^{-1}$  to  $0.15 \text{ s}^{-1}$ , representing a 4 times improvement in the bitumen recession rate by 10 mM *n*-butylamine addition. Furthermore, the equilibrium contact angle of bitumen on the glass in *n*-butylamine solutions decreased slightly from  $58^\circ$  to  $50^\circ$ , indicating that bitumen can be more easily removed from the glass surface in amine process water solutions than in process water without amine addition.

### **3.3.3 Effect of *n*-butylamine on bitumen recovery**

The results obtained from previous measurements showed that the addition of 10mM *n*-butylamine to process water at pH 8.5 improved air-bitumen attachment and bitumen recession from the glass surface. This finding suggests that flotation in 10 mM *n*-butylamine process water solution would result in a higher bitumen recovery, as compared to bitumen flotation in process water without amine addition. To confirm this hypothesis, two weathered ores were used in Denver flotation tests. The results in **Fig. 3-7** show that, for both weathered ores, I and II, bitumen recovery increased by more than 20% in 10 mM *n*-butylamine process water solution: from 71 to 93% for weathered ore I and from 53 to 74% for weathered ore II.

**Fig. 3-8** shows the effect of amine addition on bitumen froth quality. Unlike bitumen recovery, amine addition had only marginal improvement on bitumen froth quality. The noticeable increase in the bitumen/solids ratio indicates that *n*-butylamine has no negative effect on bitumen froth quality, as we expected. This finding demonstrates that *n*-butylamine is a good process aid for bitumen extraction of weathered/oxidized ores.

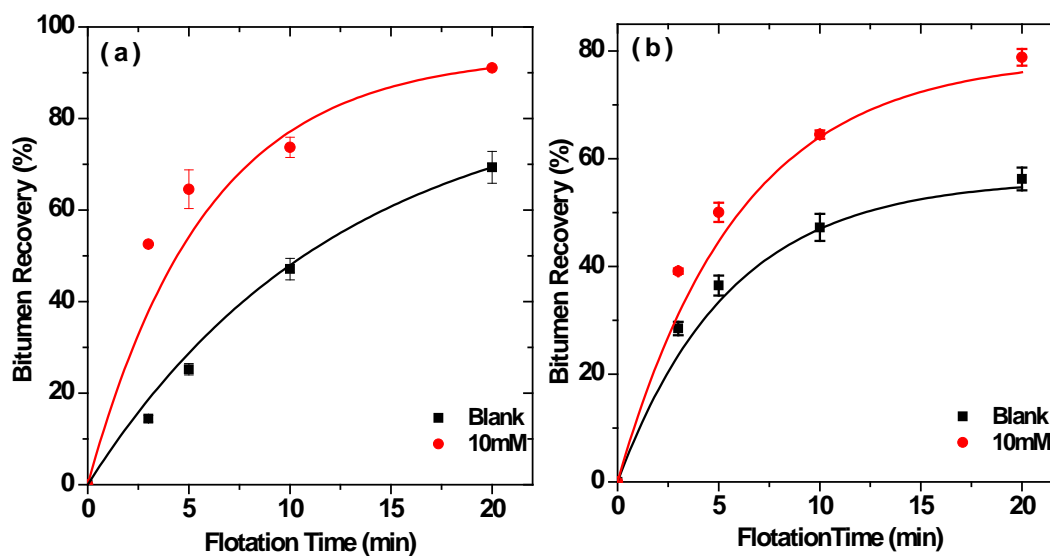


Fig. 3-7 Effect of n-butylamine addition on bitumen recovery from weathered oil sands ores at 35 °C and pH=8.5: (a) ore I; (b) ore II

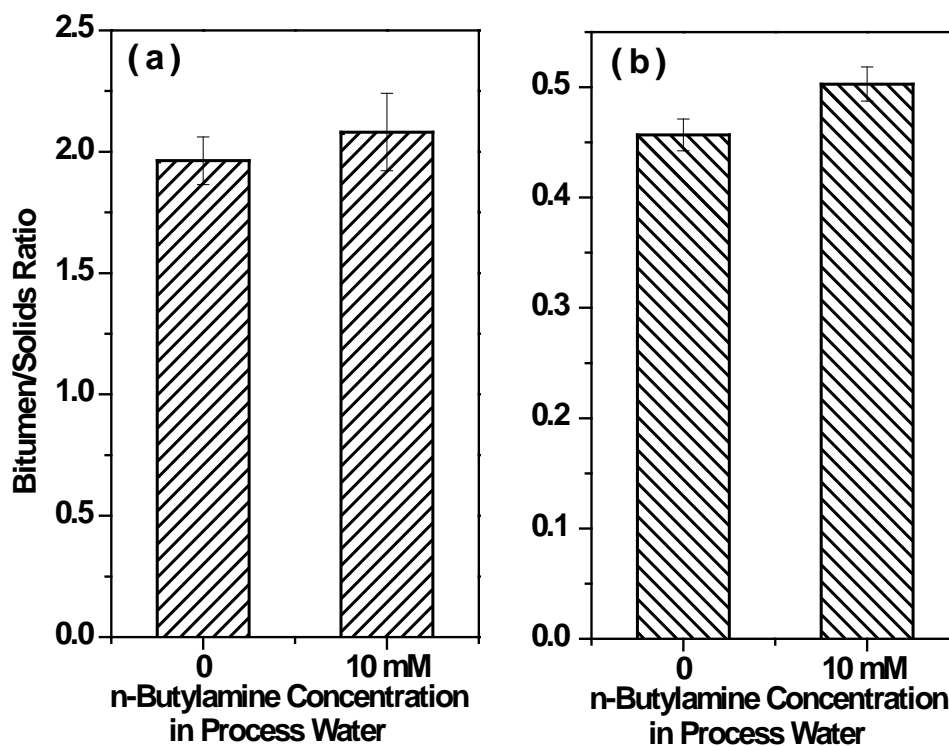


Fig. 3-8 Effect of amine addition on bitumen froth quality: (a) ore I; (b) ore II

### 3.3.4 Effect of *n*-butylamine on solid wettability

Denver cell bitumen flotation tests demonstrated that *n*-butylamine addition can improve bitumen recovery of weathered oil sands ores by approximately 20%. At the same time, it maintains the bitumen froth quality, which indicates that the addition of *n*-butylamine did not decrease the wettability of solids. To further study the effect of *n*-butylamine addition on the hydrophobicity of solids in weathered oil sands ores, fine solids were isolated from different tailings water after Denver cell flotation. The results of **Table 3-4** for the WDPT test of fine solids isolated from four different Denver cell flotation tailings slurry show a noticeable decrease in WDPT from 161 to 142 s and from 117 to 67 s for solids isolated from ores I and II, respectively. The reduction of WDPT indicates that the fines in tailings slurry for both oil sands ores became more hydrophilic when conducting bitumen flotation in 10 mM *n*-butylamine process water solution.

**Table 3-4 WDPT (s) for fine solids isolated from different tailings water**

Solids	Process water without amine addition	10mM <i>n</i> -butylamine process water solution
Ore I	161 ± 4	142 ± 2
Ore II	117 ± 3	67 ± 2

As well, the results in Table 3-3 show that the zeta potential of fines isolated from both ores increases only marginally from -38 to -34 mV for ore I and from -31 to -26 mV for ore II. It appears that only a minimal, if any, of *n*-butylamine adsorbs on solid surfaces. To account for the increased wettability of the solids as revealed by the reduced WDPT with *n*-butylamine addition, *n*-butylamine appears to solublize and remove the organic contaminants from the solids surfaces, as confirmed by the XPS results discussed below.

To better understand the effect of amine addition on surface characteristics of fines, the XPS method was used to analyze solids surface chemical composition. Carbon and sulfur are considered as feature elements of organic matter on solids surfaces, because they both increase when more organic molecules are present on solids.<sup>10</sup> From the XPS results in Table 3-5, one can note that both of these

elements were reduced when *n*-butylamine was added. The contents of alumina, silica, and oxygen, which are the main composition of solids, on the other hand, were increased with *n*-butylamine addition. A low concentration of C and S and a high concentration of Si, Al, and O reflect lower coverage of organic matter on a surface. This finding indicates that the surface of solids obtained from bitumen extraction with *n*-butylamine addition is “cleaner” of hydrocarbons. A conceptual image of the effect of *n*-butylamine on the solids surface is presented in the bottom of **Fig. 3-1(b)**. *n*-Butylamine acted as a “scavenger” for the organic matter on solids surfaces. The removal of the organic matter is responsible for the reduced hydrophobicity of solids. Although the mechanism of the “cleaning” is unclear, the XPS and WDPT tests indeed show a reduction of solids hydrophobicity with amine addition. TIOM is mainly composed of humic matter, which is negatively charged at pH around 8.6,<sup>9, 26-28</sup> and the reduction of this material from solids surface makes the solids less negatively charged. Once more, it appears that the adsorption of *n*-butylamine on solids occurs at locations of residual bitumen or organic matter in such a way that the positively charged, hydrophilic amine group faces the aqueous phase, as shown in the bottom of **Fig. 3-1(b)**. The removal of TIOM from the solids surface and adsorption of amine on the solids surface together lead to an increased zeta potential and a decreased WDPT of solids as measured.

**Table 3-5 Solids surface composition (atomic weight percentage) from different ores by XPS**

Solids	C	S	C + S	Si	Al	O	Si + Al + O
Ore I, blank	65.1	1.7	66.8	6.6	3.9	22.7	33.2
Ore I, 10mM	58.8	1.5	60.3	8.8	3.9	26.9	39.7
Ore II, blank	70.2	1.9	72.1	5.4	3.7	18.8	27.9
Ore II, 10mM	54.1	1.2	55.3	9.4	5.2	30.1	44.8

Furthermore, the reduction of C and S with amine addition is larger for ore II than for ore I. At the same time, the increase of Si, Al, and O of ore II is also greater than that of ore I. This observation suggests that the organic removal from solids surfaces of ore II was more than that from ore I. This is consistent with the

fact that the hydrophobicity reduction for ore II is larger than for ore I, as observed in WDPT tests, although the exact mechanism for such a difference remains to be established.

### 3.4 Discussion

The results obtained in this study confirm that the induction time is a suitable method to study the interaction between the air bubble and bitumen surface, the effect of water chemistry on bubble-bitumen attachment, and hence, the bitumen flotation. Improvement of the air bubble-bitumen attachment, i.e., a smaller induction time, is achieved by the addition of short-chain amines.

The induction time of the air bubble-bitumen attachment in process water without amine addition remains almost the same at pH 8 and 9 and increases drastically at pH 10. Accumulation of natural surfactants from bitumen at the bitumen/water and air/water interfaces as shown in **Fig. 3-3(b)** is considered to be the main reason for the observed increase in the induction time at pH higher than 9. When bitumen is in contact with an aqueous solution, the natural surfactants in bitumen are released from bitumen and adsorb at the bitumen/water and air/water interface, thus affecting the surface charge of the bitumen and air bubble surface on the account of increased ionization of carboxylic acid at the bitumen/water and air/water interface in an alkaline environment. The results of zeta potential measurements of bitumen in clear tailings water provided in Table 3-3 show that, without *n*-butylamine addition, the zeta potentials of bitumen in flotation tailings water for the two weathered ores were -48 and -42 mV, respectively. These results are in the range of the reported zeta potential values of bitumen in process water at pH 8.3.<sup>18</sup> These negatively charged water-soluble carboxylic ions will make the bitumen surface less hydrophobic, i.e., more difficult for an air bubble to attach. Furthermore, both air bubbles and bitumen surfaces become more negatively charged at higher pH, and thus, the repulsive force between the anions would also make the attachment more difficult.

The attachment between a bubble and particle depends upon the rupture property of the intervening liquid film and surface forces between them. When a

bubble approaches a bitumen surface, the film between the bubble and bitumen surfaces will be compressed; the drainage rate of this thin liquid film is a dominant factor in determining the attachment process. The improvement of the air bubble-bitumen attachment in amine process water solution is due to an increase in the film drainage rate. When the film is thin (< 50-100 nm), surface forces become dominant.<sup>17, 29, 30</sup> Generally speaking, three major forces act on surfaces: the long-range hydrophobic force, the van der Waal force, and the electrical double-layer force. The change of water chemistry will influence the surface properties of the air bubble and bitumen and, hence, alter the forces between them. Specifically, the van der Waal force is more dependent upon properties of materials and less sensitive to the change of the surrounding aqueous environment. The bitumen surface will become less hydrophobic because of the increased dissociation of natural surfactants with increasing pH. However, the adsorption of amine will increase the hydrophobicity, resulting in a larger long-range hydrophobic attractive force. Moreover, amine also makes the bitumen and air bubble surfaces less negatively charged, thus reducing the repulsive electrical double-layer force. The increased hydrophobic force and decreased repulsive double-layer force will therefore lower the energy barrier for the two surfaces approaching each other and lead to an increase in the film drainage rate, thereby facilitating film rupture, as measured by a smaller induction time in amine process water solution.

Typically, a 40-55°C slurry temperature is used in water-based bitumen extraction from oil sands, and 75-80°C for hot slurry extraction process<sup>31</sup>. The boiling point of *n*-butylamine is 78°C, hence, the application of *n*-butylamine on bitumen extraction will not be applicable on the hot slurry extraction process. The paper has shown that *n*-butylamine can improve bitumen recovery from weathered/oxidized oil sands ores by 20% and has no negative effect on froth quality and tailings settling velocity (not shown in this paper). However, its impact on froth treatment and water chemistry of tailings should be addressed before its implementation in commercial oil sands extraction process.

### 3.5 Conclusions

The effects of three primary short-chain amines on the attachment between the air bubble and bitumen were studied by the induction time measurement. The induction time of the air bubble-bitumen attachment in the plant recycle process water was found highly pH-dependent. All three short-chain amines used in this project reduced the induction time drastically at nearly all pH values, reaching a minimum induction time at pH 9. Among the three amines tested, *n*-butylamine was found to be the most effective in improving air-bitumen attachment. Furthermore, *n*-butylamine facilitates the recession of bitumen droplet from a glass surface in process water at pH 8.5. The zeta potential measurement revealed adsorption of *n*-butylamine on the bitumen surface, which increased hydrophobicity of bitumen, decreased the induction time of the air bubble-bitumen attachment, and facilitated bitumen liberation from the sand grains. XPS and the WDPT study showed that *n*-butylamine makes solids of weathered oil sands more hydrophilic. The improvement of bitumen recovery from weathered/oxidized oil sands ores by the addition of *n*-butylamine was established through Denver cell bitumen flotation tests. At pH 8.5, bitumen recovery increased by more than 20% for two weathered ores in 10 mM *n*-butylamine process water solutions. A shorter induction time of the air bubble-bitumen attachment correlated well with corresponding higher bitumen recovery.

### 3.6 References

- (1) Kasongo, T.; Zhou, Z.; Xu, Z.; Masliyah, J. Effect of Clays and Calcium Ions on Bitumen Extraction from Athabasca Oil Sands using Flotation. *Can. J. Chem. Eng.* **2000**, *78*, 674-681.
- (2) Su, L.; Xu, Z.; Masliyah, J. Role of Oily Bubbles in Enhancing Bitumen Flotation. *Minerals Eng* **2006**, *19*, 641-650.

- (3) Peng, F. F. Surface Energy and Induction Time of Fine Coals Treated with Various Levels of Dispersed Collector and their Correlation to Flotation Responses. *Energy Fuels* **1996**, *10*, 1202-1207.
- (4) Yoon, R.; Yordan, J. L. Induction Time Measurements for the Quartz-Amine Flotation System. *J. Colloid Interface Sci.* **1991**, *141*, 374-383.
- (5) Ye, Y.; Khandrika, S. M.; Miller, J. D. Induction-Time Measurements at a Particle Bed. *Int. J. Miner. Process.* **1989**, *25*, 221-240.
- (6) Sven-Nilsson, I. Effect of Contact Time between Mineral and Air Bubbles on Flotation. *Kolloid Z.* **1935**, *69*, 230.
- (7) Gu, G.; Xu, Z.; Nandakumar, K.; Masliyah, J. Effects of Physical Environment on Induction Time of Air-Bitumen Attachment. *Int. J. Miner. Process.* **2003**, *69*, 235-250.
- (8) Dang-Vu, T.; Jha, R.; Wu, S.; Tannant, D. D.; Masliyah, J.; Xu, Z. Effect of Solid Wettability on Processability of Oil Sands Ores. *Energy Fuels* **2009**, *23*, 2628-2636.
- (9) Sparks, B. D.; Kotlyar, L. S.; O'Carroll, J. B.; Chung, K. H. Athabasca Oil Sands: Effect of Organic Coated Solids on Bitumen Recovery and Quality. *J. Petrol. Sci. Eng.* **2003**, *39*, 417-430.
- (10) Ren, S.; Dang-Vu, T.; Zhao, H.; Long, J.; Xu, Z.; Masliyah, J. Effect of Weathering on Surface Characteristics of Solids and Bitumen from Oil Sands. *Energy Fuels* **2009**, *23*, 334-341.
- (11) Fong, N.; Ng, S.; Chung, K. H.; Tu, Y.; Li, Z.; Sparks, B. D.; Kotlyar, L. S. Bitumen Recovery from Model Systems using a Warm Slurry Extraction Process: Effects of Oilsands Components and Process Water Chemistry. *Fuel* **2004**, *83*, 1865-1880.
- (12) Dai, Q.; Chung, K. H. Hot Water Extraction Process Mechanism using Model Oil Sands. *Fuel* **1996**, *75*, 220-226.

- (13) O'Carroll, J. B. Factors Affecting Bitumen Recovery From Oil Sands, University of Ottawa, Ottawa, Canada, 2000.
- (14) Basu, S.; Nandakumar, K.; Masliyah, J. H. Effect of NaCl and MIBC/Kerosene on Bitumen Displacement by Water on a Glass Surface. *Colloids Surf. Physicochem. Eng. Aspects* **1998**, *136*, 71-80.
- (15) Drelich, J.; Miller, J. D. Surface and Interfacial Tension of the Whiterocks Bitumen and its Relationship to Bitumen Release from Tar Sands during Hot Water Processing. *Fuel* **1994**, *73*, 1504-1510.
- (16) Isaacs, E. E.; Smolek, K. F. Interfacial Tension Behavior of Athabasca Bitumen/Aqueous Surfactant Systems. *Can. J. Chem. Eng.* **1983**, *61*, 233-240.
- (17) Liu, J.; Xu, Z.; Masliyah, J. Studies on Bitumen-Silica Interaction in Aqueous Solutions by Atomic Force Microscopy. *Langmuir* **2003**, *19*, 3911-3920.
- (18) Zhao, H.; Long, J.; Masliyah, J. H.; Xu, Z. Effect of Divalent Cations and Surfactants on Silica-Bitumen Interactions. *Industrial and Engineering Chemistry Research* **2006**, *45*, 7482-7490.
- (19) Liu, J.; Zhou, Z.; Xu, Z.; Masliyah, J. Bitumen–Clay Interactions in Aqueous Media Studied by Zeta Potential Distribution Measurement. *J. Colloid Interface Sci.* **2002**, *252*, 409-418.
- (20) Bulmer, J. T.; Starr, J. In *Syn crude Analytical Methods for Oil Sand and Bitumen Processing*; AOSTRA: Edmonton, Canada, 1979.
- (21) Wang, W.; Zhou, Z.; Nandakumar, K.; Masliyah, J. H.; Xu, Z. An Induction Time Model for the Attachment of an Air Bubble to a Hydrophobic Sphere in Aqueous Solutions. *Int. J. Miner. Process.* **2005**, *75*, 69-82.
- (22) Nguyen, A. V.; Schulze, H. J.; Ralston, J. Elementary Steps in Particle—Bubble Attachment. *Int. J. Miner. Process.* **1997**, *51*, 183-195.

- (23) Basu, S.; Nandakumar, K.; Lawrence, S.; Masliyah, J. Effect of Calcium Ion and Montmorillonite Clay on Bitumen Displacement by Water on a Glass Surface. *Fuel* **2004**, *83*, 17-22.
- (24) Dang-Vu, T.; Jha, R.; Wu, S.; Tannant, D. D.; Masliyah, J.; Xu, Z. Wettability Determination of Solids Isolated from Oil Sands. *Colloids Surf. Physicochem. Eng. Aspects* **2009**, *337*, 80-90.
- (25) Grechin, A. G.; Buschmann, H.; Schollmeyer, E. Complexation of Gaseous Guests by Solid Host: I. Quantitative Thermodynamic Approach for the Reactions of  $\beta$ -Cyclodextrin with Amines using Data in Aqueous Solution. *Thermochimica Acta* **2006**, *449*, 67-72.
- (26) Warwick, P.; Hall, A.; Pashley, V.; Bryan, N. Investigation of the Permeability of Humic Molecules using Zeta Potential Measurements. *Chemosphere* **2001**, *45*, 303-307.
- (27) Childress, A. E.; Deshmukh, S. S. Effect of Humic Substances and Anionic Surfactants on the Surface Charge and Performance of Reverse Osmosis Membranes. *Desalination* **1998**, *118*, 167-174.
- (28) Fairhurst, A. J.; Warwick, P. The Influence of Humic Acid on Europium–Mineral Interactions. *Colloids Surf. Physicochem. Eng. Aspects* **1998**, *145*, 229-234.
- (29) Yoon, R. H.; Guzonas, D.; Aksoy, B. S.; Czarnecki, J.; Leung, A. In *In Role of surface forces in tar sand processing*. Fossil Fuels, Derivatives and Related Products; 1995; pp 277-289.
- (30) Pushkarova, R. A.; Horn, R. G. Bubble-Solid Interactions in Water and Electrolyte Solutions. *Langmuir* **2008**, *24*, 8726-8734.
- (31) Masliyah, J.; Zhou, Z.; Xu, Z.; Czarnecki, J.; Hamza, H. Understanding Water-Based Bitumen Extraction from Athabasca Oil Sands. *Can. J. Chem. Eng.* **2004**, *82*, 628-654.

# **Chapter 4**

## **Introduction of the Integrated Thin Liquid Film Drainage Apparatus**

## 4.1 Introduction<sup>‡</sup>

A thin liquid film forms as a result of two dispersed particles approaching each other in a liquid medium. Improving our understanding of thin liquid film stability is of profound importance as it plays a critical role in a variety of important areas, including lubrication, flotation of minerals, coating, foams and the stability of colloidal suspensions. Depending on the nature of applications, it is desirable to control the stability of thin liquid films as film rupture may or may not be beneficial. For example, film rupture is desirable in mineral flotation to form stable three phase contact for lifting desired particles using air bubbles. Although the efficiency of bubble-particle attachment depends on many factors, the hydrodynamics of the intervening liquid film thinning is shown to play a crucial role.<sup>1</sup> A stable film is, on the other hand, highly desirable to obtain a finely dispersed coating, stable emulsions or efficient lubrication.

Due to its wide range of applications, much effort has been made to study thinning hydrodynamics and stability mechanisms of thin liquid films between two dispersed particles. Interferometric methods have been widely used to investigate both symmetric (emulsions and foam films) and asymmetric (wetting films) thin liquid films.<sup>2</sup> A thin liquid film can form in one of the following three manners: 1) withdrawing the liquid in a porous cylindrical cell (i.e., in the Scheludko-Exerowa cell<sup>3</sup> and Exerowa-Scheludko porous plate cell<sup>4</sup>) during which the film is trapped between two opposing menisci; 2) moving two bubbles/droplets formed in a liquid at the end of two opposing sealed capillary tubes that share a common axis towards each other;<sup>5</sup> and 3) bringing an air bubble

---

<sup>‡</sup> Modified from following manuscripts:

- 1) Wang, L.; Xu, Z. and Masliyah, J.H. Dissipation of film drainage resistance by hydrophobic surfaces in aqueous solutions, submitted to *Proceedings of the National Academy of Sciences*.
- 2) Wang, L.; Sharp, D.; Xu, Z. and Masliyah, J.H. Measurement of interactions between solid particles, liquid droplets and/or gas bubbles in a liquid using an integrated thin film drainage apparatus, submitted to *Langmuir*.
- 3) Wang, L.; Sharp, D.; Xu, Z. and Masliyah, J.H. A novel induction timer to study interactions between an air bubble and bitumen surface, in *Separation Technologies for Minerals, Coal and Earth Resources*, SME, 2012, ed. Courtney A. Young and Gerald H. Luttrell, Englewood, CO, pp. 47-55.

towards a solid surface in a liquid<sup>6, 7</sup> or pushing air in a capillary immersed in a liquid towards a solid plate.<sup>8</sup> In all of these techniques, the thickness of the film is determined using micro interferometric method based on multiple reflection and interference of a monochromatic light. This technique allows accurate measurement of equilibrium or critical film thickness and film lifetime under a given disjoining pressure for all three types of films. The calculation of the film thickness is based on the assumption that the film is optically homogeneous and it has the same reflective index of the bulk solution. In some cases this assumption is not valid.<sup>2</sup>

The development of the surface force apparatus (SFA)<sup>9, 10</sup> and atomic force microscope (AFM)<sup>11</sup> has made it possible to directly and quantitatively measure the interaction forces between two approaching surfaces across a liquid film. SFA provides a direct measurement of colloidal forces at pN/m resolution as a function of absolute separation distance measured by optical interferometry to a nano meter resolution. However, the measurement using SFA requires the surfaces being transparent, which greatly limits its application to only a limited number of materials and systems. The introduction of colloidal probe technique to AFM makes it possible to study almost any kind of surfaces.<sup>12</sup> For the AFM probe technique, a spherical probe particle is attached to the cantilever of the AFM and the lower surface is moved up and down using a piezoelectric transducer. The interaction forces are measured by recording the cantilever deflection. The wetting film between the air bubble and particle using AFM was first studied by Ducker et al.,<sup>13</sup> Butt<sup>14</sup> and Fielden et al.<sup>15</sup> In their experiments a small air bubble was placed onto a hydrophobic substrate and the bubble was moved up to the particle on the cantilever. AFM has also been employed to measure forces between a solid particle and deformable liquid droplet or between two oil droplets in aqueous solutions.<sup>16-19</sup>

The existing SFA and AFM techniques have been successfully used to study the stability of thin liquid films between surfaces. To minimize hydrodynamic effect, most of the experiments are conducted under low approach velocities. In

real systems such as collision of air bubbles with mineral particles in flotation and thermal motion of droplets in micro emulsions, there exists significant hydrodynamic resistance between two approaching surfaces. For this reason, the application of the current techniques to study thin liquid film under dynamic condition has been rather limited, if not impractical. In this study, an integrated thin film drainage apparatus (ITFDA) was designed and constructed to directly and simultaneously measure the drainage time and force barrier of almost any kind of thin liquid films under a wide range of hydrodynamic conditions. Moreover, the ITFDA allows accurate measurement of receding and advancing contact angles, capillary force and detachment force between an air bubble (or oil droplet) and a solid surface.

## **4.2 Instrumentation**

### ***4.2.1 Instrument design***

The ITFDA was developed based on the combination of an existing, custom-designed induction time instrument<sup>20</sup> and Measurement and Analysis of Surface Interactions and Forces (MASIF) device.<sup>21, 22</sup> As shown schematically in **Fig. 4-1(a)**, the ITFDA uses a bimorph cantilever as a force sensor and a diaphragm of a high frequency speaker as the drive for a controllable, rapid and large displacement.

When studying wetting films between an air bubble and a solid surface, the air bubble is generated using a micro-syringe at the end of a glass capillary tube which is connected to the speaker diaphragm. A computer is used to generate a wave form that controls the movement of the speaker diaphragm which in turn drives the air bubble to approach or retract from the lower surface in a well controlled manner. With such a mechanism, the approach and retract velocity ( $V$ ), the range of bubble displacement (maximum force applied) as well as the duration of contact can be accurately controlled. The lower surface, say, a glass sphere in the example is clamped at the free end of a bimorph beam. The bimorph is enclosed by a fluorinated ethylene propylene (FEP) sheath and mounted on a small stainless steel chamber which is placed on a three dimensional translation

stage. Two charge-coupled device (CCD) cameras are placed perpendicular to each other near the sample chamber to align the interacting surfaces as well as to control the size of the bubble and the gap between the bubble and solid surfaces.

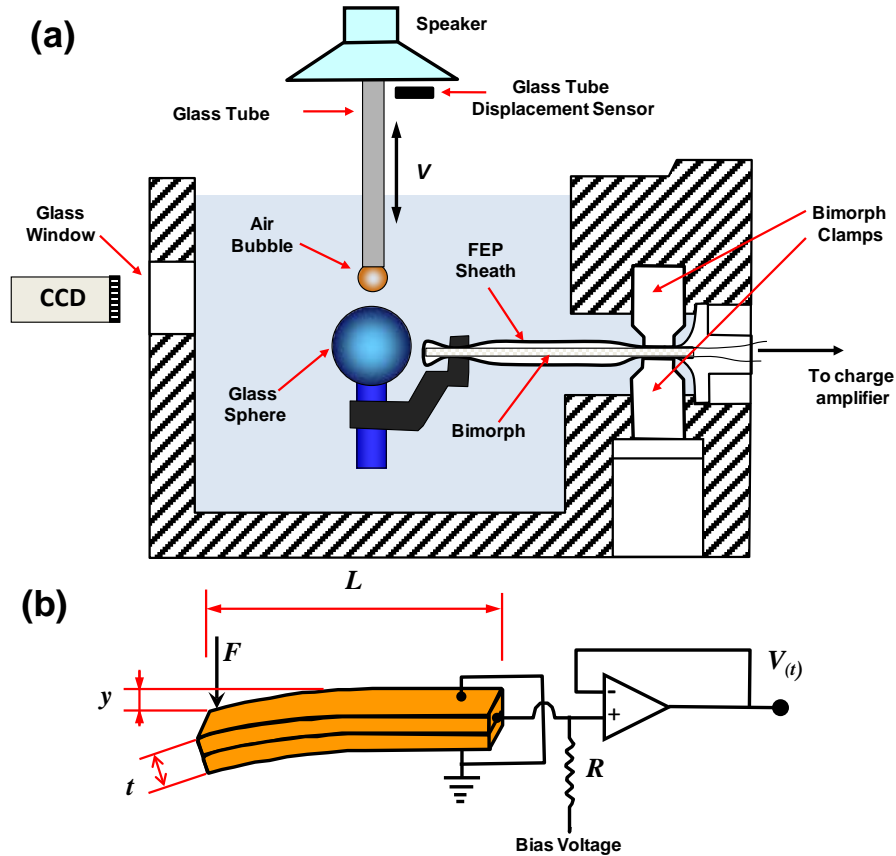


**Fig. 4-1** A schematic view of the integrated thin film drainage apparatus (ITFDA): (a) chamber configuration; (b) description of a piezoelectric bimorph and a high input impedance charge amplifier used to measure the charge generated on the bimorph cantilever under an external force.

When the two surfaces approach each other, deflection of the bimorph occurs due to the interaction forces between the surfaces. The charge generated from the deflection of the bimorph is measured using a bimorph charge amplifier interfaced with a PC. The displacement of the glass tube holding the bubble, on the other hand, is independently measured using a displacement sensor with a sensitivity of  $5 \mu\text{m}$ . The signals from the amplifier and the displacement sensor of the glass tube in response to the voltage applied to the speaker diaphragm are recorded as a

function of time, while one of the digital cameras records the entire displacement process in real time through the PC using a user-developed program, interfaced with LabVIEW 8.0. By analyzing the recorded video and bimorph signals, the entire dynamic process of the upper bubble approaching and retracting from the lower surface can be investigated. The image analysis of the video, on the other hand, allows accurate determination on the size of bubble and glass sphere, the contact area, and the receding ( $\theta_r$ ) and advancing contact angles ( $\theta_a$ ).

An important advantage of using a speaker diaphragm to drive the upper surface is the ability to conduct the measurement over a wide time range, allowing the user to study the interactions between two surfaces under dynamic and equilibrium conditions. The use of the speaker to drive the top surface allows a wide range of approach and retract speeds from  $\mu\text{m/s}$  to  $\text{mm/s}$ , particularly suitable for studying hydrodynamic resistance and its influence on drainage kinetics of thin liquid films. The speaker diaphragm also provides a larger vertical displacement, up to the mm range within a very short period of time, in comparison to commercial AFM which has a maximum z-displacement of  $20\ \mu\text{m}$ . Such a feature enables the user to accurately track the entire separation process of two surfaces.

In this study, a bimorph is used as a cantilever to measure interaction forces between two surfaces. Bimorph is a piezoelectric device which exhibits a reversible piezoelectric effect: the internal generation of electrical charge in response to a deformation of the material under an applied force or the opposite. In 1880, Jacques and Pierre Curie found that the accumulated charge was proportional to the stress applied to the piezoelectric material. As shown in **Fig. 4-1(b)**, the bimorph consists of two slabs of lead zirconate titanate materials fasten together. When a force ( $F$ ) is applied at the end of the bimorph cantilever, a compressive strain is produced on the lower surface and an expansion is created on the upper surface as shown in **Fig. 4-1(b)**, or vice versa. The charge,  $Q$ , accumulated at the bimorph surface can be calculated by:<sup>21</sup>

$$Q = \frac{3}{2} F \frac{L^2}{t^2} d_{31} \quad \text{Eqn. 4-1}$$

The charge,  $Q$ , generated by the shape change of bimorph depends on the applied force,  $F$ , the dimensions of the device (length,  $L$ , and thickness,  $t$ ) and the piezo material charge constant,  $d_{31}$ . Considered as a cantilever beam, the applied force ( $F$ ) at the end of the bimorph cantilever is given by:

$$F = \frac{L^3}{3EI} \cdot y \quad \text{Eqn. 4-2}$$

where  $E$  and  $I$  are Young's Modulus and moment of inertia of the beam, respectively. The deformation along the central axis at the end of bimorph,  $y$ , is linear with the applied force, leading to a proportional change in surface charge. Hence, the applied force and deflection of the bimorph can be described by Hooke's law ( $F = K \cdot y$ , where  $K$  is the effective spring constant of the bimorph beam). A small piece of platinum wire was placed at the end of bimorph cantilever to calibrate the bimorph. The change of accumulated charge on the bimorph was recorded by a high input impedance charge amplifier. Platinum wires with different weight were used to calibrate the bimorph cantilever. The results in **Fig. 4-2** illustrate an excellent linear relationship between the charge generated by the bimorph and the applied weight at proportional gains of 25 and 125, confirming that bimorph can be employed as a force sensor. The spring constant of the bimorph cantilever used in this study was determined to be 60- 80 N/m at a proportional gain of 125.

#### **4.2.2 Operation**

As an illustration to the operation of the instrument, the interaction between an air bubble and a hydrophilic glass surface was conducted in 1 mM KCl solutions. A schematic view of the whole instrument is shown in **Fig. 4-3**. An air bubble of 1.5 mm diameter was created at the end of the glass capillary tube using a micro-syringe. The apexes of the air bubble and the lower glass sphere were aligned centrally and separated to a distance of 0.12 mm with the aid of the two live CCD cameras. In a well sealed tubing system, the bubble size remained constant during the conditioning and measurement time. The actual sizes of the air bubble and

local radius of the glass sphere were determined accurately after the experiment by analyzing the videos using the vision analysis program.

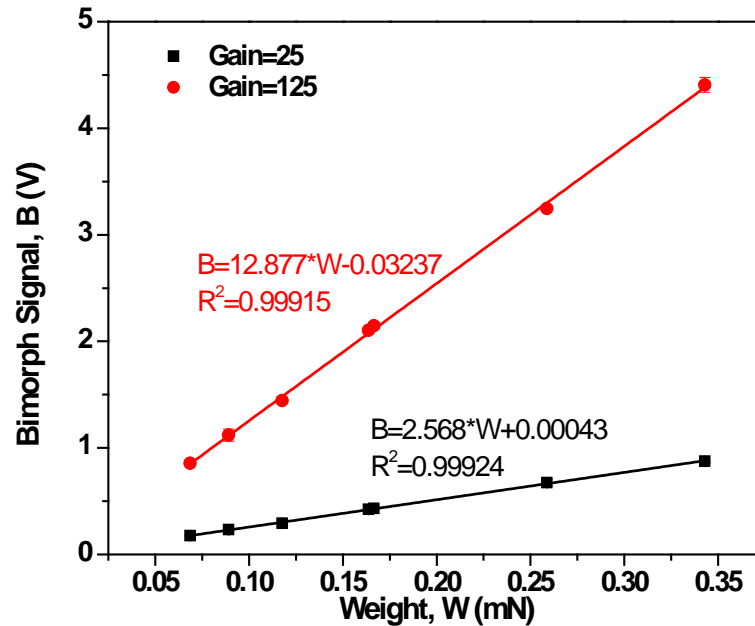


**Fig. 4-2** Calibration of bimorph force sensor with proportional gain of 25 and 125.

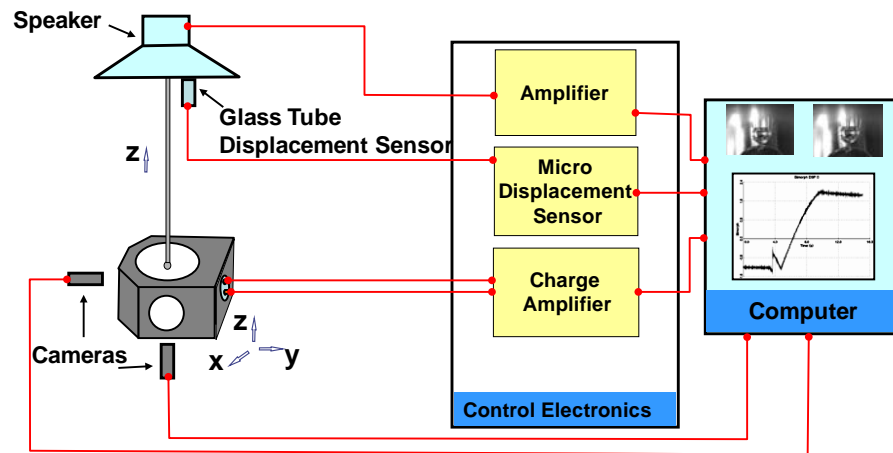


**Fig. 4-3A** schematic view of the integrated thin liquid film drainage apparatus (ITFDA).

A triangular wave with amplitude of 1 V and duration of 4 s was applied to the speaker. **Fig. 4-4** shows the raw data recorded by the device in two successive approach-retract cycles between an air bubble and a hydrophilic glass in 1 mM KCl solutions at pH 5.6, where (a) is the driving signal applied to the speaker, and

(b) and (c) are the responses of glass tube displacement sensor and bimorph, respectively. During the “approach” period, the bubble moves down towards the lower glass surface and the displacement of glass capillary tube increases from 0 to a positive value of 240  $\mu\text{m}$ . While “retract”, the bubble moves away from the lower glass surface and the displacement of glass capillary reduces. The approach ( $V_a$ ) and retract ( $V_r$ ) velocity of the bubble was determined to be 120  $\mu\text{m/s}$ . In all the figures, a positive bimorph response or displacement indicates a downward deflection of the bimorph cantilever (i.e., the glass sphere) from its free position and hence a repulsive force between the two surfaces. A negative bimorph response or displacement means pulling up of the cantilever and hence an attractive force between the two surfaces.

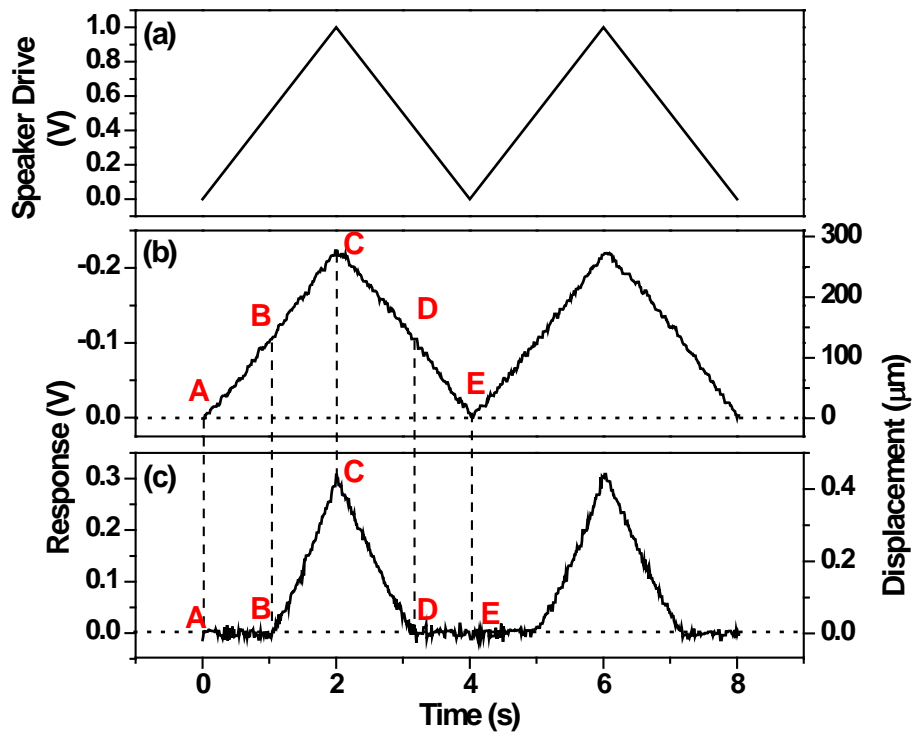


**Fig. 4-4** Raw data recorded by the ITFDA between an air bubble and a hydrophilic glass sphere in a 1 mM KCl solution at  $20 \pm 0.5^\circ\text{C}$ : (a) triangular wave generated by the computer and applied to the speaker diaphragm (two successive cycles: 0-4 and 4-8 seconds are shown); (b) corresponding displacement signal of the speaker diaphragm (glass capillary tube); and (c) bimorph response and displacement indicating interactions between air bubble

and hydrophilic glass surfaces. The diameter of air bubble and glass surfaces is 1.469 mm and 4.365 mm, respectively.

Only repulsive forces were measured between the air bubble and the hydrophilic glass surface without noticeable adhesion. Points A to C on **Fig. 4-4(b)** and (c) represent the approaching period of the bubble to the glass surface. Point A indicates the time when the bubble starts to move towards the glass surface. At a large separation distance, points A to B, there is no net (measurable) force between the two surfaces as indicated by a zero response of the bimorph sensor. At point B, a repulsive force is recorded due to repulsive hydrodynamic force and surface forces between the two surfaces. As the bubble continues moving down by the capillary tube beyond point B, the two surfaces are in contact and the bubble starts to deform progressively while pushing the glass sphere downwards at a constant rate. During the retracting period from point C to E in **Fig. 4-4(b)** and (c), the motion of the bubble is reversed. Initially during retracting, the two surfaces remain in contact until the bubble separates from glass surface at point D where the bimorph signal returns to a zero reading (i.e., the bimorph returns to its original position without upward deflection) indicating no measurable adhesion between the bubble and hydrophilic glass spheres as anticipated. Starting at point E, the process repeats for the next cycle. The measurement can terminate at point E or restart with a different set of hydrodynamic conditions. It is interesting to note that when the two surfaces are in contact, points B to D, the bimorph signal exhibits a linear increase with time from point B to C (approaching) and a linear decrease from point C to D (retracting), showing that the bubble behaves as a simple spring at this small deformation region. Such phenomenon has been reported by both experimental and theoretical studies.<sup>13, 23-26</sup> The calculated bubble spring constant in this communication is around 125 mN/m, which is very close to 115 mN/m obtained by using the model based on the bubble and solid geometries.<sup>26</sup> However, the spring constant is larger compared with 65 mN/m used in AFM studies.<sup>13, 27</sup> The reason for this difference might be due to a much larger solid surface used in our

experiments. It is worth to mention that in **Fig. 4-4(c)** there is a negligible thermal drift and hysteresis of the bimorph sensor between the two successive cycles. However, at much lower approach/retract velocities with much longer measurement time, a signal drift is inevitable. In such case, the signal can be corrected by subtracting the raw data with the linear drift.

As shown in **Eqn. 4-1** and **Eqn. 4-2**, the bimorph cantilever spring constant depends on the length of the cantilever. Therefore, the position where the sample holder is placed on the bimorph beam affects the cantilever spring constant. For this reason, the cantilever calibration constant is calibrated after each set of measurements by placing a small piece of platinum wire on the sample holder and recording the change of charge on the bimorph surface. By precisely knowing the bimorph cantilever calibration constant, the bimorph signal (measured as a potential) is converted to force and plotted with respect to measurement time and glass capillary tube displacement. Unless otherwise indicated, the signal profiles shown in this communication were smoothed to reduce the noise level.

The main feature of this apparatus is its ability to directly and simultaneously measure the film thinning time, contact angles and interaction forces between air bubble and solid surfaces, as well as investigate the dynamic properties of the two surfaces approaching each other over a wide range of approach velocities from  $\mu\text{m/s}$  to  $\text{mm/s}$ , and evaluate the entire bubble-particle attachment process (i.e., force barrier and detachment force before and after three phase contact, TPC, respectively). The bimorph force sensor used in this device is very sensitive and shows an excellent reproducibility. The present setup has a force resolution of  $0.05 \text{ mN/m}$  or  $0.1 \mu\text{N}$ . With this apparatus, interactions for a broad range of systems can be investigated, including bubble-solid; bubble-bubble; bubble-liquid; liquid-liquid and solid-liquid drop in any fluid. In this chapter, the measured interaction forces between bubble-solid; bubble-liquid; bubble-bubble and liquid-liquid in aqueous solutions are demonstrated as the examples of wide applications of ITFDA. The quantitative modeling of the measured force profiles to investigate the critical role of various physicochemical properties of colloidal

systems in determining hydrodynamic forces will be presented in the following chapters.

### 4.3 Materials and Methods

A piezo ceramic actuator, purchased from FUJI CERAMICS Corp. with dimensions of  $20 \times 3 \times 0.3$  mm and capacitance of 20 nF, was used to fabricate the force sensor. Sea water was obtained from Vancouver, British Columbia, Canada, and filtered with a 0.2  $\mu\text{m}$  filter to remove any possible fine solids. A Grane heavy crude oil from Statoil, Norway was used as an oil phase in some of the measurements. The solid sphere surface was prepared by melting a  $1.5 \pm 0.1$  mm diameter Pyrex rod under a butane-oxygen flame until the surface tension of the melting Pyrex produced a spherical surface with a diameter of roughly 4.5 mm. A glass capillary tube with an inner diameter of  $1.1 \pm 0.05$  mm (Fisher Scientific) was used to generate and displace an air bubble or an oil droplet. One end of the glass tube was placed under a butane flame to create a smooth end for reproducible generation of bubbles and oil droplets by the tube. Extreme caution was taken to avoid overheating which would result in a non-symmetric glass end. The glass sphere and capillary tube were cleaned in freshly prepared piranha solutions (3  $\text{H}_2\text{SO}_4$ :1  $\text{H}_2\text{O}_2$ , by volume) at 80-90  $^\circ\text{C}$  for half an hour and rinsed with Mili-Q water prior to their use in the experiments. The surfaces prepared in this manner were free of contamination and completely water wettable (i.e., having a contact angle of zero degree).

Octadecyltrichlorosilane (OTS), received from Sigma-Aldrich, was used to prepare 1 mM OTS in toluene (Fisher Scientific) solutions which were used to hydrophobize the hydrophilic glass spheres by surface silanation reactions.<sup>15, 28, 29</sup> Different hydrophobicities were obtained by varying the soaking time of hydrophilic glass sphere in 1 mM OTS solutions. The treated glass sphere was rinsed with toluene and anhydrous ethyl alcohol (Commercial Alcohols Inc.) and blow-dried with ultrapure nitrogen to remove residual OTS from the glass surface, avoiding the deposition of OTS precipitates from residual OTS solutions and hence the formation of rough surfaces. The Teflon holder with a bowl shaped

socket on the top of the surface and the sample chamber were left in the anhydrous ethyl alcohol under ultrasonication for half an hour, rinsed with de-ionized water and then blow-dried with ultrapure nitrogen.

Potassium chloride (KCl), purchased from Sigma-Aldrich, was used as the supporting electrolyte, and concentrated NaOH and HCl solutions were used as pH modifiers. To obtain the degassed solution, 1L of 1 mM KCl solution was boiled at 100°C for 90 min to eliminate dissolved gases. After boiling, the solution was rapidly cooled to room temperature in ice-water bath. The solution was then diluted with degassed Mili-Q water (treated the same way) to a volume of 1L to maintain the initial electrolyte concentration. This degassed 1 mM KCl solution was used in experiments immediately to minimize the dissolve of gas from environment.

For bitumen-air bubble interactions, the dip-coating method was used to create a bitumen surface covering a spherical glass substrate. Vacuum-distillation-feed bitumen obtained from Syncrude Canada Ltd. was first diluted by toluene to 10 wt% of bitumen-in-toluene solution which was centrifuged at 45,000 rpm for 30 min to remove residual fine solids. Two drops of the centrifuged bitumen solution were placed on the clean glass sphere which was then placed in a dust-free laminar flow hood for one hour to evaporate any residual toluene. The bitumen surface prepared as such was used for measurement of bitumen-air bubble interactions.

At the beginning of each experiment, the glass sphere or the Teflon holder was clamped at the end of the bimorph beam with a specially designed tool. The chamber was then filled with test solutions and the glass capillary tube was filled with the heavy oil or fresh air before being brought into the solution. When measuring interaction forces between two deformable surfaces, an oil droplet or an air bubble was placed on the lower Teflon holder by a glass capillary tube. After generation of bubbles or oil droplets on the Teflon holder, the system was left for two hours to equilibrate the interfaces and to stabilize the bimorph signals before measurements.

## 4.4 Results and Discussion

### 4.4.1 Force profiles

#### 4.4.1.1 Solid-air bubble

The bimorph deflection as a function of capillary tube displacement of an air bubble approaching and retracting from a hydrophobized glass sphere of advancing contact angle  $\theta_a = 52^\circ$  in 1 mM KCl solutions at pH 7.7 is shown in **Fig. 4-5**. As mentioned earlier, a positive value of bimorph displacement corresponds to a repulsive force while a negative bimorph displacement is the result of an attractive force between the two surfaces. The initial separation distance between the air bubble and glass surface was set to be 120  $\mu\text{m}$ , the glass capillary tube displacement increases to drive the glass tube toward the glass surface and the separation distance between two surfaces reduces. A negative value of glass capillary tube displacement needed to separate the bubble from lower solid surface would mean that the tube is being driven up from its initial position. Typically, there are four regions in a complete force profile: I) a negligible net force between the two surfaces at a large separation distance; II) thin film drainage under the influence of hydrodynamic and surface forces; III) thin film rupture and three phase contact formation during approach, including advancing of TPC line; and IV) retraction and detachment (jump-out) of the bubble from the glass sphere surface.

When the air bubble approaches the hydrophobic glass surface at a constant velocity and large separation distance, there is no measurable net interaction force acting upon the two surfaces, shown by a zero bimorph displacement as a flat base line with noise (Region I from point O up to A). As the two surfaces come into the distance where the hydrodynamic and/or surface forces begin to interact, a repulsive force (film drainage resistance) is detected at point A, represented by an increase in bimorph deflection, and the lower surface deflects downward as the aqueous film between bubble and glass surfaces starts to drain (Region II). At point B the intervening liquid film reaches a critical thickness as the bubble continues to move downwards, where the liquid film becomes unstable and

ruptures, forming a TPC. In this case, the lower hydrophobic glass surface is pulled up to the bubble surface by interfacial tension force and the “jump in” to the bubble is observed. This is shown by a dramatic drop of bimorph signal in the profile from Point B to C, as a result of the TPC line expansion on the glass surface. Right after point C in Region III, the bubble is pinned on the glass surface without any movement of TPC line.

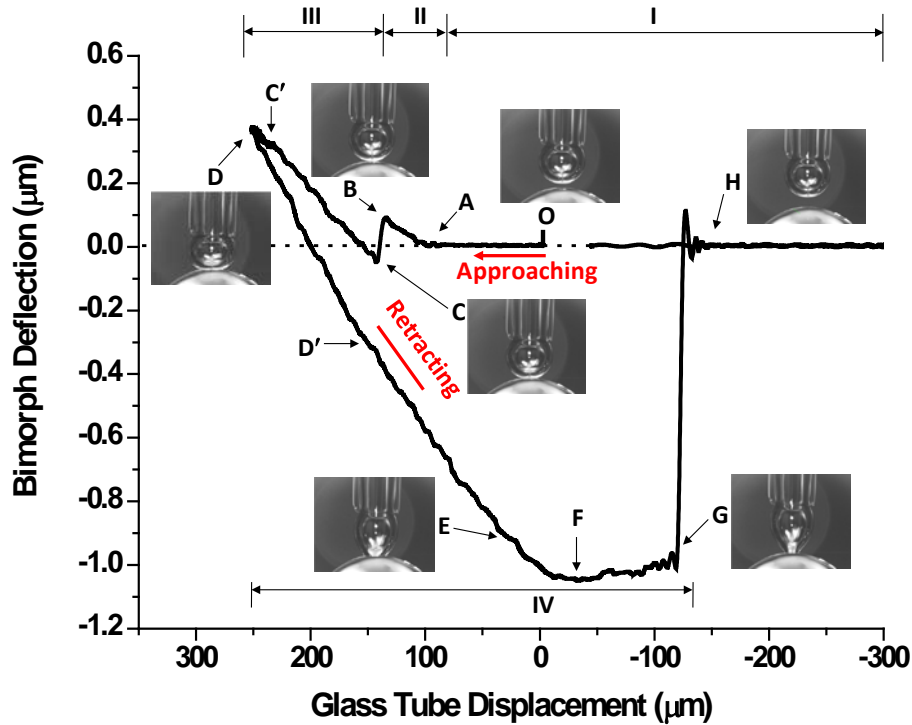


**Fig. 4-5** A typical force profile as interpreted by bimorph deflection collected during a measurement cycle between an air bubble and a partially hydrophobized glass surface ( $\theta_a = 52^\circ$ ) in 1 mM KCl solutions at pH 7.7 with approach and retract velocity ( $V_a$  and  $V_r$ ) of  $120 \mu\text{m/s}$  at  $20 \pm 0.5^\circ\text{C}$ . The still images at various key locations of signal profile are shown to help interpret the profile.

The attached bubble continues to deform against the lower glass surface thereby increasing the force pushing down on the glass sphere and reducing the contact angle. In this region, the bubble on the glass surface continues to deform against the lower glass surface under the force from the glass capillary, increasing the force pushing down the glass sphere. When the contact angle reaches  $\theta_r$  from

the deformation of the air bubble, the TPC line starts to recede, i.e., advancing of the air bubble on the glass surface. It is interesting to note that the profile contains two linear compliance regions after TPC, during approaching from point C to C' and during retracting from point D to D', demonstrating that the bubble behaves as a spring at small loading force when the bubble pins on the glass surface. The nonlinearity from point C' to D is due to the movement of TPC line<sup>23</sup> during the holding of air bubble on the glass surface, and the slightly bent of the curve from D' to E is probably a result of the large bubble deformation where the bubble no longer behaves as a spring. Also, the slopes of these two regions are different, showing the contact angle hysteresis between bubble approaching and retracting from the solid surface.<sup>23, 30, 31</sup>

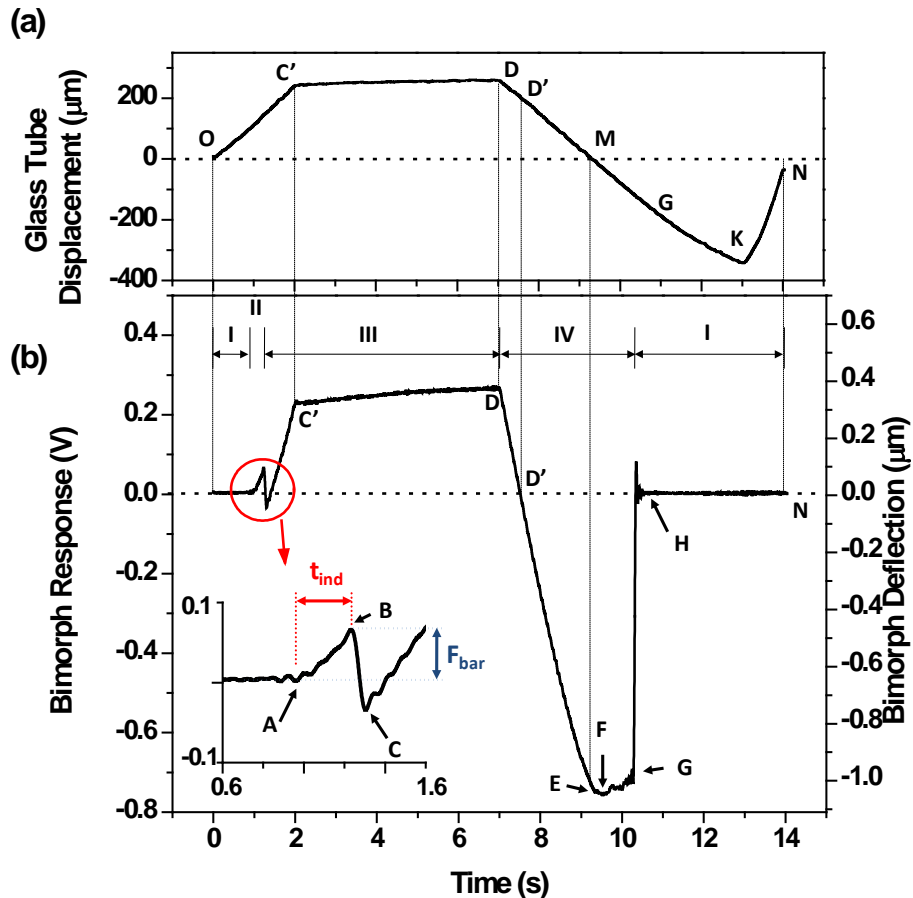


**Fig. 4-6** Glass tube displacement (a) and bimorph response (b) as a function of measurement time between an air bubble and a hydrophobized glass sphere ( $\theta_a = 52^\circ$ ) in a 1mM KCl solution at pH 7.7 with  $V_a$  and  $V_r$  of 120  $\mu\text{m/s}$  and  $T = 20 \pm$

0.5°C. The inset in (b) shows the bimorph response during the intervening liquid film drainage and rupture processes.

As the bubble retracts from the solid surface at point D, the TPC line remains stable on the glass surface from point D to E, only the contact angle increases from  $\theta_r$  towards  $\theta_a$ . During this period, the bubble starts to exert an upwards pull force on the glass surface as indicated by a negative bimorph deflection. Once the  $\theta_a$  is reached at point E, the bubble begins to slide on the glass surface, exhibiting a more gradual increase in upward lift force due to slide of TPC line. The capillary force reaches the maximum at point F and starts to decrease as the bubble continues to retract. At point G, the restoring force of the bimorph cantilever exceeds the capillary force, causing the bubble to detach from the solid surface as shown by a sudden change in bimorph signal at point G. After detachment of the bubble from the solid surface, the bimorph cantilever returns to its free position shown by a “zero” signal response at point H, while the glass tube continues to move until it returns to its original position. The maximum capillary force during retracting period is called detachment force (point F), which can be used to evaluate the stability of bubble-particle attachment. To better interpret the force curves, the glass capillary tube displacement and bimorph signal in **Fig. 4-5** are plotted as a function of measurement time as shown in **Fig. 4-6** (a) and (b), respectively. The glass tube starts to move towards lower surface from point O at a constant speed of 120  $\mu\text{m/s}$  and reaches a given displacement of 240  $\mu\text{m}$  at point C'. During this approach period, the film ruptures and TPC between air bubble and glass surface is established. The glass tube then holds the bubble on the glass surface stationary for 5 s from C' to D during which the displacement is observed to increase by about 15  $\mu\text{m}$ , accompanied by a slight increase in bimorph response as shown in **Fig. 4-6(b)**. The further displacement of the glass tube during this “holding” period is most likely due to the relaxation of speaker diaphragm after rapid movement. During this “holding” period, the stable TPC of bubble and glass surface is gradually established.

The bubble starts to retract from glass surface at point D. It is interesting to note that when the bubble retracts to the zero force position (D') and further to the original position (point M), the bubble remains to be attached to the glass surface due to the strong capillary force. To break (measure) the adhesion force, the bubble is further moved upward as shown by a negative driving signal applied to the speaker diaphragm. At point G the bubble detaches from the glass surface while the glass tube continues to move upwards to a displacement of  $-340\ \mu\text{m}$  at point K before returning to the original position (point N) at the end of the measurement. The unique large displacement range ( $\sim 600\ \mu\text{m}$ ) of the rigid capillary tube from  $240$  to  $-340\ \mu\text{m}$  driven by the speaker diaphragm enables the accurate measurement of strong adhesion forces between air bubbles and hydrophobic surfaces by the ITFDA. In this chapter the same driving profile of the capillary tube is used in all measurements unless otherwise indicated: the initial separation distance and maximum displacement of the capillary tube is set to be  $120$  and  $240\ \mu\text{m}$ , respectively, and the driving speed is controlled by altering the approach and retract time.

The curve shown in **Fig. 4-6(b)** can be similarly divided into four regions as indicated in **Fig. 4-5**, and the inset shows the bimorph signal during film drainage and rupture processes. When the air bubble and glass surfaces come to the distance where hydrodynamic and/or surface forces begin to become dominant, the bimorph beam starts to deflect at point A. The film starts to drain until it reaches the critical thickness and ruptures at point B as shown by a sudden snap into the TPC. The true film drainage time, often referred to as the induction time ( $t_{ind}$ ) and defined as the time needed for the intervening liquid film to thin down to the critical thickness, is measured from point A to B in **Fig. 4-6(b)**.

The TPC line then recedes on the glass surface to form a stable TPC of the bubble on the glass surface. It is important to note that the TPC formation is spontaneous and the thinning of the intervening liquid film dominates the total attachment time. During the film drainage as the bubble continues to move down, the repulsive force between the two surfaces increases and reaches the maximum

at the critical film thickness, point B. The maximum applied force, which is used to overcome the energy barrier between the two surfaces before TPC, is determined as force barrier ( $F_{bar}$ ) to evaluate the probability of bubble-solid attachment. A higher force barrier indicates the need of stronger external forces for the two surfaces to overcome the energy barrier prior to attachment and hence a lower probability of bubble-solid attachment.

There are two kind of forces exerted on the two interacting surfaces during the film drainage period: the repulsive hydrodynamic force and surface forces. At large separation distances, when the bubble approaches the glass surface at 120  $\mu\text{m/s}$ , the repulsive hydrodynamic force dominates the total force. However, at close separation distance, the hydrodynamic force becomes negligible with the deformation of the air bubble under the resistance of the film drainage. In this regime, the external force applied by the glass capillary through the air bubble increases to overcome the repulsive film drainage resistance with further thinning of the intervening liquid film. Eventually, the film reaches a critical thickness and ruptures at point B.

Surprisingly, when the surface hydrophobicity of the glass sphere was increased to a  $\theta_a$  of  $103^\circ$ , a very different force profile was obtained as shown in **Fig. 4-7**. Even though the bubble approach velocity increased to 240  $\mu\text{m/s}$ , the film drainage resistance detected before TPC as shown in **Fig. 4-5** and **Fig. 4-6(b)** from point A to B, was absent in **Fig. 4-7**, indicating a dissipation of film drainage resistance by the strongly hydrophobic surfaces. Instead, a sudden jump of the glass sphere into the air bubble was observed at points B to C, suggesting a strong and long-range attractive force which depressed all repulsive forces between the two surfaces at this high bubble approach velocity. This attractive force is attributed to the change in surface wettability of the glass sphere from moderate hydrophobicity of  $\theta_a = 52^\circ$  to strong hydrophobicity of  $\theta_a = 103^\circ$ .

As shown by photos at point C in the insets of **Fig. 4-5** and **Fig. 4-7**, the TPC area of the bubble and glass surface at point C increases significantly when the contact angle of glass surface increases from  $52^\circ$  to  $103^\circ$ , causing a dramatic

increase in adhesion force between the two surfaces. The bubble-glass attachment is therefore more stable as a higher external force is required to overcome the strong adhesion force holding bubble-solid surface together. It is important to note that the air bubble is initially stretched upon contact with glass sphere at point C due to a jump-up motion of the glass sphere in the absence of force barrier shown by a negative bimorph signal. As the bubble continues being pushed down by the glass capillary tube, the contact angle decreases towards  $\theta_r$  value as the pinning bubble continues to further deform downwards on the glass surface. The TPC line starts to slide once  $\theta_r$  has been reached, showing a gradual reduction in pulling up force from C to C'. The glass tube then holds the air bubble on the glass sphere from C' to D. During this “holding” period, the TPC line expands slightly and then stabilizes.

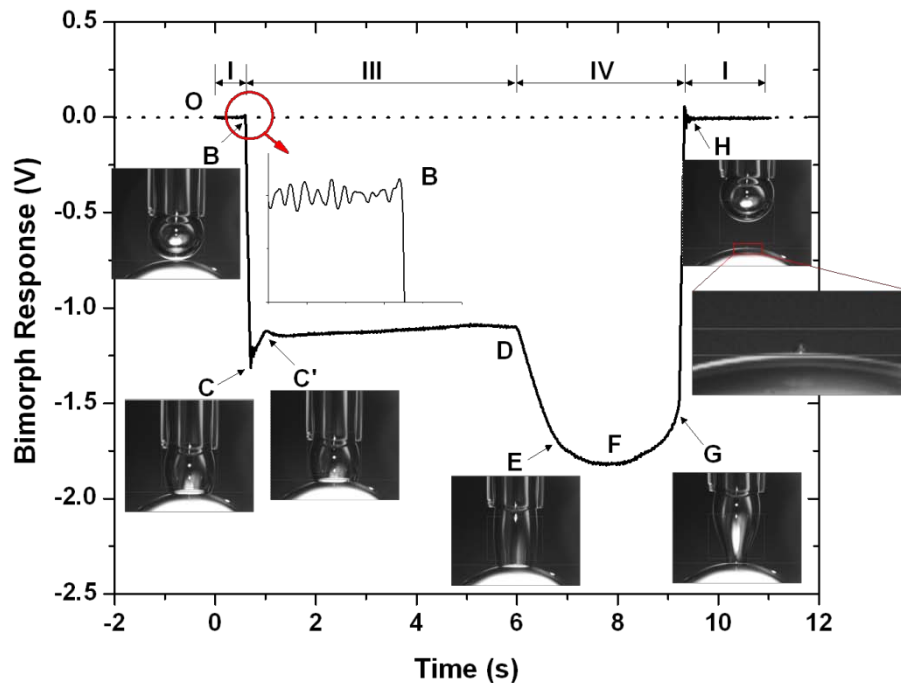


**Fig. 4-7** Bimorph response as a function of measurement time between an air bubble and a hydrophobized glass sphere of  $\theta_a = 103^\circ$  in 1mM KCl solutions of pH 7.7 with  $V_a$  and  $V_r$  of 240  $\mu\text{m/s}$  and  $T = 20 \pm 0.5^\circ\text{C}$ . The still images at various key locations of force profile are shown to help interpret the force profile.

Similar to process shown in **Fig. 4-6**, the contact angle increases towards  $\theta_a$  as the pinning bubble continuous to stretch upwards on the glass surface from point D to E during retraction in **Fig. 4-7**. Once  $\theta_a$  has been reached, TPC line starts to slide on glass surface at point E and the upward capillary force increases to a maximum at point F. As illustrated in the inset photo of **Fig. 4-7** at point G, the bubble becomes “necking”, i.e., bridging the glass capillary tube and glass sphere as the bubble is further stretched away from the glass sphere surface due to strong adhesion of the bubble on the solid. At this point, the restoring force of bimorph beam overcomes the adhesion force, and the bubble detaches from the glass surface, leaving a small orphan bubble on the glass surface at point H.

To understand the mechanism for dissipation of film drainage resistance by hydrophobic surfaces, measurements were conducted between an air bubble and the orphan bubble on the top of this highly hydrophobic surface in 1 mM KCl solution. The results in **Fig. 4-8(a)** show a negligible force between the two bubble surfaces when they are far apart from each other. Different from the interactions shown in **Fig. 4-7**, a repulsive force between points A and B is detected before a large jump in at point B, where the thin liquid film between the orphan bubble and probing bubble ruptures, leading to the coalescence of orphan bubble with the probing bubble, followed by the formation of TPC. The TPC line expands rapidly on glass surface and the glass sphere is pulled up by the increasing capillary force represented by a sharp reduction in bimorph signal from points B to C. The quick rupture of thin liquid film results in a fluctuation of bimorph response beyond point C and the signal is stabilized by the interfacial tension force in a short period. Again, during the holding period of bubble on the glass surface, a slightly increase in pull-up capillary force is observed after point C' due to the expanding of the TPC line. Replacing the 1mM KCl solution with degassed 1 mM KCl solution, the interaction between air bubble and strongly hydrophobic glass surfaces was measured to study the effect of dissolved gas in aqueous solutions. As shown in **Fig. 4-8(b)**, the dissipation of the film drainage resistance before TPC can be observed again. The force profile looks exactly the

same as the one shown in **Fig. 4-7**, demonstrating the minimum effect of dissolved gas on the strongly attractive force between the air bubble and highly hydrophobic glass surfaces.

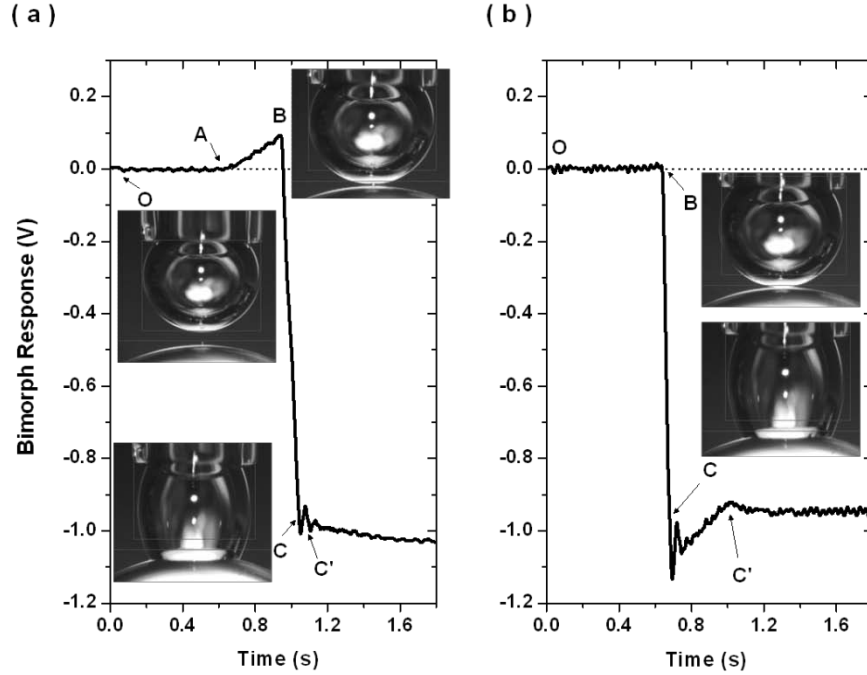


**Fig. 4-8** Bimorph response as a function of measurement time showing the film drainage period with  $V_a$  and  $V_r$  of  $240 \mu\text{m/s}$  and  $T = 20 \pm 0.5 \text{ }^\circ\text{C}$ : (a) between an air bubble and an orphan air bubble on a hydrophobized glass sphere of  $\theta_a=103^\circ$  in 1mM KCl solutions at pH 7.7, (b) between an air bubble and a hydrophobized glass sphere of  $\theta_a=103^\circ$  in degassed 1mM KCl solutions. The still images at various key locations of force profile are shown to help interpret the force profile.

Despite of the very hydrophobic nature of the clean bubbles, there exists a strong hydrodynamic repulsion at an approach velocity of  $240 \mu\text{m/s}$ , in contrast to the absence of film drainage resistance between the hydrophobic solid and bubble at the same approach velocity in either normal or degassed KCl solutions. This finding clearly indicates that the observed dissipation of film drainage resistance by hydrophobic surfaces is unlikely due to the presence of nano bubbles on the hydrophobic solid surfaces. It appears that the boundary condition at solid surface

changes from a no-slip to slip state with the increase of solid surface hydrophobicity.<sup>32-35</sup> Under the condition that the solid surface is strongly hydrophobic (i.e.,  $\theta_a = 103^\circ$ ), the water flows over the solid surface with little frictional force, presenting little resistance to the thinning of the liquid film when the air bubble approaches the solid. This nearly frictionless flow diminishes the film drainage resistance between the two approaching surfaces, pulling the air bubble onto solid surface at large separation distances beyond the range of surface forces. The presence of the orphan bubble on the solid surface changes this boundary condition, exhibiting a long range film drainage resistance before TPC formation. This is an important observation and the mechanisms for the dissipation of film drainage resistance by hydrophobic surfaces will be discussed in **Chapter 7**.

#### 4.4.1.2 Two deformable surfaces

**Bubble-oil droplet interactions:** The interactions between two deformable surfaces were also measured using the ITFDA. **Fig. 4-9** shows the bimorph signals between an air bubble and a crude oil surface in sea water at pH 7.6 (the physiochemical properties of the crude oil were reported in Chapter 5). When the two surfaces approach each other, a repulsive force is detected at point A where the film drainage resistance is significant. Since the interfacial tension of oil/water interface is much lower than air/water interface, the oil surface experiences a larger deformation than the air bubble when the two surfaces are forced in contact, as shown in the inset photo of **Fig. 4-9** at point B. The repulsive force increases as the bubble moves further down towards the oil surface and reaches a maximum at point B during which the intervening liquid film drains to its critical thickness. The thin film drainage time, measured from point A to B between the two deformable surfaces is defined as film drainage time. The film drainage time between an air bubble and an oil surface in sea water as shown in **Fig. 4-9** is determined to be 0.654 s. The rupture of the film, followed by rapid expansion of TPC line on air bubble surface, pulls the oil drop towards the bubble, as shown by a sharp reduction in bimorph signal from point B to C. The capillary tube then

holds in place the air bubble on the oil drop surface from point C to D. The upwards capillary force continues increasing as the oil spreads slowly on the air bubble, reaching a maximum when  $\theta_c$  is reached at point C'. The spread process is clearly shown in the inset photos of **Fig. 4-9** at points C and C'. The capillary force then remains nearly the same up to point D.

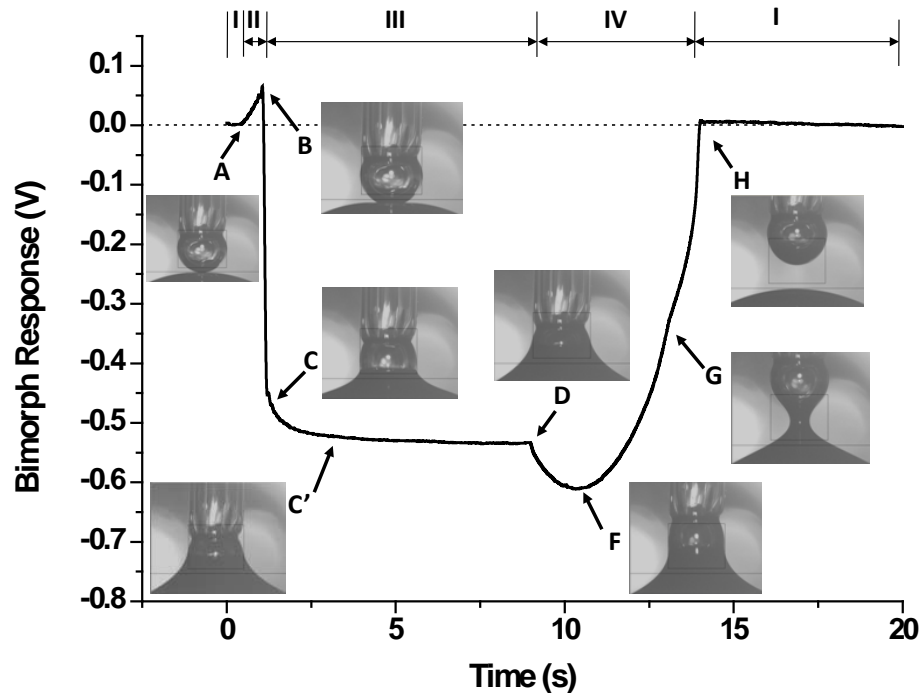


**Fig. 4-9** Bimorph response as a function of measurement time of an air bubble approaching a crude oil surface in sea water of pH 7.6 at  $V_a$  and  $V_r$  of 240  $\mu\text{m/s}$  and  $T = 20 \pm 0.5$  °C. The still images at various key locations of force profile are shown to help interpret the force profile. The diameter of the air bubble and oil drop was 1.49 and 8.52 mm, respectively.

During retraction, as the TPC line advances on the air bubble, the perimeter of the TPC line increases, leading to an increase in the capillary force shown as a signal reduction from points D to F. When the direction of the oil/water interface on TPC line reaches vertical direction as shown in the inset of **Fig. 4-9** at point F, the capillary force reaches maximum. Necking forms in the capillary bridge (point G) when the bubble is further stretched and finally the bubble detaches from the oil drop. Similar to the generation of orphan bubble on the strongly hydrophobic

glass surface after detachment, a small amount of oil is left on the air bubble, which shows the strong affinity of oil to the air bubble. Furthermore, the oil/water interfacial tension can be obtained from the measured detachment force once the bubble diameter is precisely determined by the imaging analysis of the video. For example, the oil/water interfacial tension in this case is calculated to be 13.7 mN/m - within 5% error of its true value, showing the accuracy of force measurement of the bimorph cantilever. Here, the oil/water interfacial tension was directly measured to be 13.1 mN/m using a Processor Tensiometer K12 (Krüss, Hamburg, Germany) by the Du Noüy ring method.

**Bubble-bubble interactions:** Fig. 4-10(a) shows the bimorph signal recorded when an air bubble on the glass capillary tube approaches another air bubble fixed on the bimorph sensor. Similar to the previous interaction curves, no net interaction force is detected at large separation distances. A repulsive force is detected at close separation distance at point A, represented by an increase in bimorph signal. This finding agrees with the previous measurement of a large probing bubble approaching a small orphan bubble. The following increase of bimorph signal, until point B, is a result of the applied force by the continued pushing down of the upper air bubble against the lower bubble, reflecting the film drainage resistance. At point B, the upper air bubble is held stationary against the lower air bubble, showing a constant bimorph signal. During the “holding” period of B to C, the aqueous film continues to thin until it reaches a critical thickness where it ruptures at point C. The break of the film is followed by the coalescence of the two bubbles into a larger bubble on the bimorph beam, which is characterized by a sharp drop of bimorph signal from 0.4 V at point C to -0.3 V at point D, indicating upward deflection of bimorph upon coalescence due to a larger buoyancy force. The quick coalescence of the two bubbles results in a vibration of the lower surface, shown as the oscillating signal with reducing amplitude beyond point D.

**Oil droplet-oil droplet interactions:** The measured coalescence process of the two oil droplets in Fig. 4-10(b) exhibits similar characteristics to coalescence

process of air bubbles. As shown in **Fig. 4-10**, the coalescence time of the two air bubbles and two oil droplets, measured from point A to point C, is determined to be 1.36 s and 52.9 s, respectively.

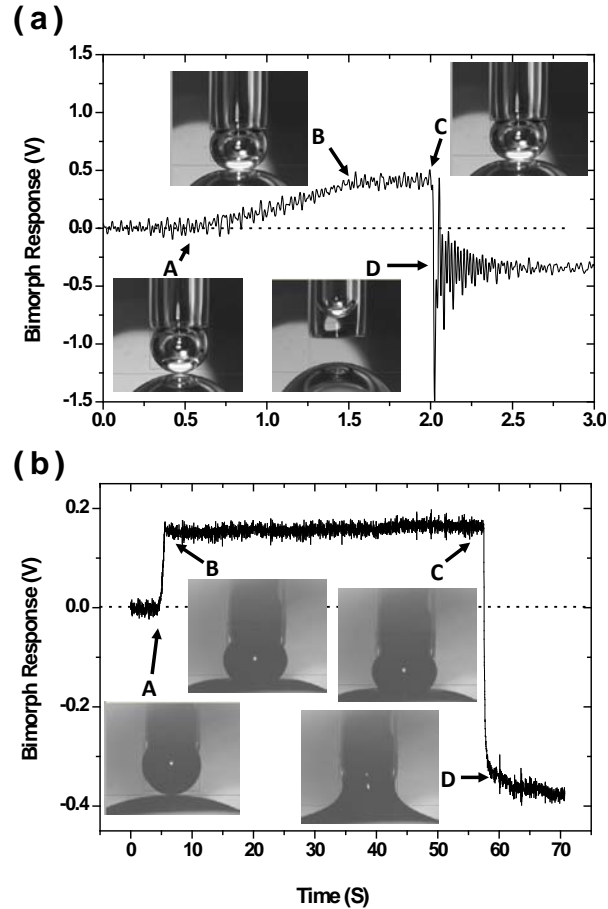


**Fig. 4-10** Bimorph signal profile (raw data) for coalescence time determination of two deformable surfaces using ITFDA with  $V_a$  and  $V_r$  of 240  $\mu\text{m/s}$  and  $T = 20 \pm 0.5$   $^\circ\text{C}$ : (a) two air bubbles in 1 mM KCl solution at pH 5.6, with maximum glass tube displacement of 360  $\mu\text{m}$ ; (b) two oil droplets in sea water at pH 7.6. In these measurements, the diameter of the upper surface was maintained within  $1.49 \pm 0.05$  mm, the diameter of lower air bubble surface and oil surface was 3.65 mm and 8.52 mm, respectively.

#### 4.4.2 Image analysis

One of the CCD cameras was used to record the bubble-glass attachment process at a 15 frame/s rate to determine  $\theta_r$  and  $\theta_a$  of the air bubble on the

hydrophobized glass surface to help understand the dynamic force profiles measured using the bimorph cantilever. The selected frames from the recorded video of interest were analyzed using the vision analysis program to calculate the contact angle. In this case the air/liquid interface on the axis-symmetrical plane is considered as a circular arc (toroidal approximation). As shown in **Fig. 4-11** for both receding (a) and advancing (b) contact angles, points were manually selected at the solid/water and air/water interfaces. These points were then fitted to a circular arc. The angle between the two fitted arcs at the intersection was considered as the contact angle. Due to the symmetry of the bubble and glass sphere, the difference between the contact angles at left and right sides of the air bubble was determined to be less than 3 degrees. The average value of the two was reported as the contact angle.

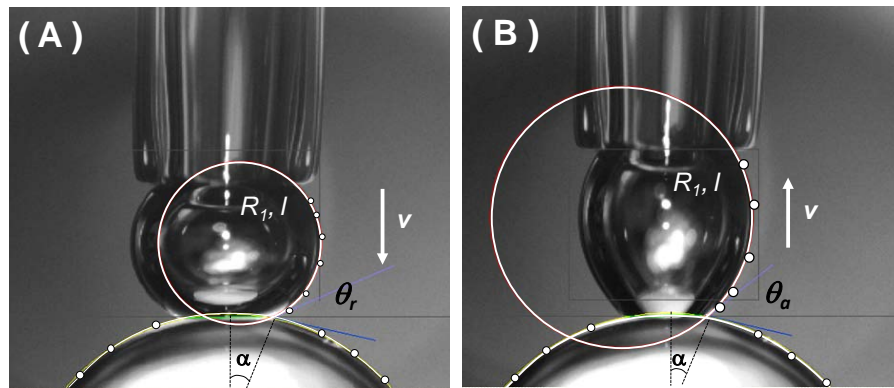


**Fig. 4-11** A schematic diagram of imaging analysis to determine dynamic (advancing and receding) contact angles and capillary forces using a vision analysis program built on LabVIEW 8.0: (a) approaching (dynamic receding contact angle) and (b) retracting (dynamic advancing contact angle) in 1mM KCl solution of pH 7.7 at  $T = 20 \pm 0.5^\circ\text{C}$ .

During the approach after TPC as shown in **Fig. 4-11**(a), the air bubble pins on the glass sphere initially due to the contact angle hysteresis, and when the contact angle equals  $\theta_r$  the TPC line starts to move downwards as the bubble continues to deform. The dynamic contact angle at the point before the TPC line starts to move is considered as  $\theta_r$ . Upon retraction, the air bubble pins again on the glass sphere

due to the contact angle hysteresis while the bubble continues to deform (stretch) upward until the contact angle increases to a critical value known as  $\theta_a$ , as shown in **Fig. 4-11(b)**. After reaching  $\theta_a$ , the bubble starts to slide on the glass sphere as the capillary tube holding the bubble continues to move up.  $\theta_r$  and  $\theta_a$  of the hydrophobized glass surface in **Fig. 4-11(a)** and (b) is determined from bubble shape analysis to be  $36^\circ$  and  $52^\circ$ , respectively.

The capillary force,  $F_C$ , which is the main contribution to the adhesion force between the bubble and glass surface after TPC is given by:<sup>13, 36, 37</sup>

$$F_C = \Delta P \pi R_2^2 \sin^2 \alpha + [-2\pi R_2 \gamma_{lv} \sin \alpha \sin(\theta - \alpha)] \quad \text{Eqn. 4-3}$$

where  $R_2$  is the radius of the glass sphere,  $\alpha$  is the half filling angle (measured at the glass sphere center) of the sphere-capillary bridge contact as shown in **Fig. 4-11**,  $\gamma_{lv}$  is the liquid-vapour interfacial tension and  $\theta$  is the contact angle of the bubble on the glass surface, measured through the aqueous solution. Applying the toroidal approximation, the Laplace pressure drop across the solid/water interface,  $\Delta P$ , can be calculated by:<sup>38</sup>

$$\Delta P = \gamma_{lv} \left( \frac{1}{R_1} + \frac{1}{l} \right) \quad \text{Eqn. 4-4}$$

where  $R_1$  and  $l$  are the principal radii of the capillary bridge and can be determined using the vision analysis program.

Substituting  $\Delta P$  in **Eqn. 4-3** with **Eqn. 4-4**, the capillary force then becomes:

$$F_C = \pi R_2^2 \sin^2 \alpha \gamma_{lv} \left( \frac{1}{R_1} + \frac{1}{l} \right) + [-2\pi R_2 \gamma_{lv} \sin \alpha \sin(\theta - \alpha)] \quad \text{Eqn. 4-5}$$

The first term on right hand side of **Eqn. 4-5** is the contribution of the Laplace pressure drop on the solid/vapor interface and the second term comes from the interfacial tension on the TPC line. A negative value of  $F_C$  indicates an attractive capillary force, while a positive value of  $F_C$  corresponds to a repulsive force. For a concave interface, both terms are negative, so  $F_C$  is negative; for a convex interface, the first term of **Eqn. 4-5** is positive, so  $F_C$  can be either positive or negative, depending on the shape of the air bubble.

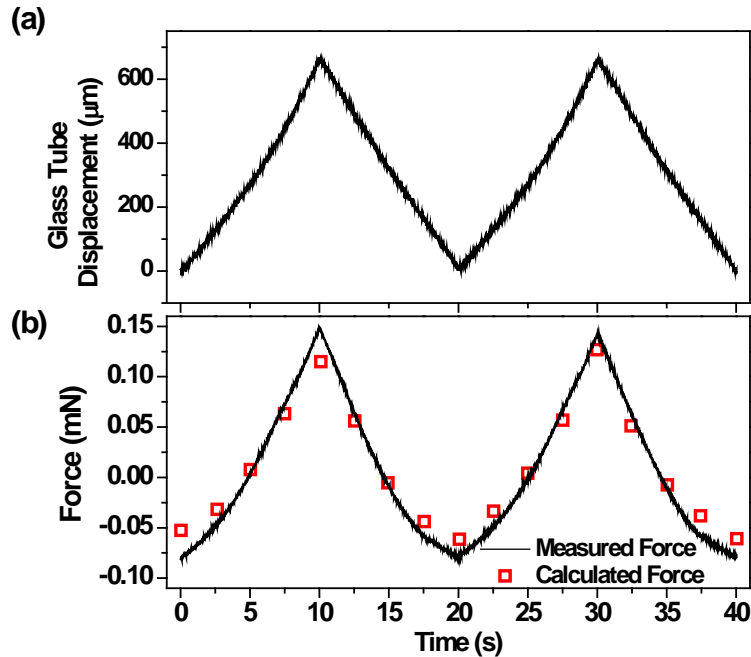


**Fig. 4-12** Validation of the toroidal approximation and the contact angle measurement. (a) Two successive cycles of the triangular movement of glass capillary tube after the TPC between air bubble and hydrophobized glass surfaces; (b) Comparison of the measured and calculated capillary force during this process in 1 mM KCl solution of pH 7.7 at  $V_a = V_r = 24 \mu\text{m/s}$ .

To calculate the capillary force, the surface tension of the aqueous solution was measured using a Processor Tensiometer K12 (Krüss, Hamburg, Germany). The excellent agreement between the calculated and measured (by bimorph cantilever) capillary force shown in **Fig. 4-12(b)** confirms suitability of toroidal approximation for analyzing the liquid/air interfaces. More importantly, the excellent agreement suggests that the capillary force can be accurately calculated based on the geometric properties (i.e.,  $R_1$ ,  $R_2$ ,  $\alpha$ ,  $l$ ,  $\theta$ ) of the interfaces using a vision analysis program applied to specific time frames of the video. It should be noted that there is a huge difference between the calculated and measured capillary force if only considering the contribution of surface tension on the capillary force. It is necessary to consider the Laplace pressure drop across the solid/vapour interface when calculating the total capillary force.

#### 4.4.3 Bitumen-air bubble interactions

The measurement was conducted between an air bubble and a bitumen surface in 1 mM KCl solutions as a function of pH. The induction time, receding and advancing contact angles, detachment force and hydrodynamic/surface forces between these two surfaces were investigated based on the measurements.

##### 4.4.3.1 Induction time

**Fig. 4-13** shows the effect of pH on the induction time of air bubble-bitumen attachment. As it can be seen from **Fig. 4-13**, the induction time remained at around 0.3 s when pH was below 7.9, and increased dramatically after pH 8 and reached 4.9 s at pH 9.45. The results revealed that the bubble and bitumen surface would have a lower tendency of attachment at high pH, which is not unexpected for bitumen. When placed in aqueous solutions, the natural surfactants in bitumen are migrated to bitumen/water interface and released to the aqueous phase. The natural surfactant, mainly the carboxylic acid group, will be progressively dissociated with increasing pH, making the interface more negatively charged.<sup>39</sup> More surfactant became ionized when the pH was larger than 8. As a result, more surfactants accumulated on the bitumen surface, making the surface more negatively charged. The water soluble polar groups (heads) at the interface facing the aqueous phase also make the bitumen surface less hydrophobic. More negatively charged bitumen surface led to an increased repulsive electrical double-layer force between the negatively charged bubble and bitumen surfaces. At the same time, the reduction of bitumen hydrophobicity reduced the long-range hydrophobic force between the two surfaces. These two aspects collectively caused an increase in repulsive force between the bubble and bitumen surfaces, which made the intervening liquid film more stable, leading to a longer induction time.

##### 4.4.3.2 Contact angle

Both advancing and receding contact angles of water on the bitumen surface decrease with increasing pH. As it is shown in **Fig. 4-14**, the advancing contact angle was about 80° when pH was below 7 and started to decrease after pH 8,

reaching  $65^\circ$  at pH 10. In case of receding contact angle, it decreased from  $40^\circ$  at pH 6 to  $25^\circ$  at pH 10. The difference between the advancing and receding contact angle values was about  $40^\circ$ , which was independent of pH. This contact angle hysteresis was believed to be caused by the roughness and heterogeneous property of the bitumen surface.<sup>40</sup> A change in the ionization state of the surfactant at TPC line as the bubble spread (water receded) and retracted (water advanced) also contribute to the observed contact angle hysteresis.

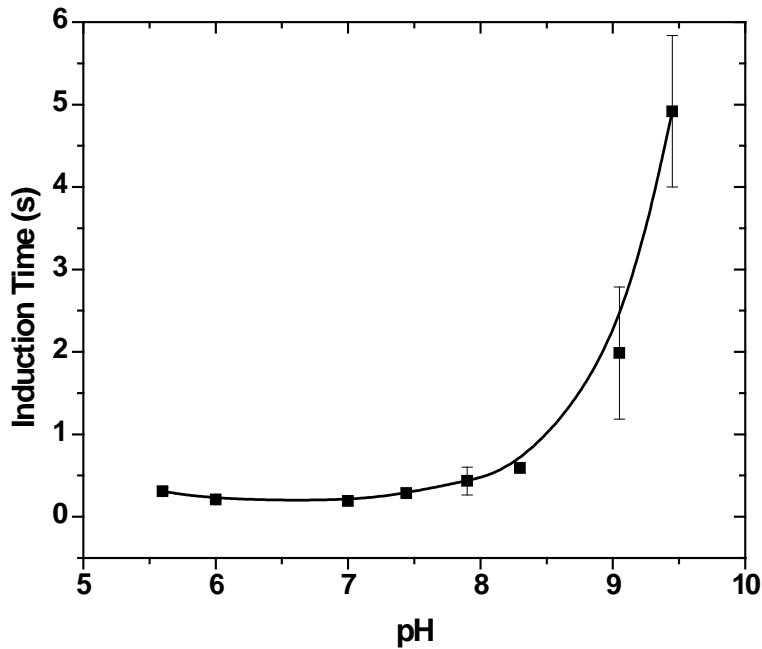


**Fig. 4-13** Effect of pH on induction time of air bubble-bitumen attachment in 1mM KCl solution with approach and retract velocity ( $V_a$  and  $V_r$ ) of  $240 \mu\text{m/s}$  at  $20 \pm 0.5^\circ\text{C}$ , the diameter of the air bubble and bitumen surface is  $1.5 \pm 0.03$  and  $4.6 \pm 0.03$  mm, respectively.

The trend of contact angle variation with pH was similar to that of induction time: they all remained constant at pH lower than 8 and started to change when pH was greater than 8, corresponding to a significant reduction in hydrophobicity of bitumen caused by the increased dissociation and accumulation of natural surfactants at bitumen/water interface. Contact angle reflects the surface properties under thermodynamic/static conditions while induction time further reveals the dynamic effect of bubble-particle attachment. Comparing the

induction time measurement with the contact angle measurements, it is not difficult to conclude that induction time measurement provides a better sensitivity than contact angle in response to the changes in surface properties. Hence, induction time measurement is preferred to study the bubble-bitumen attachments.

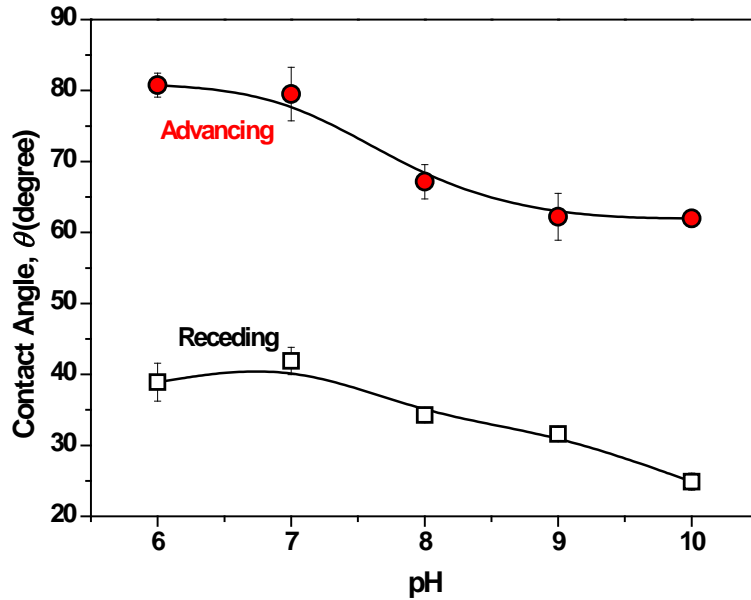


**Fig. 4-14** Effect of pH on receding and advancing contact angle of bitumen surface in 1mM KCl solution at  $20 \pm 0.5$  °C.

#### 4.4.3.3 Detachment force

The detachment forces of the bubble-bitumen aggregation were calculated based on the force profile and normalized by the perimeter of the TPC line. The results in **Fig. 4-15** show that the detachment forces were rather scattered over the pH range studied and almost the same within the experimental error when the approach/retract velocity changed from 55 to 240  $\mu\text{m/s}$ . These results demonstrate that pH did not show a significant impact on the detachment force. Considering the significant reduction in contact angle of bitumen, this finding is rather surprising. Furthermore, the detachment force was found to be independent of the approach and retract velocity.

Based on the DLVO theory, for the attachment to be possible, the bubble and bitumen must first overcome the energy barrier which can be calculated by <sup>41</sup>:

$$\begin{aligned} \text{Energy Barrier} &= \text{Detachment Energy} - \Delta G && \text{Eqn. 4-6} \\ &= \text{Detachment Energy} - \gamma_{lv}(1 - \cos \theta_r) \end{aligned}$$

where  $\Delta G$  is the work of adhesion between bubble and bitumen surfaces,  $\gamma_{lv}$  is the surface tension of the solution and  $\theta_r$  is receding contact angle. **Fig. 4-15** also shows the  $\Delta G$  between an air bubble and bitumen surfaces calculated using **Eqn. 4-6** as a function of pH. It can be seen from the figure that  $\Delta G$  remained the same at pH 6 and 7, and decreased sharply with increasing pH larger than 8. At pH 6 and 7, the detachment force and  $\Delta G$  were comparable, showing a negligible energy barrier. According to **Eqn. 4-6**, a sharp drop of  $\Delta G$  and relatively constant detachment energy at pH larger than 8 indicate an increase in energy barrier. The higher energy barrier means more energy needed for the thin liquid film to drain, resulting in a lower probability of bubble-bitumen attachment. This finding agrees well with measured sharp increase in true induction time at pH higher than 8.

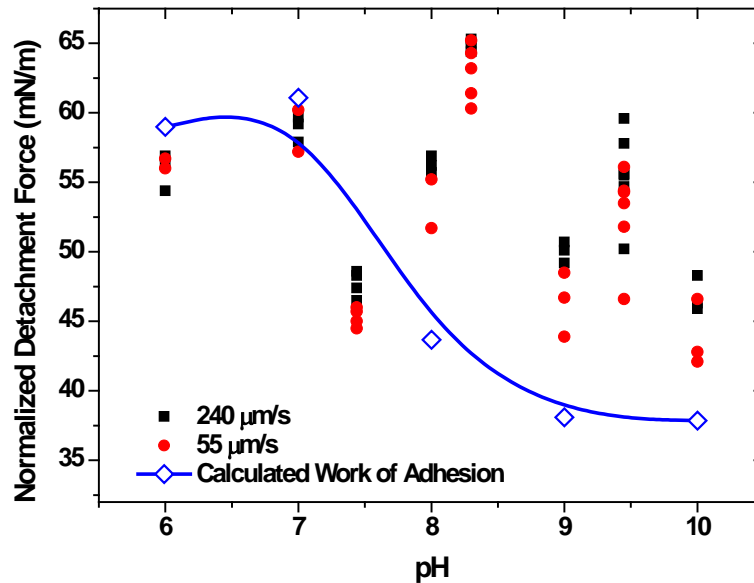


**Fig. 4-15** Effect of pH on bubble-bitumen detachment force and work of adhesion,  $\Delta G$  in 1mM KCl solutions at  $20 \pm 0.5$  °C.

#### 4.5 Conclusions

A novel device equipped with a bimorph cantilever as a force sensor was developed to measure the film drainage time and film drainage resistance of an air bubble or a liquid droplet approaching a solid, bitumen, liquid drop or air bubble

in real time over a wide range of displacement and approach/retract velocity. Coupled with a computer-interfaced video capture device and vision analysis program, this integrated thin film drainage apparatus (ITFDA) allowed accurate determination of dynamic and receding/advancing contact angles. The determination of liquid/air interface geometry allowed for accurate calculation of the capillary force between an air bubble and a solid surface after TPC. Despite the limitation of accurate determination of bubble-solid separation distance, the device featuring a force resolution of 0.05 mN/m has a unique role to obtain important dynamic information of interactions between different surfaces, i.e., solid-bubble, liquid-bubble, liquid-liquid and bubble-bubble, in a liquid.

The image analysis revealed that the contributions of interfacial tension on the TPC line and the Laplace pressure inside the capillary bridge on solid surface need to be considered to calculate accurately the capillary force after TPC. The maximum capillary force was not at the point when advancing contact angle was reached or the point where the bubble detached from the solid surface. It has been found that the induction time of air bubble-bitumen attachment remains unchanged at low pH and increases with pH above 8. Both advancing and receding contact angles of bitumen decreased with increasing pH. The solution pH was found to have a marginal effect on detachment force of bubble-bitumen attachment. The availability of this ITFDA would allow the validation/refinement of theories of film drainage resistance and studying the critical role of interfacial chemistry on film drainage resistance for a variety of complex systems of scientific and practical importance.

#### **4.6 References**

- (1) Ralston, J.; Fornasiero, D.; Hayes, R. Bubble-Particle Attachment and Detachment in Flotation. *Int. J. Miner. Process.* **1999**, *56*, 133-164.
- (2) Platikanov, D.; Exerowa, D. In *Thin liquid films*; Fundamentals of Interface and Colloid Science; Academic Press: 2005; Vol. 5, pp 1-91.

- (3) Scheludko, A. Über Das Ausfließen Der Lösung Aus Schaumfilmen. *Kolloid-Zeitschrift* **1957**, *155*, 39-44.
- (4) Mysels, K. J.; Jones, M. N. Direct Measurement of the Variation of Double-Layer Repulsion with Distance. *Discuss. Faraday Soc.* **1966**, *42*, 42-50.
- (5) Klaseboer, E.; Chevaillier, J. P.; Gourdon, C.; Masbernat, O. Film Drainage between Colliding Drops at Constant Approach Velocity: Experiments and Modeling. *J. Colloid Interface Sci.* **2000**, *229*, 274-285.
- (6) Ivanov, I.; Dimitrov, D. Thin Film Drainage. *Surfactant Sci. Ser.* **1988**, *29*, 379-396.
- (7) Tsao, H.; Koch, D. L. Observations of High Reynolds Number Bubbles Interacting with a Rigid Wall. *Phys. Fluids* **1997**, *9*, 44-56.
- (8) Platikanov, D. Experimental Investigation on Dimpling of Thin Liquid Films. *J. Phys. Chem.* **1964**, *68*, 3619-3624.
- (9) Israelachvili, J. N.; Tabor, D. Measurement of Van Der Waals Dispersion Forces in the Range 1.5 to 130 Nm. *Proc. Roy. Soc. London, Ser. A* **1972**, *331*, 19-38.
- (10) Tabor, D.; Winterton, R. H. S. Direct Measurement of Normal and Retarded Van Der Waals Forces. *Proc. Roy. Soc. , Ser. A* **1969**, *312*, 435-450.
- (11) Binnig, G.; Quate, C. F.; Gerber, C. Atomic Force Microscope. *Phys. Rev. Lett.* **1986**, *56*, 930-933.
- (12) Ducker, W. A.; Senden, T. J.; Pashley, R. M. Direct Measurement of Colloidal Forces using an Atomic Force Microscope. *Nature* **1991**, *353*, 239-241.
- (13) Ducker, W. A.; Xu, Z.; Israelachvili, J. N. Measurements of Hydrophobic and DLVO Forces in Bubble-Surface Interactions in Aqueous Solutions. *Langmuir* **1994**, *10*, 3279-3289.

- (14) Butt, H. Technique for Measuring the Force between a Colloidal Particle in Water and a Bubble. *J. Colloid Interface Sci.* **1994**, *166*, 109-117.
- (15) Fielden, M. L.; Hayes, R. A.; Ralston, J. Surface and Capillary Forces Affecting Air Bubble-Particle Interactions in Aqueous Electrolyte. *Langmuir* **1996**, *12*, 3721-3727.
- (16) Dagastine, R. R.; Stevens, G. W.; Chan, D. Y. C.; Grieser, F. Forces between Two Oil Drops in Aqueous Solution Measured by AFM. *J. Colloid Interface Sci.* **2004**, *273*, 339-342.
- (17) Gunning, A. P.; Mackie, A. R.; Wilde, P. J.; Morris, V. J. Atomic Force Microscopy of Emulsion Droplets: Probing Droplet-Droplet Interactions. *Langmuir* **2004**, *20*, 116-122.
- (18) Mulvaney, P.; Perera, J. M.; Biggs, S.; Grieser, F.; Stevens, G. W. The Direct Measurement of the Forces of Interaction between a Colloid Particle and an Oil Droplet. *J. Colloid Interface Sci.* **1996**, *183*, 614-616.
- (19) Snyder, B. A.; Aston, D. E.; Berg, J. C. Particle-Drop Interactions Examined with an Atomic Force Microscope. *Langmuir* **1997**, *13*, 590-593.
- (20) Gu, G.; Xu, Z.; Nandakumar, K.; Masliyah, J. Effects of Physical Environment on Induction Time of Air-Bitumen Attachment. *Int. J. Miner. Process.* **2003**, *69*, 235-250.
- (21) Parker, J. L. A Novel Method for Measuring the Force between Two Surfaces in a Surface Force Apparatus. *Langmuir* **1992**, *8*, 551-556.
- (22) Parker, J. L.; Attard, P. Deformation of Surfaces due to Surface Forces. *J. Phys. Chem.* **1992**, *96*, 10398-10405.
- (23) Preuss, M.; Butt, H. Direct Measurement of Particle-Bubble Interactions in Aqueous Electrolyte: Dependence on Surfactant. *Langmuir* **1998**, *14*, 3164-3174.

- (24) Hartley, P. G.; Grieser, F.; Mulvaney, P.; Stevens, G. W. Surface Forces and Deformation at the Oil-Water Interface Probed using AFM Force Measurement. *Langmuir* **1999**, *15*, 7282-7289.
- (25) Chan, D. Y. C.; Dagastine, R. R.; White, L. R. Forces between a Rigid Probe Particle and a Liquid Interface. I. the Repulsive Case. *J. Colloid Interface Sci.* **2001**, *236*, 141-154.
- (26) Attard, P.; Miklavcic, S. J. Effective Spring Constant of Bubbles and Droplets. *Langmuir* **2001**, *17*, 8217-8223.
- (27) Assemi, S.; Nguyen, A. V.; Miller, J. D. Direct Measurement of Particle-Bubble Interaction Forces using Atomic Force Microscopy. *Int. J. Miner. Process.* **2008**, *89*, 65-70.
- (28) Flinn, D. H.; Guzonas, D. A.; Yoon, R. H. Characterization of Silica Surfaces Hydrophobized by Octadecyltrichlorosilane. *Colloids Surf. Physicochem. Eng. Aspects* **1994**, *87*, 163-176.
- (29) Ishida, N. Direct Measurement of Hydrophobic particle–bubble Interactions in Aqueous Solutions by Atomic Force Microscopy: Effect of Particle Hydrophobicity. *Colloids Surf. Physicochem. Eng. Aspects* **2007**, *300*, 293-299.
- (30) Gillies, G.; Kappl, M.; Butt, H. -. Direct Measurements of Particle-Bubble Interactions. *Adv. Colloid Interface Sci.* **2005**, *114-115*, 165-172.
- (31) Johnson, D. J.; Miles, N. J.; Hilal, N. Quantification of particle–bubble Interactions using Atomic Force Microscopy: A Review. *Adv. Colloid Interface Sci.* **2006**, *127*, 67-81.
- (32) Tretheway, D. C.; Meinhart, C. D. Apparent Fluid Slip at Hydrophobic Microchannel Walls. *Phys. Fluids* **2002**, *14*, L9-L12.

- (33) Vinogradova, O. I.; Yakubov, G. E. Dynamic Effects on Force Measurements. 2. Lubrication and the Atomic Force Microscope. *Langmuir* **2003**, *19*, 1227-1234.
- (34) Cottin-Bizonne, C.; Cross, B.; Steinberger, A.; Charlaix, E. Boundary Slip on Smooth Hydrophobic Surfaces: Intrinsic Effects and Possible Artifacts. *Physical Review Letters* **2005**, *94*.
- (35) Baudry, J.; Charlaix, E.; Tonck, A.; Mazuyer, D. Experimental Evidence for a Large Slip Effect at a Nonwetting Fluid-Solid Interface. *Langmuir* **2001**, *17*, 5232-5236.
- (36) Ishida, N.; Kinoshita, N.; Miyahara, M.; Higashitani, K. Effects of Hydrophobizing Methods of Surfaces on the Interaction in Aqueous Solutions. *J. Colloid Interface Sci.* **1999**, *216*, 387-393.
- (37) Tyrrell, J. W. G.; Attard, P. Atomic Force Microscope Images of Nanobubbles on a Hydrophobic Surface and Corresponding Force-Separation Data. *Langmuir* **2002**, *18*, 160-167.
- (38) Hampton, M. A.; Nguyen, A. V. Nanobubbles and the Nanobubble Bridging Capillary Force. *Adv. Colloid Interface Sci.* **2010**, *154*, 30-55.
- (39) Masliyah, J.; Zhou, Z.; Xu, Z.; Czarnecki, J.; Hamza, H. Understanding Water-Based Bitumen Extraction from Athabasca Oil Sands. *Can. J. Chem. Eng.* **2004**, *82*, 628-654.
- (40) Drelich, J.; Miller, J. D. The line/pseudo-Line Tension in Three-Phase Systems. *Part. Sci. Technol.* **1992**, *10*, 1-20.
- (41) Laskowski, J. S.; Xu, Z.; Yoon, R. H. Energy Barrier in Particle-to-Bubble Attachment and its Effect on Flotation Kinetics. *Mines Carrières: Tech.* **1992**, 95-100.

## **Chapter 5**

### **Physicochemical Properties of Heavy Oil/Water Interface in the Context of Oil Removal from Sea Water by Froth Flotation**

## 5.1 Introduction<sup>§</sup>

Over the last fifty years, 80% of the largest volume oil spills occurred offshore.<sup>1</sup> From April 20<sup>th</sup> to July 15<sup>th</sup>, 2010, an approximate 4.9 million barrels (780,000 cubic meters) of crude oil was released into the Gulf of Mexico due to the explosion and subsequent collapse of the British Petroleum (BP) Deepwater Horizon exploration platform.<sup>2,3</sup> This environmental disaster inflicted incalculable damage to the ecosystem of the gulf. The unified command response operations employed to deal with the oil spill include: direct recovery of oil from the wellhead, in situ burning, skimming and chemical dispersion of oil.<sup>2</sup>

Direct recovery of oil from the wellhead is estimated to account for 17% removal of the oil released from the BP Horizon oil spill.<sup>2</sup> It was accomplished through the use of a riser pipe insertion tube and later a top hat system. In situ burning is estimated to account for 5% of total oil spill, which reduces the spread of oil by deliberately burning crude oil on the sea surface. This method has the lowest cost involved for its implementation,<sup>4</sup> but raises questions about production and emissions of particulate matter.<sup>5</sup> It is estimated that 3% of the oil was recovered by skimming which requires oil droplet size be sufficiently large for effective oil and water separation.<sup>6</sup> This approach requires an advanced knowledge of the interfacial properties at sea water/crude oil interface, which determines the coalescence of oil drops to sufficient sizes. In summary, it is estimated that the direct recovery, burning and skimming removed one quarter (25%) of the oil released from the wellhead, leaving the remaining 75% of the spill uncontained.

One quarter (25%) of the total oil naturally evaporates or dissolves into the water, and 24% disperses either naturally or as a result of chemical dispersion. The remaining amount (26%) washes up and is collected from the shore, or is buried in sand and sediments.<sup>2,3</sup> Oil in the residual and dispersed categories is in

---

<sup>§</sup> Modified from “Wang, L.; Curran, M.; Deng M.; Liu, Q.; Xu, Z. and Masliyah, J.H. Physicochemical properties of heavy oil/water interfaces in the context of oil removal from sea water by froth flotation, John Wiley & Sons, 2011, accepted.”

the process of being degraded. The emulsified small oil drops form relatively low concentration as oil-in-water emulsions. Although the dispersed crude oil drops are thermodynamically unstable, they are kinetically very stable due to the adsorption of natural surfactants (chemicals having a hydrophilic head and a hydrophobic tail), wax and solids at the oil/water interface.<sup>7</sup> We may not know the environmental consequences of these fugitive oils for years.

In an effort to minimize environmental consequences of the Gulf of Mexico oil spill, chemical dispersants are added to disperse 8% of the oil. These chemical dispersants consist of surfactants that attach to oil drop/water interface and reduce its interfacial tension. The decrease in interfacial tension promotes the breaking of the oil slicks into small droplets of diameter less than 100 microns and decreases the probability of oil droplet coalescence.<sup>3</sup> Dispersants Corexit 9527 and Corexit 9500A are reported to be used in the amount of 2.1 million gallons (7950 cubic meters) both at the surface and at the wellhead.<sup>8</sup> This approach does not allow any recovery of the oil. Previous studies have shown detrimental effects of dispersants on wildlife and microbial colonies.<sup>8, 9</sup> Furthermore, an adverse effect on the oxygen concentration due to increased microbial activity has also been illustrated.<sup>10</sup>

For the reasons mentioned above, it is of paramount importance to develop reliable, economical and convenient methods to separate the relatively low concentration of crude oil from water, especially with regard to the small oil droplets. Based on the differences in the natural or induced hydrophobicity of particles or oil droplets, froth flotation has been widely used, for over a century, to quickly and efficiently separate valuable minerals from gangue minerals and for wastewater treatment. The attachment of particles to air bubbles is of fundamental importance for flotation which includes many physiochemical and hydrodynamic phenomena in a dynamic system of solid particles, air bubbles and aqueous solutions containing various chemicals. The goal of this article is to investigate the interfacial properties of heavy offshore oil by determining the coalescence time of oil drops and induction time of bubble-oil attachment in sea water using

the integrated thin film drainage apparatus (ITFDA). The intention is to lay a foundation for the removal of emulsified heavy oil such as that from the Gulf of Mexico oil spill by froth flotation in an economical and environmentally friendly manner.

## **5.2 Materials and Methods**

### ***5.2.1 Materials and sample preparations***

A Grane heavy crude oil from Statoil, Norway was used in this study. The density, total acid number (TAN), water content (WC), and saturate, aromatic, resin and asphaltene (SARA) compositions of the oil are summarized in Table 5-1. Sea water was obtained from west coast of Vancouver, British Columbia, Canada. The sea water was filtered with a 0.2  $\mu\text{m}$  filter to remove fine solids. The composition of sea water and tap water determined by Atomic Absorption Spectroscopy (AAS) and salinity of the water are also listed in Table 5-1. It should be noted that the salinity of the sea water is a little bit less than the value normally reported, hence the sea water sample used in this work is more likely to be “brackish water”. Petroleum naphtha (heavy reformat) was received from Champion Technologies. All the measurements were conducted at the ambient temperature of  $20 \pm 0.5$  °C. The pH of the aqueous solutions was adjusted by reagent grade sodium hydroxide (NaOH) and hydrochloric acid (HCl) (Fisher Scientific) solutions.

Thirty drops of heavy oil were added into 100 mL of tap water or sea water at pH 9.0 and then homogenized by a Power Gen 125 (Fisher Scientific) operated at 6000 rpm for 10 min to prepare heavy oil in water emulsions. The emulsion was allowed to cream for about 30 min to equilibrate the oil/water interface. The size of the formed oil drops was determined by Focused Beam Reflectance Method (Mettler-Toledo, Greifensee, Switzerland). The average diameter of the oil drops prepared as such was determined to be approximately 10  $\mu\text{m}$  and was stable for at least two hours. The formed oil in water emulsion was used for zeta potential measurement and micro-flotation test.

**Table 5-1 Properties and composition of crude oil and water used in this study**

Crude oil properties <sup>11</sup>		Water properties		
			Sea water	Tap water <sup>**</sup>
Density (g/cm <sup>3</sup> ) @ 15°C	0.939	Density (g/cm <sup>3</sup> ) @ 20 °C	1.0166	1.00
TAN (mg g <sup>-1</sup> )	2.15	Salinity (wt % of salt in water)	2.65	-
Wax content (wt %)	0.11	Na <sup>+</sup> (ppm)	6367	9.5
Saturates (wt %)	37	K <sup>+</sup> (ppm)	297	0.8
Aromatics (wt %)	44	Mg <sup>2+</sup> (ppm)	997	13.4
Resins (wt %)	16	Ca <sup>2+</sup> (ppm)	632	45.8
Asphaltenes, hexane insoluble (wt %)	2.5	Surface tension (mN * m <sup>-1</sup> )	72.6	72.3

### 5.2.2 Measurement of oil/water interfacial properties

The oil/water interfacial tension and zeta potential of oil in water emulsions were determined. The oil/water interfacial tension was measured using a Processor Tensiometer K12 (Krüss, Hamburg, Germany) by the Du Noüy ring method. Prior to all tests, the measurement chamber was filled with de-ionized water and the surface tension was measured. The chamber and the platinum ring were considered to be clean when the surface tension of de-ionized water was measured to be  $72.8 \pm 0.5$  mN/m. After ensuring the cleanliness of the system, equal volume of oil and sea water were added into the vessel. It has been well recognized that the presence of natural surfactants at the oil/water interface reduces the interfacial tension and this interfacial tension reduces with aging time.<sup>12</sup> Hence, after positioning the ring into the sea water phase, the oil and water layers were left in contact for 30 min before measurements to allow the surface active species to migrate from the oil phase to the oil/water interface. Zeta potential of heavy oil droplets in sea water and tap water were determined using a ZetaPALS (Brookhaven Instruments Corp., New York). A diluted suspension of emulsified heavy oil was prepared by adding several drops of oil emulsions to 50 mL water of interest. The prepared suspensions were stirred with a magnetic stirrer for 5 min before measurements. Five measurements were taken for each condition. The average value together with the standard deviation were reported.

<sup>\*\*</sup> 2010 Edmonton water and wastewater performance report

### 5.2.3 Measurement of coalescence and induction times

The coalescence time of oil droplets and induction time of air bubble-oil attachment were determined by the ITFDA as described in **Chapter 4**. The experimental set up is similar to the one illustrated in **Fig. 4-1(a)**. However, in these experiments, a Teflon holder with a bowl shaped top surface was clamped at the end of a bimorph beam instead of a glass sphere to hold the oil droplets.

**Fig. 5-1** shows the bimorph signal recorded when an oil droplet A attached to the glass capillary tube approaches another oil droplet B which is fixed on Teflon holder in sea water at pH 7.6. In this test, the oil droplet drive velocity,  $V$ , is set to be  $240 \mu\text{m/s}$ . At large separation distances, there is no detectable interaction force between the two oil droplets, represented by a zero bimorph signal with electrical noise. After the two droplets arrive at a distance where the hydrodynamic and/or surface forces begin to operate, a repulsive force is shown at point 'a', represented by an increase in bimorph signal. The following sharp increase of bimorph signal until point 'b' is a result of applied force by continued push of the upper oil droplet A down against the lower oil droplet B. At point 'b', with the upper oil droplet being held stationary against the lower oil droplet, a constant bimorph signal is displayed. During the "holding" period, the thickness of the aqueous film continues to thin until the thickness of the film reaches a critical thickness whereby it ruptures. The break of the film is followed by the coalescence of the two oil droplets, which is characterized by a sharp drop of bimorph signal at point 'c' to  $-0.34 \text{ V}$  at point 'd', indicating upward deflection of bimorph upon coalescence. The subsequent spreading of the coalescing oil droplets causes a slight lift of lower surface, as indicated by a continuous drop of bimorph signal beyond point 'd'. The drainage time of the aqueous film between the two oil droplets (or air bubble-oil droplet) is known as coalescence (induction) time.<sup>13-14</sup> The coalescence time or induction time in this study is measured from point 'a' to point 'c', i.e., time for film thinning. As shown in **Fig. 5-1**, for example, the coalescence time of the two oil droplets in sea water at pH 7.6 is determined to be 52.9 s. The entire approaching and retracting processes are recorded in real time

by one of the high resolution digital video cameras interfaced with the computer that is used to simultaneously drive the speaker diaphragm and record bimorph signals.

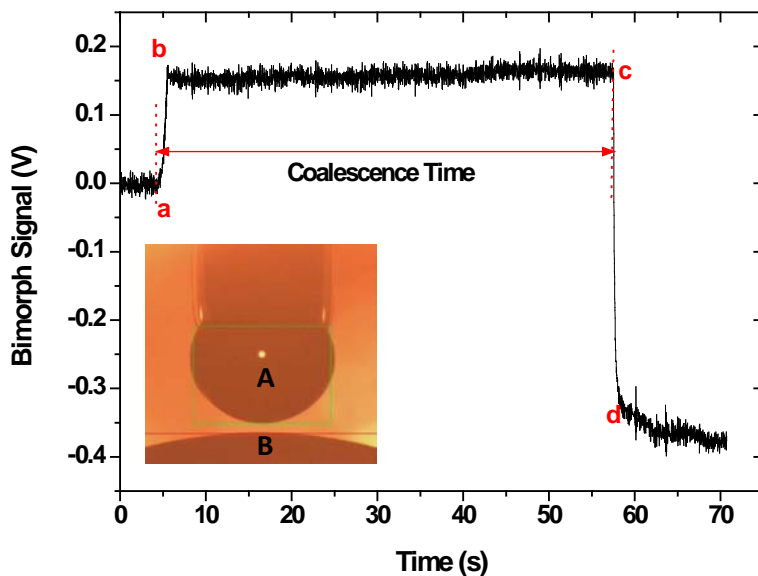


**Fig. 5-1** Bimorph signal profile for coalescence time determination of two oil drops using ITFDA. The inset figure shows the two oil droplets of diameters 1.49 mm (A) and 8.52 mm (B). The measurement was conducted in sea water at pH 7.6 and an approach and retract velocity of 240  $\mu\text{m/s}$ .

Before each experiment, the chamber was filled with test solutions followed by an oil droplet being placed on the Teflon sample holder. The glass capillary tube was filled with the heavy oil or fresh air before being brought into the solution. The system was then left for two hours to stabilize the bimorph signal. Fresh air bubbles and heavy oil droplets were created for induction time and coalescence time measurements. In this study, the size of the upper and lower droplets was controlled to be  $1.50 \pm 0.02$  mm and  $8.50 \pm 0.02$  mm, respectively. The initial separation distance between the two droplets was maintained at  $0.12 \pm 0.01$  mm, unless otherwise indicated. Thirty measurements were taken at each condition and the average value was reported with the error being the standard deviation of these 30 measurements.

#### **5.2.4 Micro-flotation test**

To demonstrate the feasibility of applying flotation to recover heavy oil from sea water, a micro-flotation test was employed. The pH of the homogenized oil-in-water emulsion was adjusted back to pH 7.6 before flotation. The emulsion was then transferred into the micro-flotation cell. The flotation was conducted for 20 min at an air flow rate of 25 mL/min. During flotation, a magnetic stir was placed on the fritted disk to better distribute the generated air bubbles. Due to the low concentration of oil in water and its sticky nature to glass, a quantitative analysis of oil from emulsion was not attempted. Instead, the tailings (the residual emulsion in the flotation cell) after the flotation test were collected to visually demonstrate the effectiveness of flotation.

### **5.3 Results and Discussion**

#### **5.3.1 Interfacial tension and zeta potentials**

The interfacial tension and zeta potential of the heavy oil/water interface were measured as a function of pH to understand the interfacial properties of the heavy oil. For comparison, naphtha, a distillation product of crude oil was used as a model oil. The naphtha/water interfacial tension was measured as a base line. As shown in **Fig. 5-2**, the interfacial tension of heavy oil/sea water interface decreased sharply with pH, from 22.7 mN/m at pH 6 to 8.9 mN/m at pH 10. The interfacial tension of naphtha-sea water was measured to be much higher than that of heavy oil/sea water interface at most pH values studied, also decreasing with pH but to a less extent. The effect of pH on the interfacial tension is explained by pH-dependent ionization of natural surfactants present at heavy oil/water interface. Substantial amounts of amphiphilic compounds such as asphaltenes, resins and naphthenic acids were found in the crude oil.<sup>11, 15</sup> These indigenous compounds contain acidic and basic functional groups. A critical pH to reach a maximum interfacial tension value was observed.<sup>16, 17</sup> Over the low pH range, the interfacial tension is mostly governed by the protonation of basic molecules, while over the high pH range, interfacial tension reduction is mainly attributed to extraction and dissociation of acidic surfactant molecules. It is therefore expected

that the pH change of the aqueous solution will affect the ionization of the natural surfactant at the interface, causing a dramatic change in oil/water interfacial properties and solubility of surfactant at the aqueous phase. The observed reduction of the heavy oil/sea water interfacial tension was mainly attributed to the increased concentration of surface active molecules at heavy oil/water interface with contributions from increased dissociation of carboxylic acid groups, maximizing the accumulation of the indigenous surfactants at the heavy oil/water interface. The drop of the naphtha/sea water interfacial tension with pH also indicates the presence of surface active components of acidic nature in naphtha at the interface. The amount of surfactants present in naphtha, however, must be much less than that in heavy oil, resulting in a higher interfacial tension of naphtha/water interface than that of the heavy oil/sea water interface, although they are similar at pH 6.

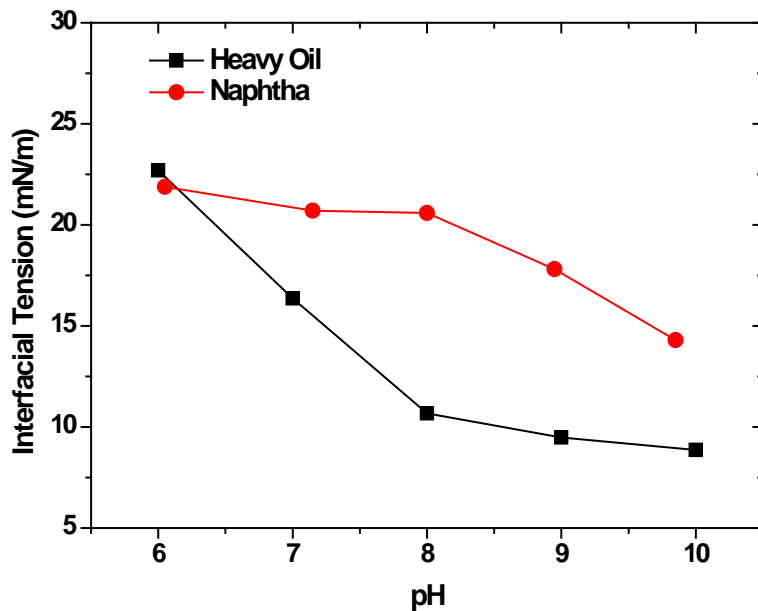


**Fig. 5-2** Interfacial tension of heavy oil/sea water and naphtha/sea water interface as a function of solution pH.

**Fig. 5-3** shows the zeta potential of emulsified heavy oil as a function of pH in tap water and sea water. The zeta potentials of heavy oil droplets were negative in both systems, which indicate the presence of anionic surface groups at oil/water interfaces. The zeta potential became more negative with increasing pH and

leveled off after pH 7 in tap water, indicating a dominant presence of a weak acid type of surfactant, most likely a carboxylic acid type at the oil/water interface. Considering a typical pKa value of 4-5, more carboxylic groups were dissociated at higher pH, resulting in a more negative surface charge of heavy oil droplets at higher pH. In contrast, in sea water, pH showed a marginal effect on the zeta potential of heavy oil droplets and the values were less negative. As shown in **Table 5-1**, the concentrations of simple electrolyte ions, such as  $\text{Na}^+$ ,  $\text{Cl}^-$  and  $\text{K}^+$  in sea water were considerably higher than that in tap water, which compressed the electrical double layer of the heavy oil droplets to a much large extent, leading to a much smaller zeta potential value and less pH-dependency. In addition, more divalent cations such as  $\text{Mg}^{2+}$  and  $\text{Ca}^{2+}$  were present in the sea water. These ions can specifically adsorb at the oil/water interface through their binding with carboxylic groups, contributing to the reduction of negative zeta potential values.

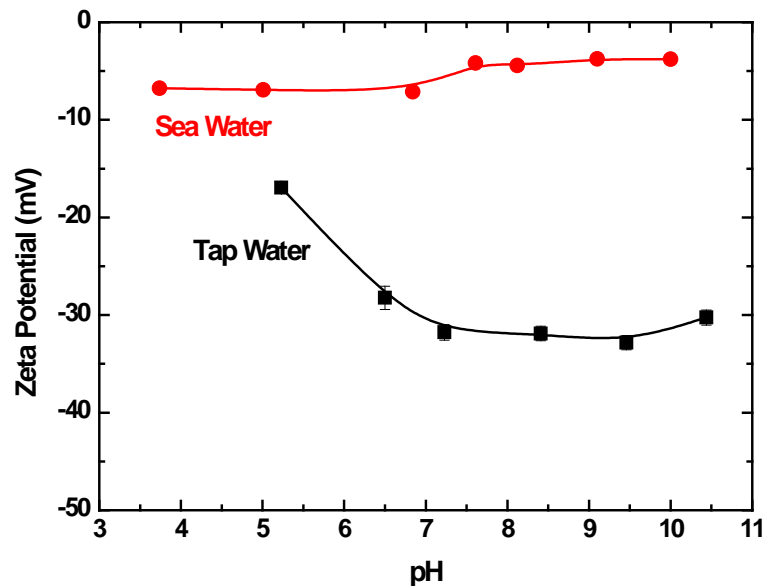


**Fig. 5-3** Zeta potential of oil droplets in tap water and sea water as a function of pH.

### 5.3.2 Interactions between oil droplets

#### 5.3.2.1 Effect of solution pH

The coalescence time of two heavy oil droplets was measured using the ITFDA in both tap water and sea water. The measurements were conducted at a constant

droplet drive velocity of 240  $\mu\text{m/s}$ . The results are shown in **Fig. 5-4**. In tap water, no coalescence was observed even at a contact time of 300 s, showing a very stable water film between oil droplets in tap water. However, the oil droplets in sea water coalesced and the coalescence time increased dramatically with increasing sea water pH, from 8.7 s at pH 6.0 to 96.7 s at pH 9.0.

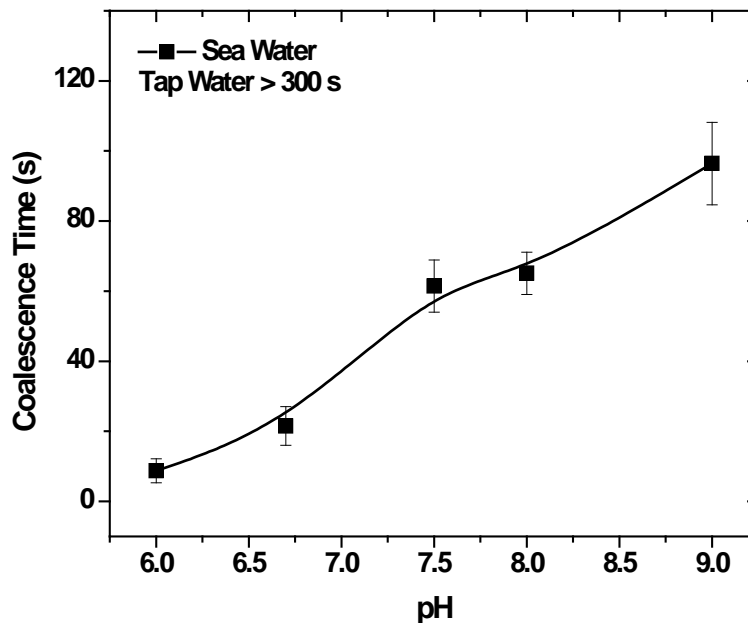


**Fig. 5-4** Coalescence time of heavy oil droplets in tap water and sea water as a function of solution pH at a droplet approach velocity of 240  $\mu\text{m/s}$ . In tap water, no coalescence was observed even at a contact time of 300 s at all pH values studied.

In tap water, the water film between two oil surfaces was very stable due to a positive disjoining pressure (a pressure used to describe the free energy change of the intervening liquid film),<sup>18</sup> resulting in a very long coalescence time (larger than 300 s as illustrated in **Fig. 5-4**). The coalescence of oil droplets in sea water indicates the water film ruptured during the interaction, suggesting a dramatic reduction of repulsive force or an increase of attractive force. Since the van der Waals forces between two similar oil droplet surfaces in water are less sensitive to the change of solution chemistry, the observed change of the film stability is probably due to a reduction of repulsive electrical double layer force. From tap water to sea water, the repulsive electrical double layer force reduced dramatically

with much less negatively charged oil surfaces and highly compressed electrical double layers. During the drainage process, the film became progressively thin until it reached a critical thickness, where the attractive forces dominated the total force and the film ruptured.

The continuous increase in the coalescence time with increasing pH indicates a lower film drainage rate at higher pHs. According to **Fig. 5-3**, the zeta potential of oil droplets in sea water remained almost the same over the pH range studied. Increasing pH would increase potential at the stern layer of oil droplets to a more negative value, however, the potential decays significantly with the distance due to a high electrolyte concentration, resulting in a very similar potential at the shear plan where the zeta potential value is measured. The calculation of the electrical double layer force between the two oil droplets (not presented here) indicates that the force changes little with the change of stern potential. Little change of van der Waals force and electrical double layer force would render a similar property of drainage film between oil droplets. Therefore, the extend-DLVO (Derjaguin-Landau-Verwey-Oberbeek) theory needs to be used to analyze the interactions between two surfaces. In the extend-DLVO, forces other than van der Waals force and electrical double layer force are considered, including attractive long range hydrophobic force, repulsive short range steric and/or hydration forces.<sup>19</sup> The increase in the coalescence time with pH may be contributed to the reduction in attractive hydrophobic force and/or increase in repulsive hydration force of hydrated carboxylate groups of natural surfactant accumulated at oil/water interface with increasing pH. As discussed previously, at high pH, more acidic groups of natural surfactant were dissociated at the oil/water interface as indicated by increased negative zeta potential values of the heavy oil droplets in tap water. A higher concentration of natural surfactants was also expected at oil/sea water interface. However, the high electrolytes concentration and the presence of divalent ions made the zeta potential measurements insensitive to the change of the oil/sea water interface. The increased adsorption and ionization of water soluble surfactant would reduce the hydrophobicity of oil/water interface. The reduction of surface hydrophobicity reduced the attractive hydrophobic force

between two oil surfaces. Moreover, the presence of more indigenous surfactants at the oil/water interface would incur a stronger hydration and steric repulsive force between hydrophilic head groups, contributing to the decreased film drainage rate, and hence, increased coalescence time with increasing pH of sea water.

### 5.3.2.2 Effect of oil droplet size and droplet approach velocity

To study the effect of heavy oil droplet size on coalescence time, the diameter of the upper oil droplet was varied from 1500  $\mu\text{m}$  to 600  $\mu\text{m}$  while the lower oil surface remained the same. As shown in **Fig. 5-5**, the coalescence time dropped from 61.4 s to 10.2 s by decreasing the size of upper oil droplet from 1500  $\mu\text{m}$  to 600  $\mu\text{m}$ . In this set of measurements, the applied force from the upper oil droplet to the lower oil droplet was kept the same during measurements as shown by the same voltage reading on the bimorph during the holding period. Consequently, a higher external pressure was applied on the lower oil droplet by the smaller upper oil droplet due to the reduced contact area. A higher pressure tends to drain the aqueous film faster, resulting in a decrease in coalescence time as was observed.

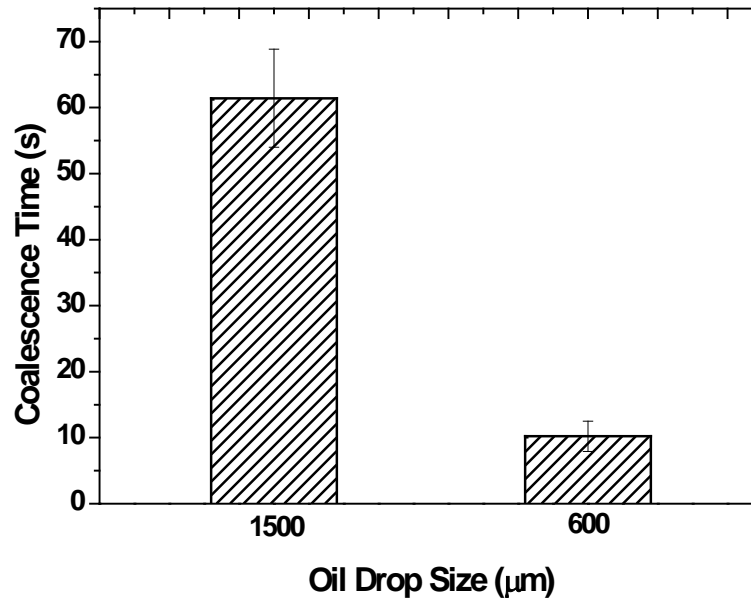


**Fig. 5-5** Effect of upper heavy oil droplet size on coalescence time in sea water at pH 7.6 with oil droplet approach velocity of 240  $\mu\text{m/s}$ .

**Fig. 5-6** shows the effect of upper oil droplet approach velocity on the coalescence time of heavy oil droplets in sea water at pH 6.0. As can be noted from the graph, the coalescence time changed little at low approach velocity region and increased sharply when the approach velocity was larger than 240  $\mu\text{m/s}$ . The thinning process of the liquid film is controlled by hydrodynamic force initially and by the surface forces at smaller separation distances. During the approaching, the liquid film between two surfaces is drained, which generates a film drainage resistance. This film drainage resistance deforms the oil/water interfaces and influences the whole drainage process. At an approach velocity smaller than 240  $\mu\text{m/s}$ , the coalescence time remained similar due to limited differences in deformation of the interfaces. At higher approach velocities, the water film between the two approach oil droplets did not have sufficient time to be expelled sufficiently. The excess water volume trapped between the two oil droplets caused a significant deformation of oil/water interfaces, forming a so-called “dimple”, where the film thickness is higher at the centre than at the barrier rim. In this case, the drainage of intervening liquid film was limited by water flow through the rim between the two oil droplets. At a high approach velocity, therefore, the repulsive film drainage resistance dominated the total force, thereby reducing the film drainage rate and increasing the coalescence time. The increase of film drainage time with approach velocity was also observed when studying the interaction between an air bubble and a hydrophobized glass surface as illustrated in **Fig. 7-6**.

### **5.3.3 Air bubble – oil droplet interactions**

Among all the sub-processes of successful mineral flotation, the attachment of the mineral particles to air bubbles is of fundamental importance. This process involves the thinning and rupture of the intervening liquid film, followed by the spread of three phase contact line on the mineral particle. The minimum contact time required for a successful air bubble-particle attachment is defined as the induction time. The induction time was first described in the early 1930s and has been extensively used in flotation research and modeling.<sup>14, 20-23</sup> To determine the

induction time in mineral flotation systems, a captive air bubble is usually moved toward and then away from a particle bed or a flat mineral surface. A shorter induction time leads to a higher recovery for both quartz flotation<sup>14</sup> and bitumen flotation.<sup>20</sup> Since the induction time can reflect the kinetics and is linked with interfacial phenomena and the hydrodynamic effect in flotation, induction time between an air bubble and heavy oil surface was investigated in this study.

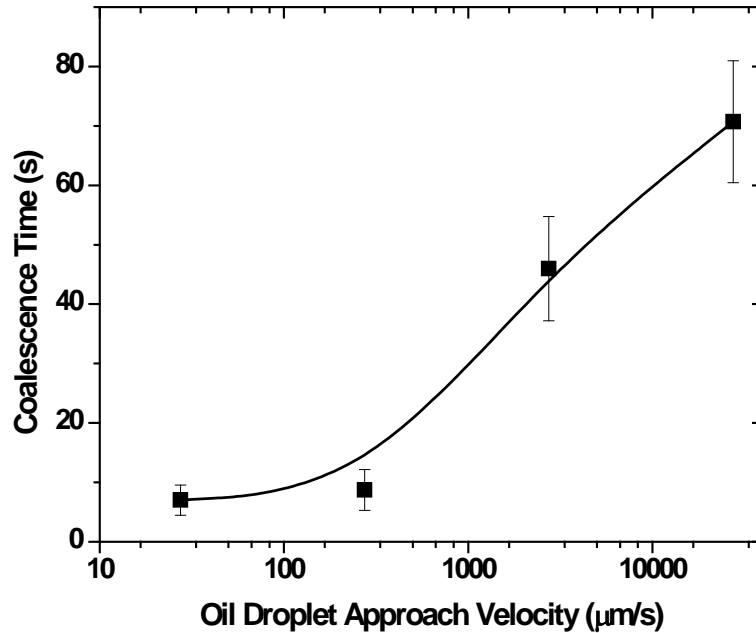


**Fig. 5-6** Coalescence time of heavy oil droplets in sea water at pH 6.0 as a function of drive velocity of the upper oil droplet.

**Fig. 5-7** shows the result of induction time measurement between an air bubble and a heavy oil droplet in sea water as a function of bubble aging time. As it can be seen from **Fig. 5-7**, the induction time of fresh air bubble attachment to heavy oil droplet in natural pH was 0.83 s, much smaller than the coalescence time of oil droplets at the same condition (61.4 s). And the induction time of air bubble-oil attachment increased from 0.8 s for a fresh bubble to 1.6 s and 6.8 s when the bubble was aged for 1 min and 5 min, respectively. The increase of induction time with aging of bubbles was mainly due to the accumulation of natural surface active species at the air/water interface with time. When placing oil droplets into sea water, surfactants migrated from heavy oil to the oil/water interface and into the aqueous solution. The accumulation of these surfactants at the oil/water

interface not only reduced the interfacial tension (**Fig. 5-2**) but also made the oil surface more negatively charged in tap water (**Fig. 5-3**).

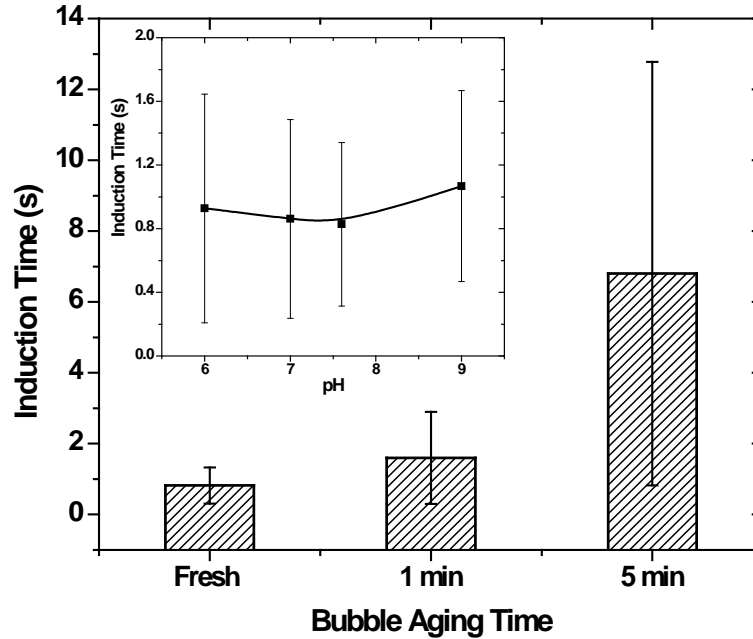


**Fig. 5-7** Aging of air bubble on induction time of air bubble-oil droplet attachment in sea water at natural pH of 7.6 and bubble approach velocity of 240  $\mu\text{m/s}$ . Inset shows the effect of pH on induction time.

When the air bubble was immersed in the aqueous solution, the adsorption of surfactant, originally from heavy oil, at the bubble/water interface was inevitable. Similar to the oil/water interface, the adsorption of surfactant at the bubble/water interface would not influence the zeta potential of bubble in an environment of a high electrolyte concentration. The marginal effect of water chemistry (i.e., solution pH) on the electrical double layer force between the air bubble and oil surface was illustrated by the almost constant induction time of bubble-oil attachment at different pH in sea water. As shown in the inset of **Fig. 5-7**, the induction time of fresh bubble-oil attachment remained around 0.9 s from pH 6 to 9 in sea water with a bubble approach velocity of 240  $\mu\text{m/s}$ . Meanwhile, the adsorption of natural surfactants at the air/water interface decreased the air bubble hydrophobicity. The decreased attractive hydrophobic force and increased repulsive hydration force reduced film drainage rate, increasing the induction time

of bubble attachment to heavy oil droplets in sea water with bubble aging time. This finding suggests the use of fresh air bubbles to recover heavy oil from oil emulsions to maximize the flotation rate.

As discussed above, it is evident that oil droplets are much easier to attach to air bubbles than to oil droplets themselves, as shown by a much shorter induction time (0.83 s) than coalescence time (61.4 s) at pH 7.6. This finding suggests that flotation of oil spill by induced air bubbles is more effective than by natural coalescence of spill oil droplets, even without considering more effective buoyancy force of air bubbles than oil for concentrating oils on water surface for effective removal and recovery.

#### ***5.3.4 Micro-flotation of crude oil***

A micro-flotation test was conducted to recover heavy oil from sea water. The results are visually compared using photographs in **Fig. 5-8**. Compared with the photograph of turbid oil emulsions after 12-hour creaming without any treatment (a), photograph (b) of tailings obtained after 20 min of micro-flotation using air bubbles is seen to be as clear as the sea water shown in photograph c. These three photographs qualitatively illustrate the effectiveness of removing oil droplets from the emulsion, confirming that micro-flotation is an excellent method to remove oil from sea water.

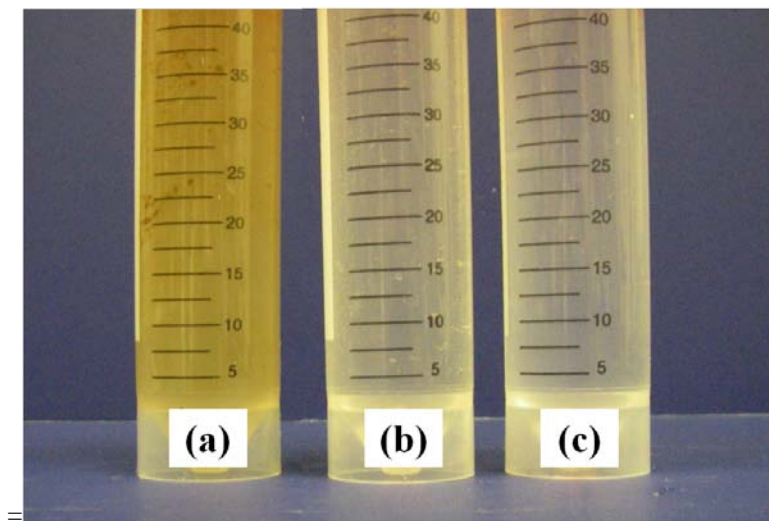


**Fig. 5-8** Photographs of samples: (a) heavy oil in sea water emulsion; (b) tailings of emulsion after 20 min of flotation and (c) sea water.

## 5.4 Conclusions

The interfacial properties of heavy oil/water interface were studied in terms of interfacial tension and zeta potential as a function of aqueous pH. The dissociation of surfactants at heavy oil/water interface not only reduced interfacial tension but also made the oil surface more negatively charged with increasing solution pH. The coalescence time of oil drops and the induction time of air bubble-heavy oil droplet attachment were determined by the ITFDA. In tap water, coalescence time was longer than 300 s if it ever happens due to the presence of strong electrical double layer repulsive forces. In sea water, however, compressed electrical double layer and hence the reduced electrostatic repulsion made the coalescence much easier to take place. The coalescence time increased with increasing pH due to the increased adsorption and ionization of natural surfactants present in the heavy oil. Large size ratio of oil droplets and low approach velocity were preferable for oil drop coalescence. Fresh air bubbles were found to promote the attachment of air bubbles to oil droplets. The induction time increased with the aging of air bubbles. Micro-flotation has been shown to be a convenient and efficient way to remove emulsified heavy oil from sea water.

## 5.5 References

- (1) Etkin, D. S. In *Historical Overview of Oil Spills from all Sources (1960-1998)*; **1999**, pp 1097-1102.
- (2) Kerr, R. A. A Lot of Oil on the Loose, Not so Much to be found. *Science* **2010**, 329, 734-735.
- (3) Lubchenco, J. BP Deepwater Horizon oil budget : what happened to the oil?
- (4) Etkin, D. S.; Tebeau, P. In *Assessing Progress and Benefits of Oil Spill Response Technology Development since Exxon Valdez*; **2003**, pp 843-850.

- (5) Schaum, J.; Cohen, M.; Perry, S.; Artz, R.; Draxler, R.; Frithsen, J. B.; Heist, D.; Lorber, M.; Phillips, L. Screening Level Assessment of Risks due to Dioxin Emissions from Burning Oil from the BP Deepwater Horizon Gulf of Mexico Spill. *Environ. Sci. Technol.* **2010**, 44, 9383-9389.
- (6) Nordvik, A. B.; Simmons, J. L.; Bitting, K. R.; Lewis, A.; Strøm-Kristiansen, T. Oil and Water Separation in Marine Oil Spill Clean-Up Operations. *Spill Sci. Technol. Bull.* **1996**, 3, 107-122.
- (7) Menon, V. B.; Nikolov, A. D.; Wasan, D. T. Interfacial Effects in Solids-Stabilized Emulsions: Measurements of Film Tension and Particle Interaction Energy. *J. Colloid Interface Sci.* **1988**, 124, 317-327.
- (8) Kujawinski, E. B.; Kido Soule, M. C.; Valentine, D. L.; Boysen, A. K.; Longnecker, K.; Redmond, M. C. Fate of Dispersants Associated with the Deepwater Horizon Oil Spill. *Environ. Sci. Technol.* **2011**, 45, 1298-1306.
- (9) Milinkovitch, T.; Kanan, R.; Thomas-Guyon, H.; Le Floch, S. Effects of Dispersed Oil Exposure on the Bioaccumulation of Polycyclic Aromatic Hydrocarbons and the Mortality of Juvenile *Liza Ramada*. *Sci. Total Environ.* **2011**, 409, 1643-1650.
- (10) Kessler, J. D.; Valentine, D. L.; Redmond, M. C.; Du, M.; Chan, E. W.; Mendes, S. D.; Quiroz, E. W.; Villanueva, C. J.; Shusta, S. S.; Werra, L. M.; Yvon-Lewis, S. A.; Weber, T. C. A Persistent Oxygen Anomaly Reveals the Fate of Spilled Methane in the Deep Gulf of Mexico. *Science* **2011**.
- (11) Simon, S.; Nenningsland, A. L.; Herschbach, E.; Sjöblom, J. Extraction of Basic Components from Petroleum Crude Oil. *Energy Fuels* **2010**, 24, 1043-1050.
- (12) Bhardwaj, A.; Hartland, S. Dynamics of Emulsification and Demulsification of Water in Crude Oil Emulsions. *Ind Eng Chem Res* **1994**, 33, 1271-1279.

- (13) Hartland, S.; Vohra, D. K. Effect of Interdrop Forces on the Coalescence of Drops in Close-Packed Dispersions. *J. Colloid Interface Sci.* **1980**, *77*, 295-316.
- (14) Yoon, R.; Yordan, J. L. Induction Time Measurements for the Quartz-Amine Flotation System. *J. Colloid Interface Sci.* **1991**, *141*, 374-383.
- (15) Sjöblom, J.; Aske, N.; Harald Auflem, I.; Brandal, Ø.; Erik Havre, T.; Sæther, Ø.; Westvik, A.; Eng Johnsen, E.; Kallevik, H. Our Current Understanding of Water-in-Crude Oil Emulsions.: Recent Characterization Techniques and High Pressure Performance. *Adv. Colloid Interface Sci.* **2003**, *100-102*, 399-473.
- (16) Bai, J.; Fan, W.; Nan, G.; Li, S.; Yu, B. Influence of Interaction between Heavy Oil Components and Petroleum Sulfonate on the Oil-Water Interfacial Tension. *J. Dispersion Sci. Technol.* **2010**, *31*, 551-556.
- (17) Nenningsland, A. L.; Simon, S.; Sjoblom, J. Surface Properties of Basic Components Extracted from Petroleum Crude Oil. *Energy Fuels* **2010**, *24*, 6501-6505.
- (18) Nguyen, A.; Schulze, H. J., Eds.; In Colloidal Science of Flotation; Surfactant Science Series; New York, **2004**; Vol. 118, pp 850.
- (19) Israelachvili, J. N. In Intermolecular and Surface Forces; Section Title: General Physical Chemistry; Academic Press: **1991**, pp 449.
- (20) Wang, L.; Dang-Vu, T.; Xu, Z.; Masliyah, J. H. Use of Short-Chain Amine in Processing of weathered/oxidized Oil Sands Ores. *Energy Fuels* **2010**, *24*, 3581-3588.
- (21) Gu, G.; Xu, Z.; Nandakumar, K.; Masliyah, J. Effects of Physical Environment on Induction Time of Air-Bitumen Attachment. *Int. J. Miner. Process.* **2003**, *69*, 235-250.

- (22) Sven-Nilsson, I. Effect of Contact Time between Mineral and Air Bubbles on Flotation. *Kolloid Z.* **1935**, 69, 230.
- (23) Gu, G.; Xu, Z.; Nandakumar, K.; Masliyah, J. Effects of Physical Environment on Induction Time of Air-Bitumen Attachment. *Int. J. Miner. Process.* **2003**, 69, 235-250.

## **Chapter 6**

**Studying Dynamic Forces between an Air Bubble and a  
Hydrophilic Glass Surface with an Integrated Thin Film Drainage  
Apparatus (ITFDA)**

## 6.1 Introduction<sup>††</sup>

The interaction between bubbles and solid surfaces in aqueous solutions plays a crucial role in various industrial processes, most notably in froth flotation which is widely used in separation of mineral particles, treatment of wastewater, recycling of fibres from waste paper, removal of toxic components from industrial effluent and separation of biological cell.<sup>1, 2</sup> The bubble-particle interactions are central to the froth flotation since the selective attachment of air bubbles and particles determines the separation between hydrophobic and hydrophilic particles in a flotation cell.<sup>3, 4</sup> Attachment between colliding mineral particles and air bubbles in flotation cells is determined by the drainage kinetics of intervening liquid films.

A number of different experimental techniques have been used to study film drainage and time dependent interactions between an air bubble and a solid surface.<sup>5</sup> One of the earliest studies on film drainage has heavily relied on the Scheludko cell, in which a captive air bubble is pressed against a flat silica surface through a capillary tube,<sup>6-9</sup> or by pulling out the liquid between two approaching surfaces.<sup>10</sup> The film thickness between the two surfaces is measured using the micro interferometric method based on multiple reflection and interference of a monochromatic light. Using this method, the time evolution of the central film thickness,  $h(0,t)$ , can be obtained. The atomic force microscope (AFM) has been widely used to make direct measurements of interactions between particle and air bubble.<sup>11-14</sup> In this technique, also called colloidal probe technique, a small bubble ( $\sim 500 \mu\text{m}$ ) is placed on a hydrophobic substrate and a spherical probe particle is attached to the cantilever of the AFM. In most of the measurements, the air bubble is moved up and down through a piezoelectric transducer to approach to and retract from the probe particle.<sup>12-14</sup> And in some measurements, the cantilever is driven to approach and retract from the lower air bubble/droplet surface.<sup>11</sup> In

---

<sup>††</sup> Modified from: “Shahalami, M.; Wang, L.; Wu, C.; Chan, D.; Xu, Z.; Masliyeh, J.H. Measurements of hydrodynamic forces and deformations in bubble-solid interactions with the integrated thin film drainage apparatus (ITFDA), *manuscript in preparation.*”

all of these AFM measurements, the interaction force as a function of bubble displacement is obtained by monitoring the deflection of the cantilever.

Thin liquid film apparatus based on Scheludko cell technique provides the center film thickness but fails to provide the interaction force between an air bubble and a solid surface. On the other hand, with the colloidal probe technique AFM can measure the interaction force but is incapable of measuring the bubble deformation. Moreover, the experiments conducted by the thin liquid film apparatus and AFM are under low Reynolds number region. For example, the reported maximum bubble approach velocity towards a particle in AFM measurement is  $98 \mu\text{m/s}$ ,<sup>15</sup> which gives a bubble Reynolds number ( $Re = 2\rho RV/\mu$ ) of 0.02, much lower than the Reynolds number of particles/bubbles in a flotation cell. It is therefore important to develop a device that measures both force and bubble deformation, meanwhile expanding the measurement to a higher Reynolds number region. For this reason, an integrated thin film drainage apparatus (ITFDA) was developed recently to measure the bubble-particle interactions under dynamic conditions.<sup>16</sup> The ITFDA is capable of measuring the dynamic forces and the geometric properties of the bubble and interacting particles simultaneously. The bubble drive velocity can be as high as  $5000 \mu\text{m/s}$ , which gives a bubble Reynolds number of 10, making the ITFDA an ideal device to study the bubble-solid interactions under dynamic conditions.

In this chapter, the ITFDA is used to measure the forces and bubble deformation between a hydrophilic glass sphere and a deformable air bubble in different liquids. The Stokes–Reynolds–Young–Laplace (SRYL) model was employed to predict the forces exerted by the moving air bubble on the glass sphere while providing the spatial and temporal evolution of the intervening aqueous film. The bubble deformation (i.e., contact area) during the interaction was measured experimentally and predicted by the SRYL model. The effect of different parameters such as pH, salt concentration, liquid surface tension, liquid viscosity and bubble drive velocity on the film pressure between two approaching interfaces was studied.

## 6.2 Experimental Methods

The dynamic interaction forces between an air bubble and a hydrophilic glass sphere were measured using the ITFDA, the device is shown schematically in **Fig. 6-1**. The ITFDA uses a bimorph cantilever as a force sensor. As a piezo material, the bimorph cantilever generates electrical charge in response to a shape deformation. The charges generated are proportional to the deformation which is determined by the external force applied at the end of the cantilever. Hence, the external force can be obtained by measuring the charge of bimorph due to its deformation. A piezo ceramic actuator with a dimension of  $20 \times 3 \times 0.3$  mm and a capacitance of 20 nF, purchased from FUJI CERAMICS Corps., is used to fabricate the force sensor. The actuator is enclosed by a fluorinated ethylene propylene (FEP) sheath and mounted on a small stainless steel chamber. A hydrophilic glass sphere with a diameter of  $4.4 \pm 0.1$  mm is clamped at the free end of the bimorph cantilever. An air bubble with a diameter of  $1.46 \pm 0.01$  mm is generated at the end of a glass tube using a micro-syringe. The glass tube is attached to a speaker diaphragm which is used to control the vertical motion of the capillary tube. The computer generates a desired wave form that controls the movement of the speaker diaphragm which in turn moves the air bubble towards or away from the lower glass sphere in a well-controlled manner. The interaction between the two surfaces causes a deflection at the end of bimorph cantilever,  $S(t)$ . The charge due to the deflection of bimorph beam can be measured and converted to the force between the air bubble and the glass sphere once the bimorph cantilever calibration constant is determined.

The glass tube has an inner diameter of  $1.1 \pm 0.05$  mm (Fisher Scientific). One end of the glass tube was placed under a butane flame to create a smooth end appropriate for bubble generation and force measurements between air bubble and solid surfaces. Extreme caution was taken to avoid overheating which would result in a non-symmetric glass end. The glass sphere used in the current study is obtained by melting a  $1.5 \pm 0.1$  mm diameter Pyrex rod under butane-oxygen flame until the surface tension of the melting Pyrex produces a spherical surface

with a diameter of 4.5 mm. The glass sphere prepared as such is molecularly smooth with a peak-to-valley distance less than 1.2 nm and is suitable for force measurements. The AFM image of the glass sphere surface is shown in **Fig. 6-2**. The capillary tube and the glass sphere were treated in freshly prepared piranha solutions (3 H<sub>2</sub>SO<sub>4</sub>:1 H<sub>2</sub>O<sub>2</sub>, by volume) at 80-90 °C for 30 min, rinsed thoroughly with Milli-Q water and blow-dried using ultra-pure nitrogen stream. The surfaces prepared in this manner were free of contamination and completely water wettable (i.e.,  $\theta = 0^\circ$ ). The sample chamber was cleaned in the anhydrous ethyl alcohol (Commercial Alcohols Inc.) under ultrasonication for half an hour, rinsed with de-ionized water and then blow-dried with ultrapure nitrogen. The bimorph beam was fastened on to the chamber wall and then the glass sphere was clamped at the free end of the bimorph under a dust-free laminar flow environment. The chamber was then filled with test solutions and placed on a three-dimensional translation stage. The capillary tube was filled with fresh air before being immersed into the solution. The system was then left for two hours to equilibrate the interfaces and to stabilize the bimorph signal before any measurement.

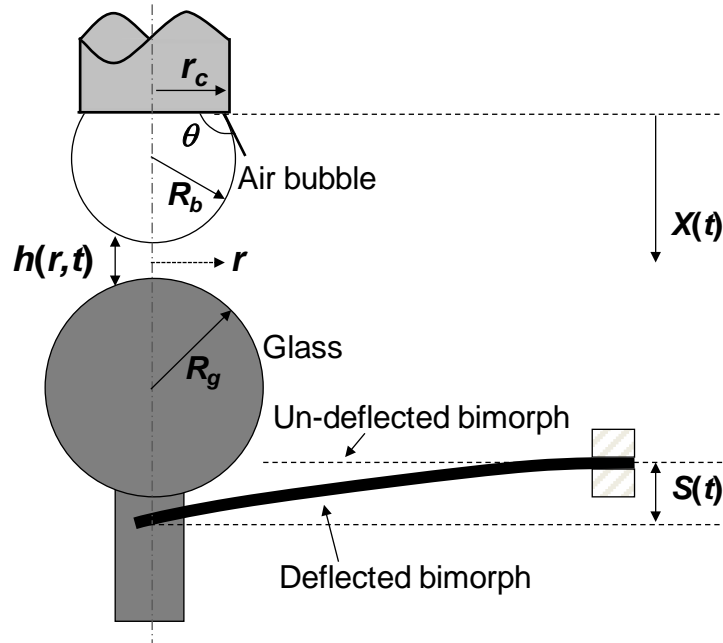


**Fig. 6-1** Schematic diagram of dynamic force measurement between an air bubble and a glass sphere, showing the key geometric configuration of the ITFDA:

separation distance between the surfaces of bubble and glass at a distance  $r$  away from the axial symmetry,  $h(r,t)$ ; inner radius of the glass tube,  $r_c$ ; angle between bubble contact and the glass tube end surface,  $\theta$ ; bubble radius of curvature,  $R_b$ ; the radius of glass sphere,  $R_g$ ; the glass tube displacement,  $X(t)$ ; and the deflection of the bimorph cantilever,  $S(t)$ .

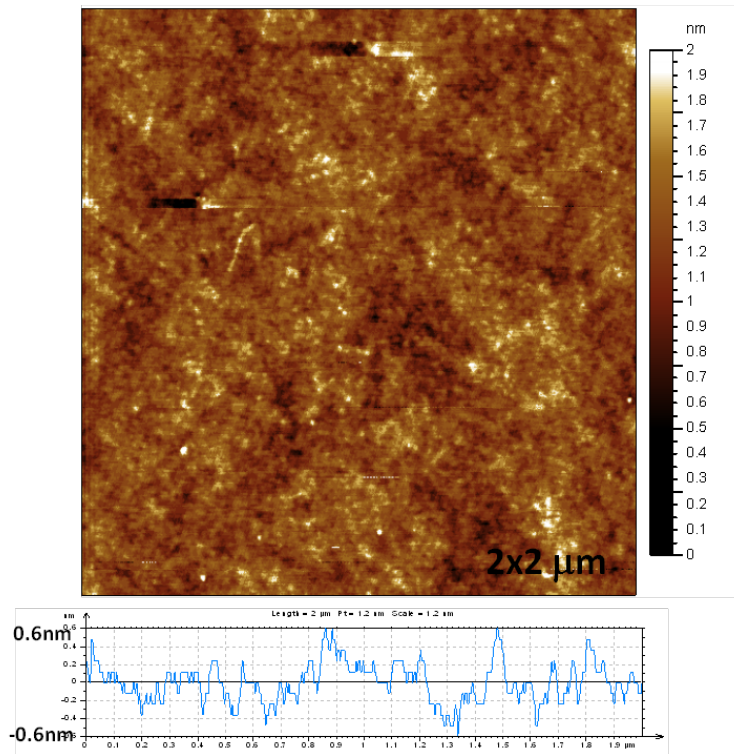


**Fig. 6-2** Contact mode AFM (Agilent Technologies, Inc., Chandler, AZ) images of clean glass surfaces in air. The lower figures show the corresponding cross-section topographic traces of the glass surface.

For force measurements, a fresh air bubble was generated at the end of glass tube. The bubble size as well as the gap between bubble and glass sphere was precisely controlled with the aid of two CCD cameras positioned perpendicular to each other near the chamber. These two cameras are also used to align the air bubble and the glass sphere to ensure the geometrical alignment is axis of symmetry. The air bubble was then driven by the speaker diaphragm through the glass tube towards or away from the lower glass sphere. In a typical force

measurement cycle as shown in **Fig. 6-3**, the glass tube drives the air bubble towards the lower glass sphere by increasing the distance  $X(t)$ , a process called “approach”. The voltage to the speaker is then reversed to move the air bubble away from the glass surface, which is called “retract” process. The time dependant voltage applied to the speaker and bimorph output are recorded simultaneously for the entire probing cycle with a video recording system. The displacement of glass tube,  $X(t)$ , is measured by a displacement sensor mounted on the speaker diaphragm with a sensitivity of 5  $\mu\text{m}$ . As shown in **Fig. 6-3(a)**, the measured  $X(t)$  (dot line) was fitted with a polynomial function to obtain a smooth curve (solid line). The instantaneous velocity  $dX(t)/dt$  was obtained by differentiating this polynomial function as shown in **Fig. 6-3(b)**. By changing the approach and retract time of the air bubble for a given displacement, different velocity profiles can be obtained. The typical velocities ranges reported in this chapter ranges from 33  $\mu\text{m/s}$  to 134  $\mu\text{m/s}$  to give a global bubble Reynolds number of 0.05 - 0.2. The values of instantaneous  $X(t)$  and  $dX(t)/dt$  were used in all data analysis and modeling. At least 10 measurements were conducted for each set of conditions. A single representative force profile was presented in this chapter (the signal was filtered with a cut-off frequency of 10 Hz for noise reduction and about 1% of recorded data was presented).

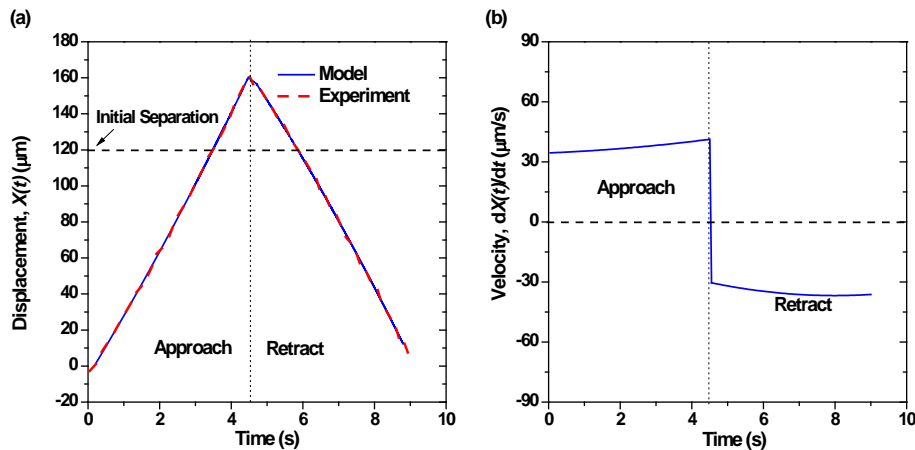


**Fig. 6-3** Time dependence of the glass tube displacement (a) and the actual glass tube velocity (b) in a measurement cycle with the setting  $V_a = -V_r = 33 \mu\text{m/s}$ . The solid line in (a) shows the polynomial fitting of glass tube displacement and the

corresponding velocity  $dX(t)/dt$  in (b). The initial apex separation distance between the air bubble and glass sphere surfaces,  $h(0,0)$ , was set at  $120\ \mu\text{m}$  as shown by the dotted line in (a). The approach part of the cycle corresponds to  $dX(t)/dt > 0$  and retract part to  $dX(t)/dt < 0$ . It is important to note that due to mechanical hysteresis of speaker diaphragm and heating of electric coil of the speaker, the approach and retract velocities are not perfectly constant for the designed duration.

The bimorph cantilever calibration constant is calibrated after each set of measurements by placing a small piece of platinum wire of known mass on the sample holder and recording the change in output voltage of the bimorph. Different wires are used to obtain the dependence of bimorph voltage on the weight applied to obtain the cantilever calibration constant. By this calibration process, the bimorph signal,  $V(t)$ , can be converted to the interaction force,  $F(t)$ , using the cantilever calibration constant. For the purpose of modeling, the detected  $V(t)$  needs to be converted to the deflection of bimorph,  $S(t)$ . The bimorph deflection,  $S(t)$ , can be obtained by analyzing the “constant compliance region” of the force curve where the glass sphere and glass tube are in contact, i.e.,  $X(t)$  equals to  $S(t)$ .  $V(t)$  is plotted as a function of  $X(t)$  and the slope of the profile in the constant compliance region is known as the bimorph materials constant. This calibration is similar to the calibration in AFM studies.<sup>15, 17</sup> The bimorph deflection,  $S(t)$ , as well as the bimorph spring constant,  $K$ , can then be calculated based on the bimorph materials constant and the cantilever calibration constant. The bimorph cantilever used in this study has a spring constant of 60 - 70 N/m. The initial separation between the bubble and the glass sphere,  $h(0,0)$ ; the radius curvature of bubble,  $R_b$ ; the radius of glass sphere,  $R_g$  as well as the angle between the air bubble and end surface of the glass tube,  $\theta$  (see **Fig. 6-1**) all can be determined from the recorded images using the image analysis program interfaced with LabVIEW 8.0.

The experimental parameters, either determined in this work or taken from literature are summarized in Table 6-1 and Table 6-2. The radii of bubble at the

end of the glass tube and the glass sphere on the bimorph have an undistorted curvature of  $730 \pm 5 \mu\text{m}$  and  $2200 \pm 50 \mu\text{m}$ , respectively. During the measurements, the initial separation between the bubble and the hydrophilic glass sphere was adjusted to  $120 \pm 10 \mu\text{m}$  with the aid of the CCD camera. The true value is obtained by image analysis with a resolution of  $6 \mu\text{m}$ . However, for the purpose of modeling this resolution is not sufficient. Therefore, the initial separation distance  $h(0,0)$  in the modeling is treated as the only adjustable parameter to fit the experimental data. The  $h(0,0)$  obtained as such ranges from  $120 \mu\text{m}$  to  $126 \mu\text{m}$ , which is in the tolerance range of the experimental error.

**Table 6-1 Value of key parameters used in this study, either measured or taken from literature.**<sup>18, 19</sup>

Parameters	Values
Radius of air bubble, $R_b$	$730 \pm 5 \mu\text{m}$
Radius of glass sphere, $R_g$	$2200 \pm 2 \mu\text{m}$
Angle between the air bubble and the end surface of glass tube, $\theta$	$132 \pm 5$ degree
Initial separation distance, $h(0,0)$	$123 \pm 3 \mu\text{m}$
Surface tension of KCl solution, $\gamma$	$70 \text{ mN/m}$
Bimorph cantilever spring constant	$64 \pm 4 \text{ N/m}$
Hamaker constant, $H$	$-8 \times 10^{-21} \text{ J}$

**Table 6-2 Zeta potential (mV) of air bubble and glass sphere in KCl solutions.**<sup>20</sup>

KCl (mM)	1	1	1	10	100
pH	2	5.6	10	5.6	5.6
Glass sphere	-5	-50	-55	-20	-5
Air bubble	-5	-30	-35	-10	-5

### 6.3 Formulation of the Problem (model)

The SRYL model, which provides quantitative information on the dynamic force and film profile, has been successfully applied to predict the interactions between deformable droplets and bubbles measured by AFM and surface force

apparatus.<sup>5, 21, 22</sup> To fully understand the dynamic interaction force recorded by ITFDA, the SRYL model was applied to analyze the system. In the ITFDA experiments, similar to the AFM the film thickness at the interaction zone is small compared to the radial dimension of the film. Therefore the liquid flow in the film can be considered as Stokes flow, where the well known Stokes–Reynolds thin film drainage model can be applied. This model describes the space–time evolution of the film thickness profile between two interacting interfaces.<sup>23-25</sup> For a film with axial symmetry, the governing equation in cylindrical coordinate system for the film thickness,  $h(r,t)$ , is given by:

$$\frac{dh(r,t)}{dt} = \frac{1}{12\mu} \frac{1}{r} \frac{\partial}{\partial r} \left[ rh^3(r,t) \left( \frac{\partial p(r,t)}{\partial r} \right) \right] \quad \text{Eqn. 6-1}$$

where  $\mu$  is the shear viscosity of the aqueous film (assumed Newtonian) and  $p(r,t)$  is the excess hydrodynamic pressure in the film in reference to the bulk pressure. Implicit in this equation is the assumption of no-slip or immobile boundary condition for all the interfaces. Theoretical predictions with the no-slip boundary condition offer the best agreement between experimental force profiles determined using the ITFDA and theoretical predictions involving deformable surfaces. Deformation of the liquid/air interface is given by the equilibrium Young-Laplace equation. Young-Laplace equation comes from the minimization of the drop surface energy in the presence of external forces, and is given by:<sup>25-27</sup>

$$p(r,t) + \Pi(r,t) = \frac{2\gamma}{R_0} - \frac{\gamma}{r} \frac{\partial}{\partial r} \left( r \frac{\partial h(r,t)}{\partial r} \right) \quad \text{Eqn. 6-2}$$

where  $\gamma$  is the interfacial tension of the air/liquid interface,  $R_0$  is the equivalent unperturbed radius of curvature of  $R_b$  and  $R_g$ , defined as  $R_0 = 2\left(\frac{1}{R_g} + \frac{1}{R_b}\right)^{-1}$ . The Stokes-Reynolds-Young-Laplace (SRYL) equations couple the film thickness  $h(r,t)$  with the hydrodynamic pressure  $p(r,t)$  and the disjoining pressure  $\Pi(r,t)$ . In this model only van der Waals forces and electrical double layer force are considered to calculate the disjoining pressure,  $\Pi(r,t)$ . Van der Waals forces between an air bubble and a hydrophilic glass sphere are calculated using Lifshitz theory<sup>19</sup> and the electric double layer force is calculated by a numerical solution

of the nonlinear Poisson-Boltzmann equation using the algorithm of Chan et al.<sup>28</sup>,  
<sup>29</sup> The SRYL equations are solved numerically in a suitable radial domain  $0 < r < r_{max}$ , where  $r_{max}$  is the outer boundary condition. The surfaces at  $r > r_{max}$  are sufficiently far apart that the effects of disjoining pressure in this region can be neglected. For  $0 < r < r_{max}$ , the initial undistorted film thickness  $h(r,0)$  is given by  $h(r,0) = h_0 + \frac{r^2}{R_0}$ . Due to axial symmetry, the boundary conditions at  $r = 0$  are  $\frac{\partial h}{\partial r} = 0$  and  $\frac{\partial p}{\partial r} = 0$ . The known limiting form of pressure  $p \approx r^{-4}$  in the form of  $\frac{\partial p}{\partial r} + \frac{4}{r}p = 0$  is imposed at the outer boundary,  $r = r_{max}$ .

The instantaneous force exerted on the drop,  $F(t)$ , which has the contribution from hydrodynamic pressure  $p(r,t)$  and disjoining pressure  $\Pi(r,t)$  is calculated from the following integral:

$$F(t) = 2\pi \int_0^{\infty} [p(r,t) + \Pi(r,t)] r dr \quad \text{Eqn. 6-3}$$

At positions outside the interaction zone, both  $p$  and  $\Pi$  are negligibly small. The final boundary condition at  $r = r_{max}$ <sup>26</sup>, which takes into account the drop deformation during the approach is:

$$\frac{\partial h}{\partial t} + \alpha \frac{\partial G}{\partial t} = V \quad \text{Eqn. 6-4}$$

where  $V$  is the glass tube velocity which is set the same for both approach and retract processes.

The  $\alpha$  in **Eqn. 6-4**, for two deformable droplets, is given by

$$\alpha = \log\left(\frac{r_{max}}{2R_0}\right) + B(\theta) - \frac{2\pi\gamma}{K} \quad \text{Eqn. 6-5}$$

For the fixed three phase contact line,

$$B(\theta) = 1 + \frac{1}{2} \log\left(\frac{1 + \cos\theta}{1 - \cos\theta}\right) \quad \text{Eqn. 6-6}$$

where  $\theta$  is the angle between the end surface of the glass tube and bubble surface as shown in **Fig. 6-1**, and  $K$  is the spring constant of the bimorph cantilever. The

quantity  $G$  in **Eqn. 6-4** is related to the instantaneous force,  $F(t)$  between the two surfaces by:

$$G = \frac{F(t)}{2\pi\gamma} \quad \text{Eqn. 6-7}$$

Since the film thickness can be as low as dozens of nm while the air bubble is in the range of 1 mm, appropriate scaling of relevant governing equations is necessary for numerical robustness. To solve the problem, following scales for physical variables are used: <sup>30</sup>

$$h_c = R_0 Ca^{\frac{1}{2}}, r_c = R_0 Ca^{\frac{1}{4}}, p_c = \frac{\gamma}{R_0}, t_c = \frac{\mu Ca^{\frac{1}{2}}}{p_c} \quad \text{Eqn. 6-8}$$

where  $Ca = \frac{\mu V}{\gamma}$  is the capillary number (the ratio of viscous forces to surface tension forces) to produce the non-dimensional form of equations. **Eqn. 6-1** and **Eqn. 6-2** or SRYL equations together with **Eqns. 3 - 6** constitute a differential algebraic equation system. The equations can be solved numerically to find the temporal evolution of the drainage, the deformation (profile) of air/liquid interface (thin films), and the time dependent forces between interacting air bubble and glass sphere. <sup>25</sup>

## 6.4 Results

The effect of different parameters (e.g., pH, salt concentrations, surface tension, viscosity of solutions and air bubble drive velocity) on the interaction forces between an air bubble and a hydrophilic glass sphere during approach-retract measurement cycle was studied. In the ITFDA measurements, the maximum glass tube displacement,  $X_{max}$ , was set at 150  $\mu\text{m}$ , unless otherwise specified. The exact value of  $X(t)$  was obtained from displacement sensor, and the  $X_{max}$  is measured to be  $150 \pm 5 \mu\text{m}$ . Note that with the initial separation of  $120 \pm 10 \mu\text{m}$ , the bubble will be pushed well beyond the contact point if the bubble does not deform when the glass tube displacement is larger than this initial separation. In other words, the bubble deforms during the interaction with the lower glass sphere. The measured force was compared with the force calculated by solving SRYL model using the parameters obtained in the experiments. By solving the

SRYL model, the profile of the draining liquid film as well as the film pressure distribution can be obtained to fully understand the hydrodynamic interactions. In this study, the film thickness of aqueous film is considered at the centre of the drainage film,  $h(0,t)$ .

#### **6.4.1 Bubble-glass interactions in KCl solutions**

The interaction forces between an air bubble and a hydrophilic glass sphere at bubble drive velocity of 33  $\mu\text{m/s}$  in KCl solutions were measured using the ITFDA. The results were compared with the predictions from the SRYL model. **Fig. 6-4** (a), (b) and (c) show the interaction force profiles between bubble and glass sphere as a function of glass tube displacement,  $X(t)$  in 1 mM KCl solutions of pH 5.6, 10 and 2, respectively. **Fig. 6-4** (d) shows the interaction force profile in 100 mM KCl solutions of pH 5.6. The point where the bubble starts to move towards the lower glass sphere is set as  $X(t) = 0$ .  $X(t)$  increases with the approach of the bubble towards the lower glass sphere, while the separation distance between the two surfaces decreases. Once  $X(t)$  reaches a maximum, it reduces with the retraction of bubble from the glass sphere. As can be seen from **Fig. 6-4**, fairly good agreement is obtained between the experimentally measured and the theoretically calculated interaction forces, demonstrating that the SRYL model can be applied with confidence to the current system with bubble drive velocity of 33  $\mu\text{m/s}$ . We can therefore use the model to infer information about the dynamic behaviour of the film during the interaction that is otherwise not accessible by current experimental techniques.

The film thickness profile  $h(r,t)$  at different stages of air bubble-glass sphere interactions illustrated in **Fig. 6-4(a)** is shown in **Fig. 6-5**. As can be seen from the film thickness profiles  $h(r,t)$  in **Fig. 6-5**, the intervening liquid film deforms during the interaction. The deformation of the liquid film changes the area of interaction and hence the total force. It is therefore important to compare the film pressure,  $p_{\text{film}}$ , instead of total force to account for the effect of film deformation. The pressure of the intervening liquid film, at different stages of interactions marked in **Fig. 6-4(a)** is obtained directly from the simulation and the results are

shown in **Fig. 6-5**. Two components of this film pressure, i.e., hydrodynamic pressure  $p(r,t)$  and the disjoining pressure  $\Pi(r,t)$  are also shown in **Fig. 6-5**. The pressures reported in this chapter are normalized with the scaling parameter,  $p_c$ , given in **Eqn. 6-8**. Therefore, the pressure drop  $\Delta p$  across the liquid/air interface becomes:

$$\Delta p(r,t) = p_c \left( 2 - p_{film}^* \right) = p_c \left[ 2 - (p^*(r,t) + \Pi^*(r,t)) \right] \quad \text{Eqn. 6-9}$$

As can be seen from **Eqn. 6-9**, when  $p_{film}^* < 2$ , the intervening liquid film will remain a concave shape where the film thickness at the center is smaller than the rest of the film due to a positive  $\Delta p$ . When  $p_{film}^* = 2$ , the film flattens with the same film thickness across the drainage film. When  $p_{film}^* > 2$ , dimple forms where the film thickness at the center is larger than at the rim of the film,  $h(rim,t)$ , i.e.,  $h(rim,t) < h(0,t)$  due to a negative  $\Delta p$ , i.e., a convex liquid/air interface at the center.

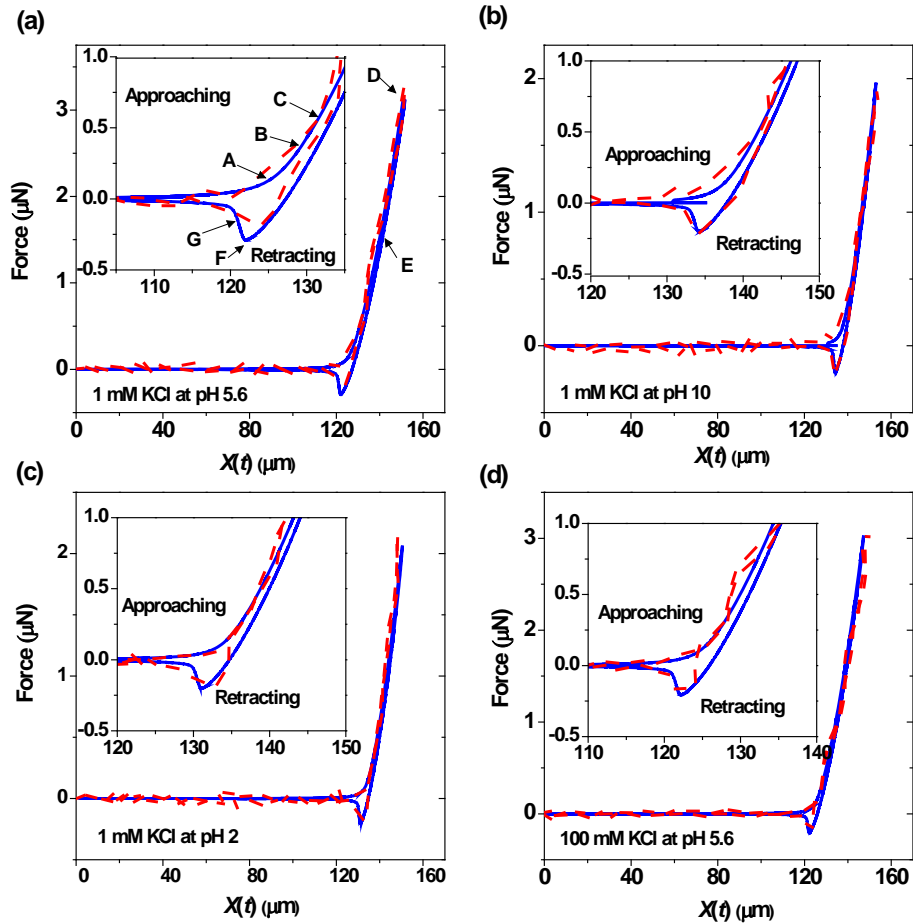


**Fig. 6-4** Comparison between the experimentally measured (dash lines) and theoretically calculated (solid lines) interaction forces as a function of  $\Delta X$  in one measurement cycle, between an air bubble and a hydrophilic glass sphere in (a) 1 mM KCl solution of pH 5.6; (b) 1 mM KCl solution of pH 10; (c) 1 mM KCl solution of pH 2 and (d) 100 mM KCl solution of pH 5.6. Insets show the force profiles while the two surfaces are in close separation distance. In these measurements, the bubble drive velocity  $V$  is  $33 \mu\text{m/s}$ , radii of air bubble and glass sphere are  $730 \pm 5 \mu\text{m}$  and  $2200 \pm 50 \mu\text{m}$ , respectively. These parameters are used in the SRYL model to calculate the interaction force profiles.

As shown in **Fig. 6-4(a)**, at small values of  $X(t)$  (up to point A in the inset of **Fig. 6-4(a)**), the force between the two surfaces remained small. **Fig. 6-5(a)** shows that during the approach with the increasing  $X(t)$  from A to D, the film pressure increases. When  $p_{\text{film}}^*(0,t) = 2$  at B, as illustrated in the  $p_{\text{film}}^*$  profile B in **Fig. 6-5(a)**, the intervening liquid film starts to flatten at the center of the film,  $h(r,t)$  profile B in **Fig. 6-5(a)**. When  $p_{\text{film}}^*$  is larger than 2, the formation of dimple is visible on profile C in **Fig. 6-5(a)**. With further approach of the air bubble towards the glass sphere from C to D, both the magnitude and the radial extent of  $p_{\text{film}}^*$  increase significantly, resulting in a larger dimple. As shown by  $h(r,t)$  profile D in **Fig. 6-5(a)**, the radius of the dimple increases from  $25 \mu\text{m}$  at C to  $75 \mu\text{m}$  at the end of the approach. It should be noted that once  $p_{\text{film}}^*$  reaches 2, the magnitude of  $p_{\text{film}}^*$  shows little increase with further approach. Hence, the increase of the measured force from point C to D as shown in **Fig. 6-4(a)** is not only due to increasing magnitude of  $p_{\text{film}}^*$ , but also, and perhaps more importantly, to increasing radial extent of  $p_{\text{film}}^*$ , which leads to a larger dimple size and hence contact area.

After D, the bubble is retracted away from the glass sphere. At the beginning of the retracting, from  $h(r,t)$  profiles D to E in **Fig. 6-5(b)**, the film thickness decreases rapidly at the rim of the drainage film ( $60 \mu\text{m} < r < 80 \mu\text{m}$ ) while the thickness at the center of the film ( $r < 50 \mu\text{m}$ ) remains the same. The change of the film thickness can be explained by investigating the variation of  $p_{\text{film}}^*(r,t)$

during the process. As shown in **Fig. 6-5(b)** from  $p^*_{\text{film}}(r,t)$  profiles D to E,  $p^*_{\text{film}}(r,t)$  at the edge of the film ( $60 \mu\text{m} < r < 80 \mu\text{m}$ ) decreases rapidly from positive values to negative values. This negative  $p^*_{\text{film}}(r,t)$  pulls the bubble towards the glass sphere, thus reducing the film thickness at the edge of the film. Meanwhile,  $p^*_{\text{film}}(r,t)$  at the center of the film ( $r < 50 \mu\text{m}$ ) remains almost the same during this process and that is why the film thickness profile in this region shows little change.

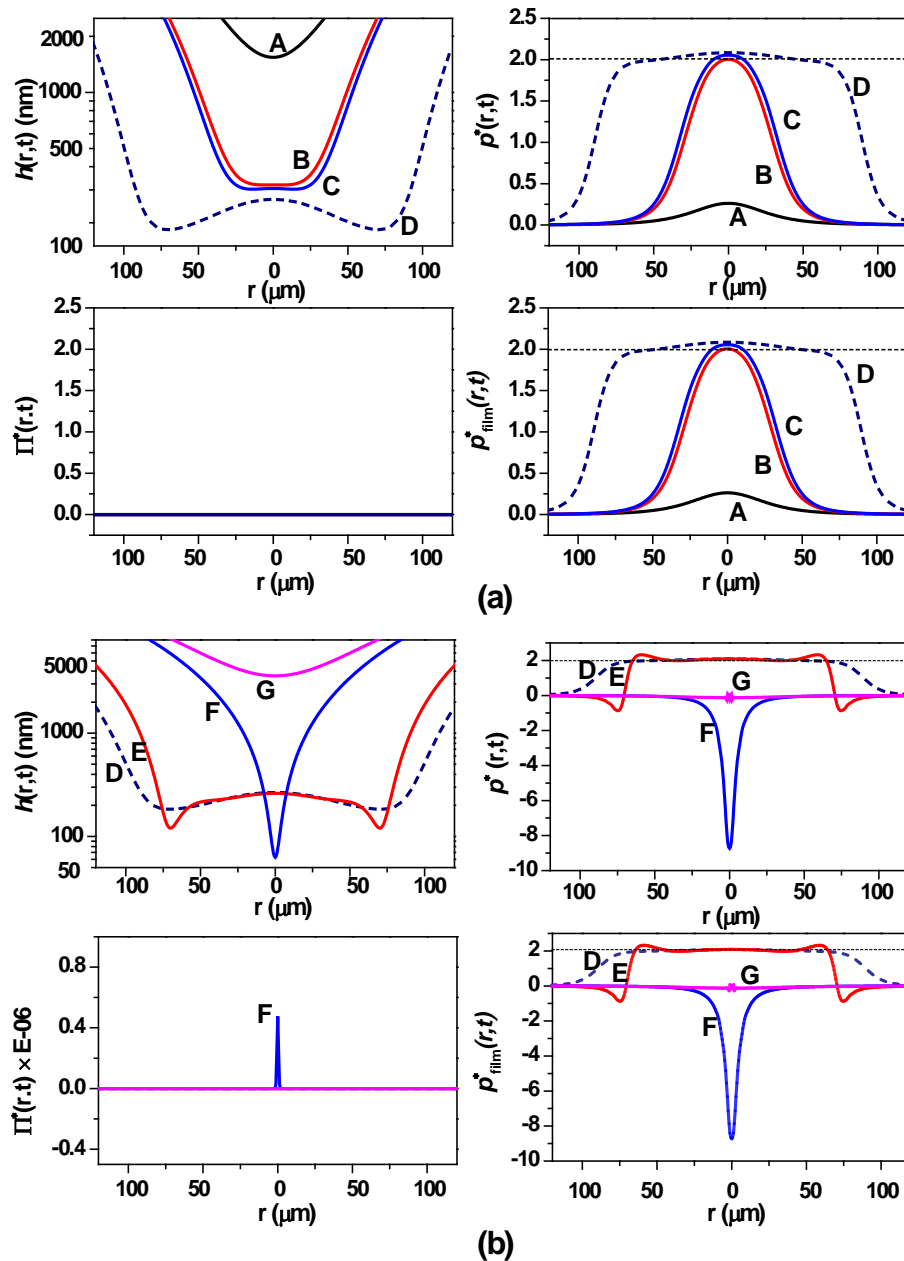


**Fig. 6-5** Variations of film thickness  $h(r,t)$ , hydrodynamic pressure  $p^*(r,t)$ , disjoining pressure  $\Pi^*(r,t)$  and film pressure  $p_{\text{film}}^*(r,t)$  in one measurement cycle between an air bubble and a hydrophilic glass sphere in 1 mM KCl solutions of pH 5.6: (a) approach and (b) retract branches. The glass tube displacement  $X(t)$  (defined in **Fig. 6-4(a)**) for the profiles during approach is: A, 125.3  $\mu\text{m}$ ; B, 129  $\mu\text{m}$ ; C, 131.2  $\mu\text{m}$  and D, 151  $\mu\text{m}$ ; and during retract is: D, 151  $\mu\text{m}$ ; E, 141  $\mu\text{m}$ ; F, 123  $\mu\text{m}$  and G, 121  $\mu\text{m}$ . The pressures are normalized with the scaling parameters,  $p_c$ , given in **Eqn. 6-8**. The parameters obtained from **Fig. 6-4(a)** are used in the calculation: bubble drive velocity  $V = 33 \mu\text{m/s}$ ; initial separation distance  $h(0,0) = 126 \mu\text{m}$ ; radii of air bubble and glass sphere are 733  $\mu\text{m}$  and 2211  $\mu\text{m}$ , respectively.

The radial extent of  $p_{\text{film}}^*(r,t)$  reduces dramatically with further retraction of the bubble from the glass sphere. It reduces from 75  $\mu\text{m}$  at  $p_{\text{film}}^*(r,t)$  profile E to about 25  $\mu\text{m}$  at profile F in **Fig. 6-5(b)**. At the same time,  $p_{\text{film}}^*(r,t)$  at the center region of the film, i.e.,  $r < 25 \mu\text{m}$ , decreases sharply from positive values to negative values in the film. This negative  $p_{\text{film}}^*(r,t)$  with large magnitude dramatically reduces the film thickness at the axial symmetry from 270 nm to 70 nm as shown in **Fig. 6-5(b)**, generating a retraction minimum in the force curve as illustrated at point F in **Fig. 6-4(a)**. This retraction minimum is purely hydrodynamic effect. When the bubble retracts away from the glass sphere, the water has to be drawn in to fill the film between the separating surfaces, leading to a negative hydrodynamic pressure as illustrated in  $p^*(r,t)$  profile F in **Fig. 6-5(b)**. A similar observation was reported by Dagastine et al.<sup>22</sup> while measuring the forces between two decane droplets in aqueous solutions using the AFM. Once the force reached the retraction minimum,  $p_{\text{film}}^*(r,t)$  increased rapidly to zero across the film as shown in profile G.

As can be noted from **Fig. 6-5**, the largest radial extent of the intervening liquid film between the air bubble and the glass sphere is about 75  $\mu\text{m}$  or 10 % of the bubble radius. Thus the extent of the bubble deformation during the interaction remains small compared with the bubble size. Therefore, **Eqn. 6-4** to

**Eqn. 6-7** used to describe the boundary conditions as well as the assumption of small deformation in the region outside the interaction zone are reasonable.

**Fig. 6-4** also shows that with the change of the solution pH from 5.6 (**Fig. 6-4(a)**) to either pH 10 (**Fig. 6-4(b)**) or pH 2 (**Fig. 6-4(c)**), or with the increase of KCl concentration from 1 mM to 100 mM (**Fig. 6-4(d)**), the force profiles are similar to each other, showing a negligible effect of water chemistry (i.e., solution pH and KCl concentration) on the measured force profiles at the bubble drive velocity of 33  $\mu\text{m/s}$ . This observation is not surprising, as the minimum film thickness reached during the measurement cycle is about 70 nm as shown in **Fig. 6-5**. At the separation distance larger than 70 nm, the disjoining pressure  $\Pi(r,t)$  remains negligible compared with the hydrodynamic pressure  $p(r,t)$ . In other words,  $p(r,t)$  dominates  $p_{\text{film}}(r,t)$  with the bubble drive velocity of 33  $\mu\text{m/s}$ .

#### **6.4.2 Effect of surface tension**

The effect of surface tension on the interaction between an air bubble and the hydrophilic glass sphere was studied by measuring and modelling the interaction forces in 1 mM KCl solutions and in ethanol. In this set of experiments, the maximum glass tube displacement was increased to 160  $\mu\text{m}$  while the initial separation distance and the bubble size remained the same. The results are shown in **Fig. 6-6** (a) and (b). Again, good agreement between the measured and predicted force profile is achieved. The results in **Fig. 6-6** (a) and (b) indicate a dramatic decrease in the maximum interaction force between an air bubble and a hydrophilic glass sphere from 6.2 to 1.6  $\mu\text{N}$  with decreasing surface tension from 70.8 to 22.4 mN/m. In this section, the film pressure at the axis of symmetry, i.e.,  $p^*_{\text{film}}(0,t)$ , is obtained directly from the simulation and plotted as a function of film thickness. **Fig. 6-7** shows that  $p^*_{\text{film}}(0,t)$  at the same film thickness increases with decreasing liquid surface tension from 70.8 mN/m in 1 mM KCl solution to 22.4 mN/m in ethanol. Furthermore, the film thickness at the end of approaching is larger for ethanol than for 1 mM KCl solution.

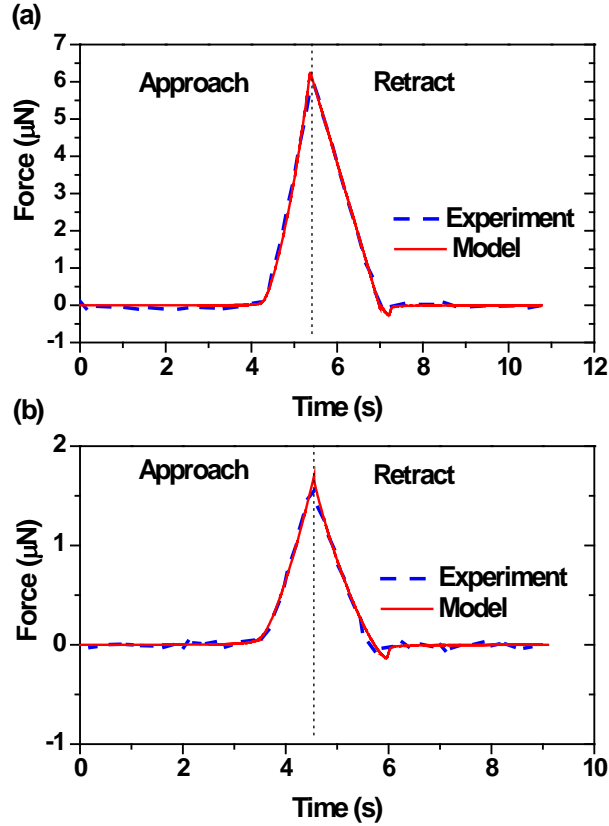


**Fig. 6-6** Comparison of the measured and predicted force between an air bubble and a hydrophilic glass sphere as a function of measurement time over a force measurement cycle in 1 mM KCl solutions (a) and ethanol (b) with the bubble drive velocity of 33  $\mu\text{m/s}$ . The maximum glass tube displacement was 160  $\mu\text{m}$ . The surface tensions of the 1 mM KCl solutions and ethanol were measured to be 70.8 mN/m and 22.4 mN/m, respectively. The parameters obtained from individual measurement were used in the SRYL model to calculate the interaction forces.

Under the same dynamic conditions, i.e., the same bubble drive velocity and bubble size in solutions with similar viscosities, the hydrodynamic force on the air bubble in ethanol and in 1 mM KCl solution should be close to each other. However, normalized by the scaling parameter,  $p_c = \gamma/R_0$ ,  $p^*_{\text{film}}(0,t)$  for ethanol is much larger than for 1 mM KCl solution due to a lower surface tension as shown in **Fig. 6-7**. With the approach of air bubble towards the glass sphere,  $p^*_{\text{film}}(0,t)$  increases with reducing film thickness. The increased  $p^*_{\text{film}}(0,t)$  in turn reduces the

bubble curvature at the apex. At a critical film thickness, when  $p^*_{\text{film}}(0,t)$  reaches value 2, the intervening liquid film starts to flatten in such a way that pressure drop across the liquid/air interface becomes zero. For example as illustrated in **Fig. 6-7**, the critical film thicknesses for the 1 mM KCl solution and ethanol are 320 nm and 570 nm, respectively. According to Young's equation:  $\Delta p = \frac{2\gamma_{lv}}{R_0}$ , the reduction of the surface tension reduces the pressure across the liquid/air interface. Therefore, the air bubble in the ethanol is easier to deform under a given pressure/force. Consequently,  $p^*_{\text{film}}(0,t)$  reaches a value 2 at a larger separation distance in ethanol than in 1 mM KCl aqueous solutions, corresponding to a critical film thickness increase from 320 nm to 570 nm when the surface tension decreases from 70.8 mN/m to 22.4 mN/m. With the same initial separation distance and maximum glass tube displacement, the easier deformation of the air bubble at a larger separation distance makes the film thickness at the end of the approach cycle to increase from 277 nm to 475 nm as illustrated in **Fig. 6-7** and **Fig. 6-8**.

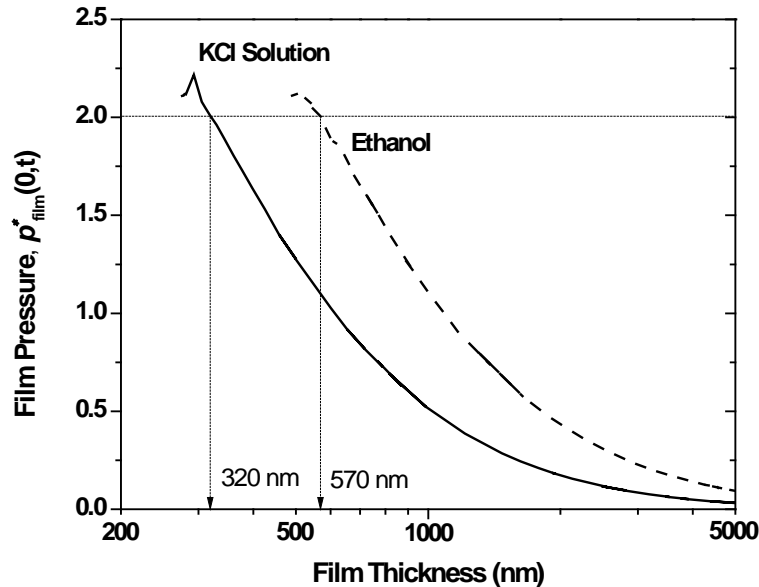


**Fig. 6-7** Film pressure  $p^*_{\text{film}}(0,t)$  of an air bubble approaching a hydrophilic glass sphere as a function of film thickness in liquid of 1 mM KCl and ethanol with bubble drive velocity of 33  $\mu\text{m/s}$ . The film pressure is normalized by the scaling parameters,  $p_c$ , given in **Eqn. 6-8**.

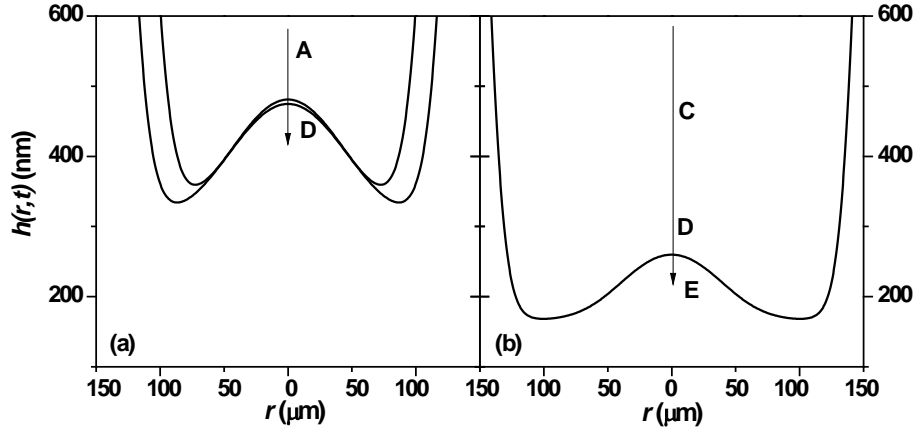


**Fig. 6-8** Comparison of the film thickness profile  $h(r,t)$  during the approaching of an air bubble towards the glass sphere in liquid of ethanol (a) and 1 mM KCl solutions (b) with bubble drive velocity of  $33 \mu\text{m/s}$ . Profiles A-C are taken at the film thickness of 567, 522 and 482 nm, respectively; profile D in (b) is taken at the film thickness of 320 nm and profile D in (a) and profile E in (b) show the film profiles at the end of the approaching.

With further reducing film thickness, the formation of dimple is expected when  $p^*_{\text{film}}(0,t)$  is larger than 2. As shown in **Fig. 6-8(a)**, dimple forms at separation distance smaller than 570 nm for ethanol and 320 nm for 1 mM KCl solution. The dimple size increases with decreasing separation distance. For example, the radii of the dimple at the end of approach cycle in ethanol (profile D in **Fig. 6-8(a)**) and 1 mM KCl solution (profile E in **Fig. 6-8(b)**) increase from small values to 90 and 100  $\mu\text{m}$ , respectively. As can be seen in **Fig. 6-7**,  $p^*_{\text{film}}(0,t)$  shows a negligible increase once it reaches 2, and even reduces with a further reduction in separation distance. This interesting observation indicates the reduction of bubble curvature at the center of the dimple/film at the closest separation distance. The increase in radial extent of the film drainage resistance and the dimple size increase the total force as the bubble approaching the glass sphere, which was shown in **Fig. 6-6**. Though the dimple size and the film drainage resistance at the end of the approach cycle is similar in 1 mM KCl solutions and in ethanol, the measured force is smaller in ethanol than in 1 mM KCl solution due to a smaller interfacial tension.

### 6.4.3 Effect of viscosity

The interactions between an air bubble and the glass sphere were also measured in silicon oil to study the effect of liquid viscosity on the interaction force. The measured and predicted interaction forces are shown in **Fig. 6-9(b)**. As can be seen from **Fig. 6-9(a)** and (b), the interaction force during the retract cycle rapidly became attractive and the magnitude of the attractive force (retraction minimum) became larger in silicon oil, with the retraction minimum increased from 0.2  $\mu\text{N}$  in ethanol to 0.6  $\mu\text{N}$  in silicon oil. Since all the other parameters were the same, this change in the retraction minimum is purely due to the hydrodynamic effect.<sup>31</sup> It is evident that the increasing liquid viscosity leads to a higher hydrodynamic repulsive force during approach cycle and a larger retraction minimum during the retraction. As shown in **Fig. 6-10**, at the same separation distance the film drainage resistance  $p^*_{\text{film}}(0,t)$  increases with increasing the liquid viscosity from 1 mPa s in ethanol to 55 mPa s in silicon oil. The hydrodynamic pressure  $p^*(r,t)$  between the air bubble and the glass sphere at the same separation distance is higher in silicon oil than in ethanol due to its higher viscosity. Therefore an increase in  $p^*_{\text{film}}$  is not unexpected.

The increasing  $p^*_{\text{film}}(0,t)$  in silicon oil makes the bubble deform at a larger separation distance. Compared with the film thickness in ethanol (**Fig. 6-11(b)**), a reduction in curvature of the liquid film can be observed in profiles A-C in **Fig. 6-11(a)** for silicon oil, indicating the presence of bubble deformation at separation distance larger than 6000 nm. The deformation of air bubble at larger separation distance increases the film thickness at the end of the approach. As shown in **Fig. 6-10**, the film thickness at the end of the approach cycle increases from 475 nm in ethanol to 5250 nm in silicon oil. Moreover,  $p^*_{\text{film}}(0,t)$  at the end of approaching in silicon oil is less than 2, indicating the absence of dimple film during the interaction. As shown in **Fig. 6-11(a)**, the intervening liquid film retains concave shape during the entire approach process.

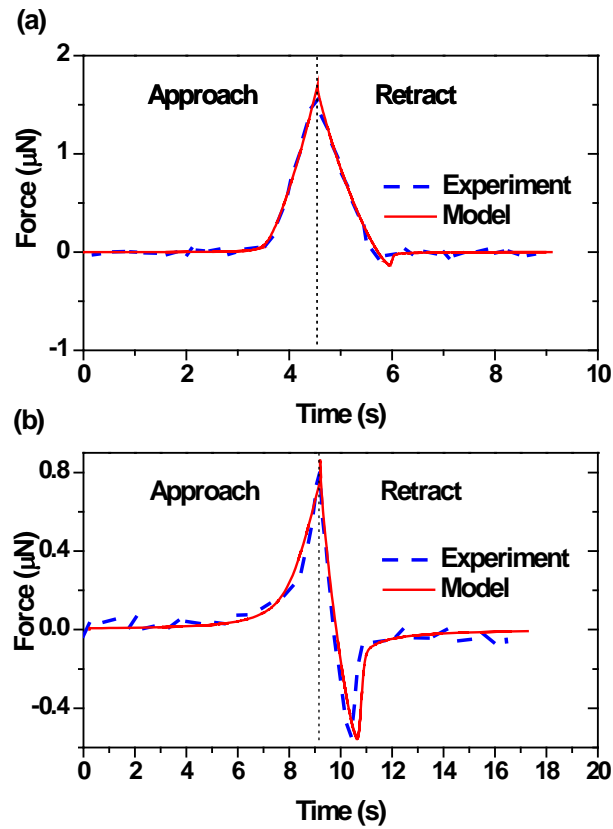


**Fig. 6-9** Comparison of the measured and predicted force between an air bubble and a hydrophilic glass sphere as a function of measurement time over a force measurement cycle in ethanol (a) and silicon oil (b) with the bubble drive velocity of  $33 \mu\text{m/s}$ . The maximum glass tube displacement was  $160 \mu\text{m}$ . The viscosities of the ethanol and silicon oil are  $1 \text{ mPa s}$  and  $55.4 \text{ mPa s}$ , respectively. The parameters obtained from individual measurement were used in the SRYL model to calculate the interaction forces.

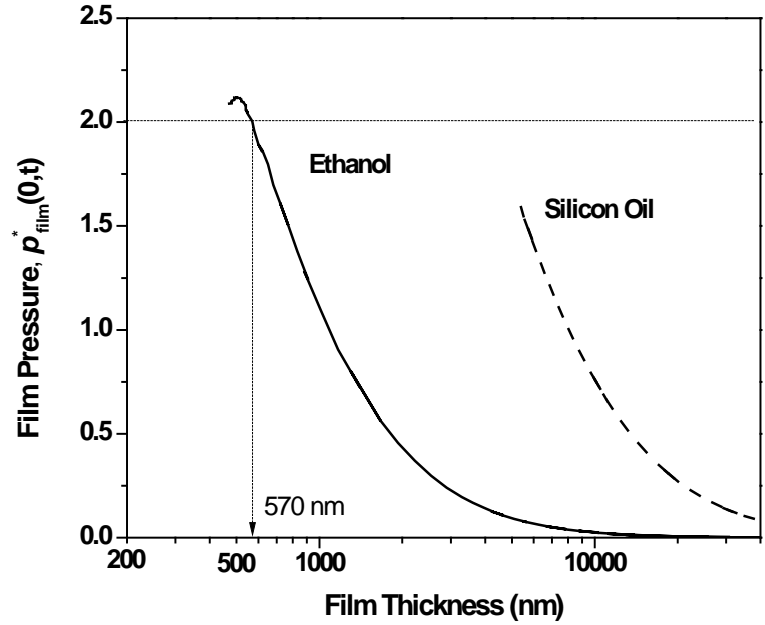


**Fig. 6-10** Film pressure  $p_{\text{film}}(0,t)$  of an air bubble approaching a hydrophilic glass sphere as a function of film thickness in liquid of ethanol and silicon oil with bubble drive velocity of  $33 \mu\text{m/s}$ .

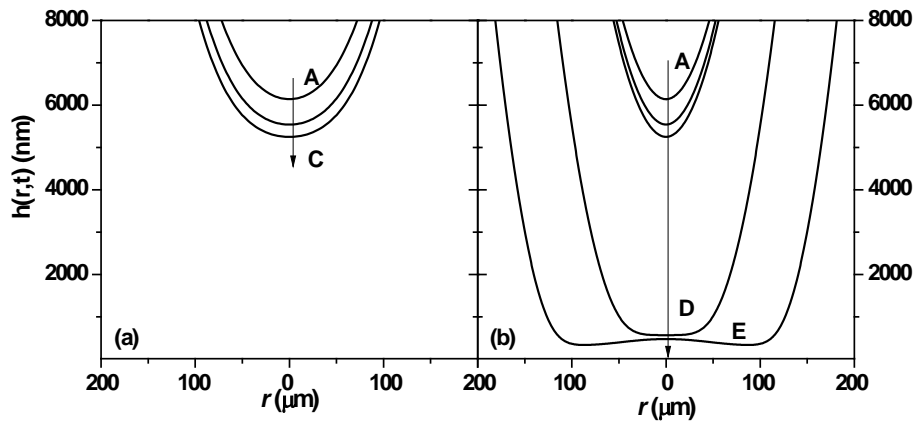


**Fig. 6-11** Comparison of the film thickness profile  $h(r,t)$  during the approaching of an air bubble towards a glass sphere in liquid of silicon oil (a) and ethanol (b) with bubble drive velocity of  $33 \mu\text{m/s}$ . Profiles A to C are taken at the film thickness of 6140, 5543 and 5250, respectively and profiles D and E in (b) show the film profiles at film thickness of 567 and 475 nm, respectively.

#### 6.4.4 Effect of bubble drive velocity

The effect of bubble drive velocity on the interaction forces between an air bubble and a hydrophilic glass sphere was studied in 1 mM KCl solutions. **Fig. 6-12** shows a good agreement between the measured (by ITFDA) and predicted (by SRYL) interaction force profiles for both approach and retract processes with bubble drive velocity of 33 and 134  $\mu\text{m/s}$ . In this case, the approach-retract interaction between the air bubble and the glass sphere is characterized by the bubble Reynolds number ( $Re = 2\rho RV/\mu$ ) of 0.2, where bubble radius and drive velocity are 730  $\mu\text{m}$  and 134  $\mu\text{m/s}$ , respectively. However, the film drainage process is characterized by film Reynolds number  $Re_f = \frac{\rho h V_f}{\mu} \ll 1$ , where  $h$  ( $\ll R_0$ ) is the characteristic film thickness and  $V_f$  is the characteristic film thinning velocity.<sup>32</sup> The small film Reynolds number allows quantitative analysis of the drainage liquid film using a lubrication theory. Consequently the evolution of the intervening liquid film,  $h(r,t)$  can be described using SRYL model. The observed good agreement demonstrates for the first time that the SRYL model can be applied with confidence to a high bubble drive velocity (i.e.,  $V = 134 \mu\text{m/s}$ ).

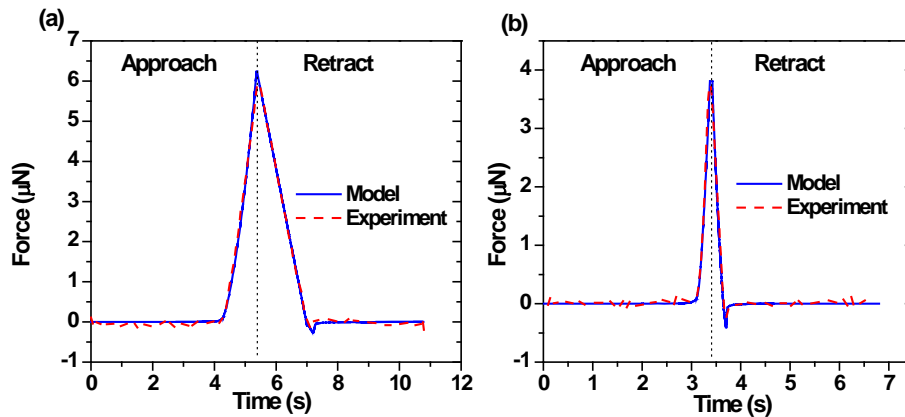


**Fig. 6-12** Comparison of measured and modeled interaction force between an air bubble and a hydrophilic glass sphere in 1 mM KCl solutions at pH 5.6 as a function of measurement time in a force measurement cycle with bubble drive velocity of (a) 33  $\mu\text{m/s}$  and (b) 134  $\mu\text{m/s}$ .

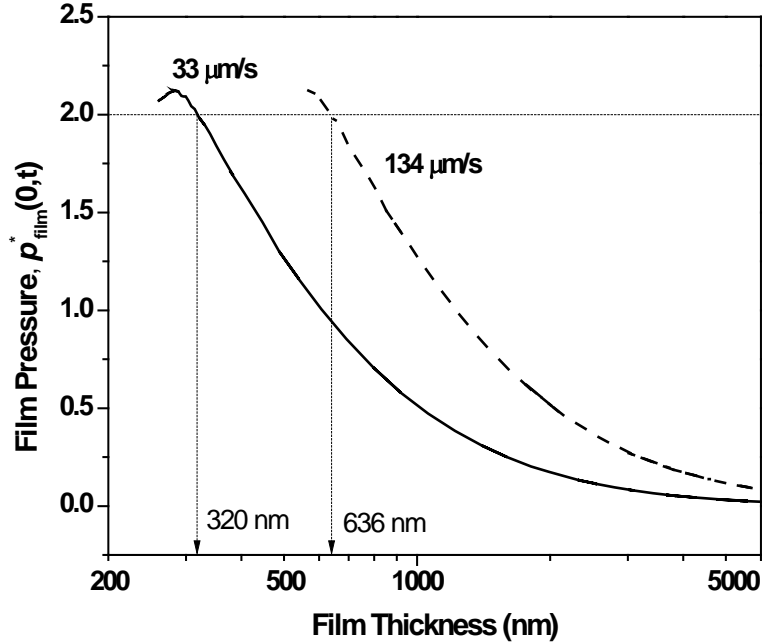


**Fig. 6-13** Film pressure  $p^*_{\text{film}}(0,t)$  of an air bubble approaching a hydrophilic glass sphere as a function of film thickness in 1 mM KCl solutions at pH 5.6 with bubble drive velocity of 33 and 134  $\mu\text{m/s}$ .

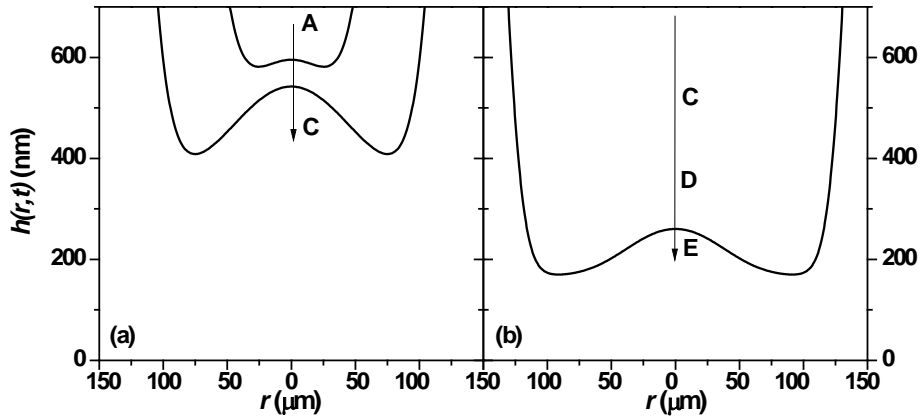


**Fig. 6-14** Comparison of the film thickness profile  $h(r,t)$  during the approaching of an air bubble towards a glass sphere in 1 mM KCl solutions with bubble drive velocity of (a) 134  $\mu\text{m/s}$  and (b) 33  $\mu\text{m/s}$ . Profiles A to C are taken at the film thickness of 635, 595 and 544 nm, respectively. Profiles D and E in (b) are taken at the film thickness of 322 nm and 274 nm, respectively.

Similarly, the film drainage resistance at the axis of symmetry  $p^*_{\text{film}}(0,t)$  and the film profiles  $h(r,t)$  were calculated using SRYL model based on the

experimental results in **Fig. 6-12**. **Fig. 6-13** shows the effect of bubble drive velocity on  $p^*_{\text{film}}(0,t)$  of an air bubble approaching a hydrophilic glass sphere as a function of film thickness. As can be seen from **Fig. 6-13**, at a given film thickness,  $p^*_{\text{film}}(0,t)$  increases with increasing bubble drive velocity from 33  $\mu\text{m/s}$  to 134  $\mu\text{m/s}$ . This result is not unexpected as the increase of approach velocity will increase the hydrodynamic pressure between the two surfaces, leading to a higher  $p^*_{\text{film}}(0,t)$ . The increase in  $p^*_{\text{film}}(0,t)$  at the same film thickness makes bubble to deform at a larger film thickness. As a result,  $p^*_{\text{film}}(0,t)$  reaches value 2 at a larger separation distance. For example, as shown in **Fig. 6-13**, the critical film thickness increases from 320 nm at bubble drive velocity of 33  $\mu\text{m/s}$  to 636 nm at bubble velocity of 134  $\mu\text{m/s}$ . Similar to **Fig. 6-11**, the film thickness profile in **Fig. 6-14** shows that with increasing  $p^*_{\text{film}}(0,t)$ , the air bubble starts to deform at a larger separation distance. The deformation of the bubble reduces the thinning rate of the intervening liquid film, thus increasing the separation distance at the end of the approach cycle as shown in **Fig. 6-13** and **Fig. 6-14**.

## 6.5 Discussion

We showed that with the change of surface tension  $\gamma$ , viscosity  $\mu$ , and bubble drive velocity  $V$ , the bubble starts to deform and stops at a different separation during the approach cycle. The change of the bubble deformation was due to variations of either hydrodynamic pressure or the air bubble Laplace pressure. It is interesting to note that by normalizing the film thickness using the scale parameter  $h_c$ , given in **Eqn. 6-8**, the film pressures shown in **Figs. 6-6, 9** and **12** all collapse into one single curve. As shown in **Fig. 6-15**, the change of  $V$ ,  $\gamma$  and  $\mu$  shows no effect on the film pressure  $p^*_{\text{film}}(0,t)$ . In other words, in systems with different  $V$ ,  $\gamma$  and  $\mu$ , the whole interaction behaves in a universal way - all hydrodynamic in its nature. The dimple forms at a universal critical thickness  $h^*(0,t) = 0.42$ , which is very close to the reported value where the surface forces are neglected.<sup>33, 34</sup> Hence, the film thickness where dimple forms can be calculated by:  $h_{\text{dimple}} = 0.42 \times R_0(\mu V/\gamma)^{1/2}$ . By extrapolation, the interactions between an air bubble and a glass sphere will also obey the dimensionless film

pressure - film thickness curve by changing the air bubble and glass sphere size. The overlap of the four curves also indicates excellent reproducibility of the ITFDA on measuring the hydrodynamic force.

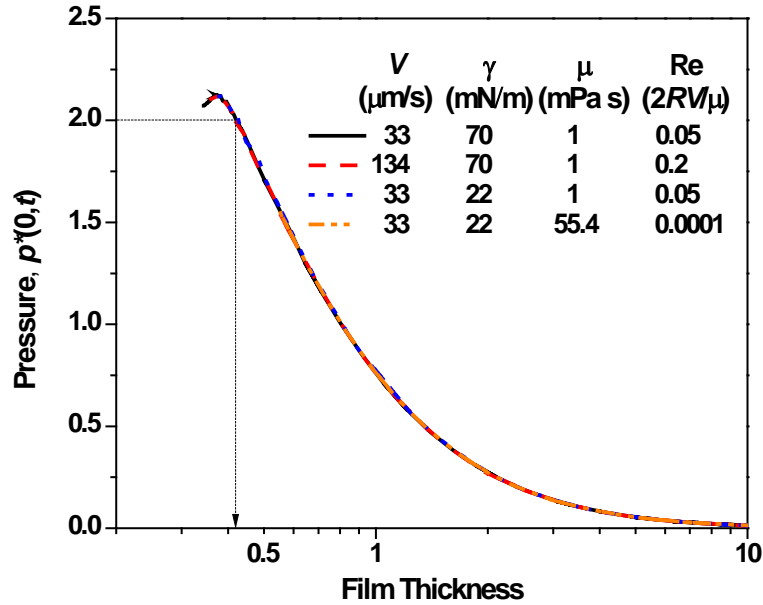


**Fig. 6-15** Effect of bubble drive velocity,  $V$ , surface tension,  $\gamma$ , and viscosity,  $\mu$ , on film pressure  $p^*_{\text{film}}(0,t)$  of an air bubble approaching a hydrophilic glass sphere as a function of dimensionless film thickness,  $h^*(0,t)$ .

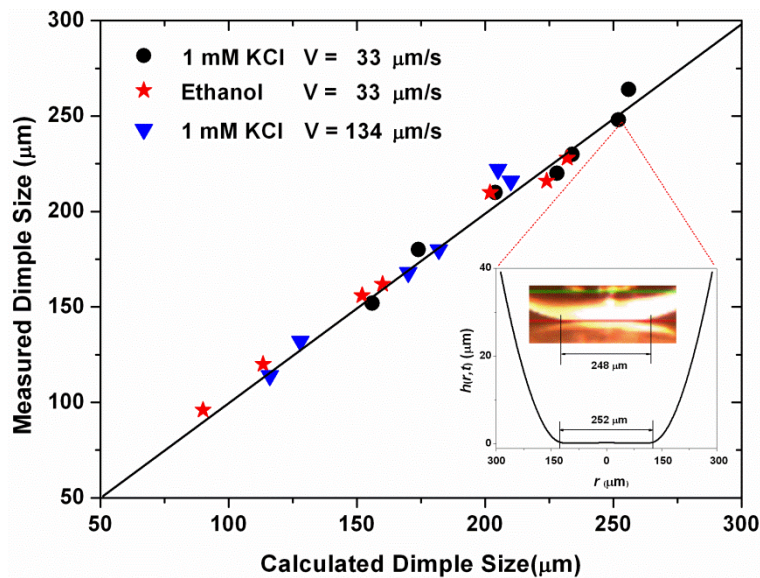


**Fig. 6-16** Comparison of experimentally measured and theoretically predicted dimple size at different stages of interactions in various sets of experiment

conditions. The calculated dimple sizes reported in this graph are based on the film thickness profiles shown in **Figs. 6-7, 10 and 13**. Inset illustrates the determination of measured and calculated dimple size.

With the image analysis program, the dimple sizes (or the diameter of the contact area) at different stages of the bubble-glass sphere interactions in various experiments conditions were determined and compared with the dimple sizes predicted by the SRYL model. **Fig. 6-16** shows excellent agreement between the experimentally measured and theoretically predicted dimple size, demonstrating that the SRYL model not only provides quantitative interaction force but also accurate description of bubble deformation.

## **6.6 Conclusions**

The effect of different physicochemical parameters such as solution pH, salt concentration, liquid surface tension, viscosity and air bubble drive velocity on the dynamic interaction force of a moving air bubble approaching to and retracting from a hydrophilic glass sphere was investigated by the ITFDA and the SRYL model. The excellent agreement between the measured and predicted interaction force profiles indicates that the SRYL model can be expanded to a wider range of hydrodynamic conditions, i.e., larger Reynolds number system and larger bubble approach velocity (up to 134  $\mu\text{m/s}$ ). The excellent agreement also makes it possible to use the model to infer quantitative information about film profiles and film drainage resistance profiles during the approach-retraction interaction.

The simulation results indicate that the minimum film thickness is reached during the retraction of the air bubble from the glass sphere due to a negative hydrodynamic pressure. Over the hydrodynamic conditions studied, the disjoining pressure was found to be negligible as compared with the hydrodynamic pressure. In other words, the hydrodynamic force dominates the total interaction force and the water chemistry such as solution pH and electrolyte concentration plays a minimum role when the bubble drive velocity is larger than 33  $\mu\text{m/s}$ . The effect of

liquid surface tension, viscosity and bubble drive velocity on the interactions between an air bubble and a glass sphere can be scaled into a dimensionless curve. The formation of dimple can be observed at the dimensionless film thickness of 0.42 under the presented dynamic conditions studied, i.e.,  $4.7 \times 10^{-7} < Ca < 1.5 \times 10^{-6}$  or  $6.7 \times 10^{-4} < Re < 0.2$ . The SRYL model was proven to predict both interaction forces and deformations within the same experiment.

## 6.7 References

- (1) Fuerstenau, D. W.; Herrera-Urbina, R. Mineral Separation by Froth Flotation. *Surfactant Science Series* **1989**, *33*, 259-320.
- (2) Ødegaard, H. The use of Dissolved Air Flotation in Municipal Wastewater Treatment. *Water Science and Technology* **2001**, *43*, 75-81.
- (3) Luttrell, G. H.; Yoon, R. -. A Hydrodynamic Model for Bubble-Particle Attachment. *J. Colloid Interface Sci.* **1992**, *154*, 129-137.
- (4) Yoon, R. H. Hydrodynamic and Surface Forces in Bubble-Particle Interactions. *Mines & carrieres.Les techniques* **1992**, 74-79.
- (5) Chan, D. Y. C.; Klaseboer, E.; Manica, R. Film Drainage and Coalescence between Deformable Drops and Bubbles. *Soft Matter* **2011**, *7*, 2235-2264.
- (6) Platikanov, D. Experimental Investigation on the "Dimpling" of Thin Liquid Films. *J. Phys. Chem.* **1964**, *68*, 3619-3624.
- (7) Ivanov, I.; Dimitrov, D. Thin Film Drainage. *Surfactant Science Series* **1988**, *29*, 379-396.
- (8) Blake, T. D.; Kitchener, J. A. Stability of Aqueous Films on Hydrophobic Methylated Silica. *Journal of the Chemical Society, Faraday Transactions 1: Physical Chemistry in Condensed Phases* **1972**, *68*, 1435-1442.
- (9) Schulze, H. J. Rupturing of Thin Liquid Films on Solid Surfaces. *Colloid and Polymer Science* **1975**, *253*, 730-737.

- (10) Pan, L.; Yoon, R. -. Hydrophobic Forces in the Wetting Films of Water Formed on Xanthate-Coated Gold Surfaces. *Faraday Discuss.* **2010**, *146*, 325-340.
- (11) Butt, H. -. A Technique for Measuring the Force between a Colloidal Particle in Water and a Bubble. *J. Colloid Interface Sci.* **1994**, *166*, 109-117.
- (12) Butt, H. -.; Jäschke, M.; Ducker, W. Measuring Surface Forces in Aqueous Electrolyte Solution with the Atomic Force Microscope. *Bioelectrochem. Bioenerget.* **1995**, *38*, 191-201.
- (13) Ducker, W. A.; Xu, Z.; Israelachvili, J. N. Measurements of Hydrophobic and DLVO Forces in Bubble-Surface Interactions in Aqueous Solutions. *Langmuir* **1994**, *10*, 3279-3289.
- (14) Fielden, M. L.; Hayes, R. A.; Ralston, J. Surface and Capillary Forces Affecting Air Bubble-Particle Interactions in Aqueous Electrolyte. *Langmuir* **1996**, *12*, 3721-3727.
- (15) Nguyen, A. V.; Nalaskowski, J.; Miller, J. D. A Study of bubble–particle Interaction using Atomic Force Microscopy. *Minerals Eng* **2003**, *16*, 1173-1181.
- (16) Wang, L.; Sharp, D.; Xu, Z.; Masliyah, J. An Integrated Thin Film Drainage Apparatus (ITFDA) to Study Interactions of Solid Particles, Liquid Droplets and Gas Bubbles in a Liquid. *manuscript in preparison* .
- (17) Johnson, D. J.; Miles, N. J.; Hilal, N. Quantification of particle–bubble Interactions using Atomic Force Microscopy: A Review. *Adv. Colloid Interface Sci.* **2006**, *127*, 67-81.
- (18) Hough, D. B.; White, L. R. The Calculation of Hamaker Constants from Lifshitz Theory with Applications to Wetting Phenomena. *Adv. Colloid Interface Sci.* **1980**, *14*, 3-41.

- (19) Israelachvili, J. N. In *Intermolecular and surface forces*; Academic Press Limited: San Diego, 1991; .
- (20) Wu, C. A Fundamental Study of Bubble-Particle Interactions through Zeta-Potential Distribution Analysis, University of Alberta (Canada), Canada, 2011.
- (21) Chan, D. Y. C.; Klaseboer, E.; Manica, R. Theory of Non-Equilibrium Force Measurements Involving Deformable Drops and Bubbles. *Adv. Colloid Interface Sci.* **2011**, *165*, 70-90.
- (22) Dagastine, R. R.; Manica, R.; Carnie, S. L.; Chan, D. Y. C.; Stevens, G. W.; Grieser, F. Dynamic Forces between Two Deformable Oil Droplets in Water. *Science* **2006**, *313*, 210-213.
- (23) Carnie, S. L.; Chan, D. Y. C.; Manica, R. Modelling Drop-Drop Interactions in an Atomic Force Microscope. *ANZIAM Journal* **2004**, *46*, C805-C819.
- (24) Manica, R.; Connor, J. N.; Carnie, S. L.; Horn, R. G.; Chan, D. Y. C. Dynamics of Interactions Involving Deformable Drops: Hydrodynamic Dimpling Under Attractive and Repulsive Electrical Double Layer Interactions. *Langmuir* **2007**, *23*, 626-637.
- (25) Carnie, S. L.; Chan, D. Y. C.; Lewis, C.; Manica, R.; Dagastine, R. R. Measurement of Dynamical Forces between Deformable Drops using the Atomic Force Microscope. I. Theory. *Langmuir* **2005**, *21*, 2912-2922.
- (26) Chan, D. Y. C.; Dagastine, R. R.; White, L. R. Forces between a Rigid Probe Particle and a Liquid Interface. I. the Repulsive Case. *J. Colloid Interface Sci.* **2001**, *236*, 141-154.
- (27) Bardos, D. C. Contact Angle Dependence of Solid Probe-Liquid Drop Forces in AFM Measurements. *Surf Sci* **2002**, *517*, 157-176.
- (28) Chan, D. Y. C. A Simple Algorithm for Calculating Electrical Double Layer Interactions in Asymmetric Electrolytes - Poisson-Boltzmann Theory. *J. Colloid Interface Sci.* **2002**, *245*, 307-310.

- (29) McCormack, D.; Carnie, S. L.; Chan, D. Y. C. Calculations of Electric Double-Layer Force and Interaction Free Energy between Dissimilar Surfaces. *J. Colloid Interface Sci.* **1995**, *169*, 177-196.
- (30) Klaseboer, E.; Chevaillier, J. P.; Gourdon, C.; Masbernat, O. Film Drainage between Colliding Drops at Constant Approach Velocity: Experiments and Modeling. *J. Colloid Interface Sci.* **2000**, *229*, 274-285.
- (31) Webber, G. B.; Edwards, S. A.; Stevens, G. W.; Grieser, F.; Dagastine, R. R.; Chan, D. Y. C. Measurements of Dynamic Forces between Drops with the AFM: Novel Considerations in Comparisons between Experiment and Theory. *Soft Matter* **2008**, *4*, 1270-1278.
- (32) Hendrix, M. H. W.; Manica, R.; Klaseboer, E.; Chan, D. Y. C.; Ohl, C. -. Spatiotemporal Evolution of Thin Liquid Films during Impact of Water Bubbles on Glass on a Micrometer to Nanometer Scale. *Phys. Rev. Lett.* **2012**, *108*.
- (33) Manica, R.; Klaseboer, E.; Chan, D. Y. C. Dynamic Interactions between Drops - A Critical Assessment. *Soft Matter* **2008**, *4*, 1613-1616.
- (34) Chan, D. Y. C.; Klaseboer, E.; Manica, R. Dynamic Deformations and Forces in Soft Matter. *Soft Matter* **2009**, *5*, 2858-2861.

## **Chapter 7**

### **Study of Air Bubble - Hydrophobic Solid Interactions using an Integrated Thin Film Drainage Apparatus**

## 7.1 Introduction<sup>‡‡</sup>

Thin liquid film drainage plays a critical role in a variety of important areas, including lubrication, flotation and stability of colloidal suspensions and foams. In mineral flotation, for example, the valuable hydrophobic particles are separated from hydrophilic particles through their selective attachment to air bubbles. The success of air bubble-particle attachment depends largely on the drainage rate of intervening liquid film between a solid particle and an air bubble in a dynamic system.<sup>1-3</sup> To facilitate selective attachment, the desirable particles are rendered hydrophobic by selective adsorption of surfactants, known as collectors. Much attention has been focused on understanding and controlling the interactions between colliding air bubbles and particles.

In early studies, a captive bubble was pressed against a flat silica surface and the film thickness was measured as a function of applied pressure using an optical interferometer, which is known as Scheludko cell.<sup>4-7</sup> A stable aqueous film was formed between the air bubble and the hydrophilic solid surface. The stability of this film is attributed to the positive disjoining pressure, which is considered arise from van der Waals forces ( $F_{vdw}$ ) and electrical double layer force ( $F_e$ ). The thickness of the film was found to decrease with increasing concentration and valence of electrolytes in solution due to a decreased  $F_e$ .<sup>6, 8</sup> Furthermore, the film becomes meta-stable and susceptible to spontaneous rupture in the presence of divalent cations<sup>9</sup> or if the silica surface is hydrophobized by adsorption of a cationic surfactant.<sup>10</sup> More recently, Pan and Yoon reported that the rate of film thinning increases with increasing hydrophobicity of the solid surfaces.<sup>11, 12</sup>  $F_{vdw}$  is repulsive in wetting films whilst  $F_e$  is also repulsive in alkaline pH where both solid/water and air/water interfaces are negatively charged.<sup>13, 14</sup> Therefore, there

---

<sup>‡‡</sup> Modified from the following manuscripts:

- 1) Wang, L.; Xu, Z. and Masliyah, J.H. Dissipation of film drainage resistance by hydrophobic surfaces in aqueous solutions, submitted to *Proceedings of the National Academy of Sciences*.
- 2) Wang, L.; Xu, Z. and Masliyah, J.H. A study of interactions between an air bubble and a hydrophobic glass surface under dynamic conditions, *manuscript in preparation*.

has to be an additional attractive force between the air bubble and the hydrophobic surface that is not considered in the classical DLVO theory to account for the film rupture.<sup>14</sup> To resolve this controversy, an extended DLVO theory was proposed to include an additional attractive force,  $F_h$  known as hydrophobic force, in the classical DLVO theory.<sup>15, 16</sup> The possible origin of  $F_h$  remains a subject of controversy, but is believed due to an extended structural force related to special orientation of water molecules around non-polar surfaces,<sup>17, 18</sup> the separation-induced cavitation,<sup>19</sup> the presence of nanobubbles on solid surfaces<sup>20-22</sup> or more recently, a structuring of H-bonded liquid in films confined between hydrophobic surfaces.<sup>23, 24</sup>

The direct measurement of interaction forces between air bubbles and solids was not possible until the introduction of colloidal probe technique in the atomic force microscope (AFM).<sup>25</sup> The earliest measurements of bubble-particle interactions using the colloid probe technique was made by Butt<sup>26</sup> and Ducker et al.<sup>27</sup>, and further refined by Fielden et al.<sup>28</sup> In their studies, a small bubble (~500  $\mu\text{m}$ ) was placed on a hydrophobic surface. A spherical probe particle was attached to the cantilever of AFM. The air bubble below the probe particle was moved up and down through a piezoelectric transducer. The net interaction force was measured by recording the cantilever deflection using a split photodiode detector. These studies showed a “jump” of hydrophobic particles into the air bubbles in simple electrolyte solutions due to long-range attractive hydrophobic force  $F_h$ . The jump-in distance was found to be related to the particle hydrophobicity. The hydrophobic attraction becomes smaller with decreasing contact angle of particles.<sup>28-30</sup> The attractive  $F_h$  was found to disappear when sodium dodecyl sulfate (SDS) was added into the solution, which is due to the adsorption of SDS at the bubble/liquid and solid/water interfaces with the hydrophilic head groups facing the aqueous solution, making the surfaces hydrophilic.<sup>27, 31</sup> As the two surfaces approached each other, a repulsive force was detected before attachment at high approaching velocities,<sup>29, 30</sup> while spontaneous rupture of the intervening liquid film without any resistance was observed at low approach velocity.<sup>26-28, 31</sup> The distinct difference indicates the presence of a repulsive hydrodynamic force,

$F_{HD}$ .  $F_{HD}$  was found to increase with increasing approach velocity of an air bubble to a solid surface.<sup>17</sup>

Under flotation conditions,  $F_{HD}$  dominates the total force until the separation distance between the two surfaces reduces below approximately 50 nm. This is where surface forces are important for further thinning of the intervening liquid films. Eventually the attractive  $F_h$  prevails, which results in a spontaneous film rupture and leads to the formation of three phase contact (TPC). The presence of attractive  $F_h$  to counter balance the repulsive force or the film drainage resistance (mainly consists of  $F_{HD}$ ,  $F_{vdw}$  and  $F_e$ ) leads to an energy barrier between the two interacting surfaces.<sup>15</sup> The external energy of a particle approaching an air bubble must be greater than this energy barrier to reach a thermodynamically stable state of TPC. The time needed for the film drainage, i.e., the thinning of intervening liquid film to a critical thickness ( $T_c$ ) where film ruptures, is known as the induction time.<sup>32, 33</sup> Induction time between an air bubble and mineral particles/bitumen surface has been studied extensively.<sup>32-35</sup> The induction time, linked to the energy barrier, is a critical parameter needed to model bubble-particle attachment in flotation. Lower energy barrier and hence a shorter induction time correspond to a higher probability of bubble-particle attachment.<sup>32, 36</sup>

In flotation, the air bubbles and particles are brought together due to the liquid movement where  $F_{HD}$  plays a critical role in the air bubble-particle interactions. However, most studies on thin film stability between air bubble and solid surfaces using the techniques discussed above were conducted at low approach velocities to minimize hydrodynamic effect. Induction time technique, although provides a dynamic condition close to a flotation environment, fails to measure the force applied during the measurement, which greatly limits its use. Recently, the development of an integrated thin film drainage apparatus (ITFDA) made it possible to study the physicochemical properties of thin liquid films confined between two surfaces under dynamic conditions.<sup>37</sup> In this study, the interaction force between an air bubble and a hydrophobized glass sphere in aqueous

solutions was measured using ITFDA to investigate the role of bubble drive velocity ( $V$ ) and solid hydrophobicity in bubble-particle attachment, mainly focusing on the measurement of force barriers before TPC and induction time over a wide range of hydrodynamic conditions.

## **7.2 Materials and Methods**

### ***7.2.1 Materials and sample preparation***

A piezo ceramic actuator, purchased from FUJI CERAMICS Corp. with a physical dimension of  $20 \times 3 \times 0.3$  mm and capacitance of 20 nF, was used to fabricate the force sensor. The solid surface was prepared by melting a  $1.5 \pm 0.1$  mm diameter Pyrex rod under a butane-oxygen flame until the surface tension of the melting Pyrex produced a spherical surface with a rough diameter of 4.5 mm. A glass tube with an inner diameter of  $1.1 \pm 0.05$  mm (Fisher Scientific) was used to generate and displace the air bubble. One end of the glass tube was placed in a butane flame to fuse the glass chip if there was any, creating a smooth end suitable for bubble generation and force measurement between the air bubble and solid surfaces. The glass sphere and capillary tube were treated in freshly prepared piranha solution (3 H<sub>2</sub>SO<sub>4</sub>:1 H<sub>2</sub>O<sub>2</sub>, by volume) at 80 - 90 °C for half an hour, and rinsed with Mili-Q water. The surfaces prepared in this manner were free of contamination and completely water-wet with a contact angle value of zero.

Octadecyltrichlorosilane (OTS), received from Sigma-Aldrich, was used to prepare 1 mM OTS in toluene (Fisher Scientific) solutions which were used to treat the hydrophilic glass spheres. The treated glass sphere was rinsed with toluene and anhydrous ethyl alcohol (Commercial Alcohols Inc.) to remove residual OTS from the glass sphere, and blow-dried with ultrapure nitrogen. The sample chamber was left in the anhydrous ethyl alcohol under ultrasonication in a bath for half an hour, rinsed with the de-ionized water and then blow-dried with ultrapure nitrogen. Potassium chloride (KCl), purchased from Sigma-Aldrich, was used as supporting electrolyte, and stock solutions of NaOH and HCl were used as pH modifiers. A non-ionic surfactant, DF250 (Dow Chemical Canada. Inc), was

used to prepare 0.3 mM DF 250 + 1 mM KCl solutions to study the effect of surfactant on interactions of air bubble with hydrophobized solid surfaces.

### 7.2.2 Treatment of glass sphere

To change the hydrophobicity of hydrophilic silica surfaces, OTS molecules are often used to react with the hydroxyl group on solid substrate surface, a reaction called silanation, to form a self-assembled monolayer.<sup>30, 38</sup> It has been reported that different hydrophobicity can be achieved by varying the reaction time of silanation.<sup>30, 38</sup> In this study, the hydrophilic glass spheres were treated with 1 mM OTS in toluene solutions for 5 s, 10 s, 10 min and 10 hr to obtain different hydrophobicities of the glass spheres. **Fig. 7-1** shows typical AFM images of (a) a clean glass surface and (b) a surface treated with 1 mM OTS in toluene solutions for 10 min. The imaging was conducted in air. As it can be seen from these images, the distance between the highest and lowest points on both clean and treated glass surfaces is less than 1.2 nm, indicating that both surfaces are sufficiently smooth and suitable for force and contact angle measurements. It appears that a mono-layer of OTS molecules has been reacted on the silica surface with reaction time of 10 min.

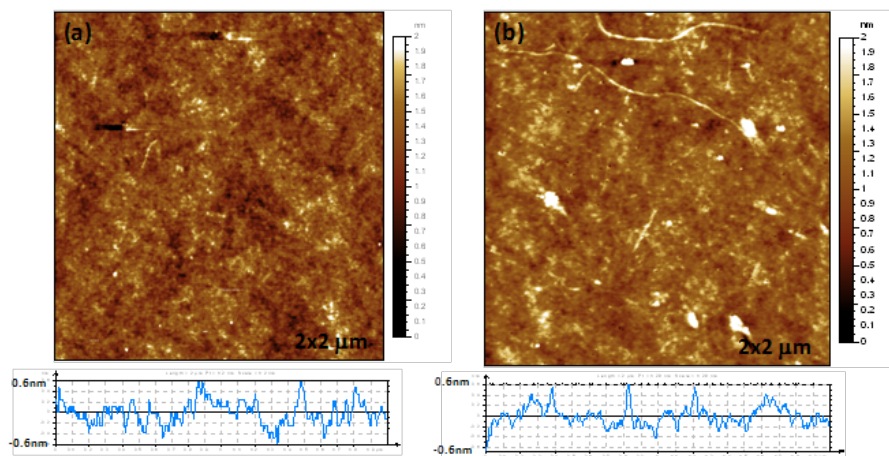


**Fig. 7-1** Contact mode AFM (Agilent Technologies, Inc., Chandler, AZ) images of glass surfaces in air: (a) clean glass surface; and (b) treated with 1mM OTS in toluene solution for 10 min. The lower figures show the corresponding cross-section topographic traces of the glass surface.

It is recognized that the receding contact angle can be determined from AFM force profile of bubble-particle interactions. Nguyen et al.<sup>29, 39</sup> suggested that the depth of solid penetration into an air/water interface in a typical force measurement could be influenced by the hydrodynamic drag and the subsequent deformation of air/water interface. Therefore, the calculated  $\theta_r$  from the AFM force curve would be affected by the speed of particle movement. In this study, the movements of TPC line and bubble/water interface were directly analyzed by examining the recorded videos using the vision analysis program to obtain the receding/advancing contact angle values.<sup>37</sup> As a result, the contact angle values obtained using our method would be less dependent on the bubble drive velocity ( $V$ ). As shown in **Fig. 7-2**, both receding ( $\theta_r$ ) and advancing ( $\theta_a$ ) contact angles increased with increasing OTS reaction time. For example,  $\theta_r$  of glass sphere in 1 mM KCl solutions at pH 5.6 increased from 21.1° to 89.4° when the reaction (soaking) time increased from 5 s to 10 hr, and correspondingly,  $\theta_a$  increased from 38.1° to 102.7°. With the increase of reaction time, the coverage of OTS molecules on the glass surfaces increases, resulting in a higher contact angle value. As shown in **Fig. 7-2**, the contact angle decreases with increasing ethanol content of 1 mM KCl-ethanol solutions. For a given surface, the wettability of solid can also be controlled by changing the surface tension of liquids. As shown in the Young Equation:  $\cos\theta = \frac{\gamma_{as} - \gamma_{ws}}{\gamma_{wa}}$  (where  $\theta$  is the contact angle of the glass surface measured through aqueous phase,  $\gamma$  is the interfacial tension, and the subscripts  $a$ ,  $s$  and  $w$  represent air, solid and water phase, respectively),  $\theta$  decreases with decreasing the surface tension of liquids. In this study, ethanol-in-water solutions were also used to study the effect of solids wettability on hydrodynamic forces. The hydrophobicity of the glass surface was determined prior to each experiment. In this case, the glass sphere was placed in 1 mM KCl solution and the air bubble was driven at  $V = 48 \mu\text{m/s}$  to attach to the glass sphere. It was found that  $\theta$  of the glass sphere in KCl solutions remained the same up to 24 hr, demonstrating a stable OTS layer on the glass surface. As illustrated

in the inset of **Fig. 7-2**, the increase of ethanol content progressively decreases the surface tension of aqueous solutions, which in turn decreases the contact angle as observed.

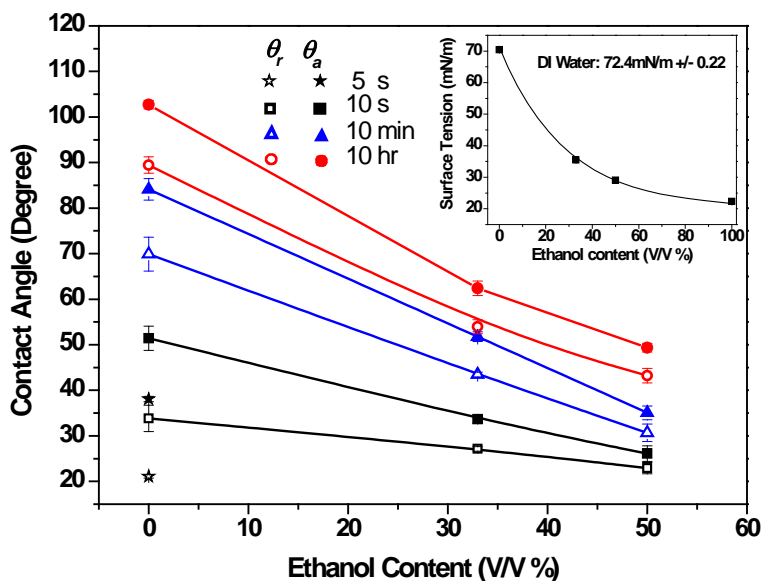


**Fig. 7-2** Receding ( $\theta_r$ ) and advancing ( $\theta_a$ ) contact angles of glass surfaces reacted with OTS for different period of time in 1 mM KCl – ethanol solutions as a function of ethanol volume content, at  $T = 20 \pm 0.5$  °C. The inset shows the effect of ethanol content on surface tension of 1 mM KCl - ethanol solutions. As a reference, the surface tension of de-ionized water was measured to be  $72.4 \pm 0.22$  mN/m. Five measurements were performed in each case, and the average and standard deviation values are reported.

### 7.2.3 Experimental

The interactions between an air bubble and a glass sphere were measured by the ITFDA. More details about this apparatus were given in section 4.2 in Chapter 4.<sup>37, 40</sup> Briefly, a piezo ceramic actuator known as bimorph is employed as a force sensor to directly measure the interaction forces. As shown in the inset of **Fig. 7-3**(bottom), an air bubble is generated using a micro-syringe at one end of the glass tube which is connected to a speaker diaphragm on the other end. A triangular or trapezoidal electrical wave is generated by the computer to control the movement of the speaker diaphragm which in turn drives the air bubble to

approach to and/or retract from the glass sphere surface in a well controlled manner. With such an arrangement, the approach and retract velocity ( $V_a$  and  $V_r$ , respectively) as well as the range of displacement of the air bubble can be accurately controlled. The extent (applied force) and duration of the contact between the air bubble and solid surface can also be well controlled. The fused glass sphere is clamped at the free end of the bimorph. The bimorph is enclosed by a fluorinated ethylene propylene (FEP) sheath and mounted on a small stainless steel chamber which is placed on a three-dimensional translation stage. Two cameras are placed perpendicular to each other near the sample chamber to align the interacting surfaces as well as to control the size of the air bubble and the initial gap between the bubble and glass sphere. During the measurement, the interaction forces between the air bubble and the glass sphere surface causes a deflection at the free end of the bimorph, which in turn generates a charge at the bimorph surface. The change of the bimorph surface charge measured as voltage is recorded as a function of time. The signal can then be converted to force profile once the cantilever calibration constant is obtained at the end of each experiment.

**Fig. 7-3** shows a representative glass tube displacement (top) and bimorph signal profile (bottom) obtained from a single measurement between an air bubble and a hydrophobic glass sphere of  $\theta_a = 38^\circ$  in 1 mM KCl solutions of pH 5.6. In this measurement, the initial separation distance between the air bubble and the glass sphere,  $h_0$ , was set at 120  $\mu\text{m}$ . A trapezoidal wave was generated to produce a movement of glass tube holding the air bubble, that first approached the glass sphere with a displacement of 240  $\mu\text{m}$  in 1 second (points A to C in **Fig. 7-3**(top)), then held the air bubble in contact with the glass sphere for 2 seconds (points C to F), retracted the air bubble from the glass sphere with the same velocity (points F to J) and finally moved the air bubble back to the original position (point J to K). It should be noted that during the retraction (points F to J), when the glass tube reached the original position (point G) the air bubble remained attaching to the glass sphere. To measure the adhesion force, the glass

tube was further moved up to point J to separate the air bubble from the glass sphere and then returned to point K at the end of the measurement.

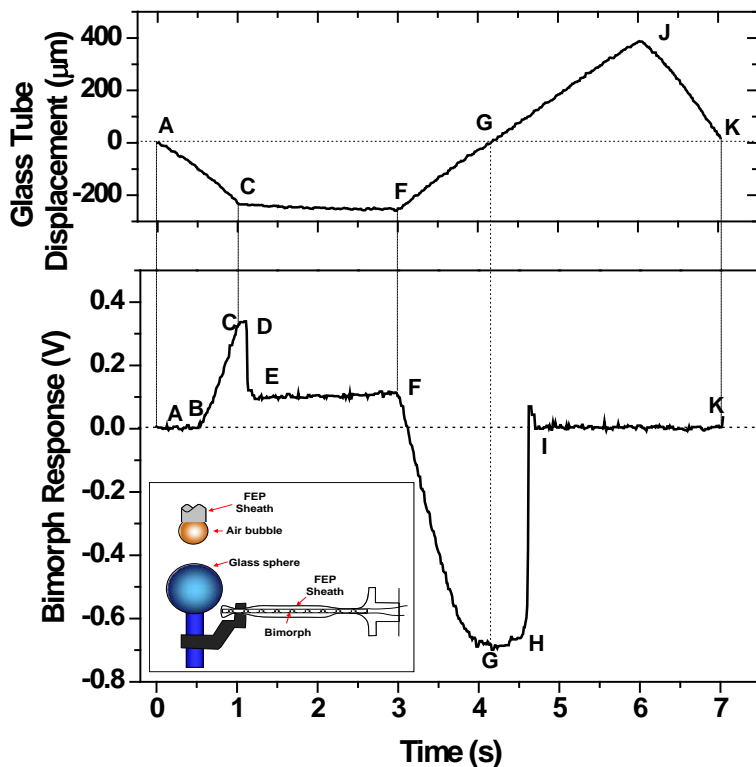


**Fig. 7-3** A representative glass tube displacement (top) and bimorph signal (bottom) as a function of measurement time between an air bubble and a hydrophobic glass sphere ( $\theta_a = 38^\circ$ ) in 1 mM KCl solutions of pH 5.6. The bubble drive velocity was set at 240  $\mu\text{m/s}$ . Inset graph shows a schematic configuration of the integrated thin film drainage apparatus (ITFDA).

As shown in **Fig. 7-3** (bottom), points A to C correspond to the bimorph signal during the approach cycle. When the separation distance between the two surfaces is large (points A to B), there is no measurable interaction forces as indicated by a zero bimorph signal, showing only some noises. As the bubble continues to approach the glass sphere, the separation distance between the two surfaces reduces. When the hydrodynamic force and/or surface forces become significant (detectable), a repulsive force between these two surfaces is detected as indicated by an increase in bimorph signal (point B). The repulsive force (film drainage resistance) continues to increase as the bubble is further driven down by the glass

tube and reaches the maximum at point C. During the “holding” period, from point C to F, the bimorph signal remains constant initially and drops from 0.34 V at point D to 0.09 V at point E, indicating the rupture of the liquid film between the two surfaces and the formation of TPC. The interfacial tension force at the TPC line pulls the glass sphere up, exhibiting a “jump in” of the glass sphere at point D. The signal remains almost the same after point E until point F where a sharp drop in signal is observed, reflecting the retracting of the bubble from the glass sphere, and hence an increase of attractive capillary force from the bubble. Eventually, the capillary force reaches the restoring force of the bimorph and the bubble detaches from the glass sphere at point H, where the bimorph signal returns to zero as indicated at point I. Depending on the stability of the thin liquid film, the rupture of the film can happen at any time during the measurement, i.e., approach, hold or retract period. From this force profile, the induction time or film drainage time can be accurately measured as the time from point B to point D. For example, the induction time for the system in **Fig. 7-3** is determined to be 0.59 s. This represents the most accurate measurement of true induction time as it can accurately detect thin film rupture for the first time.

For the measurements reported in this chapter, the diameter of the air bubbles and glass spheres were controlled at  $1.5 \pm 0.1$  mm and  $4.3 \pm 0.1$  mm, respectively. The initial separation distance ( $h_0$ ) between the air bubble and glass sphere was set at 120  $\mu\text{m}$ . Two types of bubble drive profiles were used in the experiments: triangular movements (without holding) with maximum displacement of 150  $\mu\text{m}$  to study the effect of  $V$ ; and trapezoidal movements with maximum displacement of 240  $\mu\text{m}$  to study the effect of solids hydrophobicity, surface tension of the bulk solution and the presence of surfactants in aqueous solutions on the force barrier and induction time before TPC. More accurate values of bubble size ( $R_b$ ), glass sphere radius ( $R_g$ ) and  $h_0$  were obtained by analyzing the videos recorded during the measurements using an image analysis program interfaced with LabVIEW 8.0.<sup>37</sup> At least five measurements were conducted for each experiment condition, and the average value was reported with standard deviations.

## 7.3 Results and Discussion

### 7.3.1 Effect of bubble drive velocity, $V$

The interactions between an air bubble and a glass sphere of  $\theta_a = 37.4^\circ$  were measured at different  $V$  as a function of time. The air bubble approached to and then retracted from the glass sphere in a triangular pattern with a maximum glass tube displacement of  $150\ \mu\text{m}$ . Different  $V$  can be obtained by varying the approach and retract time for a given maximum glass tube displacement. Therefore, the total measurement time of experiments for the different approach/retract velocities is different. To compare the force profiles of different  $V$  values, the measurement time  $t$  was scaled by the total measurement time for each experiment,  $t_{total}$ . In this manner, the same value of  $t/t_{total}$  for a different  $V$  value corresponds to the same glass tube displacement. For example, as shown in **Fig. 7-4** when  $t/t_{total} = 0.25$ , the glass tube reaches the maximum displacement of  $150\ \mu\text{m}$ . When  $t/t_{total} < 0.25$ , air bubble is approaching to the glass sphere, and when  $t/t_{total} > 0.25$ , the air bubble is retracting from the glass sphere.

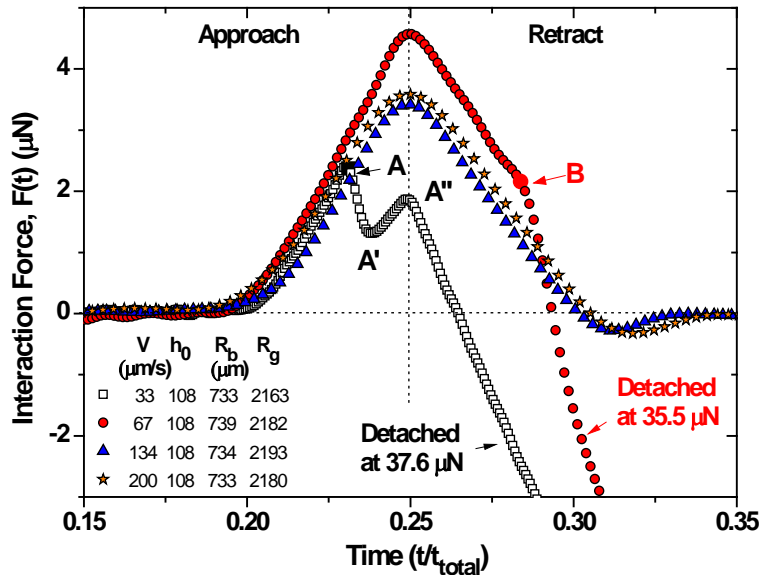


**Fig. 7-4** Effect of bubble drive velocity,  $V$ , on interaction forces,  $F(t)$ , of an air bubble approaching to and retracting from a glass sphere in 1 mM KCl solutions. The receding ( $\theta_r$ ) and advancing ( $\theta_a$ ) contact angle of glass surface were measured to be  $21.1 \pm 0.1^\circ$  and  $37.4 \pm 0.9^\circ$ , respectively. Here  $h_0$ ,  $R_b$  and  $R_g$  are

the initial separation distance, non-deformed bubble and glass sphere radii, respectively. The values of  $h_0$ ,  $R_b$ ,  $R_g$  are determined using the image analysis program. Time  $t$  was scaled by the total measurement time,  $t_{total}$ , to compare the force profiles of different  $V$  value, and only force profiles at close separation distance are presented to help interpret the data.

As shown in **Fig. 7-4**, the film rupture occurred for the cases of  $V = 33$  and  $67 \mu\text{m/s}$ , leading to the formation of TPC between the air bubble and the glass sphere. On retraction, a strong adhesion around  $36 \mu\text{N}$  was measured. When  $V$  increased to  $134$  and  $200 \mu\text{m/s}$ , there is no indication of film rupture and no adhesion was observed on retraction. The interaction force increased as the bubble moved towards the glass sphere. At  $V = 33 \mu\text{m/s}$ , the film ruptured during the approach cycle (i.e.,  $t/t_{total} < 0.25$ ), demonstrated by a sudden drop of measured force (points A to A'). The force then increased continuously with the further movement of air bubble towards the glass sphere, reaching the maximum at the end of the approach cycle (point A" where  $t/t_{total} = 0.25$ ). The force then reduced rapidly and changed from repulsion to attraction (negative value) with the retraction of bubble away from the glass sphere (i.e.,  $t/t_{total} > 0.25$ ), indicating a strong adhesion. In this case, the film was able to thin to the critical thickness  $T_c$  during the approach cycle, causing the rupture of the film and the formation of TPC as observed at point A.

When the drive velocity increased to  $67 \mu\text{m/s}$ , the intervening liquid film remained stable during approach cycle, as indicated by the absence of sudden change in the force profile. Interestingly, the film rupture occurred during the retraction of bubble from the glass sphere at point B, as shown by a sudden change in the force profile. It appears that the film thickness was larger than  $T_c$  during the approach cycle, and reached  $T_c$  during the retraction of bubble away from the glass sphere. A stable intervening liquid film indicates the film thickness being larger than  $T_c$  during the approach cycle with increasing bubble drive velocity. Such observation is not unexpected, as illustrated in **Fig. 6-11** in **Chapter 6**, increasing the bubble drive velocity increases the film drainage

resistance at the same film thickness.<sup>41</sup> Moreover, the increase in film drainage resistance makes the bubble to deform at a larger separation distance and hence increases the film thickness during the approach cycle. In other words, during the approach cycle the film thickness remained larger than  $T_c$ , therefore no film rupture is observed.

It is well documented that in contrast to the case involving only equilibrium interactions, for the systems involving dynamic interactions, the closest separation distance, and hence the opportunity for film rupture to occur, can take place as the surfaces move apart.<sup>42-44</sup> This behavior is the response of the deformable surface to the negative hydrodynamic pressure generated by the retraction of the two surfaces.<sup>44</sup> Upon separation of the air bubble from the glass sphere, water has to be drawn in to fill the thickening film between the two surfaces, generating a negative hydrodynamic pressure which actually reduces the film thickness. As shown in **Fig. 6-4** in **Chapter 6**, the film thickness continuously reduces at the beginning of the retraction (Profiles D to F). Once the film thickness reaches  $T_c$ , the film ruptures and the formation of TPC can be observed, shown as a sudden drop of the force profile at point B in **Fig. 7-4**. The rupture of the liquid film during retraction was also reported while studying the interactions between two bubbles with approach-retract movement in aqueous solutions.<sup>43</sup>

With further increasing bubble drive velocity  $V$  from 67 to 134 and 200  $\mu\text{m/s}$ , the film remained stable as indicated by the absence of sudden signal change or a strong adhesion in the whole time dependant force profiles shown in **Fig. 7-4**. Instead, the force profiles demonstrated a pure hydrodynamic feature: the force increases with the approaching of air bubble towards the glass sphere, reaches a maximum at the end of approach cycle (i.e.,  $t/t_{total} = 0.25$ ), rapidly becomes attractive when the bubble moves away from the glass sphere and generates an attractive minimum in the force profile. As mentioned earlier, increase in the bubble drive velocity increases the film thickness during the approach cycle. It is therefore more difficult for the film to reach  $T_c$  at higher bubble drive velocities. At bubble drive velocity equals or larger than 134  $\mu\text{m/s}$ , the minimum film

thickness reached during retraction is larger than  $T_c$ . Consequently, a stable liquid film was maintained during the whole measurement cycle, leading to a force profile with a pure hydrodynamic feature.

### ***7.3.2 Effect of electrolyte concentration and pH***

The interaction forces of an air bubble approaching to and retracting from a hydrophobized glass sphere of  $\theta_a = 38.2^\circ$  were measured in 1 mM and 100 mM KCl solutions at pH 5.6 with drive velocity  $V = 33 \mu\text{m/s}$ . In this case, the measurement time between different sets of experiments remains the same. Hence, the force profiles are plotted as a function of measurement time. As shown in **Fig. 7-5**, during the experiments the air bubble approaches to the glass sphere from 0 to 4.5 s and then retracts away from the glass sphere after 4.5 s. The results in **Fig. 7-5** show that when an air bubble approached the glass sphere in 1 mM KCl solutions, the intervening liquid film ruptured as indicated by a sudden drop of force profile from  $0.7 \mu\text{N}$  at point A to  $-3.3 \mu\text{N}$  at point A'. When the experiment was conducted in 100 mM KCl solutions at pH 5.6, no visible jump in was observed in the force profile. However, a strong adhesion with value of  $21.6 \mu\text{N}$  can be observed during retraction, indicating the establishment of TPC during the interactions. The TPC between these two surfaces suggests the jump in of the glass sphere to the air bubble was too small to be detected by the bimorph force sensor.

With the increasing electrolyte concentration, the compression of electrical double layers at bubble and glass surfaces would reduce  $F_e$  between two surfaces and make the water film less stable. Therefore a smaller force barrier with a jump in of glass sphere into the air bubble rather than “no” jump in would be expected. It is well documented that the jump in distance of the particle into the air bubble is a strong indicator of the solid hydrophobicity.<sup>31, 45</sup> The change of the jump in behavior of glass sphere in solutions with different electrolyte concentration might not directly due to the surface charge but to the solid wettability. As illustrated in the insets (a) and (b) of **Fig. 7-5**,  $\theta_a$  of the glass surface reduced from  $38.2^\circ$  in 1 mM KCl solutions to  $23.5^\circ$  in 100 mM KCl solutions. The reduction of

solid hydrophobicity reduced the TPC area of bubble-glass attachment and decreased the adhesion from 47.4  $\mu\text{N}$  to 21.6  $\mu\text{N}$  when the air bubble detached from the glass sphere. The reduction of the methylated silica hydrophobicity due to increasing electrolyte concentration has also been reported,<sup>14</sup> which is believed to link with the solid surface potential.<sup>46</sup>

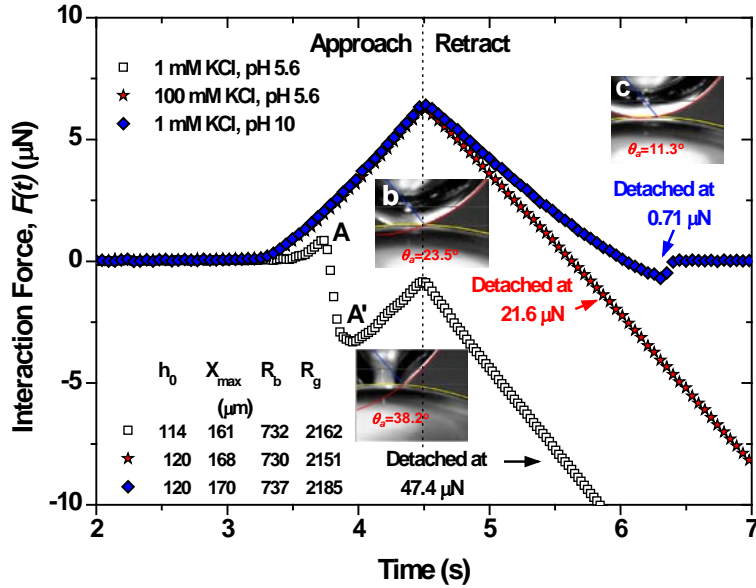


**Fig. 7-5** Effects of electrolyte concentration and solution pH on air bubble-hydrophobized glass sphere interactions in KCl solutions with  $V = 33 \mu\text{m/s}$ . Here  $h_0$ ,  $X_{max}$ ,  $R_b$  and  $R_g$  are the initial separation distance, maximum glass tube displacement, non-deformed bubble and glass sphere radii, respectively. The values of  $h_0$ ,  $R_b$ ,  $R_g$  were obtained using the image analysis program. The inset photos illustrate the determination of  $\theta_a$  using the image analysis program: (a)  $\theta_a = 38.2^\circ$  in 1 mM KCl solutions at pH 5.6; (b)  $\theta_a = 23.5^\circ$  in 100 mM KCl solutions at pH 5.6 and (c)  $\theta_a = 11.3^\circ$  in 1 mM KCl solutions at pH 10.

When the pH of 1 mM KCl solution increased from 5.6 to 10, no detectable jump in was observed in the force profile as shown in **Fig. 7-5**. Only a small adhesion with value of 0.77  $\mu\text{N}$  was measured during the retraction, thereby showing a dramatic reduction of solid hydrophobicity when the solution pH increased to 10. The change of the glass wettability can be explained by the amphoteric behavior of the glass sphere. The silanol group (SiOH) at the glass

surface can either accept or donate protons, thereby imparting a positive ( $\text{SiOH}_2^+$ ) or negative charge ( $\text{SiO}^-$ ) of glass surface, depending on the pH. The adsorption of these water soluble ions at the glass sphere would therefore change the wettability of the glass surface. When the pH increased from 5.6 to 10, the glass surface became more negatively charged due to a higher concentration of water soluble  $\text{SiO}^-$  at the surface, making the glass surface more hydrophilic. As illustrated by the insets of (a) and (c) in **Fig. 7-5**, the value of  $\theta_a$  of the glass surface was found to drop from  $38.2^\circ$  to  $11.3^\circ$  when the solution pH increased from 5.6 to 10. The decrease of solid hydrophobicity dramatically reduced the TPC contact area, leading to a large drop of adhesion from 47.4 to 0.71  $\mu\text{N}$ . The pH dependent of the hydrophobized glass wettability has also been reported in aqueous solutions.<sup>14</sup>

47

As a conclusion, the electrolyte concentration and solution pH change the glass sphere hydrophobicity, therefore affecting the dynamic interactions between an air bubble and a hydrophobized glass sphere.

### **7.3.3 Effect of solids hydrophobicity**

As discussed above, the increase of bubble drive velocity  $V$  changes the film drainage behavior between the air bubble and the hydrophobic glass sphere due to an increased film drainage resistance and hence the film thickness. In order to measure the induction time, a trapezoidal movement of glass tube with maximum displacement of 240  $\mu\text{m}$  and 5 s length of holding was generated to drive the air bubble. In these measurements, the air bubble approached to the glass sphere with the setting velocity, in contact with the lower glass sphere for 5 s with little displacement of glass tube and then retracted from the glass sphere with the same velocity. The holding time was set at 5 s to ensure that the film ruptured before or during the holding period and a stable TPC was established. As shown in **Fig. 7-3**, the film remained stable when the maximum force was reached at point C and ruptured during the holding period at point D, indicating that the force barrier under this condition was larger than the maximum force at point C. Hence, under this condition the force barrier, which is defined as the maximum force before

TPC during the approach cycle, was not considered. In other words, the force barrier values reported in this chapter are under conditions that the film rupture happened during the approach cycle.

To study the effect of bubble drive velocity  $V$  and solid hydrophobicity on film drainage of air bubble-hydrophobized solid interactions, the force barrier before TPC during approach cycle and the induction time were measured in 1 mM KCl solutions at pH 5.6 as a function of  $V$ . As shown in **Fig. 7-6**, increasing  $V$  increased the force barrier ( $F_{bar}$ ) between approaching air bubble and the hydrophobic glass sphere, indicating an increase of film drainage resistance. For example, on a glass sphere of  $\theta_a = 38.2^\circ$ ,  $F_{bar}$  remained small when  $V$  was smaller than  $48 \mu\text{m/s}$ , and dramatically increased from  $4.5 \mu\text{N}$  to  $12.8 \mu\text{N}$  and  $38.4 \mu\text{N}$  when  $V$  increased from 48 to 120 and 240  $\mu\text{m/s}$ , respectively.

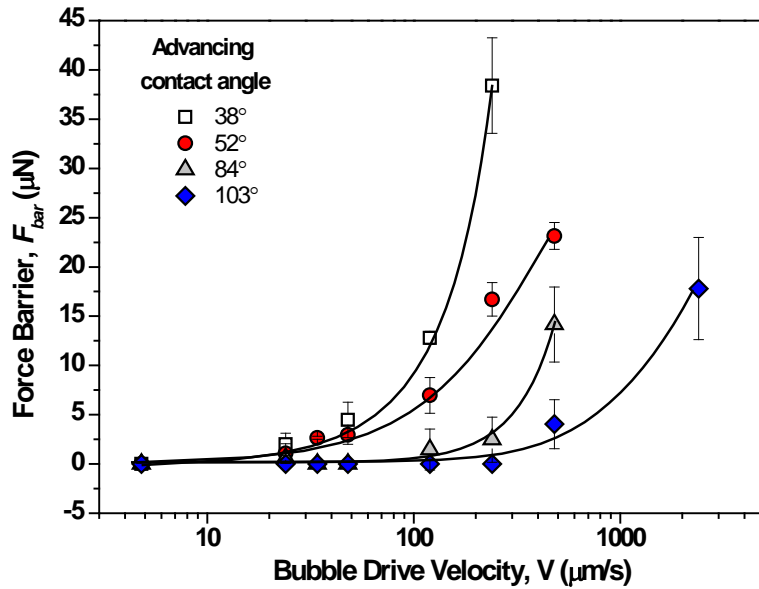


**Fig. 7-6** Effect of glass sphere hydrophobicity on force barrier ( $F_{bar}$ ) between an approaching air bubble and a hydrophobized glass sphere prior to TPC formation in 1 mM KCl solutions at pH 5.6 and  $20 \pm 0.5^\circ\text{C}$  as a function of bubble drive velocity,  $V$ . The diameters of air bubble and glass sphere were  $1.5 \pm 0.1 \text{ mm}$  and  $4.3 \pm 0.1 \text{ mm}$ , respectively.

The motion of the glass tube is speculated to cause additional flow around the glass sphere and hence to add additional force on the measured force by the

bimorph. To quantify this effect if presents, experiments were conducted to determine the force from the capillary tube with a bubble cap on the glass sphere fixed on the bimorph when the glass tube approached the glass sphere. As shown in **Fig. 7-7(a)**, the initial separation distance between the glass tube and the glass sphere and the maximum glass tube displacement were set at  $1290\ \mu\text{m}$  and  $240\ \mu\text{m}$ , respectively (the same value as the bubble-glass sphere interactions where an air bubble was attached at the end of the glass tube). Different drive velocities were tested to determine the moving glass tube on the measured force due to the moving water around the capillary. The results in **Fig. 7-7 (b)** show a negligible force on the bimorph during the motion of the glass tube. The results demonstrate that over the velocity range of capillary tube displacement in our study (up to  $2400\ \mu\text{m/s}$ ) we can safely neglect the effect of the flow disturbance due the capillary tube on the measured forces by the bimorph sensor. Therefore, the change on the measured force by the bimorph sensor is due to the air bubble.

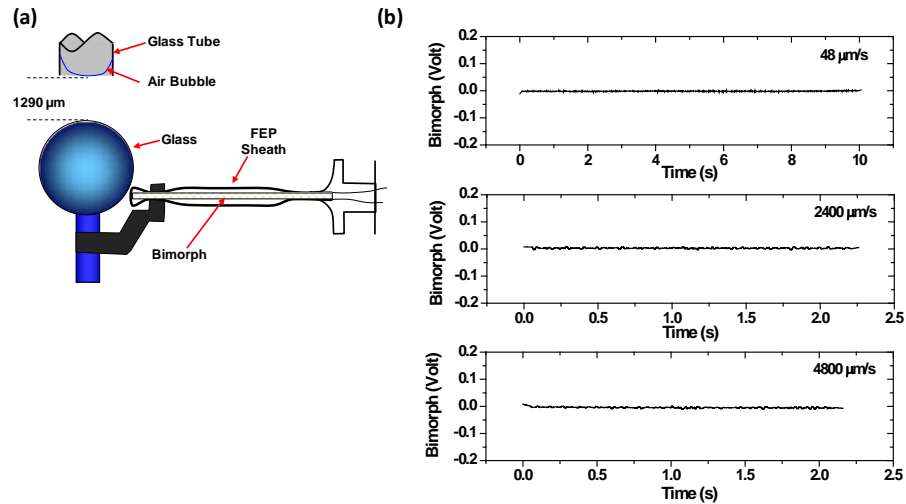


**Fig. 7-7** (a) A schematic configuration of the experimental set up; (b) Effect of glass tube velocity ( $48 - 4800\ \mu\text{m/s}$ ) on the force measurement of the bimorph. The initial separation distance between the end of the glass tube and the glass sphere, and the maximum glass tube displacement were set at  $1290\ \mu\text{m}$  and  $240\ \mu\text{m}$ , respectively.

Glass wettability shows a significant impact on the force barrier, as illustrated in **Fig. 7-6**. An increase of solid hydrophobicity (i.e.,  $\theta_a$ ) dramatically reduces the force barrier. For example, the force barrier reduced from 12.8 to 6.96, 1.45 and 0  $\mu\text{N}$  with the increase of  $\theta_a$  from  $38^\circ$  to  $52^\circ$ ,  $84^\circ$  and  $103^\circ$ , respectively. More importantly, the increase of solid hydrophobicity diminished the film drainage resistance, rendering a zero force barrier. The force barrier remained undetectable up to  $V = 240 \mu\text{m/s}$  when the glass surface was highly hydrophobic (i.e.,  $\theta_a = 103^\circ$ ), and up to  $V = 48 \mu\text{m/s}$  for a moderately hydrophobic surface (i.e.,  $\theta_a = 84^\circ$ ). The reduced and diminished force barrier suggests that a strong and long-range attractive force which depresses the repulsive forces between the two surfaces even at high bubble drive velocities. This attractive force is attributed to the change in the wettability of the glass sphere from low hydrophobicity to high hydrophobicity. Such observation is believed not due to the presence of nano/micro bubbles on the solid surface as discussed previously in **Section 4.4.1.1** of **Chapter 4**, but rather to the change of the solid boundary conditions.<sup>37, 40</sup> Detailed discussions on the effect of solid hydrophobicity on the dissipation of force barrier will be presented in **Section 7.4**.

The induction time of air bubble-glass sphere attachment was also measured as a function of  $V$  and glass surface hydrophobicity. The results are presented in **Fig. 7-8**. Compared with **Fig. 7-6**, it is not difficult to conclude that both induction time and force barrier remained small at low  $V$ , and both increased with increasing  $V$  and decreased with increasing solid hydrophobicity at the same  $V$  value. The decrease of induction time with increasing glass hydrophobicity at the same  $V$  indicates that the film drainage rate increases at higher solid hydrophobicity, which is consistent with the results reported by the thin film pressure balance apparatus.<sup>11, 12</sup> Such observation demonstrates the important role of solid hydrophobicity in the film drainage.

The thinning of the liquid film is controlled by the film drainage resistance (hydrodynamic force and surface forces). When the bubble approaches the glass sphere, the bubble deforms in such a way that not all water is expelled, leading to

a formation of a “dimple”, the drainage rate is therefore dependent on the water flow rate at the barrier rim. Consequently, it takes a longer time for the film thickness to reach the  $T_c$ , as indicated by an increase in the induction time with increasing bubble drive velocity. However, it seems that once  $V$  reaches a critical value, the induction time remains constant. As shown in **Fig. 7-8**, the induction time levelled off when  $V$  was larger than  $34 \mu\text{m/s}$  for a glass sphere of  $\theta_a = 38^\circ$  and  $52^\circ$ . As mentioned above, the film drainage rate is controlled by the flow of liquid through the rim. It is highly possible that the increasing the air bubble drive velocity would increase the rim thickness which in turn would actually increase the film drainage rate. Therefore, even when the film thickness increases at high air bubble drive velocities, the film drainage time (induction time) remains the same due to an increased film drainage rate.

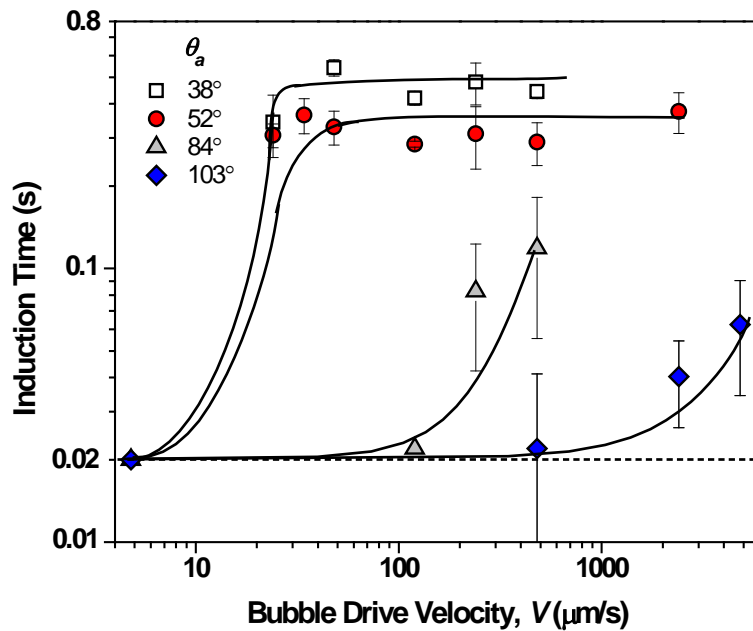


**Fig. 7-8** Effect of air bubble drive velocity ( $V$ ) and glass sphere hydrophobicity ( $\theta_a$ ) on induction time of bubble-glass sphere attachment in 1 mM KCl solutions at pH 5.6 and  $20 \pm 0.5^\circ\text{C}$ .

### 7.3.4 Effect of surface tension

**Fig. 7-9** shows the effect of surface tension on the induction time of air bubble-hydrophobized glass attachment. The change of surface tension was achieved by

mixing 1 mM KCl solutions and ethanol, as shown in the inset of **Fig. 7-2**, the surface tension of solution reduced from 70.4 to 35.3 and 29 mN/m when the ethanol volume content increased from 0 to 33.3% and 50%, respectively. Correspondingly, the contact angle of the glass surface reduced from  $51.4^\circ$  to  $33.6^\circ$  and  $26.1^\circ$  when the glass sphere was immersed in solutions with surface tension of 70.4, 35.3 and 29 mN/s, respectively. As can be seen from **Fig. 7-9**, the induction time of the bubble-glass sphere of  $\theta_a = 51.4^\circ$  remained around 0.3 s in 1 mM KCl solutions with  $V$  ranged from 24 to 480  $\mu\text{m/s}$ . A slight increase of induction time to around 0.5 s and a dramatic increase of induction time can be observed when the surface tension decreased to 35.3 mN/m and 29 mN/m, respectively. The increase in induction time with decreasing surface tension is probably due to the decreasing glass hydrophobicity ( $\theta_a$ ) which reduced the film drainage rate. Additionally, as shown in **Fig. 6-6** in **Chapter 6**, with the reduction of surface tension, the bubble starts to deform at a larger separation distance at the same  $V$ .<sup>41</sup> Hence, it takes a longer time for the film to drain due to a larger film thickness and a slower film drainage rate in lower surface tension solutions, leading to a higher induction time as shown in **Fig. 7-9**.

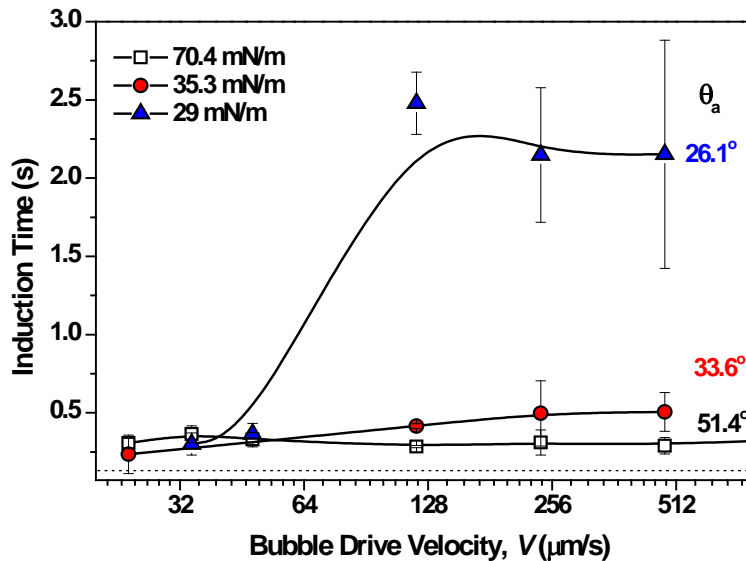


**Fig. 7-9** Effect of surface tension on induction time of air bubble-glass sphere attachment in ethanol - 1 mM KCl solutions as a function of air bubble drive

velocity,  $V$ . Numbers in the figure show the hydrophobicity of the glass sphere ( $\theta_a$ ) in corresponding solution.

### 7.3.5 Effect of surfactant

In flotation, frother is added to generate and stabilize air bubbles to facilitate particle flotation. The effect of a non-ionic frother DF 250 on interactions of an air bubble with a glass sphere was studied. As illustrated in **Fig. 7-10**, the force barrier before TPC in 0.03 mM DF 250+1 mM KCl solutions increased compared with the 1 mM KCl solutions without DF 250 at pH 5.6. As a non-ionic surfactant, the adsorption of the molecules at the air/water and solid/water interfaces would not change the surface charge, thus the electrical double layer force is believed to remain almost the same. However, the adsorption of the DF 250 molecules at the air/water and solid/water interfaces with the polar heads facing the aqueous solution would render the air bubble and glass surfaces less hydrophobic. As shown in the insets of (a) and (b) in **Fig. 7-10**,  $\theta_a$  of glass surface reduced from  $51.4^\circ$  to  $43.6^\circ$  with the presence of 0.03 mM DF 250 in 1 mM KCl solutions, thus increasing the force barrier as observed in **Fig. 7-10**.

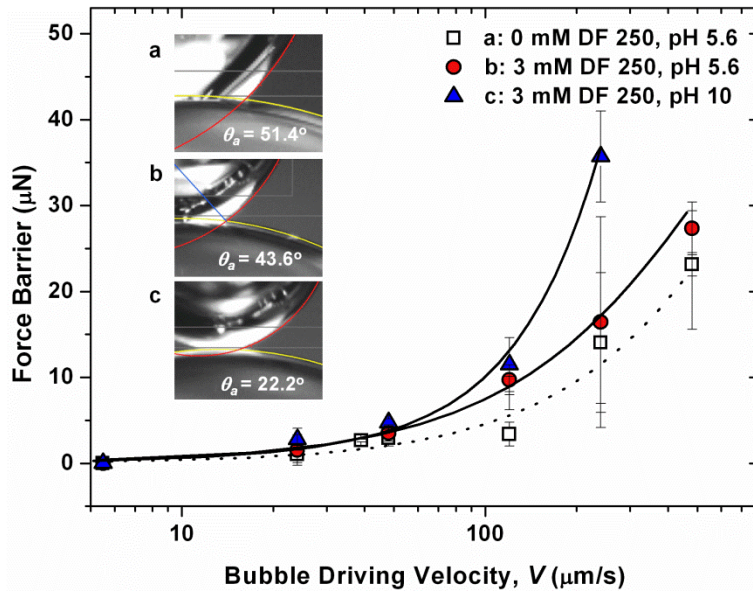


**Fig. 7-10** Effect of DF 250 and pH on force barrier ( $F_{bar}$ ) between air bubble and hydrophobized glass sphere attachment before TPC with a function of bubble drive velocity ( $V$ ). The inset photos illustrate the determination of  $\theta_a$  using the

image analysis program: (a)  $\theta_a = 51.4^\circ$  in 1 mM KCl solutions at pH 5.6; (b)  $\theta_a = 43.6^\circ$  in 0.03 mM DF 250 + 1 mM KCl solutions at pH 5.6 and (c)  $\theta_a = 22.2^\circ$  in 0.03 mM DF 250 + 1 mM KCl solutions at pH 10.

Moreover, the force barrier increased when pH increased from 5.6 to 10 in 0.03 mM DF 250+1 mM KCl solutions. Such observation is also believed to link with the amphoteric behavior of the glass surface, as it can be seen in **Fig. 7-10**,  $\theta_a$  decreases from  $43.6^\circ$  at pH 5.6 to  $22.2^\circ$  at pH 10 in a 0.03 mM DF 250+1 mM KCl solutions. A less hydrophobic nature of the glass surface at pH 10 increased the repulsive force between the two surfaces, made the film rupture more difficult to occur and therefore increasing the force barrier before TPC. Moreover, surface tension gradient, interfacial viscosity and surface elasticity can also be responsible for the observed phenomena when surfactants are present at interfaces.<sup>42, 48</sup>

#### **7.4 Reduction of Film Drainage Resistance**

We showed that the air bubble drive velocity and glass sphere hydrophobicity both play important role in the air bubble-hydrophobized glass attachment under dynamic conditions. As illustrated in **Fig. 7-6.**, the increase of the glass sphere hydrophobicity decreases the resistance between the air bubble and the glass sphere, leading to a dissipation of force barrier before TPC. The increase of air bubble drive velocity leads to an increase of the force barrier.

It is recognized that the bubble deforms when it reaches the boundary proximity of a solid surface during the approach. The deformed interface determines the boundary condition of the thin liquid film where the intervening liquid must flow during the interaction. The flow of this liquid generates a pressure in the film that in turn determines the shape of the interface, thus giving rise to a repulsive film drainage force (resistance) on the glass sphere. The bubble deformation changes the area of interaction and hence the total boundary surface force. It is therefore important to account for the effect of bubble deformation on the measured total force to elucidate the effect of surface hydrophobicity on dissipation of film drainage resistance. For this reason,  $F_{bar}$  determined as shown

in **Fig. 7-6** is normalized with the interaction area to obtain an average pressure ( $\bar{p}$ ) of the drainage film, i.e.,  $\bar{p} = \frac{F_{bar}}{\pi r^2}$ , which is referred to as film drainage resistance. Here,  $r$  is the radius of the projected area of interaction at the point where the film ruptures. Note that the average pressure obtained by the equation above is in a vertical direction.

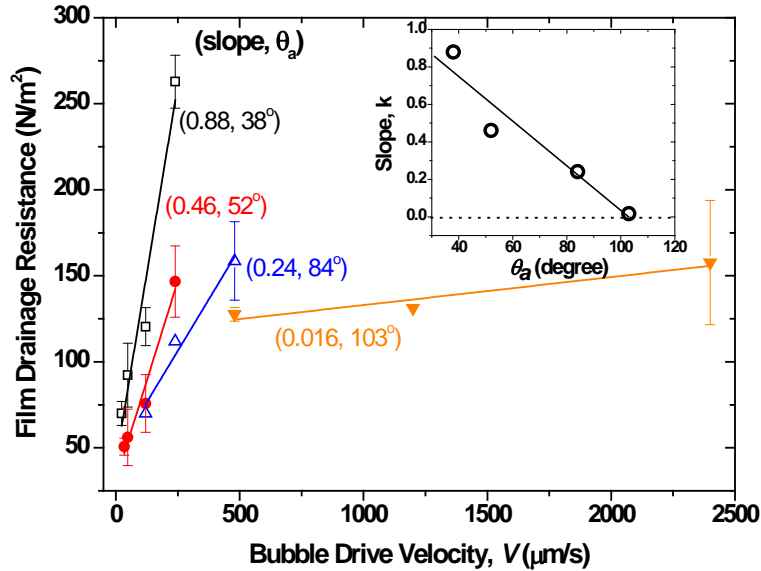


**Fig. 7-11** Effect of glass hydrophobicity ( $\theta_a$ ) on film drainage resistance ( $\bar{p}$ ) between an approaching air bubble and a hydrophobized glass sphere prior to three phase contact formation in a 1 mM KCl solution at pH 5.6 and  $20 \pm 0.5^\circ\text{C}$ . Solid lines show a linear fitting of the pressure as a function of bubble drive velocity. The inset illustrates the effect of glass hydrophobicity on the slope,  $k$ , as given by **Eqn. 7-1**.

As it can be seen from **Fig. 7-11**, for a given solid wettability ( $\theta_a$ ), the film drainage resistance increases linearly with bubble drive velocity,  $V$ . At a given bubble drive velocity, the film drainage resistance decreases with increasing  $\theta_a$ . Moreover, as shown in the inset of **Fig. 7-11**, the dependence (slope) of the film drainage resistance on bubble drive velocity decreases almost linearly with increasing  $\theta_a$ , illustrating progressive dissipation of film drainage resistance by increased surface hydrophobicity.

Since for a given contact angle, the surface forces are independent of approach velocity, the measured increase in film drainage resistance with increasing bubble drive velocity is most likely linked with the hydrodynamic resistance of liquid film drainage. This hydrodynamic resistance at the point of film rupture,  $p$ , between two surfaces approaching each other can be described by:<sup>49</sup>

$$p = \left[ \frac{3\mu RS}{T_c^2} \right] V = k V \quad \text{Eqn. 7-1}$$

where  $\mu$  is the viscosity of the solution;  $T_c$ , the separation distance at the point of film rupture;  $V$ , the surface approach velocity;  $S$ , dimensionless function used to consider the slip boundary condition; and  $R$ , unperturbed radius of the system. Here  $R$  is given by  $R = \frac{R_1 R_2}{R_1 + R_2}$ , where  $R_1$  and  $R_2$  are the radii of the upper and lower surfaces, respectively.

For two hydrophilic surfaces,  $S = 1$ . When the slip boundary condition is applicable at the surface,  $S$  becomes less than unity.<sup>50, 51</sup> For a given glass surface,  $T_c$  and  $S$  remain the same at the rupture point. One would therefore obtain a linear relationship between  $p$  and  $V$ , i.e.,  $p = k \cdot V$ , which can be clearly seen in **Fig. 7-11**. As illustrated in the inset of **Fig. 7-11**, the slope  $k$  decreases with increasing surface hydrophobicity ( $\theta_a$ ). Since increasing  $\theta_a$  would lead to an increase in  $T_c$ ,<sup>52</sup> the observed decrease in the slope as given in **Eqn. 7-1** with increasing  $\theta_a$  is not unexpected. However, a slight increase of  $T_c$  from 36 nm to 47 nm in the studied contact angle range does not account for a dramatic reduction in the slope observed in **Fig. 7-11**. Therefore, the reduction of slope observed in **Fig. 7-11** is most likely due to a dramatic decrease of  $S$  with the increasing  $\theta_a$ , i.e., increasing slippage boundary layer thickness with increasing  $\theta_a$ , manifested by an increased reduction in film drainage resistance. By extrapolation, solids with  $\theta_a$  larger than  $106^\circ$  would lead to a zero slope with a negligible film drainage resistance over the bubble approach velocities studied, indicating a complete slippage of the liquid film on this type of solids. Interestingly, this contact angle value is close to the lower limit of contact angle value for smooth superhydrophobic surfaces,<sup>53</sup> providing another scientific insight of superhydrophobic surfaces.

## 7.5 Conclusions

The interactions between an air bubble and a hydrophobized glass sphere were measured under a wide range of drive velocity using ITFDA. The results show that both bubble drive velocity and glass hydrophobicity play important roles in the intervening film drainage in the approach-retract movements of two surfaces. The liquid film ruptured during approaching at low drive velocity, during retracting at medium drive velocity and remained stable at high drive velocity. The film became more stable with increasing solution pH and electrolyte concentration due to a reduced solid hydrophobicity. The reduction of bulk solution surface tension and the presence of surfactant in solutions also reduced the glass hydrophobicity, making the liquid film more stable and increased the induction time and force barrier before TPC.

We also reported that film drainage resistance can be greatly diminished or accurately controlled by increasing or controlling the solid surface hydrophobicity. The film drainage resistance was found to increase linearly with increasing bubble drive velocity. The dependence (slope) of film drainage resistance on bubble drive velocity decreases linearly with increasing advancing contact angle of solid, indicating that hydrophobization of solid surface appears to be a practical approach to reduce film drainage resistance.

## 7.6 References

- (1) Yoon, R. H. The Role of Hydrodynamic and Surface Forces in Bubble-Particle Interaction. *Int. J. Miner. Process.* **2000**, *58*, 129-143.
- (2) Nguyen, A.; Schulze, H. J., Eds.; In *Colloidal science of flotation*; surfactant science series; New York, 2004; Vol. 118, pp 850.
- (3) Nguyen, A. V.; Schulze, H. J.; Ralston, J. Elementary Steps in particle-bubble Attachment. *Int. J. Miner. Process.* **1997**, *51*, 183-195.
- (4) Platikanov, D. Experimental Investigation on Dimpling of Thin Liquid Films. *J. Phys. Chem.* **1964**, *68*, 3619-3624.

- (5) Ivanov, I.; Dimitrov, D. Thin Film Drainage. *Surfactant Sci.Ser.* **1988**, *29*, 379-396.
- (6) Blake, T. D.; Kitchener, J. A. Stability of Aqueous Films on Hydrophobic Methylated Silica. *J. Chem. Soc. , Faraday Trans. 1* **1972**, *68*, 1435-1442.
- (7) Schulze, H. J. Rupturing of Thin Liquid Films on Solid Surfaces. *Colloid Polym. Sci.* **1975**, *253*, 730-737.
- (8) Read, A. D.; Kitchener, J. A. Wetting Films on Silica. *J. Colloid Interface Sci.* **1969**, *30*, 391-398.
- (9) Schulze, H. J.; Stockelhuber, K. W.; Wenger, A. The Influence of Acting Forces on the Rupture Mechanism of Wetting Films - Nucleation Or Capillary Waves. *Colloids Surf. , A* **2001**, *192*, 61-72.
- (10) Aronson, M. P.; Princen, H. M. Aqueous Films on Silica in the Presence of Cationic Surfactants. *Colloid Polym. Sci.* **1978**, *256*, 140-149.
- (11) Pan, L.; Jung, S.; Yoon, R. H. Effect of Hydrophobicity on the Stability of the Wetting Films of Water Formed on Gold Surfaces. *J. Colloid Interface Sci.* **2011**, *361*, 321-330.
- (12) Pan, L.; Yoon, R. H. Hydrophobic Forces in the Wetting Films of Water Formed on Xanthate-Coated Gold Surfaces. *Faraday Discuss.* **2010**, *146*, 325-340.
- (13) Israelachvili, J. N. In *Intermolecular and Surface Forces*. ACADEMIC PRESS INC: San Diego, CA, 1991; , pp 450.
- (14) Laskowski, J.; Kitchener, J. A. Hydrophilic-Hydrophobic Transition on Silica. *J. Colloid Interface Sci.* **1969**, *29*, 670-679.
- (15) Yoon, R.; Mao, L. Application of Extended DLVO Theory, IV. Derivation of Flotation Rate Equation from First Principles. *J. Colloid Interface Sci.* **1996**, *181*, 613-613.

- (16) Mao, L.; Yoon, R. Predicting Flotation Rates using a Rate Equation Derived from First Principles. *Int. J. Miner. Process.* **1997**, *51*, 171-181.
- (17) Israelachvili, J. N.; Pashley, R. M. Measurement of the Hydrophobic Interaction between Two Hydrophobic Surfaces in Aqueous Electrolyte Solutions. *J. Colloid Interface Sci.* **1984**, *98*, 500-514.
- (18) Claesson, P. M.; Blom, C. E.; Herder, P. C.; Ninham, B. W. Interactions between Water-Stable Hydrophobic Langmuir-Blodgett Monolayers on Mica. *J. Colloid Interface Sci.* **1986**, *114*, 234-242.
- (19) Claesson, P. M.; Christenson, H. K. Very Long Range Attractive Forces between Uncharged Hydrocarbon and Fluorocarbon Surfaces in Water. *J. Phys. Chem.* **1988**, *92*, 1650-1655.
- (20) Parker, J. L.; Claesson, P. M.; Attard, P. Bubbles, Cavities, and the Long-Ranged Attraction between Hydrophobic Surfaces. *J. Phys. Chem.* **1994**, *98*, 8468-8480.
- (21) Attard, P. Bridging Bubbles between Hydrophobic Surfaces. *Langmuir* **1996**, *12*, 1693-1695.
- (22) Hampton, M. A.; Nguyen, A. V. Nanobubbles and the Nanobubble Bridging Capillary Force. *Adv. Colloid Interface Sci.* **2010**, *154*, 30-55.
- (23) Wang, J.; Yoon, R. -.; Eriksson, J. C. Excess Thermodynamic Properties of Thin Water Films Confined between Hydrophobized Gold Surfaces. *J. Colloid Interface Sci.* **2011**, *364*, 257-263.
- (24) Wang, J.; Li, Z.; Yoon, R.; Eriksson, J. C. Surface Forces in Thin Liquid Films of n-Alcohols and of Water-Ethanol Mixtures Confined between Hydrophobic Surfaces. *J. Colloid Interface Sci.* .
- (25) Ducker, W. A.; Senden, T. J.; Pashley, R. M. Direct Measurement of Colloidal Forces using an Atomic Force Microscope. *Nature* **1991**, *353*, 239-241.

- (26) Butt, H. Technique for Measuring the Force between a Colloidal Particle in Water and a Bubble. *J. Colloid Interface Sci.* **1994**, *166*, 109-117.
- (27) Ducker, W. A.; Xu, Z.; Israelachvili, J. N. Measurements of Hydrophobic and DLVO Forces in Bubble-Surface Interactions in Aqueous Solutions. *Langmuir* **1994**, *10*, 3279-3289.
- (28) Fielden, M. L.; Hayes, R. A.; Ralston, J. Surface and Capillary Forces Affecting Air Bubble-Particle Interactions in Aqueous Electrolyte. *Langmuir* **1996**, *12*, 3721-3727.
- (29) Nguyen, A. V.; Nalaskowski, J.; Miller, J. D. A Study of bubble-particle Interaction using Atomic Force Microscopy. *Minerals Eng* **2003**, *16*, 1173-1181.
- (30) Ishida, N. Direct Measurement of Hydrophobic particle-bubble Interactions in Aqueous Solutions by Atomic Force Microscopy: Effect of Particle Hydrophobicity. *Colloids Surf. Physicochem. Eng. Aspects* **2007**, *300*, 293-299.
- (31) Preuss, M.; Butt, H. Direct Measurement of Particle-Bubble Interactions in Aqueous Electrolyte: Dependence on Surfactant. *Langmuir* **1998**, *14*, 3164-3174.
- (32) Yoon, R.; Yordan, J. L. Induction Time Measurements for the Quartz-Amine Flotation System. *J. Colloid Interface Sci.* **1991**, *141*, 374-383.
- (33) Ye, Y.; Khandrika, S. M.; Miller, J. D. Induction-Time Measurements at a Particle Bed. *Int. J. Miner. Process.* **1989**, *25*, 221-240.
- (34) Gu, G.; Xu, Z.; Nandakumar, K.; Masliyah, J. Effects of Physical Environment on Induction Time of Air-Bitumen Attachment. *Int. J. Miner. Process.* **2003**, *69*, 235-250.
- (35) Wang, L.; Dang-Vu, T.; Xu, Z.; Masliyah, J. H. Use of Short-Chain Amine in Processing of weathered/oxidized Oil Sands Ores. *Energy Fuels* **2010**, *24*, 3581-3588.

- (36) Laskowski, J. S.; Xu, Z.; Yoon, R. H. Energy Barrier in Particle-to-Bubble Attachment and its Effect on Flotation Kinetics. *Mines Carrières: Tech.* **1992**, 95-100.
- (37) Wang, L.; Sharp, D.; Xu, Z.; Masliyah, J. H. Measurement of interactions between solid particles, liquid droplets and/or gas bubbles in a liquid using an integrated thin film drainage apparatus. *Submitted to Langmuir* .
- (38) Flinn, D. H.; Guzonas, D. A.; Yoon, R. H. Characterization of Silica Surfaces Hydrophobized by Octadecyltrichlorosilane. *Colloids Surf. Physicochem. Eng. Aspects* **1994**, 87, 163-176.
- (39) Nguyen, A. V.; Nalaskowski, J.; Miller, J. D. The Dynamic Nature of Contact Angles as Measured by Atomic Force Microscopy. *J. Colloid Interface Sci.* **2003**, 262, 303-306.
- (40) Wang, L.; Xu, Z.; Masliyah, J. H. Dissipation of Hydrodynamic Forces by Hydrophobic Surfaces in Aqueous Solutions. *Submitted to Proceedings of the National Academy of Sciences*.
- (41) Shahalami, M.; Wang, L.; Wu, C.; Chan, D.; Xu, Z.; Masliyah, J. H. Measurement of Dynamic Forces between an Air Bubble and a Hydrophilic Glass Surface with ITFDA. *Manuscript in preparation* .
- (42) Chan, D. Y. C.; Klaseboer, E.; Manica, R. Film Drainage and Coalescence between Deformable Drops and Bubbles. *Soft Matter* **2011**, 7, 2235-2264.
- (43) Vakarelski, I. U.; Manica, R.; Tang, X.; O'Shea, S. J.; Stevens, G. W.; Grieser, F.; Dagastine, R. R.; Chan, D. Y. C. Dynamic Interactions between Microbubbles in Water. *Proc. Natl. Acad. Sci. U. S. A.* **2010**, 107, 11177-11182.
- (44) Dagastine, R. R.; Manica, R.; Carnie, S. L.; Chan, D. Y. C.; Stevens, G. W.; Grieser, F. Dynamic Forces between Two Deformable Oil Droplets in Water. *Science* **2006**, 313, 210-213.

- (45) Preuss, M.; Butt, H. Measuring the Contact Angle of Individual Colloidal Particles. *J. Colloid Interface Sci.* **1998**, *208*, 468-477.
- (46) Hanly, G.; Fornasiero, D.; Ralston, J.; Sedev, R. Electrostatics and Metal Oxide Wettability. *Journal of Physical Chemistry C* **2011**, *115*, 14914-14921.
- (47) Gribanova, E. V.; Molchanova, L. I.; Mazitova, K. B.; Rezakova, G. N.; Dmitrieva, N. A. Study of the Relation of Contact Angles on Quartz and Glass to the pH of the Solution. *Kolloidn. Zh.* **1983**, *45*, 316-320.
- (48) Chan, D. Y. C.; Klaseboer, E.; Manica, R. Theory of Non-Equilibrium Force Measurements Involving Deformable Drops and Bubbles. *Adv. Colloid Interface Sci.* **2011**, *165*, 70-90.
- (49) Vinogradova, O. I. Drainage of a Thin Liquid Film Confined between Hydrophobic Surfaces. *Langmuir* **1995**, *11*, 2213-2220.
- (50) Bhushan, B.; Wang, Y.; Maali, A. Boundary Slip Study on Hydrophilic, Hydrophobic, and Superhydrophobic Surfaces with Dynamic Atomic Force Microscopy. *Langmuir* **2009**, *25*, 8117-8121.
- (51) Wang, Y.; Bhushan, B. Boundary Slip and Nanobubble Study in micro/nanofluidics using Atomic Force Microscopy. *Soft Matter* **2009**, *6*, 29-66.
- (52) Albijanic, B.; Ozdemir, O.; Nguyen, A. V.; Bradshaw, D. A Review of Induction and Attachment Times of Wetting Thin Films between Air Bubbles and Particles and its Relevance in the Separation of Particles by Flotation. *Adv. Colloid Interface Sci.* **2010**, *159*, 1-21.
- (53) Shirtcliffe, N. J.; McHale, G.; Atherton, S.; Newton, M. I. An Introduction to Superhydrophobicity. *Adv. Colloid Interface Sci.* **2010**, *161*, 124-138.

# **Chapter 8**

## **Conclusions and Recommendations for Future Research**

The conclusions of this thesis and the recommendations for the future research are summarized in this chapter.

## **8.1 Conclusions**

Water based flotation technology is used to commercially extract bitumen from Athabasca oil sands. First of all, the colloidal chemistry of bitumen extraction from oil sands by water-based processes is reviewed, providing an overview on key physicochemical interactions involved in oil sands processing. The main research techniques used to study these interactions are summarized. Among the various elementary processes, efficient attachment between bitumen and air bubble is critical for success of bitumen flotation. To improve the processability of poor processing oil sands ores, short-chain primary amine was added to improve the attachment between air bubbles and bitumen particles by reducing the induction time. The adsorption of amine at the bitumen-water interface increased the bitumen hydrophobicity and reduced its zeta potential, thus dramatically decreased the induction time of air bubble-bitumen attachment. It was found that the bitumen recovery of weathered/oxidized oil sands ores increased by 20% when conducting the flotation under the conditions with minimum induction time. The results also show that with the addition of short-chain amine, the fine solids in the tailing became more hydrophilic, thus leading to increased bitumen froth quality.

Equipped with a bimorph cantilever as the force sensor, the integrated thin film drainage apparatus (ITFDA) was successfully developed to measure the film drainage time and force barrier to further understand the interactions involved in air bubble-solid attachment. Coupled with a computer-interfaced video capture and vision analysis program, the ITFDA allows accurate determination of dynamic and receding/advancing contact angles. The determination of liquid-air interface geometry allows for accurate calculation of the capillary force between an air bubble and a solid surface after TPC. The excellent agreement of calculated and measured capillary force indicates the high accuracy of force measurements of the bimorph cantilever. The interactions between air bubble-bitumen, oil

droplet-oil droplet and air bubble-oil droplet were studied by the ITFDA in terms of force barrier and induction time/coalescence time.

Using the parameters mostly obtained from the current experiments, an excellent agreement between the force measured by the ITFDA and calculated by solving SRYL equations has been shown. The results further illustrate the accuracy of force measurement by the ITFDA as well as the appropriate use of SRYL to calculate the dynamic force between mm scale deformable surfaces with  $V \sim 100 \mu\text{m/s}$ . With the model, the spatial-temporal evolution of the trapped water film can be obtained. The results show that the minimum film thickness is reached during the retraction of air bubble from the glass sphere that is due to a strong attractive hydrodynamic force. For a given set of system parameters at bubble drive velocities higher than  $33 \mu\text{m/s}$ , the hydrodynamic force dominates the total force and the effect of surface force is negligible. The effect of liquid surface tension, viscosity and bubble drive velocity on the interactions between an air bubble and a glass sphere can be scaled into a dimensionless universal curve.

Interactions between an air bubble and a hydrophobized glass sphere were measured using the ITFDA under dynamic conditions to study the effect of bubble drive velocity and solid hydrophobicity on air bubble-solid interactions. Film thinning rate was directly determined from the measured force barrier and induction time. The results show that hydrodynamic force played an important role in the intervening film drainage. In the approach-retract movements of two surfaces, the liquid film ruptured during the approach cycle at low bubble drive velocity  $V$ . It ruptured during the retract cycle at medium  $V$ , and the film remained stable at high  $V$ . The film became more stable with the increase of solution pH and electrolyte concentration, attributed to a reduced solid hydrophobicity. The reduction in the bulk solution surface tension and the presence of surfactant also reduced the glass hydrophobicity, making the liquid film more stable, increased the induction time and force barrier before TPC.

We also reported that film drainage resistance can be greatly diminished or accurately controlled by increasing or controlling the solid surface

hydrophobicity. The film drainage resistance was found to increase linearly with increasing bubble drive velocity. The dependence (slope) of film drainage resistance on air bubble drive velocity decreased linearly with increasing advancing contact angle of the solid, thereby indicating that hydrophobization of solid surface appears to be a practical approach to reduce film drainage resistance.

## 8.2 Recommendations for future research

Future research should address the following areas:

- In **Chapter 3**, it has been found that the addition of short-chain amine is able to dramatically reduce the induction time of air bubble-bitumen and thus increase bitumen recovery of poor processing oil sands ores. However, a systematic study is required to further investigate the effect of water chemistry, i.e., cations, amine concentration and addition of fine solid etc, on the air bubble-bitumen interactions.
- The current setup of ITFDA provides much information important on bubble-particle interactions. However, integration of the current setup with a thin liquid film balance would make a more advanced device. The new device can provide all of the parameters important to the bubble-particle interaction: interaction force, film profile at the interaction zone, film drainage time, advancing/receding contact angle etc.
- Excellent agreement between measured and predicted interaction force as well as the bubble deformation of bubble-hydrophilic glass sphere demonstrates a promising way to use the SRYL equations to predict the interaction force between an air bubble and a hydrophobic solid surface. The model can probably be achieved by adding an attractive hydrophobic force in the calculation or probably more importantly, changing the boundary condition at the hydrophobic solid surface.
- A well established model to predict the interaction force between an air bubble and a hydrophobic glass sphere will provide the film drainage resistance and film thickness profiles to fully understand the observations

reported in **Chapter 7**, i.e., rupture of the film at different stages of the interactions, the linear relationship between the film drainage resistance and the bubble drive velocity, a decreasing slope (less dependant of the film drainage resistance on the bubble drive velocity ) with the increasing glass hydrophobicity, etc.

- The use of non-slip boundary condition at both air/water and solid/water interfaces gives the best agreement between the experimental and theoretical predicted interaction forces between air bubble-glass sphere. It is not quite clear whether the addition of surfactant such as SDS and DF 250 would affect the boundary condition or not. Therefore, it would be important to measure the interactions in the presence of surfactant, using ITFDA and employ the SRYL model to predict the measured data.
- The experiment results in **Chapter 7** show that the change of surface tension has a dramatic effect on the induction time of air bubble-hydrophobic glass attachment. It should be noted that the contact angle values vary with the change of surface tension. A systematic study is required to further investigate the effect of surface tension and viscosity on the film drainage while keeping the contact angle at the same value.

# **Chapter 9**

## **Appendix**

This section provides detail procedures on the fabrication of bimorph force sensor, calibration of bimorph sensor, data processing, sensitive study and contact angle determination.

### 9.1 Fabrication of bimorph force sensor

A piezo ceramic actuator as shown in **Fig. 9-1** was purchased from FUJI CERAMICS Corp. to fabricate the force sensor. The actuator has dimensions of  $20 \times 3 \times 0.3$  mm and capacity of 20 nF (Material number: PZT, C-82). As shown in **Fig. 9-1(b)**, the bimorph consists of two slabs of lead zirconate titanate materials fasten together with a piece of shim in between. The objective of the fabrication is to connect to titanate surfaces (A and C) to one terminal of the bimorph holder and connect the middle shim of the bimorph (B) to the other terminal of the holder as illustrated in **Fig. 9-1(b)**.

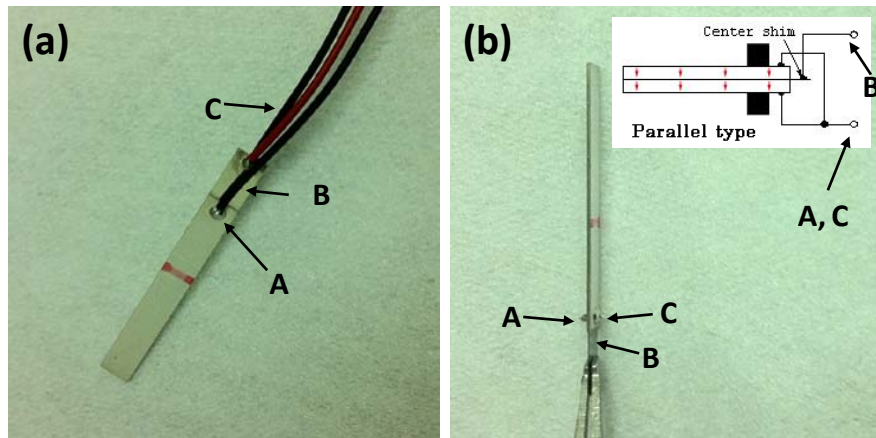


**Fig. 9-1** Photographs of the bimorph force sensor: (a) original ceramic actuator; (b) ceramic actuator with wires removed. The inset in (b) shows the wire connection diagram of the bimorph.

As illustrated in **Fig. 9-2**, a FEP sheath, a bimorph holder, two pieces of wires with 5 mm length and a piece of actuator are needed to fabricate the bimorph force sensor. First of all, the FEP sheath and bimorph holder are cleaned with toluene and ethanol, rinsed with Milli-Q water and dried to remove the grease and dirt. The connection between the wires and the bimorph surfaces are removed by soldering pit as illustrated in **Fig. 9-1 (b)**.

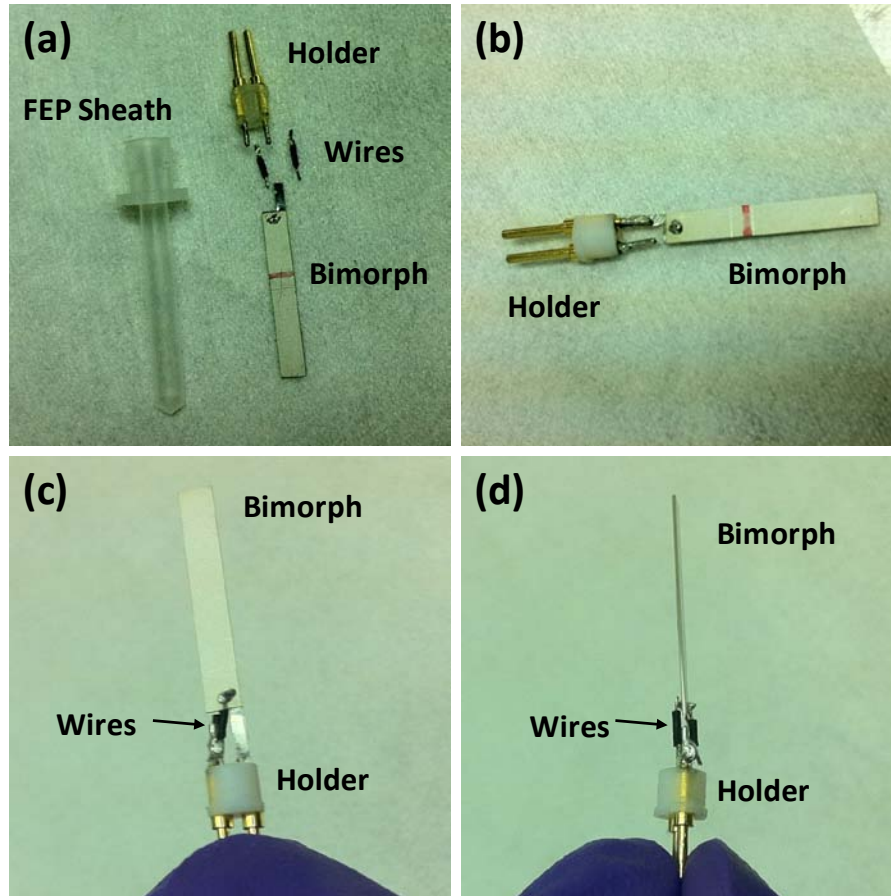


**Fig. 9-2** Photographs showing the procedures of fabricating the bimorph force sensor.

**Fig. 9-3** shows the procedure of soldering. It should be noted that the time for soldering is about 1 s, prolonging contact of soldering pit to the ceramic actuator surface will damage the actuator. The center shim is then cut into half and connected to one of the terminal of the holder, **Fig. 9-2(b)**. And then the two wires are used to connect the bimorph surfaces and the other terminal of the holder. **Fig. 9-2 (c)** and **(d)** show the pictures of the fabricated bimorph sensor. Ideally, the surface of actuator and the terminals should be on the same level, i.e., zero angle between the actuator and the terminals. The bimorph sensor prepared as such is then put into the FEP sheath (**Fig. 9-4**) and used for experiments.

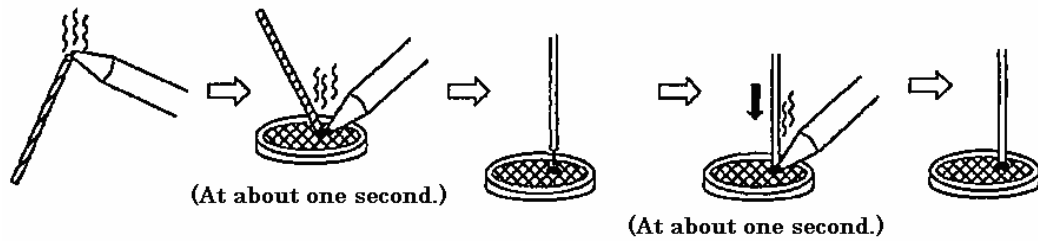


**Fig. 9-3** Schematic view of the soldering procedures to solder a wire on to a ceramic actuator surface.



**Fig. 9-4** Photograph of bimorph force sensor used in the experiments.

**Note:**

- The use of solder should be kept in a minimum amount, i.e., minimizing the size of the soldering point.
- Gloves should be worn during the whole process to avoid contamination of the holder and the actuator.
- Connect the bimorph to the charge amplifier to check the correct connection. The signal should be continuously drifting at the beginning of the measurement. An abrupt increase or decrease to saturation shows a bad connection.

**9.2 Bimorph sensor calibration**

The obtained bimorph sensor needs to be calibrated before use. The bimorph sensor is assembled into the chamber as illustrated **Fig. 4-1** and connected to the charge amplifier. Once the charge amplifier is on for 15 min, the signal should be

stabilized. By switching on/off the charge amplifier to drain the charge on the bimorph surface and changing the bias value, a stable bimorph signal or a signal with a small linear drift within the measurement time should be obtained. An example of a stable bimorph signal is illustrated in **Fig. 9-5**, the signal has an electrical noise with an amplitude of 0.02 V which can be removed in the latter data processing.

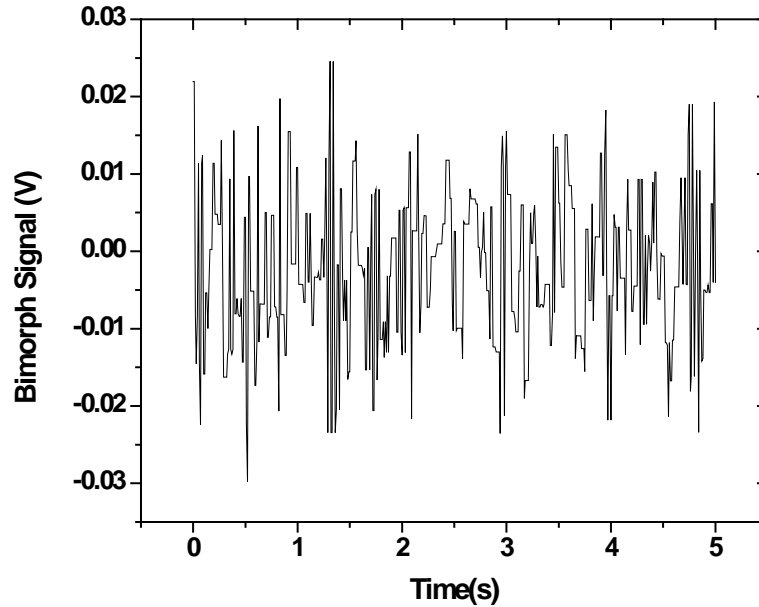


**Fig. 9-5** Example of a stable bimorph signal with electrical noise.

Once a stable bimorph signal is obtained, a small piece of platinum wire is placed at the end of the bimorph. The change of the bimorph signal is recorded either by the data acquisition software or just printing the screen. **Fig. 9-6** shows an example of screen shot which records the change of bimorph signal (from point A to B) by placing a piece of platinum wire at the end of the bimorph. The voltage change can be obtained using the scale of the y axis as a reference. For example, the change of bimorph voltage was determined to be 1.42 V from point A to B. The wire is then removed from the bimorph with tweezers. After the signal is stabilized, the procedure is repeated for another four times and the average value is used.

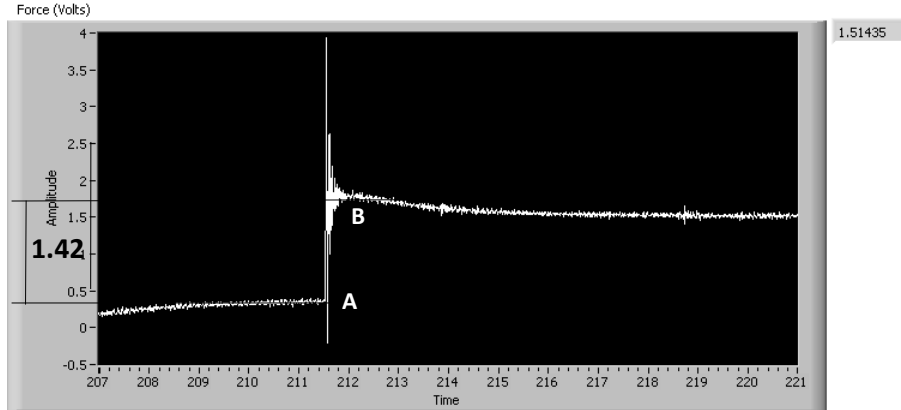


**Fig. 9-6** Example of screen shot showing the change of bimorph signal when placing a small piece of platinum at the end of the bimorph cantilever.

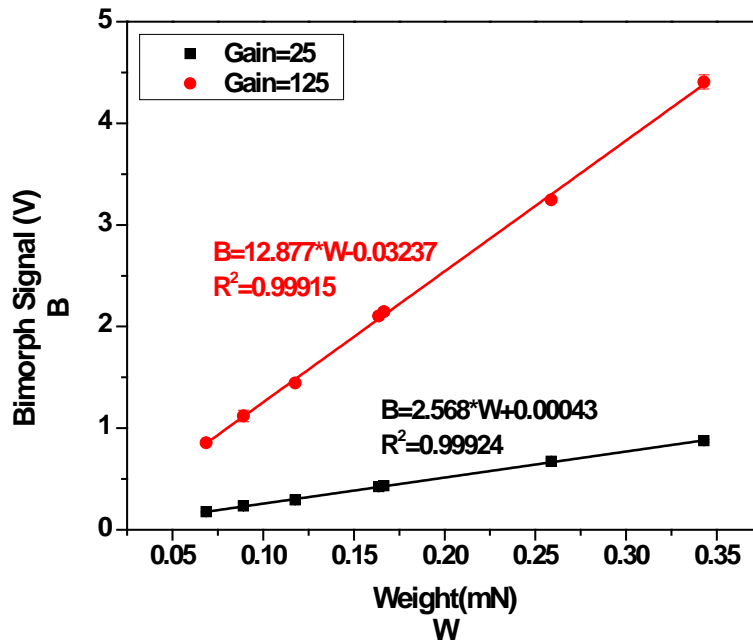


**Fig. 9-7** Calibration of bimorph force sensor with proportional gain of 25 and 125.

Several pieces of platinum wires should be used to calibrate the bimorph cantilever, and the corresponding voltage change is plotted as a function of platinum wire weight. **Fig. 9-7** shows the change of bimorph signal as a function of weight applied at the end of the cantilever with proportional gain of 25 and 125, seven different wires were used. As can be seen, excellent linear fitting was obtained, demonstrating that the bimorph cantilever is a good force sensor to measure the interaction force. The obtained slope referred as bimorph constant

can be used to convert the bimorph signal to the interaction force, i.e., interaction force = bimorph signal/slope. Since the bimorph constant varies with the change of the bimorph clamp position, the bimorph constant needs to be calibrated before disassembling the bimorph from the chamber after experiments. However, only two pieces of wires are needed in calibration, the obtained bimorph constant should be very close to the original constant value.

**Note:**

- Placing and removing the platinum wire with tweezers should be handled with extreme caution to avoid a direct touch between the tweezers and the bimorph. Tweezers with sharp tips should be used.
- The weight of the platinum wires should be chosen in such a way that the corresponding change of the bimorph signal in the calibration covers the bimorph signal range in the experiments.

### **9.3 Data Processing**

The obtained data from experiments need to be processed before use which includes noise reduction and drift correction. **Fig. 9-8** presents the raw bimorph data collected from the experiments. As it can be seen from the figure, without processing the noise is significant. The red solid line in **Fig. 9-8** demonstrates the signal after filtering the raw data with a cut of frequency of 10 Hz. With the filter, more detail information can be obtained. For example, as shown in **Fig. 9-8**, the hydrodynamic attraction during retraction can be observed.

As can be seen in **Fig. 9-8**, there is a small linear drift of the bimorph signal during the measurement. This drift can be corrected using the “subtract a straight line” function in the Origin software. Divided by the bimorph constant, the bimorph signal can be converted to the interaction force, and the results are shown in **Fig. 9-9**.

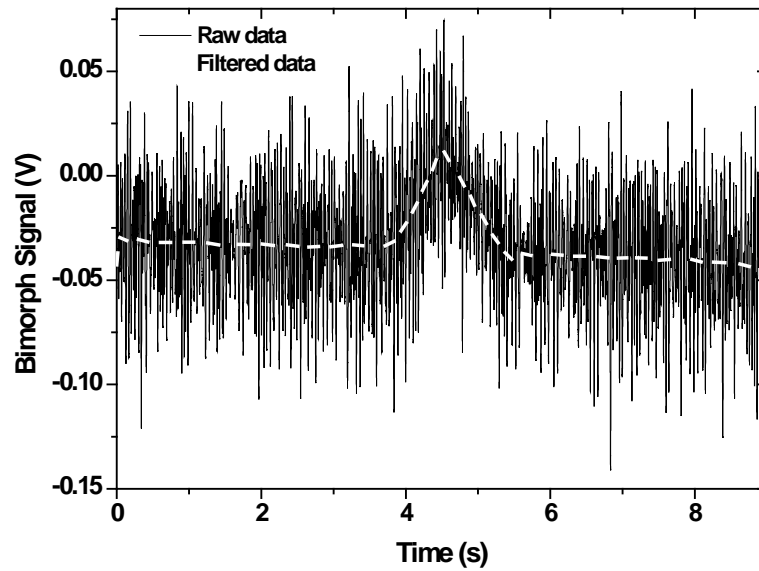


**Fig. 9-8** Bimorph signal obtained from a single measurement between an air bubble and a hydrophilic glass sphere in 1 mM KCl solution with bubble drive velocity of  $33 \mu\text{m/s}$ . Black solid line represents the raw signal and the red dash line shows the filtered data.

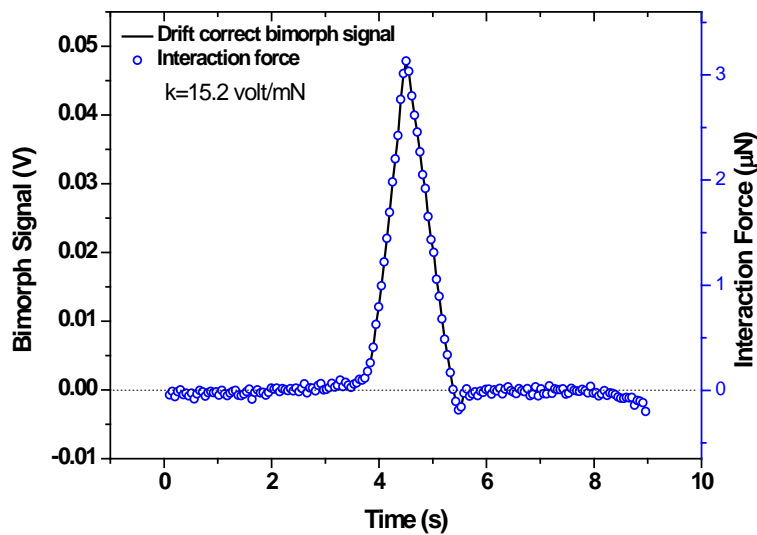


**Fig. 9-9** Processed bimorph signal (solid line) and the interaction force (circle symbol) as a function of measurement time between an air bubble and a hydrophilic glass sphere. The bimorph constant is  $15.2 \text{ V/mN}$ .

**Note:**

- Both noise reduction and drifting correction can be achieved using functions in Origin software.

Similarly, noise reduction is applied on the glass tube displacement data (**Fig. 9-10**).

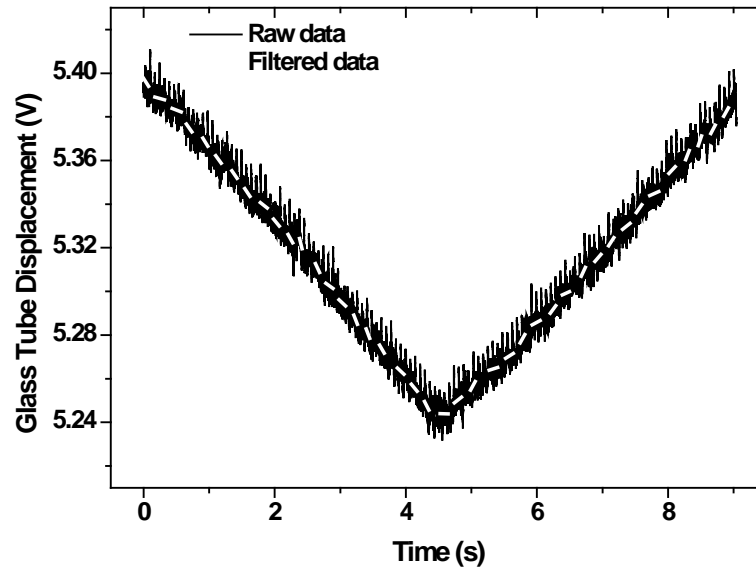


**Fig. 9-10** Glass tube displacement data,  $X(t)$ , obtained from a single measurement. Black solid line represents the raw signal and the red dash line shows the filtered data.

The glass tube displacement,  $X(t)$  ( $\mu\text{m}$ ) can be obtained using the equation below:

$$X(t) (\mu\text{m}) = k_g * X(t) (\text{V})$$

Where  $k_g = 993.4 \mu\text{m/V}$  is the calibration factor of the glass tube displacement. The results are presented in **Fig. 9-11**.

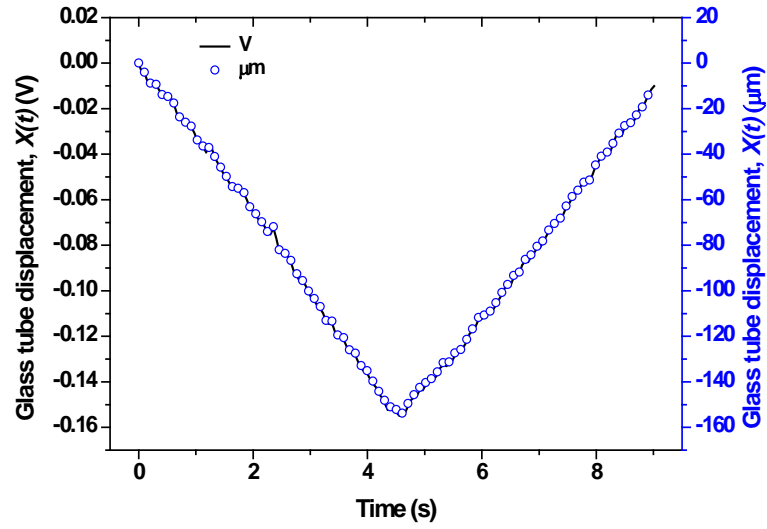


**Fig. 9-11** Processed glass tube displacement,  $X(t)$ , as a function of measurement time in unit of V (solid line) and  $\mu\text{m}$  (circle symbol).

The interaction force as a function of glass tube displacement,  $X(t)$ , can then be obtained and the results are shown in **Fig. 9-12**.

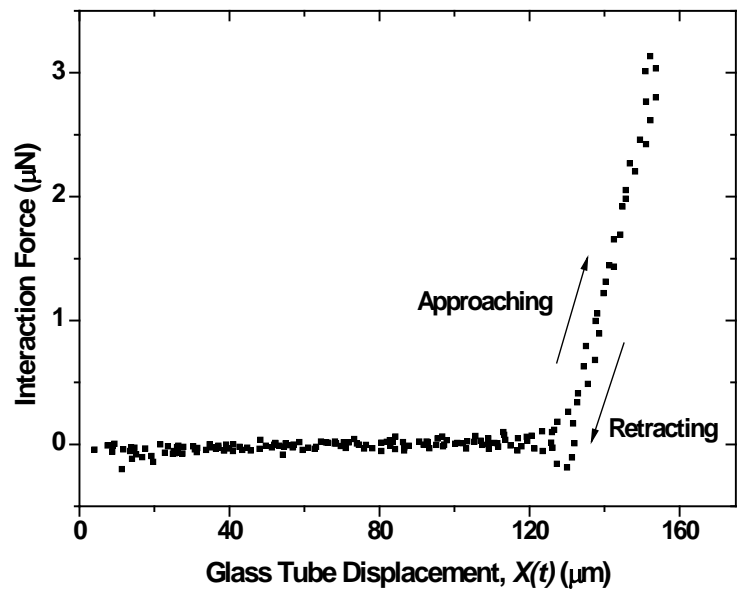


**Fig. 9-12** Interaction force between an air bubble and a hydrophilic glass sphere as a function of glass tube displacement,  $X(t)$ .

## 9.4 Sensitivity study

A reproducibility test of the ITFDA was conducted to study the instrument sensitivity. The interaction forces between an air bubble and a hydrophobized glass sphere of  $\theta_a = 37.4^\circ$  in 1 mM KCl solution of pH 5.6 were measured using the ITFDA and the results are shown in **Fig. 9-13**. In this set of experiments, the initial separation and the maximum glass tube displacement were set as 120  $\mu\text{m}$  and 240  $\mu\text{m}$ , respectively. The glass tube drove the air bubble towards the glass sphere in 2 s to give an approach velocity of 120  $\mu\text{m/s}$ . Very similar force curves were obtained, i.e., the film ruptured during the approach cycle at point A with the force barrier of  $0.112 \pm 0.006$  V and induction time of  $0.42 \pm 0.03$  s, the air bubble detached from the glass sphere with adhesion of  $0.74 \pm 0.01$  V, showing a good reproducibility of the instrument.

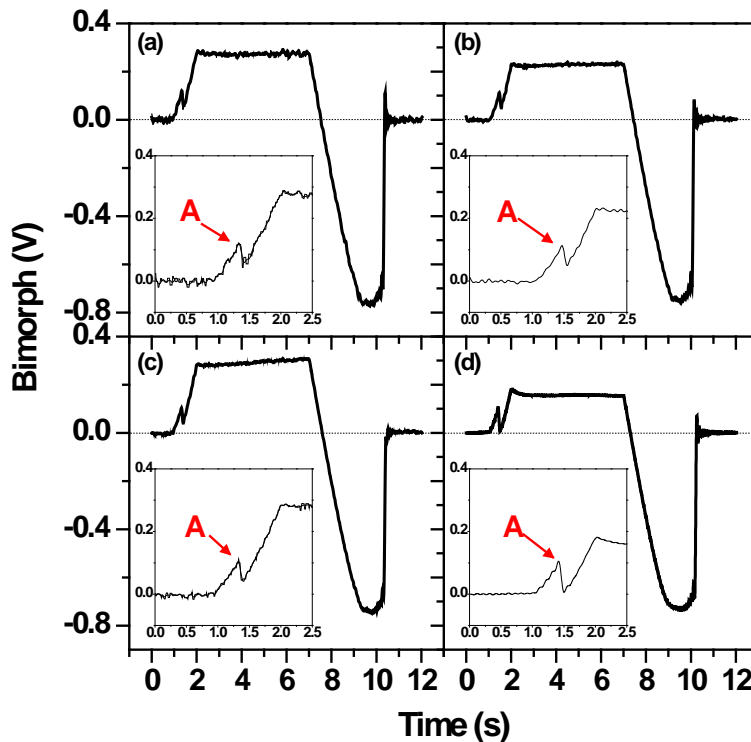


**Fig. 9-13** Four consecutive force curves measured by the ITFDA between an air bubble and a hydrophobized glass sphere of  $\theta_a = 37.4^\circ$  in 1 mM KCl solution at pH 5.6. Insets show the signal profiles where the film rupture happened.

It should be noted that the maximum force reached during the entire interaction (i.e., holding of the air bubble on the glass sphere) was different between different measurements. For example, the maximum force reached in **Fig. 9-13(d)** is 0.182 V, much smaller than the other three (~0.26 V). As mentioned earlier, the initial separation and the maximum glass tube displacement were set as 120  $\mu\text{m}$  and 240  $\mu\text{m}$ , respectively. However, due to the limited resolution of the CCD camera, the initial separation between the air bubble and the glass sphere varies around  $120 \pm 6 \mu\text{m}$ . The minor difference of the initial separation distance will affect the maximum force reached at the end of approach cycle. With the maximum glass tube displacement remains the same, a larger initial separation distance will result in a smaller maximum force, or vice versa. For example, the observed decrease in the maximum force in **Fig. 9-13(d)** is probably due to a slightly larger initial separation distance. The tests show that the force barrier, induction time and the adhesion are independent of the initial separation distance. For this reason, only force barrier, induction time and adhesion were reported in the entire thesis, and the maximum force reached during the interaction is not considered as a parameter.

### 9.5 Contact angle measurement

As illustrated in **Fig. 4-11**, use of the image analysis makes it possible to obtain the geometric properties of interfaces in the air bubble-glass interactions. **Fig. 9-14** illustrates the determination of the contact angle  $\theta$  between two circles at the intersection of C. Points A and B are the center of the two circles, respectively.  $\theta$  can be calculated by the following equation:

$$\begin{aligned}\theta &= \theta_1 + \theta_2 \\ &= \arcsin\left(\frac{r}{R_1}\right) + \arcsin\left(\frac{r}{R_2}\right)\end{aligned}$$

Where  $r$  is the radius of the contact area between two circles,  $R_1$  and  $R_2$  are radii of the two circles, respectively.

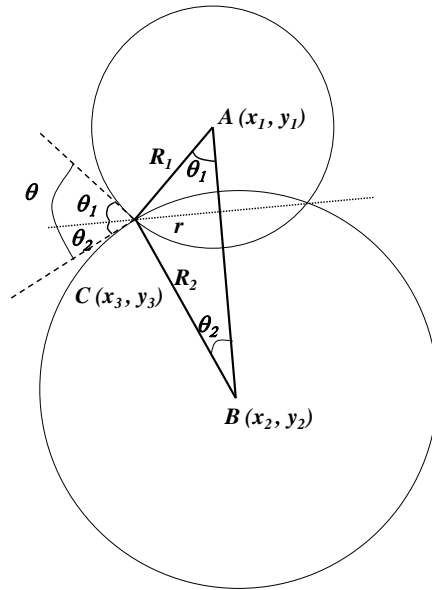


**Fig. 9-14** A schematic view showing the determination of the contact angle  $\theta$  at intersection C between two circles.

**Note:**

- All the parameters mentioned above can be obtained using the image analysis program.
- In the image analysis program, 1 pixel = 6  $\mu\text{m}$ .